



M Ű E G Y E T E M 1 7 8 2



BUDAPEST UNIVERSITY OF TECHNOLOGY AND ECONOMICS
Faculty of Transportation Engineering and Vehicle Engineering



Department of Aeronautics, Naval Architecture and Railway Vehicles

VIRTUAL PROTOTYPING OF GAS TURBINE COMPONENTS – AERODYNAMIC REDESIGN AND ANALYSIS OF ACADEMIC JET ENGINE

PhD thesis

by Mrs. Foroozan Zare

Dr. Árpád Veress
Supervisor

Budapest, 2020

To

My parents

Table of Contents

Acknowledgments.....	5
Declaration.....	6
Nomenclature	7
Abstract.....	13
1. Introduction	15
1.1. Aims and Outline of the Thesis	15
1.2. Organization of the Thesis	16
1.3. Introduction of Gas Turbines	17
2. Mathematical Model Development for Thermo-Dynamic Cycle Analysis and Optimization of Turbojet Engines.....	21
2.1. Introduction	21
2.2. Novel Closed-Form Expression for Critical Pressure and Optimum Pressure Ratios of Turbojet Engines.....	23
2.3. Modell Development for Thermo-Dynamic Cycle Analysis of Turbojet Engines with Verification and Plausibility Check	30
2.3.1. Triple-Spool Mixed Turbofan Jet Engine	30
2.3.2. Dual-Spool Mixed Turbofan Engine.....	41
2.3.3. Single-Spool Turbojet Engine without Afterburner.....	44
2.4. Verification and Plausibility Check of the New Equation for the Optimum Compressor Total Pressure Ratio	47
2.4.1. Analysis of Single-Spool Turbojet Engines with Afterburning.....	47
2.4.2. Numerical Representation – Verification of the New Equation for Optimum Total Pressure Ratio of the Compressor	49
2.5. Conclusions	53
3. Redesign of the Academic Turbojet Engine	55
3.1. Introduction	55
3.2. Design Process of the Gas Turbine.....	57
3.3. General Concerns and Design Aspects.....	58
3.4. Redesign Procedure of the Turbojet Engine	59
3.5. Conclusions	62
4. CFD Analysis of the Redesigned Academic Jet Engine	63
4.1. Flow Modelling of the Separated Engine Components	64
4.1.1. CFD analysis of the centrifugal compressor	64

4.1.2.	CFD analysis of the combustion chamber	67
4.1.3.	CFD analysis of the axial turbine	71
4.1.4.	CFD analysis of the exhaust nozzle.....	74
4.2.	CFD Analysis of the Full Model.....	76
4.3.	Conclusions	80
5.	Discussion, Conclusion and Verification of the Results	81
5.1.	Verification of the results.....	81
5.2.	Conclusions	85
6.	Novel Application of Inverse Design Method by Means of Redesigning Compressor Stator Vanes in the Redesigned Jet Engine	86
6.1.	Introduction of Optimization Methods for CFD in General	86
6.2.	Inverse Design Based Optimization	90
6.3.	Redesign and Optimization of the Compressor Vanned Diffuser for the Academic Jet Engine	91
6.4.	Verification of the Results by ANSYS CFX.....	99
6.4.1.	Inviscid analysis of the optimized vane (at Rooftop $C_p=-1.8$) by CFX	99
6.4.2.	Viscous analysis of the optimized (at Rooftop $C_p=-1.8$) vane by CFX	101
6.5.	Conclusions	105
7.	Conclusions	107
8.	List and Summary of the Thesis	111
	Bibliography	115
	Author's Publications	122
	APPENDIX A – Aerodynamic Redesign of the Academic Jet Engine's Components	124
A.1	Compressor Design and Analysis	125
A.2	Inlet Channel.....	137
A.3	Design Aspects of the Combustion Chamber	138
A.4	Turbine Design	140
A.5	Aspects and Design of Exhaust Nozzle.....	156
	APPENDIX B - Introduction of the Used CFD Methodology by Means of ANSYS CFX.....	157
B.1	Governing Equation	158
B.2	Turbulence Modelling [48].....	158
B.3	Spray Breakup Models for Combustion	159
B.4	Combustion.....	163
B.5	Numerical Method.....	164

APPENDIX C - Numerical Algorithm of 2D Inhouse Inviscid Flow Solver [54]	166
C.1 Governing Equations.....	167
C.2 Finite Volume Discretization Method	167
C.3 Boundary Conditions.....	169
C.4 Wall Modification Algorithm.....	170
APPENDIX D - Constrained Optimization [54].....	172
D.1 Introduction.....	173
D.2 Stratford's Separation Prediction Method	173
D.3 Constrained Optimization of Stratford's Limiting Pressure Distribution	174

Acknowledgments

First, I am deeply grateful to my supervisor Dr. Árpád Veress for his guidance, support and encouragement. The completion of this dissertation would not have been possible without the support of my supervisor. I consider myself very fortunate for having conducted this research under his supervision.

I would like to show appreciation to my colleague Mr. László Sábitz and Mr. Attila Gubovits for the valuable support, guidance and suggestions throughout my work and improving my knowledge.

I would like to express my special thanks to Dr. Dániel Rohács, head of Department, who provided me consultation for the present dissertation.

I am thankful to Dr. Abbas Talimian, my colleague, for the useful remarks during our frequent discussions and his guidance. This thesis has been done with his kind support on my work.

I also would like to express thanks to the members of the Department of Aeronautics, Naval Architecture and Railway Vehicle for their endless support in improving my knowledge about aircraft engines and providing friendly atmosphere as well.

Finally, I would like to offer my heartfelt thanks to Mr. Gábor Rácz and Mr. Roland Rákos in the Engineering Calculations Team at Knorr-Bremse R&D Center Budapest for their endless and kind guidance and support in the field of CFD modelling and analysis.

The present work has been supported by the Hungarian national EFOP-3.6.1-16-2016-00014 project, titled "Investigation and development of the disruptive technologies for e-mobility and their integration into the engineering education" (IDEA-E).

Declaration

Undersigned, Zare Foroozan, I hereby state that this PhD thesis is my original own work, which has been done after registration for the degree of PhD at *Budapest University of Technology and Economics, Faculty of Transportation Engineering and Vehicle Engineering, Kálmán Kandó Doctoral School of Transportation and Vehicle Engineering* and has not been previously included in a thesis or dissertation submitted to this or any other institution for a degree, diploma or other qualifications. I have used only the sources listed in the Bibliography in the thesis. All parts taken from other works, either in a word for word citation or rewritten keeping the original contents, have been unambiguously marked by a reference to the source.

Berlin, 31.12.2020.

.....
Foroozan Zare

Nomenclature

Variables (Latin)

A	Cross sectional area [m ²]
a	Speed of sound [m/s]
B	Boundary layer blockage [-]
b	Meridional depth of passage [m]
C_f	Specific heat of the fuel [J/kg/K]
C_p	Specific heat at constant pressure [J/kg/K], Pressure coefficient [-]
C_{pD}	Pressure recovery coefficient [-]
\bar{C}_p	Mean (between T_i and T_{i+1}) specific heat at constant pressure [J/kg/K], Canonical pressure distribution [-]
c	Absolute velocity [m/s], Chord length [m]
D	Diameter [m], Jacobian [variable]
D_{Nozzle}	Injector nozzle diameter [m]
D_p	Droplet diameter [m]
E	Specific total energy [J/kg]
\vec{e}_x, \vec{e}_y	Signs of vector components in x and y directions in Cartesian coordinate system
$F(U), G(U)$	Inviscid flux vectors [variable]
f	Fuel to air mass flow rates ratio [-]
H	Altitude [m], Vector of numerical flux function [variable]
h	Specific enthalpy [J/kg],
h_{tot}	Specific total enthalpy [J/kg]
K	Loss coefficient [-]
k	Turbulence kinetic energy per unit mass [J/kg], Boltzmann constant [J/K]
L_0	Theoretical air mass required to burn 1 kg fuel at stoichiometry condition [kg/kg]
l	Blade length [m]
M	Mach number [-], Moment [Nm]
\dot{m}	Mass of flow rate [kg/s]
\dot{m}_{air}	Air mass flow rate enters in the engine [kg/s]
\dot{m}_{nozzle}	Mass flow rate of injector nozzle [kg/s]
N	Rotational speed [rev/min]
N_b	Number of boundaries
n_x, n_y	Components of local outward pointing unit normal vector [-]
P	Power [W]
p	Pressure [Pa]
pr_{stage}	Pressure ratio (static/total) [-]
Q	Heat [J/s]

Q_R	Lower heating value of the fuel [J/kg]
$q(\lambda)$	Dimensionless mass flow rate – gas dynamic function [-]
R	Specific gas constant [J/kg/K], Relative radius [-]
\mathbf{R}	Set of real numbers
\Re	Residual [variable]
\mathbf{R}^+	Set of positive real numbers
Re	Reynolds number [-]
RPM	Revolution per Minute [1/min]
r	Total pressure recovery factor [-], Radius [m], Degree of reaction [-]
S	Entropy [J/s]
\mathbf{S}_M	Momentum source [kg/m ² /s ²]
\mathbf{S}_E	Energy source [kg/m/s ³]
s	Specific entropy [J/kg]
T	Temperature [K], Thrust [N]
$TSFC$	Thrust Specific Fuel Consumption [kg/kN/h]
t	Time [s], Blade pitch [m]
\mathbf{U}	Vector of conservative variables [variable], Velocity vector [m/s]
$U_{P,initial}$	Initial velocity of droplet [m/s]
u	Component of velocity vector in x direction [m/s], Tangential (blade or frame) velocity [m/s]
V	Velocity [m/s]
V_n	Normal velocity to the interface [m/s]
v	Component of velocity vector in y direction [m/s], Courant number
W	Power [W], Vector of characteristic variables [variable]
W_x	Total shaft power per unit mass flow rate [J/kg]
w	Component of velocity vector in z direction [m/s], Relative velocity [m/s]
x	Cartesian coordinate in space [m]
y	Cartesian coordinate in space [m]
y^+	Dimensionless wall distance [-]
z	Number of blades [-]

Variables (Greek Symbols)

α	Absolute direction (angle) [degree], Inlet flow angle [degree]
α_k	Constant for the Runge-Kutta time iteration [-]
β	By-pass ratio [-], Relative direction (angle) [degree], Gas dynamic constant [-]
Γ	Boundary of the control volume (domain, face in 2D) and cell face (edge in 2D) length [m]
γ	Ratio of specific heats [-]
Δ	Difference [-]

δ	Boundary layer thickness [m]
δ_{bc}	Air income ratio due to the turbine blade cooling [-]
δ_{tech}	Bleed air ratio for technological reasons [-]
ε	Reduction rate of cross section due to the blades [-]
η	Efficiency [-]
$\Lambda(x,y)$	Domain in x, y space
λ	Thermal conductivity [W/mK], Swirl factor [-], Dimensionless velocity [-]
μ	Dynamic viscosity [kg/s/m]
ν	Kinematic viscosity [m ² /s]
ξ	Power reduction rate of the auxiliary systems [-]
π	Total pressure ratio [-]
$\pi(\lambda)$	Dimensionless pressure – gas dynamic function [-]
ρ	Density [kg/m ³]
σ	Slip factor [-]
τ	Elements of the stress tensor [N/m ²], Shear stress [N/m ²]
$\boldsymbol{\tau}$	Stress tensor
$\tau(\lambda)$	Dimensionless temperature – gas dynamic function [-]
φ	Speed coefficient [-]
Ω	Area of the control volume (domain, face in 2D) and finite volume (domain, face in 2D) [m ²]
ω	Specific turbulence dissipation rate [1/s], Angular velocity [1/s]

Subscripts and Superscripts

A	Afterburner
a	Axial component
al	Afterburner liner
b	Burning
bc	Blade cooling
C	Compressor
c	Compressor, Critical
$crit$	Critical
cc	Combustion chamber
d	Diffuser, derivative
f	Fuel, Fan, Flow
h	Hub
hp	High pressure
i,j,k	Variables for spatial and sum indexing
id	Ideal
in	Inlet

<i>init</i>	Initial
<i>ip</i>	Intermediate pressure
<i>L</i>	Left side of the cell interface
<i>Le</i>	Leading edge
<i>lp</i>	Low pressure
<i>m</i>	Mechanical, Meridional, Mean
<i>mix</i>	Mass flow weighted parameter for air-gas mixture
<i>n</i>	Nozzle, Variables normal to the surface
<i>n+1</i>	Parameter at the boundary (next time step)
<i>opt</i>	Optimum
<i>out</i>	Outlet
<i>p</i>	Particle
<i>R</i>	Right side of the cell interface
<i>r</i>	Rotor
<i>req</i>	Required
<i>rotor</i>	Impeller of the compressor
<i>s</i>	Isentropic, Specific, Stator
<i>st</i>	Stoichiometric condition
<i>stage</i>	Compressor stage
<i>stat</i>	Static
<i>T</i>	Turbine
<i>TE</i>	Trailing edge
<i>t</i>	Tip
<i>tech</i>	Bleed air mass flow rate or ratio removal for technological reason
<i>th</i>	Thermal, Theoretical
<i>tot, to</i>	Total
<i>u</i>	Tangential component
<i>w</i>	Tangential (whirl) component
<i>w1</i>	Parameters at the relative flow velocity at segment 1
<i>w2</i>	Parameters at the relative flow velocity at segment 2
<i>wm</i>	Parameters at the mean relative flow velocity between segment 1 and 2
θ	Tangential (component)
<i>o</i>	Degree, Parameters at maximum velocity (minimum pressure) at Stratford's method
<i>0</i>	Stagnation or total condition (e. g.: enthalpy, pressure, temperature)
<i>1</i>	Impeller inlet or eye, Upstream condition
<i>2</i>	Impeller outlet or tip
<i>3</i>	Inlet section of the vanned diffuser
<i>4</i>	Diffuser exit

1, 2, 3	Number of turbine and compressor spool
0-9	Engine cross sections
∞	Parameters at far upstream condition, Infinite

Accents and Operators

–	Average, Vector
→	Vector
^	Roe's average state space
∇	Nabla operator
⊤	Transpose of a vector or matrix
∂	Symbol of derivative
δ	Identity matrix or Kronecker Delta function

Abbreviations

ACO	Ant Colony Optimization
APU	Auxiliary Power Unit
BVM	Burning Velocity Model
CAB	Cascade Atomization Breakup
CAD	Computer Aided Design
CFD	Computational Fluid Dynamics
CMC	Ceramic Matrix Composite
D	Dimension
DNS	Direct Numerical Simulation
DS	Directional Solidification
EA	Evolutionary Algorithms
ECFM	Extended Coherent Flame Model
EDM	Eddy Dissipation Model
ES	Evolutionary Strategy
ETAB	Enhanced Taylor Analogy Breakup
FEM	Finite Element Method
FDM	Finite Different Method
FRC	Finite Rate Chemistry
GA	Genetic Algorithm
GP	Genetic Programming
GUI	Graphical User Interface
HP	Horsepower, High Pressure
ILU	Incomplete Lower Upper
ISRE	Isentropic Radial Equilibrium Equation

LCS	Learning Classifier System
LP	Low Pressure
MUSCL	Monotone Upstream Schemes for Conservation Laws
NBC	Numerical Boundary Condition
PBC	Physical Boundary Condition
PDF	Probability Density Function
PSD	Power Spectral Density
ps	Pressure side
R&D	Research and Development
RANS	Reynolds Averaged Navier-Stokes
Re	Reynolds number
RK	Runge-Kutta
RPM	Revolution per Minute
SA	Simulated Annealing
SQP	Sequential Quadratic Programming
SST	Shear Stress Transport
ST	Specific Thrust
SX	Single Crystal Alloy
ss	Suction side
TAB	Taylor Analogy Breakup
TBC	Thermal Barrier Coating
TFC	Turbulent Flame Closure
TSFC	Thrust Specific Fuel Consumption
TMB-C ₉ H ₁₂	1,2,4 Trimethylbenzene
UAV	Unmanned Aerial Vehicle
vs.	versus

Abstract

Today, beside many known applications of the gas turbine engines as in the energy sector for example, the turbojet engines – as the specific type of the gas turbines – are the most relevant propulsion systems for aeronautical applications at low-speed supersonic flow regime between the low by-pass and ramjet engines. Moreover, they can be an essential platform amongst the gas turbine engines for establishing new contributions in development processes. Hence, the main goal of the present thesis is

- i. to determine, verify and validate calculation processes, which can be used for modelling, design and analysing jet engines in aerodynamic point of view with especial care for an academic jet engine under investigation,
- ii. to introduce new calculation approaches for improving accuracy and advancing/optimising technical characteristics of the investigated propulsion system and
- iii. to provide information about the actual status, application range, advantages, challenges of the applied mathematical models and tools in the R&D environment.

The aerodynamic design process consists of five main steps.

1. The first step is the thermodynamic cycle analyses to determine the desired operational point with the outcomes of the thermodynamic state variables at each cross section of the engine, which satisfies the expected goal functions. Although the subject of the present thesis is a single spool academic turbojet engine, the thermodynamic model developments are introduced for other single-, dual- and triple-spool jet engines for the sake of complexity. The $T-s$ diagram and the main characteristics of the engines are determined by concentrated parameter-distribution type methods implemented in MATLAB environment. The governing equations are based on mass, energy balance and thermodynamical processes with viscous flow assumption. As many information are available in the open literature about single-, dual- and triple-spool engines are considered, nonlinear constraint optimization method is used for identifying the unknown parameters as losses, efficiencies and technical data in case of they are not available and in case of need. The temperature and component mass fraction dependent gas properties are calculated by iteration cycles in case of functional dependencies. A new closed-form expression (the unknown parameter is calculated by an analytical equation directly/explicitly) is derived for determining the critical pressure in choked flow condition at converging nozzle with considering losses and process-dependent gas properties. New explicit equation is derived also and verified for calculating the optimum total pressure ratio of the compressor pertaining at maximum specific thrust at choked and unchoked nozzle flow conditions for single-spool turbojet engines.
2. The second step of the design process, in general, is the determination of the RPM and main geometrical sizes of the engine [1] following the cycle analyses and making decision about the operational point of the jet engine by using the TSFC-ST (Thrust Specific Fuel Consumption – Specific Thrust) map in the function of turbine inlet total temperature and total pressure ratio of the compressor. However, in the present case, as centrifugal compressor is selected for pressurizing the ambient air, the RPM and main geometrical sizes of the engine are determined by the mean line design of the centrifugal compressor assembly and turbine.
3. The third step of the design process is the mean line and the 3D design of the engine components as intake channel, compressor, combustion chamber, turbine and nozzle. The outcomes of the design are the all necessary dimensions for creating the 3D geometry of the jet engine. Based on the known or established dimensions, the 3D model of the gas turbine is created in a CAD software.

4. Following the model verification in the fourth step, Computational Fluid Dynamics (CFD) analyses are completed to crosscheck the differences between the designed and the analysed characteristics. The results of the CFD simulations are compared with the available measured data and conclusions are drawn about the efficiency of the used analytical and numerical methods.
5. Finally, in the fifth step, inviscid inverse design method has been implemented and applied for redesigning compressor vanned diffuser of the academic jet engine. The fluid dynamic results of the redesigned vane structure are verified by a commercial CFD software by means of inviscid and viscous flow assumptions. The effect of the new geometry is compared also with the baseline one.

The above mentioned 5 steps design process focuses on the aerodynamic design only. The other contributions as mechanical (both static and dynamic (e.g.: collision)), vibration (e.g.: eigenfrequencies, harmonic response, PSD (Power Spectral Density)), thermal, fatigue, creep, wearing, durability and ageing aspects of the solid components and joints including design loops together with the already mentioned aerodynamic design scenarios and extending that with control, electronics, tests, production related topics and investigating off-design performances for instance are indispensable part of the design process but they are excluded from the present study.

1. Introduction

1.1. Aims and Outline of the Thesis

The goal of the present thesis is to determine, verify and validate calculation processes, which can be used for modelling, design and analysing jet engines in aerodynamic point of view with especial care for a specific single spool academic jet engine under consideration. The introduction of new calculation approaches for improving accuracy and technical characteristics of the investigated propulsion systems with providing information about the actual status, application range, advantages and challenges of the considered mathematical models and tools in the R&D environment are also the part of the present work. Beside the available triple-, dual- and single-spool turbojet engines with their characteristics found in the international open literature due to the highest technical coverage with respect to the thermodynamic analysis, a single spool academic turbojet engine is considered in the redesign process. The basis of the applied single spool engine is the TSz-21 starter gas turbine, which was used originally for MiG-23 and Szu-22 Russian fighters. This engine has been reconstructed to be an academic jet propulsion system by Dr. Beneda and Dr. Pásztor from 2005-2008 and it is still under development with especial care for control systems [2].

The presented aerodynamic design process has four main steps as

1. Thermo-dynamic cycle analysis for determining the design (operational) point,
2. Mean line and 3D design of the engine for having geometrical sizes and CAD models,
3. Computational Fluid Dynamics (CFD) analysis for verification of the design and plausibility check by the available data and
4. Inverse design of the solid walls, vanned diffuser in the present case.

Following the market research, the determination of the customer requirements, the specifications and the selection of the cycle type of the turbomachinery layout, the first step of the engine design is the thermodynamic cycle analysis for determining the design point. A concentrated parameter distribution-type method has been developed, implemented and verified for analysing the characteristics of jet propulsion engines by means of a) available or b) expected specifications as follows.

- a) Regarding the scenario about the available specifications due to the extended technical coverage, the following triple-, dual- and single-spool turbojet engines are considered in the analyses [3]:
 - i. HK-32 and HK-25 triple spool mixed turbofan engines at take-off condition with afterburner,
 - ii. HK-22 and HK-144A dual spool mixed turbofan engines at take-off and at flight conditions with and without afterburning respectively, HK-8-4 and HK-86A dual spool mixed turbofan engines at take-off condition without afterburning and
 - iii. ВД-7 and KP7-300 singles spool turbojet engines without afterburner and ПД-9Б and the АЛ-21Ф3 single spool turbojet engines with afterburning at take-off condition. (The last two engines are considered also for verification and plausibility check of the new equations for the optimum compressor total pressure ratio.)

The developed mathematical model for analysing the above-mentioned engines is based on the mass and energy balance together with the thermo-dynamic process equations including frictional (viscous) flow related losses. Constrained nonlinear optimisation is used for determining the unknown parameters as efficiencies, losses, power reduction rates of the auxiliary systems, bleed air ratios for technological reasons, air income ratios due to blade cooling and total temperatures in the afterburner (if it is the case) for example by means of having parameter-state, which provides the closest results to the available thrusts

and thrust specific fuel consumptions. The temperature and component mass fraction dependent gas properties as specific heat at constant pressure and ratio of specific heats are determined by iteration cycles. As part of the model development, a new closed-form equation is derived for determining the critical pressure in choked flow condition at converging nozzle with considering losses and process-dependent gas properties. New explicit expression is derived also for calculating the optimum total pressure ratio of the compressor pertaining at maximum specific thrust at choked and unchoked nozzle flow conditions. ПД-9Б and the АЛ-21Ф3 single spool turbojet engines with afterburning at take-off condition are used for verification and plausibility check of the new equation about the optimum compressor total pressure ratio.

b) Concerning the case about the expected specifications or design scenario in other words, the already developed and verified thermodynamic cycle analysis mentioned in point a) above is used to redesign the TSz-21 gas turbine to have a 330 N thrust low sized academic jet engine. The specific thrust and thrust specific fuel consumption distributions are determined in the function of the turbine inlet total temperature and compressor total pressure ratio by the thermodynamic analysis for determining the operating point of the engine.

The second step of the engine aerodynamic design is the determination of the geometrical sizes and CAD model preparation of the assembly. The mean line design and its 3D extension have been considered, realized for creating the compressor and turbine segments in line with the outcomes of the thermo-dynamical cycle analysis described in point b) above. The configuration and the sizing of the intake channel as well as the combustion chamber and exhaust nozzle are determined by using the dimensions of the compressor and turbine, beside guidelines, theoretical and practical solutions, suggestions and experiences for shaping. As the all geometrical dimensions become available at the end of this state, the 3D model generations are completed for the intake channel, compressor, combustion chamber, turbine and exhaust nozzle.

CFD analyses are performed in the third step of the design process to crosscheck the differences between the expected and the computed characteristics of the engine. Two different simulation approaches are applied for that purpose: 1. separated engine components and 2. full engine model (all engine components are together). The results of the simulations are compared with the results of the i. thermodynamic cycle analysis, ii. mean line design and iii. available measured data for verification and plausibility check. Conclusions are drawn about the agreement and the effectivity of the used analytical and numerical methods.

Finally, a 2D inviscid inverse design method is implemented and used for improving the characteristics of the vanned diffuser in the compressor in order to increase total pressure recovery factor, static pressure-rise, flow turning in axial direction and the mass flow rate per unit length beside having the expectation to keep the original geometrical configuration and dimensions as much as possible. The results of the inverse design method are verified by a commercial CFD code at both inviscid and viscous flow conditions.

1.2. Organization of the Thesis

The aims, the outline and the structure of the thesis are presented in the first chapter of the thesis along with the introduction, the global background and the research topics in the field of the gas turbines.

Deduction and introduction of novel analytical equations

- i. for the critical pressure at choked flow condition of converging nozzle and
- ii. for the compressor optimum total pressure ratio pertaining at maximal specific thrust at unchoked and choked nozzle flow conditions for single-spool turbojet engine

are completed in the first part of the dissertation's second chapter. Advanced mathematical models for cycle analyses of triple-, dual- and single-spool turbojet engines have been developed and introduced in the middle part of the chapter 2 for creating a framework for the investigations, in which losses (viscous flow) and process-dependent gas properties are considered. Finally, verification, test and plausibility investigations of the analytical cycle-analysis and the new algebraic expressions are completed and presented. The new results introduced in this chapter are appeared in Thesis 1, 2, 3 and 5.

Redesign process of the considered academic jet engine is presented in chapter 3. This part starts with a general introduction of the engine design. Then it continues with the definition of the requirements as the expected thrust (330 N) at the given ambient conditions. The next step is the thermo-dynamical cycle analyses for determining the specific thrust and thrust specific fuel consumption distribution in the function of turbine inlet total temperature and total pressure ratio of the compressor. After selecting the operational point with respect to the available technology, the compressor, the inlet diffuser, the combustion chamber, the turbine and the exhaust nozzle design are completed. The 3D model of the parts and the assembly are the output of the present step including both the solid and fluid domains. The new results introduced in chapter 3 are found in Thesis 3 and 5.

Two CFD approaches are introduced in the chapter 4 for analysing the performance of the engine. The components as compressor, inlet diffuser, combustion chamber, turbine and exhaust nozzle are investigated separately in the first approach for determining the thermo-dynamical and flow parameters. The all segments of the academic jet engine are built up in one CFD model and analysed in the second part of the chapter 4. The new results introduced in this section are in Thesis 5.

Designed (expected), analysed and measured [4] thermodynamic parameters of the engine are compared with each other and discussed in chapter 5. There are two reasons of this investigation. The first one is to get information about the relevancies of the design process by means of determining the differences between designed and analysed data. The second one is to compare the output parameters of the analyses with available measured data for plausibility check. The thermo-dynamic parameters as total temperature, static temperature, total pressure and static pressure – in case of availability – along the engine length together with the expected, calculated and available thrust are considered in the comparison. The new results introduced in chapter 5 are appeared in Thesis 3 and 5.

Implementation and application of the inverse design method are presented in the chapter 6. The vanned diffuser of the centrifugal compressor is redesigned to increase the total pressure recovery factor, static pressure rises, flow turning in axial direction and mass flow rate. The advantages of the new vane with respect to the baseline design and the verification of the used method are completed and presented by using a commercial CFD code ANSYS CFX. The new results introduced in this section are found in Thesis 4 and 5.

1.3. Introduction of Gas Turbines

The developments of the electronics, informatics, advanced materials, structural mechanics, thermo- and fluid dynamics related technologies are strongly available in the aircraft industry; significant numbers of researches are going on these areas [5, 6]. This is especially true for the turbomachinery [7] and jet engines, which are the only relevant propulsion systems of the high power commercial and military airplanes today (see Fig. 1.1) It is i. due to high power-density ratio (~ 20-30 HP/kg) compared to piston engines (~ 1-2 HP/kg) ii. due to their relatively light-weight structures and compact sizes, which makes their installation cost efficient and iii. due to their streamlining body. Additionally, gas turbines are utilized also in other sectors of industry such as oil and gas in energy production for example. Although these engines in comparison with piston ones do not have high thermal efficiency (28 to 40%) they have substantial advantages in powerfulness, simplicity and

low maintenance cost demands. The gas turbines are less sensitive for overloads; they produce less vibration due to the well balanced and rather axisymmetric rotational components. These engines have high availability (97 %) and reliability (> 99%), they have low emission (there is no lubricant in the combustion chamber and no soot during transient loads) they contain fewer moving parts and represent lower sensitivity for the quality of the fuel compared to the piston engines. Additionally, there is no need for liquid-based cooling system, but the maximum allowable temperature ($\sim 1500\text{ C}^\circ$) at the turbine inlet section must be limited due to the metallurgical reasons [8].

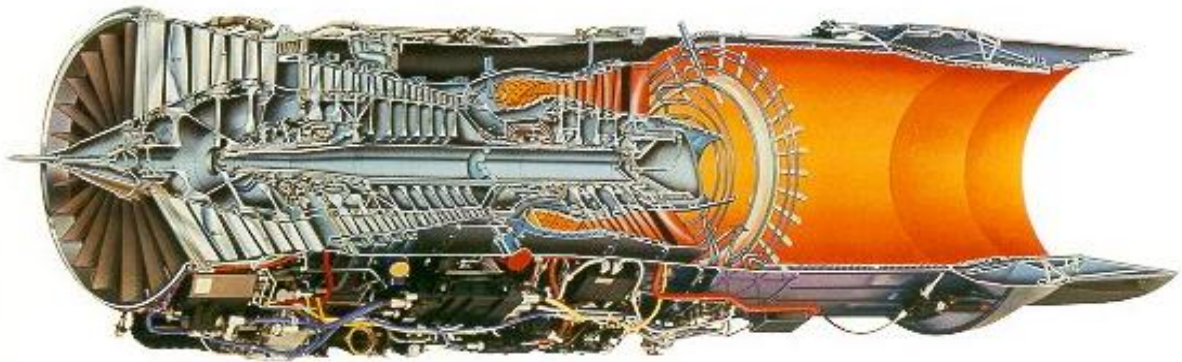
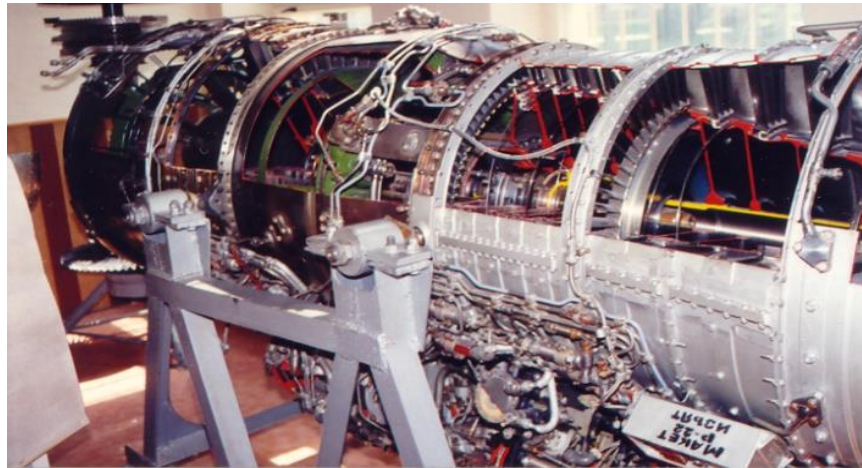


Figure 1.1 The opened real assembly of the Tumansky R-29 Turbojet engine (above) and F100-PW-229 Turbofan engine (below) [9]

The last 20 years has large effect on gas turbine technology development [10] including the advancement in materials and production. It results – in association with growing pressure ratio of compressor (e.g. the core overall pressure ratio of the Rolls-Royce UltraFan engine is aimed to be more than 70:1 for a typical large engine application [11]) and increasing turbine inlet temperature – enhancing thermal efficiency of gas turbine cycle around 40 %. The higher turbine inlet rotor temperature increases the specific core power also, which is

depicted in Fig. 1.2. The specific core power has a tendency to approach the limit of stoichiometric condition for hydrocarbons and ideal performance by using less cooling air in the combustion chamber, higher burning efficiency and pressure recovery factor, better isolation, advanced materials for improved thermal resistance and blade cooling technologies as it is shown in Fig. 1.3, where the variation of the allowable gas temperature in the turbine is also shown in the function of the year of introduction.

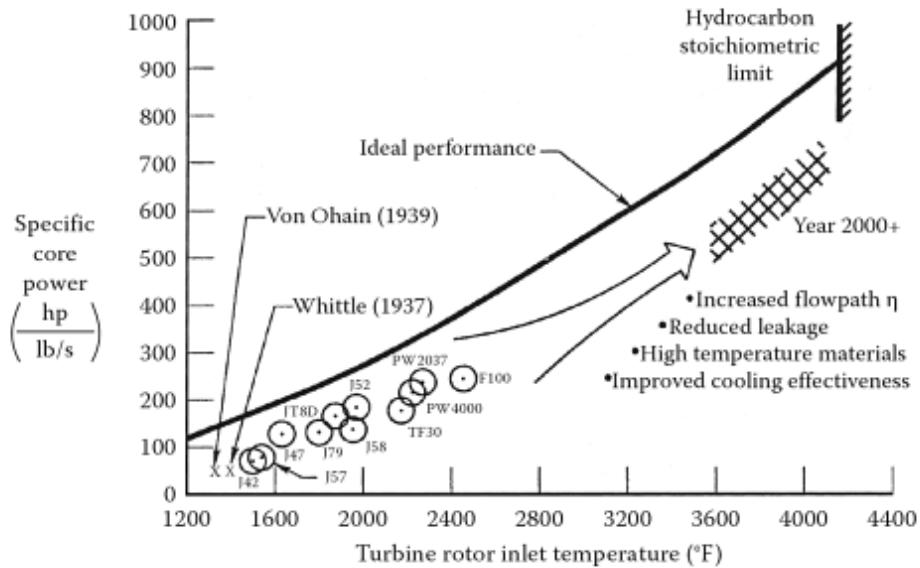


Figure 1.2 Specific core power vs. turbine rotor inlet temperature [10]

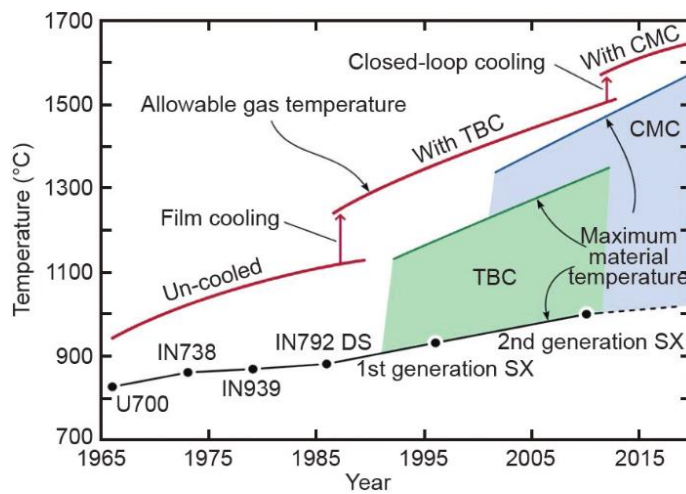


Figure 1.3 Variation of maximum allowable material and gas temperature over years (TBC: thermal barrier coating; SX: single crystal alloy; CMC: ceramic matrix composite) [12]

The gas turbines are frequently used as aero engines. Beside high reliability and high performance, satisfying operations all over the flight envelope are the key specification of their design. According to the expectation for the gas turbines, the consideration of acceptable thrust/weight ratio is essential also.

It can be summarised that improved pressure ratio of compressor and the temperature of turbine beside decreasing the losses and increasing the efficiencies are considered in the design and development processes of the gas turbines to have the expected output performance together with increasing the thrust/weight ratio.

2. Mathematical Model Development for Thermo-Dynamic Cycle Analysis and Optimization of Turbojet Engines

The extensive need and the wide-range application of gas turbines-based propulsion systems at different configurations and operational conditions are observable today. It leads the manufacturers and experts to come up with more and more effective ways of design and development by means of using several mathematical models with the optimum form and choice of the most suitable methods. This approach, so called “virtual or digital prototyping”, can significantly reduce design cost in the development processes. In order to response to the arisen expectations, following the first chapter about general introduction, the aim of the present chapter is to give overview about

- i. the available thermo-dynamical models on analyses, design and optimisation of gas turbines with especial care on jet engines by the scientific literature,
- ii. derivation novel algebraic equation for
 - a. determining the critical pressure in choked flow condition at converging nozzle with considering losses and process-dependent gas properties,
 - b. calculating the optimum total pressure ratio of the compressor pertaining at maximum thrust for single spool turbojet engine at choked and unchoked nozzle flow conditions with considering losses and process-dependent gas properties,
- iii. mathematical model development for thermo-dynamic cycle analysis of triple-, dual- and single-spool turbojet engines with verification
 - a. for the sake of the highest-level coverage in conjunction with different types of engines,
 - b. for having accurate model for the analyses and
 - c. for having basic platform for investigating the new equations and finally
- iv. analysing, testing and verifying the new expression for optimum compressor total pressure ratio introduced in point ii.

The governing equations of the advanced model developments for cycle analysis are the mass, energy balance and thermo-dynamical process-equations with viscous flow assumption. The temperature and component mass fraction dependent gas properties are calculated by iteration cycles in case of functional dependencies. Triple-, dual- and single-spool jet engines, with the available structural and operational condition, are considered for the model development and analyses in order to cover the widest range of the possible applications. The unknown input parameters as efficiencies (mechanical, isentropic of fan, compressor and turbine units, burning and exhaust nozzle), the pressure recovery rates (in the inlet diffuser, combustion chamber and afterburner or turbine exhaust pipe), the power reduction rate of the auxiliary systems, the bleed air ratio for technological reasons, the air income ratio due to blade cooling, the total pressure ratio of the intermediate pressure compressor and fan, and the total temperature in the afterburner, if they are considered in the specific cases, are determined by constraint nonlinear optimization. The goal function of the optimization is to minimize the difference between the calculated and available thrust and thrust specific fuel consumption if they are given in the datasheet of the engines found in [3].

2.1. Introduction

Beside the technical characteristics of the gas turbines today, still certain amounts of potentials are available for improving their efficiencies, power and emissions. Although the experiences and the know-how of the gas turbine manufacturers are increasing continuously, the suitable application of different mathematical models and processes can significantly contribute to decrease the cost, time and capacity in the early phase of gas

turbine design and developments. Many scientific publications are subjected to the thermodynamic-based simulation approaches, which confirm also the need for creating more accurate calculation methods.

Homaifar et al. [13] presented an application of genetic algorithms to the system optimization of turbofan engines. The goal was to optimize the thrust per unit mass flow rate and overall efficiency in the function of Mach number, compressor pressure ratio, fan pressure ratio and bypass ratio. Genetic algorithms were used in this article because they were able to quickly optimize the objective functions involving sub functions of multivariate. Although the model used here to represent a turbofan engine is a relatively simple one, the procedure would be the same with a more elaborate model. Results of assorted runs fixed with experimental and single parameter optimization results. Chocked condition was not considered, and the air and gas properties were constant or averaged at the given sections of the engine based on the used reference.

Guha [14] determined the optimum fan pressure ratio for separate-stream as well as mixed-stream bypass engines by both numerical and analytical ways. The optimum fan pressure ratio was shown to be predominantly a function of the specific thrust and a weak function of the bypass ratio. The gas properties were constant in the expression of optimum fan pressure ratio for separate-stream bypass engines at real flow condition.

Silva and his co-workers [15] presented an evolutionary approach called the StudGA which is an optimization design method. The purpose of their work was to optimize the performance of the gas turbine in terms of minimizing fuel consumption at nominal thrust output, maximize the thrust at the same fuel consumption and minimizing turbine blade temperature.

Al-Hamdan et.al [16] worked on the modelling and simulation of a gas turbine for power generation. A computer program has been developed and introduced for the simulating gas turbine components by means of satisfying the matching conditions between them analytically. The matching conditions can be analysed for design and off-design operational modes. This research can also help in designing an efficient control system for the gas turbine engine of an application including being a part of power generation plant.

Henriksson et.al [17] developed a model-based thrust estimation for turbofan engines. Two different model-based thrust estimation filters were applied to a low bypass ratio turbofan engine. The two estimators were based on a simple gross thrust model and on a thermodynamic semi-transient model, respectively. The filter parameter estimation as well as the corresponding validation of parameters was based on the use of the “leave one out cross validation” technique.

Turan [18] in 2012 investigated the design parameters on a small gas turbine by using the exergetic and energetic approaches. These parameters included the pressure ratio of compressor and turbine inlet temperature. The results demonstrated that with increasing the turbine inlet temperature is being accompanied in decreasing exergy efficiency in the investigated operating range. On the other hand, increasing the pressure ratio of compressor along with increase in flight Mach number resulted in an increasing exergy efficiency of the engine. It was declared that studying the effect of investigated parameters indicates how much improvement is possible for the small turbojet engine to achieve better energy and exergy consumption.

Khaliq et.al [19] presented a thermodynamic methodology for performance evaluation of combustion gas turbine cogeneration system with reheat. The effects of process steam pressure and pinch point temperature used in the design of heat recovery steam generator and reheat on energetic and exergetic efficiencies have been investigated. Based on the results, the present method is useful in selection and comparison of combined energy production systems from thermodynamic performance point of view.

Sanjay [20] investigated the effect of variation of thermodynamic cycle parameters on rational efficiency and component-wise non-dimensionalized exergy destruction of a basic gas turbine-based gas-steam combined cycle. It was shown that the rational efficiency is higher in case of higher turbine inlet temperature. The sum of exergy destruction of all components of the combined cycle plant was lower at higher value of compressor pressure ratio. Also, exergy destruction was minimized with the adoption of multi-pressure-reheat steam generator configuration.

Atashkari et.al [21] applied multi-objective genetic algorithms for Pareto approach optimization of thermodynamic cycle of ideal turbojet engines. A new diversity preserving algorithm was proposed to enhance the performance of multi-objective evolutionary algorithms with more than two objective functions. Beside the advancement of the new algorithm, it was shown that some interesting and important relationships among optimal objective functions and decision variables involved in the thermodynamic cycle of turbojet engines can be discovered consequently. It was also demonstrated that the results of four-objective optimization can include those of two-objective optimization and, therefore, provide more choices for optimal design of thermodynamic cycle of ideal turbojet engines.

In 2001 Lazzaretto et.al [22] presented a model for gas turbine design and off-design. The problem due to the missing information about stage-by-stage performance were overcome by constructing artificial machine maps through appropriate scaling techniques applied to generalized maps taken from the literature and validating them with test measurement data from real plants. The results of the simulations were used for neural network training: problems associated with the construction and use of neural networks was discussed and their capability as a tool for predicting machine performance was analysed.

Mattingly [23] published a detailed theoretical review about the rocket and gas turbine propulsion. There is a description also in that literature how the thermo-dynamical cycles determine the mean characteristic of the jet engines. The author presented a closed-form equation for the optimum compressor pressure ratio at maximum specific thrust at ideal (inviscid) flow condition. The effects of temperature and fuel to air ratio were not considered in parameters describe the gas properties.

As the above-mentioned scientific literatures use simplifications e.g.: - where it is relevant - excluding the effect of choked, real (viscous) flow condition at converging nozzle and some of them consider gas properties without applying local temperature and fuel to air ratio, it also confirms the need for developing physically advanced, more accurate mathematical models, calculations, equations and optimizations.

2.2. Novel Closed-Form Expression for Critical Pressure and Optimum Pressure Ratios of Turbojet Engines

New equations have been introduced in the present subchapter for the optimum pressure ratio pertaining at maximum specific thrust for single spool turbojet engine

- i. for unchoked and
- ii. for the choked flow conditions.

A novel equation is also derived for the last item (ii.) in order to consider critical pressure for converging nozzle flow. Closed-form expression means that the unknown parameter is calculated by an analytical equation directly/explicitly. The optimum pressure ratio and the maximum possible thrust can be calculated by these equations for turbojet engines immediately, easily and short without using complex, rather long mathematical calculations.

The expressions apply the real (viscous) flow assumptions and the temperature and mass fraction dependencies of the relevant gas properties.

The derivation of the optimum pressure ratio at thermodynamic conditions with losses and variable gas properties is based on finding the extreme value of the specific thrust in the function of the compressor pressure ratio. Hence, as the first step, the expression of the thrust is introduced in Eq. (2.1) [24].

$$T = [\dot{m}_g V_9 - \dot{m}_{air} V_0] + A_9(p_9 - p_0) \quad (2.1)$$

The mass flow rate at the exhaust nozzle is determined by (2.2) [25].

$$\dot{m}_g = \dot{m}_{air} [(1 - \delta_{tech})(1 + f_{cc} + f_A)(1 + \delta_{bc})] \quad (2.2)$$

Concerning the well fitted converging-diverging nozzle, if the pressure ratio of the nozzle is over the critical one the flow at the exit has ambient pressure, the flow is unchoked and the velocity is supersonic. First, converging-diverging nozzle is considered (see Fig. 2.1) with correctly expanded flow conditions ($p_9=p_0$, unchoked flow condition) for deriving the optimum pressure ratio. Secondly, for extending the application range of the equation, the optimum compressor pressure ratio at maximum specific thrust is also derived for only converging nozzle at *choked nozzle flow condition*.

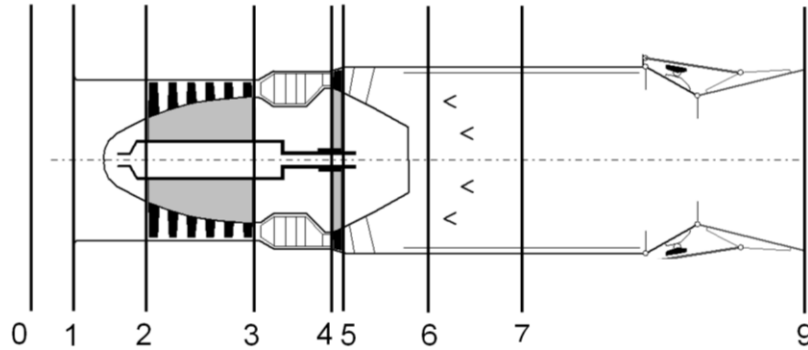


Figure 2.1 Layout of single spool turbojet engine with afterburner [26]

2.2.1. Unchoked Flow Condition

As $p_9=p_0$, only the outlet velocity (V_9) in Eq. (2.1) depends on the compressor pressure ratio. Hence, the detailed derivation of the expression of the outlet velocity in the function of the compressor pressure ratio is introduced after preliminary discussion about the gas properties.

Beside the unvarying gas properties such as specific gas constants, it is worth taking into consideration the effect of the local temperature and mass fraction when determining the specific heats at constant pressure and the ratios of the specific heats. These variables can be changed not only at each cross section of the engine, but also at different operational conditions in the function of the compressor pressure ratio. They can be determined as standalone or mean value depends on the application case. Iteration processes are applied in the followings if the temperature and/or mass fractions are the variables of the unknown parameters, to gain the equilibrium between the temperature dependent gas properties and the questionable unknown thermodynamic parameters [25].

In the derivation, first, the total enthalpy with the mean specific heat at constant pressure is expressed in Eq. (2.3) to determine the total temperature at the outlet section of the engine.

$$\begin{aligned}
h_{09} &= h_9 + \frac{V_9^2}{2} \Rightarrow \bar{C}_{pmix}(T_{09}, T_9, f)T_{09} = \bar{C}_{pmix}(T_{09}, T_9, f)T_9 + \frac{V_9^2}{2} \Rightarrow T_{09} = \\
&= T_9 + \frac{V_9^2}{2\bar{C}_{pmix}(T_{09}, T_9, f)}
\end{aligned} \tag{2.3}$$

Here, as usual, the fuel to air ratio, f is calculated by the available fuel mass flow rate divided by the available air mass flow rate at the investigated section.

The next step is to express the velocity at the exit of the nozzle at thermodynamic condition with losses and variable gas properties in the function of the total pressure ratio of the exhaust nozzle (Eq. (2.4)).

$$V_9 = \sqrt{2\bar{C}_{pmix}(T_{09}, T_{9s}, f)\eta_n T_{09} \left(1 - \frac{1}{(\pi_n)^\alpha}\right)} \tag{2.4}$$

Parameter α in Eq. (2.4) is introduced in Eq. (2.5). The goal of this simplification is to make the expression of the exhaust velocity simpler. The ratio of specific heats is calculated in the function of the temperature and fuel to air ratio by Eq. (2.6).

$$\alpha = \frac{\bar{\gamma}_{mix}(T_{07}, T_{9s}, f) - 1}{\bar{\gamma}_{mix}(T_{07}, T_{9s}, f)} \tag{2.5}$$

$$\bar{\gamma}_{mix} = \frac{\bar{C}_{pmix}(T_{09}, T_{9s}, f)}{\bar{C}_{pmix}(T_{09}, T_{9s}, f) - R_{mix}} \tag{2.6}$$

The total pressure ratio of the nozzle is expressed by the pressure ratio of the compressor and the turbine and the pressure recovery rate of the diffuser, combustion chamber and afterburner liner (see Eq. (2.7)).

$$r_d \pi_c r_{cc} r_{al} = \pi_T \pi_n \Rightarrow \pi_n = \frac{r_d r_{cc} r_{al} \pi_c}{\pi_T} \tag{2.7}$$

By substituting Eq. (2.7) into Eq. (2.4) the velocity at the exhaust is reformulated as shown in Eq. (2.8).

$$V_9 = \sqrt{2\bar{C}_{pmix}(T_{09}, T_{9s}, f)\eta_n T_{09} \left(1 - \left(\frac{\pi_T}{r_d r_{cc} r_{al} \pi_c}\right)^\alpha\right)} \tag{2.8}$$

The power balance of the compressor and turbine spool is used to establish the connection between the total pressure ratio of the compressor and the turbine (see Eq. (2.9) and (2.10)).

$$W_C = \eta_m W_T \tag{2.9}$$

$$\dot{m}_2 \bar{C}_{pmix}(T_{02}, T_{03}, f = 0)(T_{03} - T_{02}) = \eta_m \dot{m}_4 (1 - \zeta) \bar{C}_{pmix}(T_{04}, T_{05}, f_T)(T_{04} - T_{05}) \tag{2.10}$$

\dot{m}_2 and \dot{m}_4 are the mass flow rates at the inlet of the compressor and turbine respectively and are expressed in Eq. (2.11).

$$\dot{m}_2 = \dot{m}_{air}, \quad \dot{m}_4 = \dot{m}_{air} [(1 - \delta_{tech})(1 + f_{cc})(1 + \delta_{bc})] \quad (2.11)$$

Eq. (2.12) is formed by replacing the mass flow rates in Eq. (2.10) by Eq. (2.11) and introducing isentropic efficiencies and isentropic relationship between the temperatures and pressures.

$$\begin{aligned} & \frac{1}{\eta_{C,s}} \bar{C}_{pmix}(T_{02}, T_{03}, f = 0) T_{02} ((\pi_C)^\beta - 1) = \\ & = \eta_m \eta_{T,s} (1 - \delta_{tech})(1 + \delta_{bc})(1 + f_{cc})(1 - \xi) \bar{C}_{pmix}(T_{04}, T_{05}, f_T) T_{04} \left(1 - \frac{1}{(\pi_T)^\varepsilon}\right) \end{aligned} \quad (2.12)$$

β and ε in the superscripts represent compact forms of the exponents for the isentropic processes in the compressor and the turbine respectively (see Eq. (2.13)). They are the function of the temperature and the local mass fraction of the air and burnt gases.

$$\beta = \frac{\bar{\gamma}_{mix}(T_{02}, T_{03}, f=0)^{-1}}{\bar{\gamma}_{mix}(T_{02}, T_{03}, f=0)}, \quad \varepsilon = \frac{\bar{\gamma}_{mix}(T_{04}, T_{05}, f_T)^{-1}}{\bar{\gamma}_{mix}(T_{04}, T_{05}, f_T)} \quad (2.13)$$

Parameter ϕ is introduced to include all the parameters in Eq. (2.12) except for ε , π_T , π_C and β and it is shown in Eq. (2.14).

$$\phi = \frac{\bar{C}_{pmix}(T_{02}, T_{03}, f = 0) T_{02}}{\bar{C}_{pmix}(T_{04}, T_{03}, f_{cc}) T_{04} \eta_m \eta_{C,s} \eta_{T,s} (1 - \delta_{tech})(1 + \delta_{bc})(1 + f_{cc})(1 - \xi)} \quad (2.14)$$

Eq. (2.15) is formed by rearranging Eq. (2.12) and expressing the total pressure ratio of the turbine.

$$\pi_T = \left(1 - \phi((\pi_C)^\beta - 1)\right)^{(-1/\varepsilon)} \quad (2.15)$$

The velocity at the exhaust of the nozzle (see Eq. (2.16)) is derived by substituting Eq. (2.15) into Eq. (2.8).

$$V_9 = \sqrt{2 \bar{C}_{pmix}(T_{09}, T_{9s}, f) \eta_n T_{09} \left[1 - \left(\frac{1}{(1 - \phi((\pi_C)^\beta - 1))^{\frac{1}{\varepsilon}} \pi_C \kappa}\right)^\alpha\right]} \quad (2.16)$$

κ in Eq. (2.16) represents the multiplication of the pressure recovery rates in the diffuser, in the combustion chamber and in the afterburner liner ($\kappa = r_d r_{cc} r_{al}$).

Finally, the specific thrust (Eq. (2.17)) is expressed by inserting Eq. (2.16) into Eq. (2.1) at the start and at unchoked nozzle flow condition.

$$\begin{aligned} \frac{T}{\dot{m}_{air}} = & [(1 - \delta_{tech})(1 + f_{cc} + f_A)(1 \\ & + \delta_{bc})] \sqrt{2 \bar{C}_{pmix}(T_{09}, T_{9s}, f) \eta_n T_{09} \left[1 - \left(\frac{1}{(1 - \phi((\pi_C)^\beta - 1))^{\frac{1}{\varepsilon}} \pi_C \kappa}\right)^\alpha\right]} \end{aligned} \quad (2.17)$$

The objective of the optimization process is to determine the optimum pressure ratio of the compressor, which pertains at maximum specific thrust. The reason of considering the specific thrust (thrust per unit mass flow rate of air) is to exclude the effect of compressor pressure ratio on the mass flow rate of air. The condition for the maximum specific thrust is shown by Eq. (2.18).

$$\frac{\partial \left(\frac{T}{\dot{m}_{air}} \right)}{\partial \pi_C} = 0 \quad (2.18)$$

Two sub steps of the derivation process are shown in the next two equations.

$$\begin{aligned} & \frac{\partial \left(\frac{T}{\dot{m}_{air}} \right)}{\partial \pi_C} \\ & [(1 - \delta_{tech})(1 + f_{cc} + f_A)(1 + \delta_{bc})] \left[\frac{1}{(1 - \phi((\pi_C)^\beta - 1))^{\frac{1}{\varepsilon}} \pi_C} \right]^\alpha \cdot \\ & \cdot \alpha \left[\frac{\frac{\phi(\pi_C)^\beta \beta}{(1 - \phi((\pi_C)^\beta - 1))^{\frac{1}{\varepsilon}} (\pi_C)^2 \varepsilon (1 - \phi((\pi_C)^\beta - 1))}}{1} \right] \left(1 - \phi((\pi_C)^\beta - 1) \right)^{\frac{1}{\varepsilon}} (\pi_C) \quad (2.19) \\ & = -\frac{1}{2} \frac{1}{\sqrt{1 - \left[\frac{1}{(1 - \phi((\pi_C)^\beta - 1))^{\frac{1}{\varepsilon}} \pi_C} \right]^\alpha}} \end{aligned}$$

$$\begin{aligned} & \frac{\partial \left(\frac{T}{\dot{m}_{air}} \right)}{\partial \pi_C} = \\ & [(1 - \delta_{tech})(1 + f_{cc} + f_A)(1 + \delta_{bc})] \left[\frac{(1 - \phi(\pi_C)^\beta + \phi)^{-\frac{1}{\varepsilon}}}{(\pi_C)} \right]^\alpha \alpha (\phi(\pi_C)^\beta \beta - \varepsilon + \varepsilon \phi(\pi_C)^\beta - \varepsilon \phi) \quad (2.20) \\ & = \frac{1}{2} \frac{1}{(\pi_C) \sqrt{1 - \left[\frac{(1 - \phi(\pi_C)^\beta + \phi)^{-\frac{1}{\varepsilon}}}{(\pi_C)} \right]^\alpha \varepsilon (-1 + \phi(\pi_C)^\beta - \phi)}} \end{aligned}$$

After completing the derivation and performing arrangements and simplifications, the final form of the optimum pressure ratio is presented in Eq. (2.21).

$$\pi_{C_opt} = \sqrt[\beta]{\frac{\varepsilon(1 + \phi)}{\phi(\varepsilon + \beta)}} \quad (2.21)$$

2.2.2. Choked Flow Condition at Converging Exhaust Nozzle

Although converging-diverging nozzle is used for single spool turbojet engines (e.g. PД-9Б and АЛ-21Ф3) designed for high flight speed (over Mach number 1), as it is shown in Fig. 2.1, the extension of the method is discussed in the present section for increasing the application range of the method for converging type nozzle at choked flow condition.

A similar procedure is applied to evaluate the optimum pressure ratio of the compressor in a choked condition as it was in the previous subchapter. The velocity at the exit of the converging nozzle is the speed of sound when it is in a choked condition and it is not a function of the compressor pressure ratio explicitly. However, beside the exhaust velocity, the exhaust pressure also contributes to generating thrust (see p_9 in Eq. (2.1)). This pressure is the critical pressure and can also be expressed in the function of the compressor pressure ratio as it is shown below. The total pressures at the inlet and at the outlet section of the turbine are calculated by Eq. (2.22) and (2.23) respectively.

$$p_{04} = r_{cc}\pi_C p_{02} \quad (2.22)$$

$$p_{05} = \frac{p_{04}}{\pi_T} = \frac{r_{cc}\pi_C p_{02}}{(1 - \phi((\pi_C)^\beta - 1))^{-\frac{1}{\varepsilon}}} \quad (2.23)$$

The total pressure at the inlet section of the nozzle (see Eq. (2.24)) is determined by the turbine outlet total pressure and the total pressure recovery rate of the afterburner liner.

$$p_{07} = r_{al}p_{05} = \frac{r_{cc}r_{al}\pi_C p_{02}}{(1 - \phi((\pi_C)^\beta - 1))^{-\frac{1}{\varepsilon}}} \quad (2.24)$$

The total enthalpy and subsequently the total temperature at section “9” is introduced in the next steps (see Eq. (2.25) and (2.26)).

$$\begin{aligned} h_{09} &= h_9 + \frac{V_9^2}{2} \rightarrow \bar{c}_{pmix}(T_{09}, T_9, f)T_{09} = \bar{c}_{pmix}(T_{09}, T_9, f)T_9 + \frac{V_9^2}{2} \rightarrow T_{09} = \\ &= T_9 + \frac{V_9^2}{2\bar{c}_{pmix}(T_{09}, T_9, f)} \end{aligned} \quad (2.25)$$

$$T_{09} = T_9 + \frac{1}{\bar{c}_{pmix}(T_{09}, T_9, f)} \frac{V_9^2}{2} \frac{a_9^2}{a_9^2} \Rightarrow T_{09} = T_9 + \frac{1}{\bar{c}_{pmix}(T_{09}, T_9, f)} M_9^2 \frac{\gamma_{mix}(T_9, f)R_{mix}T_9}{2} \quad (2.26)$$

The critical condition corresponds to $M_9=1$ and $T_9=T_C$, so Eq. (2.26) is reformulated accordingly. The isentropic static temperature at point “9” is expressed by the equation of isentropic nozzle efficiency and it is given by Eq. (2.27).

$$T_{9s} = T_{09} - \frac{1}{\eta_n} \frac{(T_{09} - T_C)\bar{c}_{pmix}(T_{09}, T_C, f)}{\bar{c}_{pmix}(T_{09}, T_{9s}, f)} \quad (2.27)$$

The thermodynamic process between point “7” and “9s” is isentropic (see Eq. (2.28)).

$$\frac{p_c}{p_{07}} = \left(\frac{T_{9s}}{T_{09}}\right)^{\frac{\bar{\gamma}_{mix}(T_{09}, T_{9s}, f)}{\bar{\gamma}_{mix}(T_{09}, T_{9s}, f) - 1}} \quad (2.28)$$

A new closed-form expression (Eq. (2.29)) is introduced to determine the critical pressure at the exit of the converging nozzle after substituting the isentropic static temperature in Eq. (2.27), and the total temperature at nozzle exit in Eq. (2.26) into Eq. (2.28). Here, the dependencies of the temperature variations and fuel to air ratios in the specific heats at constant pressure and so in the ratios of the specific heats are also considered. While the critical static pressure at the outlet section of the exhaust system is coupled with the total and static exit temperatures, iteration cycles are used to determine the unknown thermodynamic parameters. Eq. (2.29)

gives higher critical pressure by 9.3 % for the ПД-9Б engine than its original form (see Eq. 2.59) with constant gas data according to the theory of ideal gases (the ratio of specific heats for gas=1.33).

$$p_9 = p_c = p_{07} \left[1 - \frac{1}{\eta_n} \left(1 - \frac{2\bar{C}_{pmix}(T_{09}, T_c, f)}{2\bar{C}_{pmix}(T_{09}, T_c, f) + \gamma_{mix}(T_c, f)R_{mix}} \right) \frac{\bar{C}_{pmix}(T_{09}, T_c, f)}{2\bar{C}_{pmix}(T_{09}, T_c, f)} \right]^{\frac{\bar{\gamma}_{mix}(T_{09}, T_{9s}, f)}{\bar{\gamma}_{mix}(T_{09}, T_{9s}, f) - 1}} \quad (2.29)$$

By substituting Eq. (2.24) in Eq. (2.29) and Eq. (2.29) in Eq. (2.1) the thrust can be expressed as follow:

$$T = [\dot{m}_9 V_9 - \dot{m}_{air} V_0] + +A_9 \left[\left(p_{02}(r_{cc} r_{al} \pi_c) \left(1 - \phi((\pi_c)^\beta - 1) \right)^{\frac{1}{\varepsilon}} \cdot \left[1 - \frac{1}{\eta_n} \left(1 - \frac{2\bar{C}_{pmix}(T_{09}, T_c, f)}{2\bar{C}_{pmix}(T_{09}, T_c, f) + \gamma_{mix}(T_c, f)R_{mix}} \right) \frac{\bar{C}_{pmix}(T_{09}, T_c, f)}{2\bar{C}_{pmix}(T_{09}, T_c, f)} \right]^{\frac{\bar{\gamma}_{mix}(T_{09}, T_{9s}, f)}{\bar{\gamma}_{mix}(T_{09}, T_{9s}, f) - 1}} - p_0 \right) \right] \quad (2.30)$$

The determination of the optimum pressure ratio pertaining at maximum thrust in choked converging nozzle flow conditions begins by completing the derivation presented in Eq. (2.31) and continues with simplifications shown in Eq. (2.32).

$$\frac{\partial T}{\partial \pi_c} = \left((1 - \phi(\pi_c)^\beta + \phi)^{\frac{1}{\varepsilon}} - \frac{(1 - \phi(\pi_c)^\beta + \phi)^{\frac{1}{\varepsilon}} \phi(\pi_c)^\beta \beta}{\varepsilon(1 - \phi(\pi_c)^\beta + \phi)} \right) \quad (2.31)$$

$$\frac{\partial T}{\partial \pi_c} = \left(\frac{(1 - \phi(\pi_c)^\beta + \phi)^{\frac{1}{\varepsilon}} \varepsilon - (1 - \phi(\pi_c)^\beta + \phi)^{\frac{-1+\varepsilon}{\varepsilon}} \phi(\pi_c)^\beta \beta}{\varepsilon} \right) \quad (2.32)$$

Completing the arrangements and simplifications, the final form of the expression for the optimum compressor total pressure ratio is given by Eq. (2.33).

$$\pi_{c_opt} = \sqrt[\beta]{\frac{\varepsilon(1 + \phi)}{\phi(\varepsilon + \beta)}} \quad (2.33)$$

Based on Eq. (2.21) and (2.33) the optimum pressure ratios for the convergent-divergent nozzle at correctly expanded flow conditions ($p_9=p_0$ and no shock waves form) and only convergent nozzle at choked flow conditions are the same. This new closed-form explicit expression involves simplifications, because the gas properties and unknown variables – including specific heats, efficiencies, pressure recovery rates – and the incoming mass flow rate of air in case of choked converging nozzle are constant in the derivation process. Due to the proximity to the operational point, the presented approximation used the same recovery rates, efficiencies, power reduction rate of the auxiliary systems, bleed air ratio and air income ratio due to the blade cooling. Concerning these simplifications, further investigations are needed to determine their effects on the optimum total pressure ratio.

Test, verification and the plausibility check of the above-mentioned new equations are found in subchapter 2.4. after subchapter 2.3, which is dedicated for introducing advanced thermo-dynamical model developments and verifications for triple-, dual- and single-spool turbojet engines due to the widest technical coverage and relevancies.

2.3. Modell Development for Thermo-Dynamic Cycle Analysis of Turbojet Engines with Verification and Plausibility Check

Thermodynamic model-development with testing, applications and verifications are introduced in the present subchapter for triple-, dual- and single-spool turbojet engines for the sake of the highest-level complexity with respect to the engine configuration. The most complex engine type is the triple-spool one, so it is considered only in the detailed model developments and description, meanwhile the governing equations for the dual- and single-spool turbojet engines can easily be deduced from them with considering less power balance equations according to the available pool number and without by-pass, if it is the case. The calculation approach, the processes and the determination of the gas parameters are the same in the all three versions.

2.3.1. Triple-Spool Mixed Turbofan Jet Engine

The triple-spool turbofan jet engines are frequently used in commercial and military applications due to their outstanding normalized range factor and emission at relatively high flight Mach number and at wide operational range. HK-32 (see Fig. 2.2) and HK-25 mixed turbo jet engines are considered in mathematical model-development for thermodynamic cycle analysis to test and verify the results first. The Kuznetsov HK-32 is an afterburning triple-spool low bypass mixed turbofan jet engine, which powers the Tupolev Tu-160 supersonic bomber, and was fitted to the later model Tupolev Tu-144LL supersonic transporter. It is the largest and most powerful engine ever fitted on a combat aircraft. It produces 245 kN of thrust in maximum afterburner [27]. The Kuznetsov HK-25 is a turbofan mixed aircraft engine used in the Tupolev Tu-22M strategic bomber. It can equal the HK-321 engine as one of the most powerful supersonic engines in service today. It is rated at 245 kN thrust. It was superior to many other engines because of its improved fuel consumption [28].



Figure 2.2 HK-32 afterburning triple-spool low bypass mixed turbofan jet engine [29]

Introduction, general remarks, considerations, derivation of the advanced mathematical model of triple-spool turbofan jet engine is found in next parts below.

Introduction and General Considerations

Take-off (start) condition (maximum thrust at sea level) with $M = 0$ is considered in most of the investigated cases as data belong to that operational mode are available in the technical specification of the engines.

The ambient parameters of pressure and temperature at static sea level conditions are obtained from the ISA (International Standard Atmosphere) [30]:

- Ambient static pressure: =101325 Pa
- Ambient static temperature: = 288.15 K

A layout with the considered cross sections of a typical triple-spool mixed turbofan jet engine with afterburner is shown in Fig. 2.3.

The operation of the engine is the following. The ambient air enters the engine at section 1. The operational fluid suffers from pressure drop in the inlet diffuser, which is between port 1 and 2. The compressed air is generated from cross section 2 to 3 in the internal (core) section. The compressor unit consists of three main segments as low, medium and high-pressure components. The low-pressure compressor unit operates as fan module also and the by-passed air leaves the downstream section of the last fan stage is not directly exhausted, but it flows in a duct around the engine core and it is mixed with the hot gases leaving the turbine at section 6. The combustion chamber is located between port 3 and 4 in the internal section, where the heat is generated by adding fuel to the compressed air and burn develops at reaching activation temperature. The flow stream with high total enthalpy expands and provides energy to the high, medium and low-pressure turbines in the internal section, which is transmitted to spool of the high and medium compressor segments and to the fan respectively. The afterburner for elevating thrust is located between section 6 and 7. The exhaust gases with unburned oxygen leave the engine across the nozzle (7-9) with losses for producing thrust.

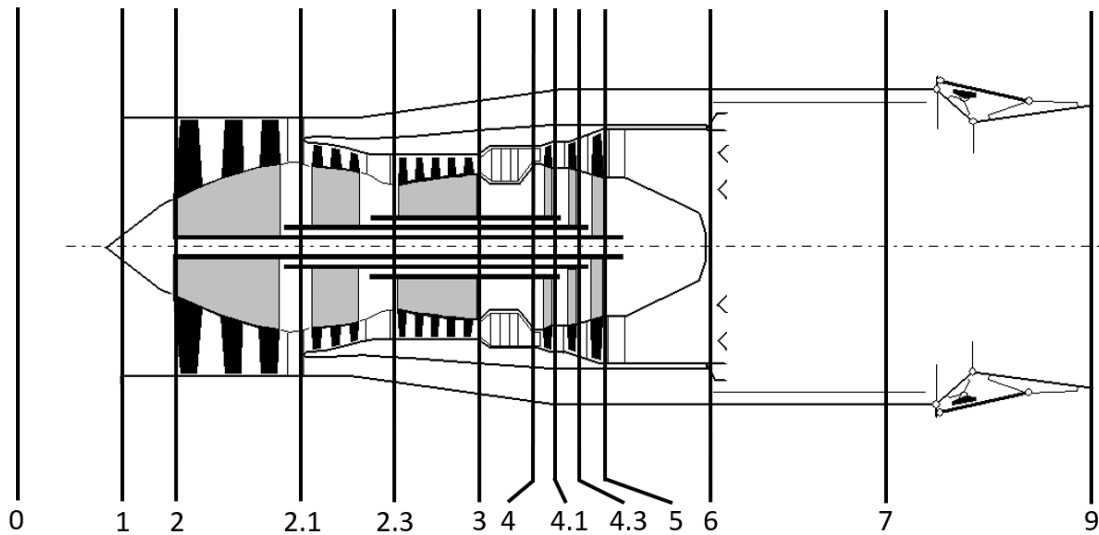


Figure 2.3 Layout of the mixed triple-spool turbofan jet engine with afterburner [26]

Regarding the present investigations, real engine specifications are considered for plausibility analysis. However, based on the available literature [3], there are known and unknown data which can be distinguished. The known parameters are the incoming air mass flow rate, pressure ratio of the compressor, turbine inlet total temperature and the length and the diameter of the engine. Except for the last two, these are also considered as input parameters of the analyses. The unknown parameters are; efficiencies (mechanical, isentropic of compressor and turbine, burning and exhaust nozzle), losses (total pressure recovery factor of inlet diffuser, combustion chamber and afterburner or turbine exhaust pipe), power reduction rates of the auxiliary systems, total pressure ratio of the fan and intermediate pressure compressor, bleed air ratios for technological reasons, air income ratios due to blade cooling and total temperature at the afterburner. In order to determine these unknown parameters, constrained nonlinear optimization method is applied with the goal function to minimize the deviations between the calculated and given thrust and thrust specific fuel consumption.

Beside the unvarying material properties, such as specific gas constants, it is important to take the local temperature and mass fraction conditions into consideration in determining gas properties, such as, the specific heat at constant pressure and the ratio of the specific heats. These variables can be changed not only at each cross section of the engine, but also at different operational conditions belonging to different compressor pressure ratios. Eq. (2.34) and (2.36) shows the expressions how they are determined as the mean value through the considered process. Eq. (2.35) and (2.37) presents their standalone value at given temperature and fuel to air mass flow rates ratio. Iteration processes are applied if the temperature and/or fuel to air ratio is the variable of the unknown parameter to gain the balance between the temperature and mass fraction dependent material properties and the determined unknown thermo-dynamical parameter. The block diagram of such type of iteration process is depicted in Fig. 2.4 for determining the isentropic and real temperatures caused by the compression process.

$$\bar{C}_{pmix}(T_i, T_{i+1}, f) = \frac{1000 \sum_{j=0}^n \frac{a_j + f c_j}{(j+1)(f+1)} \left[\left(\frac{T_{i+1}}{1000} \right)^{j+1} - \left(\frac{T_i}{1000} \right)^{j+1} \right]}{T_{i+1} - T_i} \quad (2.34)$$

$$C_{pmix}(T, f) = \sum_{j=0}^n \frac{a_j + f c_j}{f+1} \left(\frac{T}{1000} \right)^j \quad (2.35)$$

$$\bar{\gamma}_{mix} = \frac{\bar{C}_{pmix}(T_i, T_{i+1}, f)}{\bar{C}_{pmix}(T_i, T_{i+1}, f) - R_{mix}} \quad (2.36)$$

$$\gamma_{mix} = \frac{C_{pmix}(T, f)}{C_{pmix}(T, f) - R_{mix}} \quad (2.37)$$

The polynomial constants for air and kerosene fuel are a_j and c_j according to [1]. The values of the polynomial constants for the used gases are shown in Table 2.1.

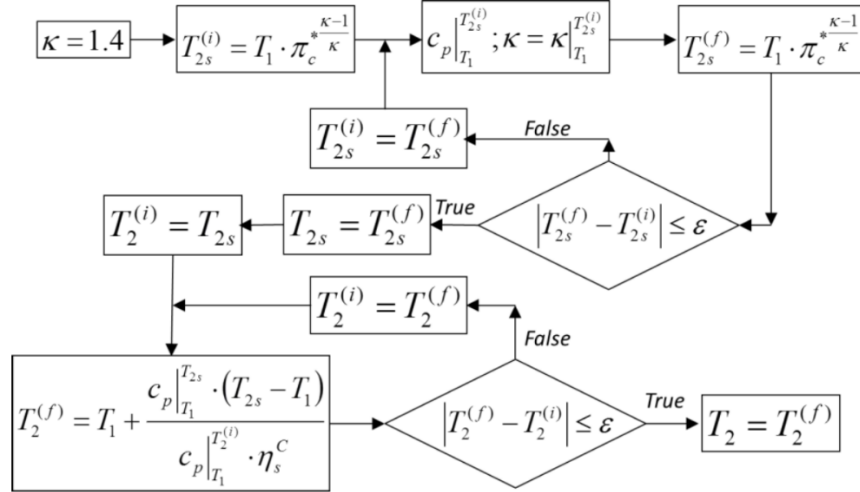


Figure 2.4 Iteration cycle including mean specific heat at constant pressure for determining outlet temperature (i =initial, f =final) at real and adiabatic compression process between stage 1 and 2 (the κ in the flow chart is γ and * means total quantities) [31]

Table 2.1 Polynomial constants used for computing the material properties of gases [1]

a_j	Value	c_j	Value
a_0	1043.797	c_0	614.786
a_1	-330.6087	c_1	6787.993
a_2	666.7593	c_2	-10128.91
a_3	233.4525	c_3	9375.566
a_4	-1055.395	c_4	-4010.937
a_5	819.7499	c_5	257.6096
a_6	-270.54	c_6	310.53
a_7	33.60668	c_7	-67.426468

Mathematical Model of Triple-Spool Mixed Turbofan Engines

The used physical and mathematical approaches and models have been derived and introduced in the present subchapter.

Regarding to most general aspects, the first step of the analysis is to determine the total temperature and pressure at the inlet with using static ambient temperature, pressure and flight Mach number by using Eq. (2.38) and (2.39) [24].

$$T_{02} = T_{01} = T_{00} = T_0 \left(1 + \frac{\gamma - 1}{2} M^2\right) \quad (2.38)$$

$$p_{01} = p_{00} = p_0 \left(1 + \frac{\gamma - 1}{2} M^2\right)^{\frac{\gamma}{\gamma - 1}} \quad (2.39)$$

The goal of the favourable intake design is to minimize flow losses by appropriate inlet duct and nose shaping to enable a pressure recovery factor close to unity. Due to friction of the airflow in contact with the intake wall and the occasional separation, a loss in total pressure will always be present.

The total pressure at fan (or compressor) intake is determined by the total pressure recovery factor of the intake:

$$p_{02} = p_{01}r_d \quad (2.40)$$

The total pressure and temperature at the outlet of the fan is expressed as follow:

$$p_{02.1} = p_{02}\pi_f \quad (2.41)$$

$$T_{02.1} = T_{02} + \frac{\bar{C}_{pmix}(T_{02}, T_{02.1s}, f = 0)(T_{02.1s} - T_{02})}{\bar{C}_{pmix}(T_{02}, T_{02.1}, f = 0)\eta_{f,s}} \quad (2.42)$$

Similarly, the total pressure and temperature at the outlet of intermediate (medium) pressure compressor is determined by the next equations:

$$p_{02.3} = p_{02.1}\pi_{ip,C} \quad (2.43)$$

$$T_{02.3} = T_{02.1} + \frac{\bar{C}_{pmix}(T_{02.1}, T_{02.3s}, f = 0)(T_{02.3s} - T_{02.1})}{\bar{C}_{pmix}(T_{02.1}, T_{02.3}, f = 0)\eta_{ip,C,s}} \quad (2.44)$$

The total pressure ratio of the high-pressure compressor is calculated by Eq. (2.45) considering that the overall total pressure ratio of the compressor and the total pressure ratio of the fan and intermediate compressor is given.

$$\pi_{hp,C} = \frac{\pi_c}{\pi_f\pi_{ip,C}} \quad (2.45)$$

The total pressure at the outlet of the high-pressure compressor is calculated by the previously determined total pressure ratio of the high-pressure compressor as follows:

$$p_{03} = \pi_{hp,C}p_{02.3} \quad (2.46)$$

The total temperature at the outlet of the high-pressure compressor is computed by using the isentropic efficiency of the high-pressure compressor (see Eq. (2.47)). Iteration cycle is used at this stage also, as it is in the case of low and intermediate pressure compressor units, due to the fact that the specific heat at constant pressure depends on the total temperature.

$$T_{03} = T_{02.3} + \frac{\bar{C}_{pmix}(T_{02.3}, T_{03s}, f = 0)(T_{03s} - T_{02.3})}{\bar{C}_{pmix}(T_{02.3}, T_{03}, f = 0)\eta_{hp,C,s}} \quad (2.47)$$

Total pressure recovery factor has been considered because of viscous flow modelling to determine the total pressure at the outlet of the combustion chamber ($p_{04} = p_{03}r_{cc}$). Stagnation energy balance of the combustion chamber is applied for determining the mass flow rate of the fuel, meanwhile the expected turbine inlet total temperature is fixed due to the given technological level. Eq. (2.48) includes five terms (from left to right) as 1. stagnation enthalpy of the incoming pure air into the combustion chamber, 2. stagnation enthalpy of the

fuel, 3. heat generation by the combustion, 4. stagnation enthalpy of the hot gas at the stoichiometric burnt condition, which leaves the combustion chamber and finally 5. stagnation enthalpy of the pure air, that is found at the outlet section of the combustion chamber.

$$\begin{aligned}
 & \underbrace{\frac{\dot{m}_{air}}{1+\beta} (1 - \delta_{tech}) C_{pmix}(T_{03}, f = 0) T_{03}}_1 + \underbrace{\dot{m}_{fcc} C_f T_{0,fcc}}_2 + \underbrace{\eta_b Q_R \dot{m}_{fcc}}_3 = \underbrace{(\dot{m}_{air,st,cc} + \dot{m}_{fcc})}_{\text{}} \\
 & \underbrace{C_{pmix}(T_{04}, f_{st,cc}) T_{04}}_4 + \underbrace{\left(\frac{\dot{m}_{air}}{1+\beta} (1 - \delta_{tech}) - \dot{m}_{air,st,cc} \right) C_{pmix}(T_{04}, f = 0) T_{04}}_5
 \end{aligned} \tag{2.48}$$

$\delta_{tech} = \dot{m}_{tech} / \left(\frac{\dot{m}_{air}}{1+\beta} \right)$ in Eq. (2.48) represents the certain amount of mass flow rate re-movements in the high-pressure compressor due to technological reason. $Q_R = 42$ MJ/kg is the lower heating value of the used fuel. $\dot{m}_{air,st,cc}$ (see Eq. (2.49)) is the air mass flow rate, which is involved in the burning process at stoichiometric condition and $L_0 = 14.72$ kg/kg. The definitions of the fuel to air mass flow rates ratios in the combustion chamber are found in Eq. (2.50).

$$\dot{m}_{air,st,cc} = \dot{m}_{fcc} L_0 \tag{2.49}$$

$$f_{cc} = \frac{\dot{m}_{fcc}(1+\beta)}{\dot{m}_{air}(1-\delta_{tech})}, f_{st,cc} = \frac{\dot{m}_{fcc}}{\dot{m}_{air,st,cc}} \tag{2.50}$$

Iteration cycle is applied for Eq. (2.48) in order to elaborate the coherent values of the fuel to air ratios and the specific heats at constant pressure.

Power equilibrium of the high-pressure compressor and turbine is used to determine the total temperature ($T_{04.1}$) at the outlet section of the high-pressure turbine:

$$\begin{aligned}
 & \frac{\dot{m}_{air}}{1+\beta} \bar{C}_{pmix}(T_{02.3}, T_{03}, f = 0) (T_{03} - T_{02.3}) = \\
 & = \eta_m \dot{m}_{4-4.1} (1 - \zeta) \bar{C}_{pmix}(T_{04}, T_{04.1}, f_{hp,T}) (T_{04} - T_{04.1})
 \end{aligned} \tag{2.51}$$

The mass flow rate of the operational fluid in the high-pressure turbine is shown in Eq. (2.52).

$$\dot{m}_{4-4.1} = \frac{\dot{m}_{air}}{1+\beta} (1 - \delta_{tech}) (1 + f_{cc}) (1 + \delta_{bc}) \tag{2.52}$$

δ_{bc} represents the incoming air mass flow rate in high-pressure turbine for blade cooling (see Eq. (2.53)).

$$\delta_{bc} = \dot{m}_{bc} (1 + \beta) / (\dot{m}_{air} (1 - \delta_{tech}) (1 + f_{cc})) \tag{2.53}$$

The total pressure at the turbine exit is computed by isentropic thermodynamic process and in the function of the turbine isentropic efficiency.

Similar approach is used also for the intermediate- and low-pressure compressor-turbine units to determine the exit total temperature and pressure of the intermediate- and low-pressure turbines. Iteration cycles are applied in the power balance equations for updating the specific heats at constant pressure in the turbine

segments too.

The total pressure recovery factor of the bypass liner 2.1-6 and engine core section 5-6 (see Fig. 2.3) is included in the afterburner liner location corresponds to 6-7, which approximation has negligible effect for the output of the analyses. This simplification is due to the fact that, as it is already mentioned, there are no available (measured) or calculated (by CFD for example) data for the pressure recovery factors and so reducing their numbers makes the parameter fitting simpler and faster.

The by-passed and core flows are mixed at section 6. Although the velocities and the static pressure should be the same for the flow streams enter in the mixing domain [24], slight difference can be observed. So, mass flow weighted averaging procedure is applied for determining the common total pressure. The mixing loss is going to be considered in pressure recovery factor of the afterburner liner. Mass conservation law is used for calculating the total mass flow rate in section 6. Total enthalpy balance is used for having the total temperature of the gas mixture as follow:

$$\dot{m}_{by_pass} C_{p,air}(T_{02.1}, f = 0)T_{02.1} + \dot{m}_5 C_{p,mix}(T_{05}, f_5)T_{05} = \dot{m}_6 C_{p,mix}(T_{06}, f_6)T_{06} \quad (2.54)$$

Iteration process is applied here also as the specific heat at constant pressure is the function of the resulted total temperature. The \dot{m}_{by_pass} is the mass flow rate in the fan section:

$$\dot{m}_{by_pass} = \frac{\beta}{1 + \beta} \dot{m}_{air} \quad (2.55)$$

The \dot{m}_5 is the mass flow rate at the outlet of the high-pressure turbine:

$$\dot{m}_5 = \frac{\dot{m}_{air}}{1 + \beta} [(1 - \delta_{tech})(1 + f)(1 + \delta_{bc})] \quad (2.56)$$

The \dot{m}_6 is the mass flow rate after mixing part:

$$\dot{m}_6 = \frac{\dot{m}_{air}}{1 + \beta} [(1 - \delta_{tech})(1 + f)(1 + \delta_{bc}) + \beta] \quad (2.57)$$

The afterburner is located between cross section 6. and 7. (see Fig. 2.3). If the afterburner operates, the total energy balance has been considered for this segment in order to calculate the fuel mass flow rate ($\dot{m}_{f,A}$) enters into the afterburner as it is shown in Eq. (2.58).

$$\begin{aligned} & \dot{m}_{air,6} C_{p,mix}(T_{06}, f = 0)T_{06} + \dot{m}_{f,A} C_f T_{0,f,A} + \eta_b Q_R \dot{m}_{f,A} \\ & + (\dot{m}_{air,st,cc} + \dot{m}_{f,cc}) C_{p,mix}(T_{06}, f_{st,cc})T_{0,6} \\ & = (\dot{m}_{air,st,cc} + \dot{m}_{f,cc}) C_{p,mix}(T_{07}, f_{st,cc})T_{07} \\ & + (\dot{m}_{air,st,A} + \dot{m}_{f,A}) C_{p,mix}(T_{07}, f_{st,A})T_{07} + (\dot{m}_{air,6} - \dot{m}_{air,st,A}) C_{p,mix}(T_{07}, f \\ & = 0)T_{07} \end{aligned} \quad (2.58)$$

The left side of Eq. (2.58) shows the incoming total enthalpies and energy into the system and the right-hand side represents the leaving total enthalpies. The first term in Eq. (2.58) is the stagnation enthalpy of pure air, which is available at section 6. The second and third term is the total enthalpy of the fuel entering afterburner and heat generated by the combustion respectively. The last term in the left-hand side is the total enthalpy of

the incoming hot gases, which are already burnt previously in the combustion chamber. The total enthalpy of the hot gases of the combustion chamber and the afterburner are represented by the first two terms in the right side of Eq. (2.58). The last term is the total enthalpy of the pure air, which leaves the system. Iterative calculation procedure is used here also to determine the fuel mass flow rate, which is a function of the fuel to air mass flow rates ratio ($f_{st,A} = \dot{m}_{f,A} / \dot{m}_{air,st,A}$) of the afterburner at stoichiometric condition and the specific heat at constant pressure. Total pressure recovery factor has been considered in the afterburner liner due to viscous flow conditions to determine the total pressure at the outlet of the afterburner section ($p_{07} = p_{06} r_{at}$ as $p_{06} = p_{05}$).

Expansion process occurs in the exhaust nozzle is shown in Fig. 2.5. In order to clarify whether the examined converging duct is choked or not, the inlet condition of the nozzle and its isentropic efficiency is considered for determining the critical pressure according to Eq. (2.59) [25].

$$p_c = p_{07} \left(1 - \frac{1}{\eta_n} \left(\frac{\gamma_{gas} - 1}{\gamma_{gas} + 1} \right)^{\frac{\gamma_{gas}}{\gamma_{gas} - 1}} \right) \quad (2.59)$$

However, as it is already introduced in subchapter 2.2.2, there is a new equation (Eq. (2.29)) for critical pressure, which has higher accuracy than Eq. (2.59). This is because it considers the temperature and component dependent gas properties. Hence, this expression is used hereafter if it is relevant.

If the critical pressure calculated either by Eq. (2.29) or Eq. (2.59) is higher than ambient static pressure, the nozzle flow is considered to be choked, which means that the exit pressure of the nozzle is equal with the critical pressure p_c . If the ambient pressure is higher than the critical pressure, then the nozzle flow is unchoked, therefore the exhaust pressure of the exit is equal to the ambient pressure. After having this information and determining the pressure, the temperature and the velocity at the exit of the exhaust nozzle can be calculated by conventional gas dynamic relationships according to the equations found in [25].

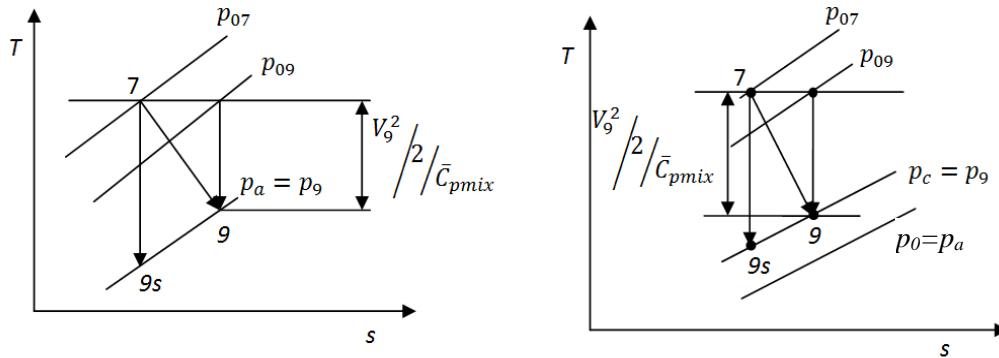


Figure 2.5 Nozzle flow with losses for unchoked (left side) and for choked (right side) flow conditions

Finally, as all parameters are available, the thrust and thrust specific fuel consumption is determined, as they are shown in Eq. (2.60) and (2.61) respectively.

$$T = [\dot{m}_g V_9 - \dot{m}_{air} V_0] + A_9 (p_9 - p_0) \quad (2.60)$$

$$TSFC = \frac{\dot{m}_{f,cc} + \dot{m}_{f,A}}{T} \quad (2.61)$$

The mass flow rate leaves the engine is found in Eq. (2.62) [25].

$$\dot{m}_9 = \frac{\dot{m}_{air}}{1 + \beta} [(1 - \delta_{tech})(1 + f_{cc} + f_A)(1 + \delta_{bc}) + \beta] \quad (2.62)$$

Verification of Thermo-dynamic Cycle Analysis for Triple-Spool Mixed Turbofan Engines

First, as it is already mentioned in the first paragraph of the present subchapter (2.3.1), HK-32 and HK-25 triple spool mixed turbofan engines are used as two gas turbines in start (take-off) condition to analyse and verify the simulation method. The afterburner operates and converging nozzles are considered in both cases. The available input parameters of the two selected engines are presented in Table 2.4 according to [3]. However, as it was mentioned earlier, there are also several unavailable parameters, which are determined by parameter identifications. The missing losses (total pressure recovery factor of inlet diffuser, combustion chamber and afterburner or turbine exhaust pipe), efficiencies (isentropic of the compressor, fan and turbine, mechanical, burning, and exhaust nozzle) (see them in Table 2.2), power reduction rate of the auxiliary systems, bleed air ratios for technological reasons, air income ratio due to blade cooling, total pressure ratio of the fan and intermediate pressure compressor, and last but not least the total temperature of the afterburner (see them in Table 2.3) are identified by nonlinear constrained optimization. Matlab's "fmincon" function is used for that purpose. The constrained minimization is the problem of finding a vector \mathbf{x} that is a local minimum to a scalar function $f(\mathbf{x})$ subject to constraints on the allowable \mathbf{x} : $\min f(\mathbf{x})$ such that one or more of the following holds: $c(\mathbf{x}) \leq 0$, $ceq(\mathbf{x}) = 0$, $A\mathbf{x} \leq \mathbf{b}$, $Aeq\mathbf{x} = \mathbf{beq}$, $\mathbf{l} \leq \mathbf{x} \leq \mathbf{u}$ [32]. "fmincon" function can use Trust Region Reflective, Active Set, Sequential Quadratic Programming and Interior Point Algorithms [32] to find the unknown loss and technical parameters mentioned before over the given ranges while the goal function of the optimisation is to minimize the differences between the calculated and available specific thrust and thrust specific fuel consumption found in the available technical literature [3]. More information about the used constrained nonlinear optimization algorithms is found in [32] and [33]. The used ranges for the constrained optimisation in the present section are shown in Table 2.2 and Table 2.3.

Table 2.2 Considered ranges of the unknown parameters in the constrained optimisation

	Pressure recovery rates and efficiencies of the engine components								
	r_d	r_{cc}	r_{al}	$\eta_{C,s}$	$\eta_{f,s}$	$\eta_{T,s}$	η_m	η_b	η_n
Given ranges for the constrained optimization	0.88 0.94	0.93 0.97	0.88 0.97	0.81 0.88	0.81 0.88	0.86 0.94	0.98 0.999	0.92 0.98	0.92 0.98

Table 2.3 Applied ranges of the unknown parameters in the constrained optimisation

	Power reduction rate for the auxiliary systems (ξ), bleed air ratio for technological reasons (δ_{tech}), air income ratio due to blade cooling (δ_{bc}), total pressure ratio of the fan (π_f) and intermediate pressure compressor ($\pi_{ip,C}$), and total temperature in the afterburner (T_{07})					
	ξ	δ_{tech}	δ_{bc}	π_f	$\pi_{ip,C}$	$T_{07}[\text{K}]$
Given ranges for the constrained optimization	0.004 0.012	0.02 0.2	0.05 0.12	1.1 2.3	2 4	1700 2200

Table 2.5, Table 2.6 and Table 2.7 show the results of the parameter identification. The calculated data are in the reasonable range therefore they can be accepted.

Table 2.4 Operational data of the HK-32 and HK-25 turbofan engines from the available specification [3], [27] and [28]

Type of engine	The main characteristics of the engine (take-off condition)					
	T_{04} [K]	π_c	β	\dot{m}_{air} [kg/s]	T [kN]	$TSFC$ [kg/(kNh)]
HK-32	1630	28.4	1.4	290	245	-
HK-25	1600	26	1.44	280.9	245	205.3

The thrust and thrust specific fuel consumption – belong to the parameters found in Table 2.5, Table 2.6 and Table 2.7 – are shown in Table 2.8. The relative maximal deviation between the given and the calculated data during the parameter fitting is 0.122 % in case of thrust and 0.195 % at the thrust specific fuel consumption.

Although both engines have the same thrust, the $TSFC$ of HK-32 engine is higher (see Table 2.8) due to the higher temperature in the combustion chamber and in the afterburner. HK-32 engine has lower total pressure recovery factor (higher pressure loss) in the combustion chamber (r_{cc}), afterburner liner (r_{al}) and intake duct (r_d). The HK-32 has lower mechanical, nozzle and burning efficiency beside lower fan and compressor isentropic efficiencies in comparing with HK-25.

Although more investigations would be needed, the obtained results together with the plausible parameter identifications and verification show, that the thermodynamic model is suitable for analysing processes of the triple-spool turbojet engines.

Table 2.5 Identified efficiencies of the HK-32 and HK-25 turbofan engines

Type of Engine	Mechanical, nozzle, burning and isentropic (high-pressure turbine, intermediate-pressure turbine, low-pressure turbine, fan, high-pressure compressor and intermediate-pressure compressor) efficiencies						
	η_m	η_n	η_b	$\eta_{hp,T,s}$ $\eta_{ip,T,s}$ $\eta_{lp,T,s}$	$\eta_{f,s}$	$\eta_{hp,C,s}$	$\eta_{ip,C,s}$
HK-32	0.99	0.94	0.94	0.89	0.84	0.83	0.84
HK-25	0.992	0.95	0.97	0.89	0.86	0.87	0.87

Table 2.6 Identified total pressure recovery factors of the investigated turbofan engines

Type of Engine	Total pressure recovery factors of comb. chamber (r_{cc}) afterburner liner (r_{al}) and intake duct (r_d)		
	r_{cc}	r_{al}	r_d
HK-32	0.95	0.9	0.91
HK-25	0.96	0.94	0.94

Table 2.7 Identified parameters of the investigated turbofan engines

Type of Engine	Total pressure ratio of the fan (π_f) and intermediate pressure compressor ($\pi_{ip,C}$), bleed air ratio for technological reasons (δ_{tech}), air income ratio due to blade cooling (δ_{bc}), power reduction rate for the auxiliary systems (ξ) and total temperature in the afterburner (T_{07})					
	π_f	$\pi_{ip,C}$	δ_{tech}	δ_{bc}	ξ	T_{07} [K]
HK-32	2	3	0.16	0.116	0.005	1800
HK-25	2.19	3	0.18	0.0952	0.005	1780

Table 2.8 Comparisons of the available data with the outputs of the parameter identification

Type of Engine	Available data (take-off condition)		Outputs of the parameter identification (take-off condition)		Relative differences (%) between the available and calculated data	
	T [kN]	$TSFC$ [kg/(kNh)]	T [kN]	$TSFC$ [kg/(kNh)]	T	$TSFC$
HK-32	245	-	245.1	229.4	0.04	-
HK-25	245	205.3	245.3	205.7	0.122	0.195

The thermo-dynamical cycles of the engine processes are found in Fig. 2.6 and 2.7. The red curve-sections (or lighter and thinner in greyscale) represent the constant pressures in the T - s diagrams (total from points 0-7 and static at 9). The processes between the engine states denoted by numbers are plotted by thicker black lines. This visualization effect is the reason of the constant pressure line goes below the process line in case of pressure decrement just after sections “2.1” and “3”.

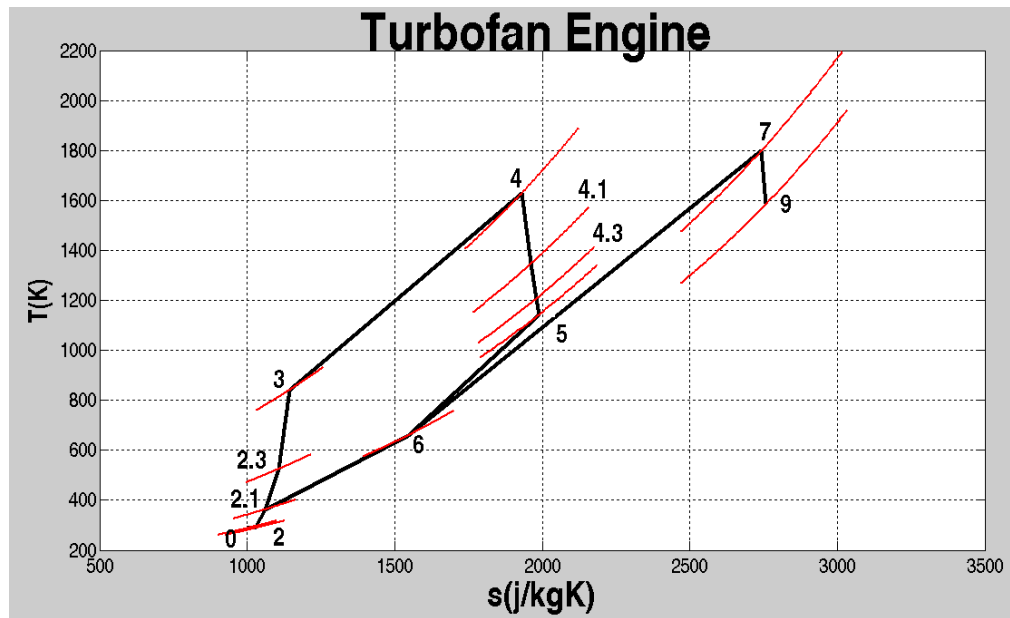


Figure 2.6 Thermo-dynamical cycle of the HK-32 turbofan engine with afterburner (the red curve sections (the lighter thinner ones in greyscale) in the T - s diagrams are the constant pressure curves (total from 0-7 and static at 9) belong to the shown numbers of the engine cross sections)

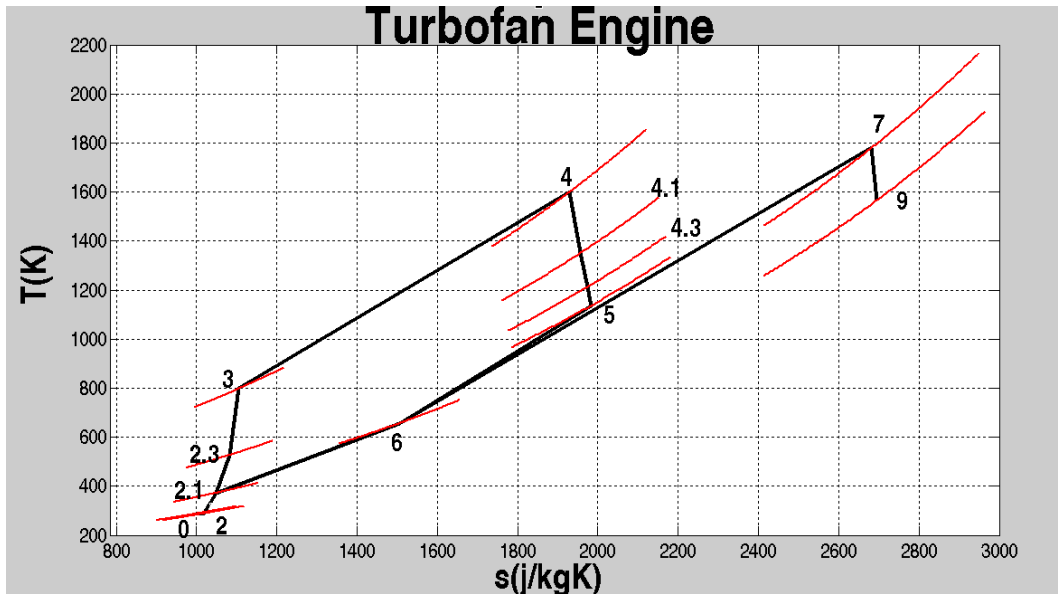


Figure 2.7 Thermo-dynamical cycle of the HK-25 turbofan engine with afterburner (the red curve sections (the lighter thinner ones in greyscale) in the T - s diagrams are the constant pressure curves (total from 0-7 and static at 9) belong to the shown numbers of the engine cross sections)

The analysis of the HK-32 and HK-25 engines are also completed by using the conventional Eq. (2.59) for determining the critical pressure at the exit of the converging nozzle in case of the same thermo-dynamical conditions. The effect of the fuel to air mass flow rates ratio and temperature are not considered in the ratio of specific heats in Eq. (2.59), the flow is supposed to be pure gas with $\gamma_{gas}=1.33$. The results of the calculations are shown in Table 2.9. The average value of the relative deviations between the resulted and the available thrust and thrust specific fuel consumption is 0.119 % by using a variant of the new equation (Eq. (2.29)) for the critical pressure and 3.13 % in case of the conventional equation. The “variant” in the present context means that the true specific heat is considered (a specific heat belongs to the given temperature and fuel to air ratio) instead of the average one at the given temperature range in the total enthalpy equation (Eq. 2.25).

Table 2.9 Effect of the conventional and a variant of the new equation for critical pressure on the thrust and the thrust specific fuel consumption in case of HK-32 and HK-25 turbofan mixed jet engines

Type of Engine	Relative difference (a variant of the new equation)		Relative difference (conventional equation)	
	T [kN]	$TSFC$ [kg/(kNh)]	T [kN]	$TSFC$ [kg/(kNh)]
HK-32	0.04 %	-	3.27 %	-
HK-25	0.122 %	0.195 %	2.85 %	3.27 %

2.3.2. Dual-Spool Mixed Turbofan Engine

A simplified layout of a dual-spool mixed turbofan engine is shown in Fig. 2.8. Beside the inlet diffuser (1-2) and exhaust nozzle (7-9), the gas turbine has combustion chamber (3-4), afterburner (6-7), two shafts, two compressor- and two turbine-units. The compressor that is closer to the intake is the low-pressure compressor (fan, in this case) (2-2.1) and it is driven by the low-pressure turbine (4.1-5). The high-pressure compressor (2.1-3), which is located at the downstream of the fan, is driven by the high-pressure turbine (4-4.1). The

ambient air comes into the diffuser and then it is compressed before entering the combustion chamber in the core section of the engine. Here, fuel is injected and mixed with the air and combustion takes place. After the turbine (4-5) and afterburner (6-7), the hot gas arrives to the nozzle (7-9), produces high velocity jet and thrust while they are exhausted at section (9). The by-passed air, after the fan, flows in the annular section of the engine (2.1-6), out of the core, and mixes with the hot gas after section 6. The same mathematical models and

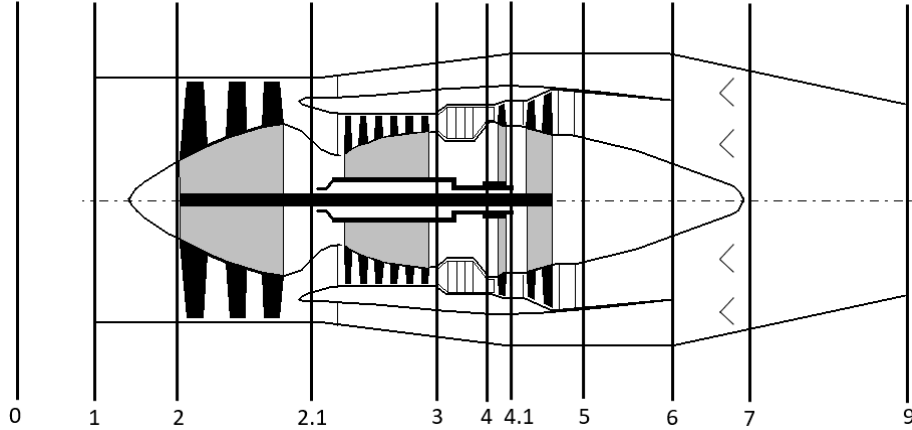


Figure 2.8 Layout and the main sections of the dual-spool mixed turbofan engine [26]

thermo-dynamical processes are used in the present case than it was introduced in the subchapter 2.3.1. for triple-spool mixed turbojet engine, but they are adopted for the actual conditions. It means for example that only two spools are considered: beside the fan, one compressor and high- and low-pressure turbine units are applied.

Verification of Thermo-dynamic Cycle Analysis for Dual-Spool Mixed Turbofan Engines

HK-22 and HK-144A turbofan engines are used as two bypass engines with afterburning at start (take-off) and without afterburning at flight conditions meanwhile HK-8-4 and HK-86A are selected as two bypass engines at take-off condition without afterburning in order to investigate further and verify the simulation method. The available specifications of these gas turbines are found in [3]. The used data for the parameter identifications and simulations are shown in Table 2.10 for take-off and flight conditions.

Table 2.10 Available data for dual-spool mixed turbofan engines [3]

Type of engine	Input data used in the simulations (turbine inlet temperature, compressor total pressure ratio, bypass ratio, mass flow rate of incoming air, thrust and thrust specific fuel consumption) (take-off/flight condition)				Known available data for parameter identification (thrust and thrust specific fuel consumption) (take-off/flight condition)		Altitude and Mach number for flight condition
	T_{04} [K]	π_c	β	\dot{m}_{air} [kg/s]	T [kN]	$TSFC$ [kg/(kNh)]	
HK-22	1326/1115	15/14.1	0.623/0.653	241/84	196/27.4	190/91.7	11/.8
HK-144A	1326/1115	15/14.1	0.623/0.7	241/96	195/29.2	190/93.8	11/.94
HK-8-4	1190/-	10.8/-	1.04	222	103/27	60/-	11/.8
HK-86A	1172/-	12.9/-	1.18/-	288/-	127/31.6	53.1/-	11/.8

The calculation of the unknown variables such as total pressure recovery factors, efficiencies, total pressure ratios of fan, bleed air ratios for technological reasons, air income ratios due to blade cooling, power reduction rates for the auxiliary systems and total temperatures of the afterburners are like at the triple-spool turbofan engines, which is discussed earlier in the subchapter 2.3.1. except for the mentioned differences. Referring to Table 2.10 as the input data of the analysis, the identified parameters are shown in Table 2.11, 2.12 and 2.13.

Table 2.11 Identified efficiencies of the investigated dual-spool mixed turbofan engines

Type of engine	Efficiencies (nozzle, mechanical, burning, low pressure turbine isentropic, high pressure turbine isentropic, fan isentropic and high-pressure compressor isentropic) of the cycles at take-off/flight condition						
	η_n	η_m	η_b	$\eta_{lp,T,s}$	$\eta_{hp,T,s}$	$\eta_{f,s}$	$\eta_{hp,C,s}$
HK-22	0.95/0.96	0.99/0.99	0.97/0.97	0.88/0.87	0.89/0.9	0.85/0.85	0.85/0.86
HK-144A	0.95/0.96	0.99/0.99	0.97/0.97	0.88/0.87	0.88/0.89	0.85/0.86	0.86/0.86
HK-8-4	0.95/-	0.99/-	0.96/-	0.89/-	0.87/-	0.85/-	0.86/-
HK-86A	0.95/-	0.995/-	0.95/-	0.89/-	0.87/-	0.85/-	0.86/-

Table 2.12 Identified total pressure recovery factors of the investigated dual-spool mixed turbofan engines

Type of engine	Total pressure recovery factors of intake duct (r_d), combustion chamber (r_{cc}) and afterburner liner (r_{al}) (take-off/flight conditions)		
	r_d	r_{cc}	r_{al}
HK-22	0.89/0.91	0.94/0.96	0.9/0.9
HK-144A	0.89/0.9	0.95/0.95	0.85/0.9
HK-8-4	0.9/-	0.96/-	-/-
HK-86A	0.9/-	0.95/-	-/-

Table 2.13 Identified parameters of the investigated dual-spool mixed turbofan engines

Type of engine	Total pressure ratio of the fan (π_f), bleed air ratio for technological reasons (δ_{tech}), air income ratio due to blade cooling (δ_{bc}), power reduction rate for the auxiliary systems (ξ) and total temperature of the afterburner (T_{07}) (take-off/flight conditions)				
	π_f	δ_{tech}	δ_{bc}	ξ	T_{07} [K]
HK-22	1.8/2.18	0.18/0.18	0.0713/0.071	0.008/0.007	1750/-
HK-144A	1.4/2.15	0.18/0.18	0.0595/0.0595	0.008/0.001	1750/-
HK-8-4	1.1/-	0.18/-	0.071/-	0.008/-	-/-
HK-86A	1.3/-	0.18/-	0.059/-	0.008/-	-/-

The thrust (T) and thrust specific fuel consumption ($TSFC$) has been used to check directly how far the calculated results of the analyses are from the data available in the specifications [3]. The results of the four turbofan engines are presented in Table 2.14. The maximum relative deviation between the available and the calculated data by parameter identification is 1.46 %. The results are plausible, the efficiencies and pressure recovery factors are higher at lower engine performance (flight condition) than at start condition in most of the cases.

Table 2.14 Comparisons of the available data with the outputs of the parameter identification for dual-spool mixed turbofan engines

Type of engine	Available data by [3] (take-off/flight condition)		Results of the parameter identification (take-off/flight condition)		Relative differences (%) between the available and calculated data	
	T [kN]	$TSFC$ [kg/(kNh)]	T [kN]	$TSFC$ [kg/(kNh)]	T	$TSFC$
HK-22	196/27.4	190/91.7	198.1/27	191/91.2	1.07/1.46	0.53/0.55
HK-144A	195/29.2	190/93.8	195.6/29.5	190.5/93.4	0.31/1.03	0.26/0.43
HK-8-4	103/27	60/-	102/-	60/-	0.97/-	0/-
HK-86A	127/3	53.1/-	127.4/-	53.09/-	0.31/-	0.02/-

2.3.3. Single-Spool Turbojet Engine without Afterburner

Single-spool turbojet engines are considered in the third part of the thermo-dynamical model's verification and plausibility check-part of the present thesis. A meridian cross section of a typical single-spool turbojet engine without afterburner is shown in Fig. 2.9.

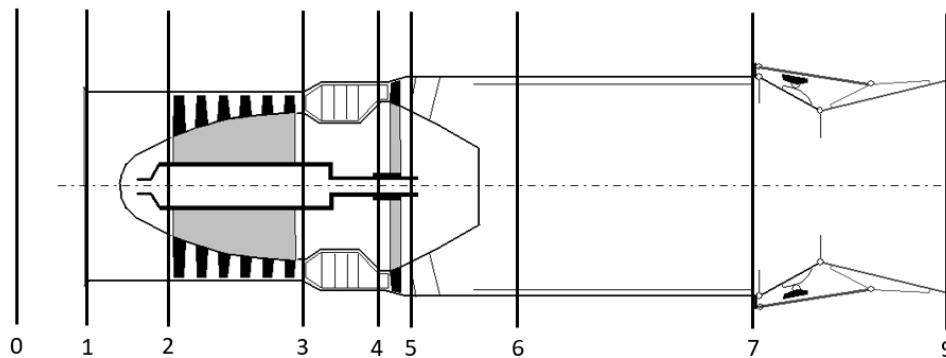


Figure 2.9 Layout of the single-spool turbojet engine without afterburner [26]

The same methodology, mathematical models and thermo-dynamical processes are used in the present case also as they were introduced in the subchapter 2.3.1. for triple-spool turbofan engines, but these are adopted for the actual conditions. It means for example that here only the core flow is present meanwhile one compressor-turbine unit and afterburner-free structure is applied.

Verification of Thermo-dynamic Cycle Analyses for Single-Spool Turbojet Engines without Afterburner

ВД-7 and KP7-300 turbojet engines have been selected for the analysis and for the verification of the calculation method in case of a single spool turbojet engine. The available specifications of these gas turbines at take-off condition without afterburning are found in [3] and are represented in Table 2.15.

Table 2.15 Available technical specifications of the single-spool turbojet engines (take-off condition) [3]

Type of single spool turbojet engines	Input data, which are used in the simulations			Known available data for parameter identification	
	T_{04} [K]	π_c	\dot{m}_{air} [kg/s]	T [kN]	$TSFC$ [kg/(kNh)]
ВД-7	1090	11.2	187	107.8	82
KP7-300	1330	4.5	35.5	21.1	132

The determination of the unknown variables such as total pressure recovery factors, efficiencies, bleed air ratios for technological reasons, air income ratios due to blade cooling and power reduction rates for the auxiliary systems are similar to those are described for triple spool turbofan engines introduced in subchapter 2.3.1. As it was the case before also, constrained nonlinear optimisation method is used for determining these unknowns to find such a parameter-state, which provides the closest results to the available thrusts and thrust specific fuel consumptions of the engines. The results of the parameter identifications are found in Table 2.16 and 2.17.

Table 2.16 Identified unknown parameters of the investigated single-spool turbojet engines

Type of engine	Total pressure recovery factors (diffuser and combustion chamber) and efficiencies (compressor and turbine isentropic, mechanical, burning and nozzle)						
	r_d	r_{cc}	$\eta_{c,s}$	$\eta_{T,s}$	η_m	η_b	η_n
ВД-7	0.9	0.94	0.85	0.88	0.99	0.97	0.96
KP7-300	0.91	0.95	0.85	0.87	0.995	0.96	0.96

Table 2.17 Identified unknown parameters of the investigated single-spool turbojet engines

Type of engine	Power reduction rates due to the auxiliary systems, bleed air ratios for technological reasons, air income ratios due to blade cooling and total temperatures in the afterburner			
	ξ	δ_{tech}	δ_{bc}	T_{07} [K]
ВД-7	0.009	0.15	0.0698	-
KP7-300	0.01	0.18	0.0712	-

Similarly to the previous scenarios of the verification, thrust (T) and thrust specific fuel consumption ($TSFC$) has been used to check directly how far the calculated results of the analyses are from the data available in the specifications. The results of the parameter identification for the investigated single spool jet engines are presented in Table 2.18. The maximum relative deviation between the available and the resulted data is 0.95 %.

Table 2.18 The available and the resulted thrusts and thrust specific fuel consumptions by the parameter identification for single-spool turbojet engines

Type of engine	Available data by [3] (take-off condition)		Results of the parameter identification (take-off condition)		Relative differences (%) between the available and calculated data	
	T [kN]	$TSFC$ [kg/(kNh)]	T [kN]	$TSFC$ [kg/(kNh)]	T	$TSFC$
БД-7	107.8	82	108	81.7	0.186 %	0.37 %
KP7-300	21.1	132	21.3	132.7	0.95 %	0.53 %

The real thermo-dynamical cycles of the БД-7 turbojet engine without afterburner is calculated and plotted in T - s diagram (see Fig. 2.10). The red curve-sections (or lighter and thinner in greyscale) represent the constant pressures in the T - s diagram (total from points 1-5 and static at 9). The processes between the engine states are denoted by numbers are plotted by thicker and black lines. Similarly, to the previous cases, the visualization effect is the reason of the constant pressure line goes below the process line in case of pressure decrement just after section “3”.

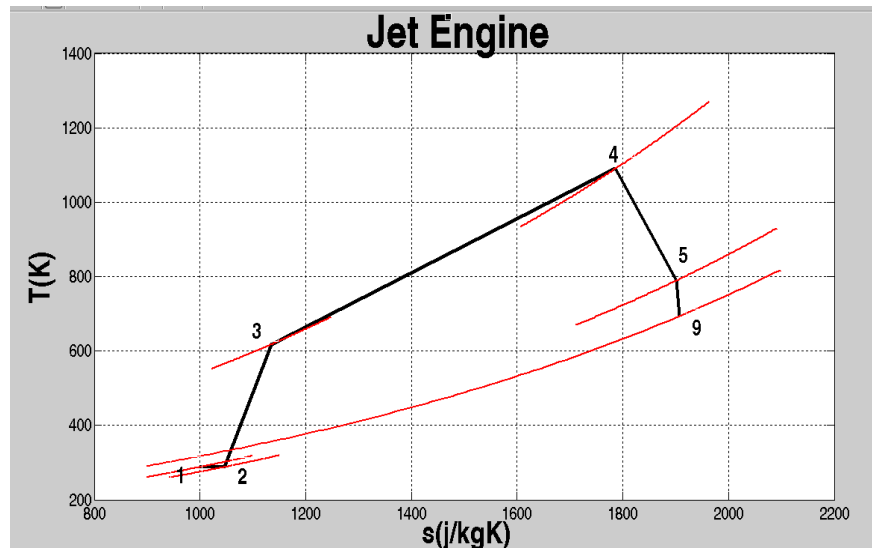


Figure 2.10 T - s diagram of the БД-7 turbojet engine without afterburner

2.4. Verification and Plausibility Check of the New Equation for the Optimum Compressor Total Pressure Ratio

РД-9Б and АЛ-21Ф3 turbojet engines at take-off condition (maximum thrust at sea level condition) with afterburning have been considered for further verification of the simulation method and to test the new equation for the optimum total pressure ratio of the compressor belongs to the maximum specific thrust.

2.4.1. Analysis of Single-Spool Turbojet Engines with Afterburning

A meridian cross section of a typical single spool turbojet engine with afterburner is shown in Fig. 2.11. Section “0” represents the ambient conditions and “9” is the outlet of the exhaust nozzle. The afterburner is found between section 6-7. Real flow conditions are considered in the mathematical model of each segment of the assembly including pressure recovery factors and efficiencies as they are relevant similarly to the previous cases. Temperature and fuel to air mass flow rates ratio dependencies are considered for specific heats as it is mentioned in the subchapter 2.3.1.

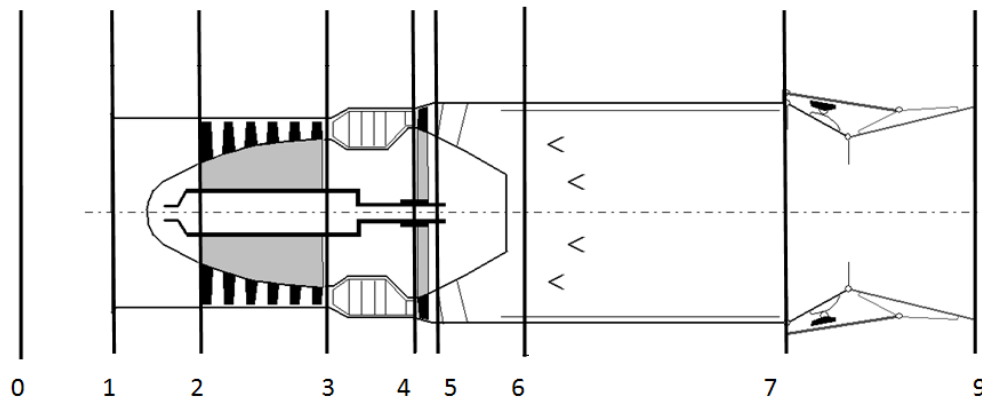


Figure 2.11 Layout of the single-spool turbojet engine without afterburner [26]

Regarding the ambient conditions, static pressure and temperature at sea level are considered. These data are obtained from the ISA (International Standard Atmosphere) [30] also: ambient static pressure: $p_0=101325$ Pa, ambient static temperature: $T_0=288.15$ K, meanwhile the flight Mach number: $M = 0$. The reason of this take-off condition (maximum thrust at sea level) is – as it is already mentioned – that the engine specifications are available at that operational mode in the technical datasheet of the engines [3].

The calculation methodology is summarized in subchapter 2.3.3 has been used in the present case also considering afterburning additionally. The mathematical model and the simulation approach of the afterburner is described in subchapter 2.3.1 for triple-spool mixed turbojet engines that can be used also for single-spool turbojet propulsion system after the needed adaptations. The known parameters of the engines are presented in Table 2.19. However, similarly to the previous scenarios, there are also unknown parameters of the engines, which are shown in Table 2.20. and 2.21. Matlab’s “fmincon” function has been used for constrained nonlinear optimization to find these non-available parameters. Minimising the differences between the available and

resulted thrust and thrust specific fuel consumption is the goal functions of the parameter identifications, meanwhile the unknown parameters – over the given ranges – are computed by the procedure. The results and the parameter ranges (upper and lower limits) are found in Table 2.20. and 2.21 too.

Table 2.19 Available operational data of the ПД-9Б and АЛ-21Ф3 turbojet engines at start condition [3]

Type of turbojet engine	Known input data, which are used in the simulation			Known available data for parameter identification	
	T_{04} [K]	π_c	\dot{m}_{air} [kg/s]	T [kN]	$TSFC$ [kg/(kNh)]
Single spool engine (ПД-9Б) with afterburner	1150	7.5	43.3	32.4	163
Single spool engine (АЛ-21Ф3) with afterburner	1385	15	104	110	190

Table 2.20 Identified parameters with the ranges of the investigated ПД-9Б and АЛ-21Ф3 turbojet engines at start condition

Type of turbojet engine	Pressure recovery rates and efficiencies of the engine components							
	r_d	r_{cc}	r_{al}	$\eta_{c,s}$	$\eta_{T,s}$	η_m	η_b	η_n
Single spool turbojet engine with afterburner (ПД-9Б)	0.9	0.94	0.91	0.83	0.87	0.995	0.97	0.95
Single spool turbojet engine with afterburner (АЛ-21Ф3)	0.9	0.93	0.89	0.82	0.88	0.99	0.94	0.92
Given ranges for the constrained optimization	0.88	0.93	0.88	0.81	0.87	0.99	0.94	0.92
	0.94	0.97	0.97	0.88	0.94	0.995	0.97	0.96

Table 2.21 Identified parameters and ranges of the investigated ПД-9Б and АЛ-21Ф3 turbojet engines at start condition

Type of turbojet engine	Power reduction rate of the auxiliary systems, bleed air ratio for technological reasons, air income ratio due to blade cooling and total temperature in the afterburner			
	ξ	δ_{tech}	δ_{bc}	T_{07} [K]
Single spool turbojet engine with afterburner (ПД-9Б)	0.005	0.077	0.0534	1700
Single spool turbojet engine with afterburner (АЛ-21Ф3)	0.005	0.07	0.06	1900
Given ranges for the constrained optimization	0.005	0.02	0.05	1700
	0.01	0.18	0.06	2200

Table 2.22 shows that the resulted thrust and thrust specific fuel consumption of the optimization is close to the available data. The highest relative differences between the known and the resulted values in the parameter fitting is 0.0617 % for the thrust and 0.0245 % for *TSFC* at PД-9Б engine, while the unknown parameters are presented in Table 2.20. and 2.21. are within the expected intervals.

Table 2.22 The available and the resulted thrust and thrust specific fuel consumption used in the optimization for parameter identification

Type of turbojet engine	Available data		Output of the optimization	
	<i>T</i> [kN]	<i>TSFC</i> [kg/(kNh)]	<i>T</i> [kN]	<i>TSFC</i> [kg/(kNh)]
Single spool turbojet engine (PД-9Б) with afterburner	32.4	163	32.42	162.96
Single spool turbojet engine (АЛ-21Ф3) with afterburner	110	190	110	190

The thermodynamic cycle including real engine processes of the PД-9Б engine in the *T-s* diagram is plotted in Fig. 2.12. The red curves (with smaller thickness) represent the constant pressures. The processes between the engine sections denoted by numbers are shown by thicker lines. This visualization effect is the reason for the constant pressure lines going below the process line in case of the pressure decrement just after sections “3” and “5” in this case also.

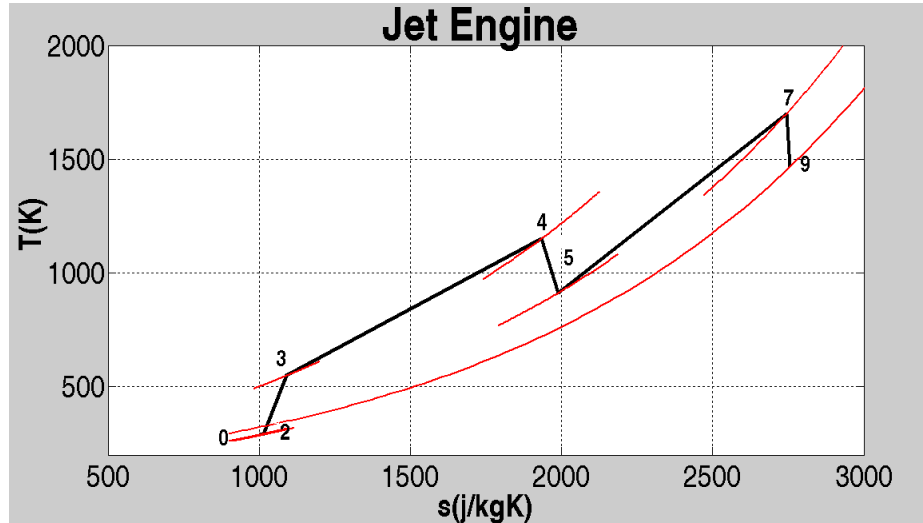


Figure 2.12 *T-s* diagram of the PД-9Б turbojet engine with afterburning

2.4.2. Numerical Representation – Verification of the New Equation for Optimum Total Pressure Ratio of the Compressor

The goal of the present subchapter is to verify the correctness and investigate the accuracy of the new expression for the optimum compressor total pressure ratio (see Eq. (2.21) and (2.33) in subchapter 2.2). Hence, a numerical representation of the optimum pressure ratio is completed. In this context, the numerical

representation is a searching algorithm over the expected pressure ratio range in order to find the total pressure ratio pertaining at maximum thrust. The same calculation method and the same parameters are used in the new expressions and in the numerical representation, which includes the application of the real (viscous) flow properties. The loss coefficients and other parameters, which were previously unknowns and were determined by the constrained nonlinear optimization based on the available engine data, can change at different operational conditions and at different pressure ratios. However, in this work, these variations are not considered, and all these unknown parameters are assumed to be constant at all pressure ratios except for the isentropic compressor efficiency which is the function of the fixed polytropic efficiency and compressor total pressure ratio for the fixed technology level. Fig. 2.13. and 2.14. show the compressor pressure ratio-thrust function as numerical representation.

The optimum pressure ratios are 10.5 and 23 at maximum thrust 33500 N and 114000 N for PД-9Б and AJI-21Φ3 engines respectively in the numerical representations. These values, provided by Eq. (2.21 and 2.33), are 10.2 and 22.8, and the corresponding maximum thrusts are 33680 N and 114400 N respectively. The highest difference between the maximum thrusts using a numerical method and using the new equation is 0.54 %. This deviation is due to the fact that the specific heats at constant pressure and parameters correspond to certain operational modes and the real flow assumptions in the specific thrust and thrust equations (Eq. (2.17 and 2.30)) are assumed to be constant during the derivation. However, the resulting difference is negligible, and the results are accepted in engineering point of view.

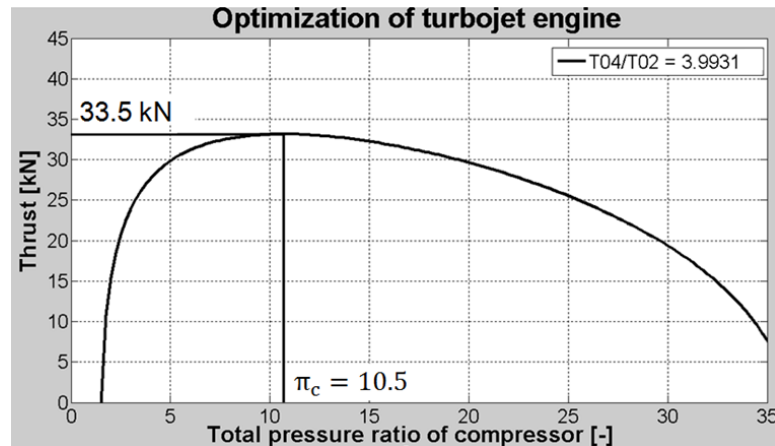


Figure 2.13 Thrust vs. total pressure ratio of the compressor for PД-9Б turbojet engines with afterburner

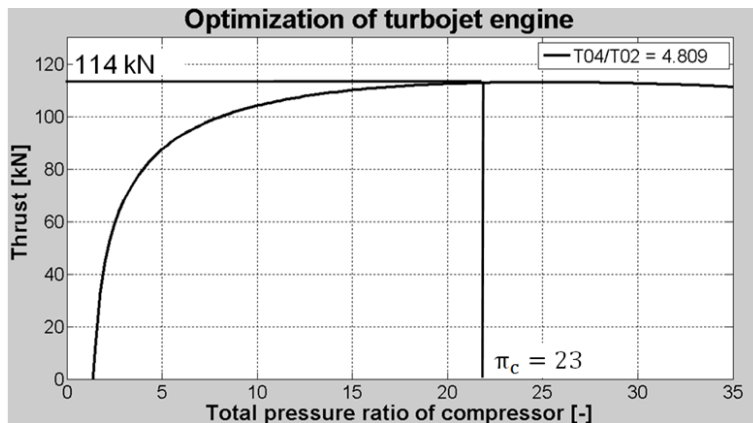


Figure 2.14 Thrust vs. total pressure ratio of the compressor for AJI-21Φ3 turbojet engines with afterburner

The specific thrusts in the function of compressor total pressure ratios for the both engines are shown in case of correctly expanded converging-diverging nozzle flow conditions and at different T_{04}/T_{02} ratios in Fig. 2.15 and 2.16. Higher turbine inlet temperature increases the specific thrust and the maximum values of that belong to higher compressor total pressure ratios. The thrust specific fuel consumption in the function of compressor total pressure ratio for the both engines are shown in case of correctly expanded flow conditions and at different T_{04}/T_{02} ratios in Fig. 2.17. The maximum specific thrust and minimum $TSFC$ belong roughly to the same compressor total pressure ratio ranges at the both investigated cases.

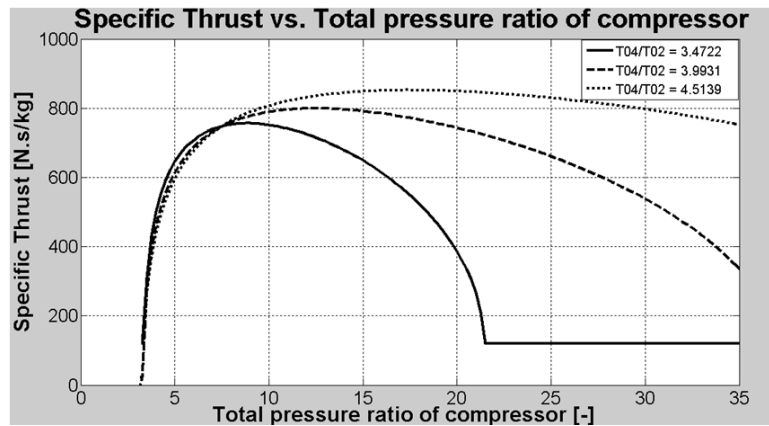


Figure 2.15 Specific thrust vs. total pressure ratio of the compressor for PD-9B turbojet engines with afterburner

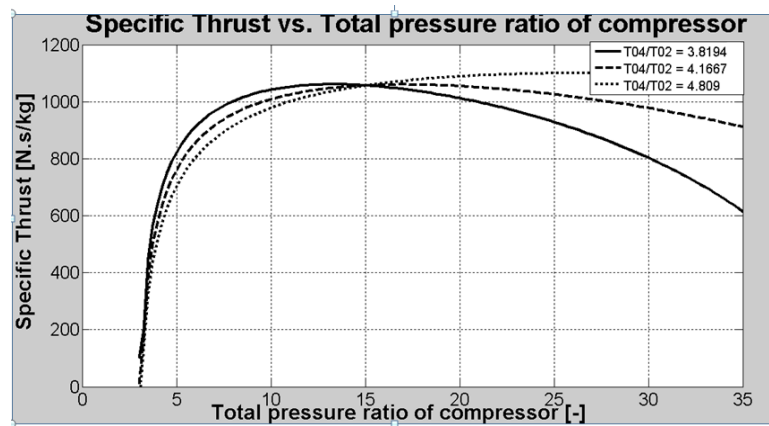


Figure 2.16 Specific thrust vs. total pressure ratio of the compressor for AL-21F3 turbojet engines with afterburner

Four different test scenarios are investigated to determine the effect of the pressure recovery factors, efficiencies and parameter dependent specific heats for the thermodynamic cycle, for the optimum pressure ratio and so for the maximum thrust of a single-spool turbojet engine. The results of this analysis are found in Table 2.23. The ■ sign in the column of viscous flow conditions means that the pressure recovery factors and efficiencies are considered in the calculation, meanwhile □ represents that they are not. In case of the real flow conditions and variable specific heats, which are considered in the Eq. (2.21) and (2.33), the optimum pressure ratio at the new equation is higher with 40 % and 53.3 % than the pressure ratio given in [3]. It corresponds to 3.39 % and 3.64 % thrust rising for PD-9B and AL-21F3 jet engines respectively. In addition, besides keeping

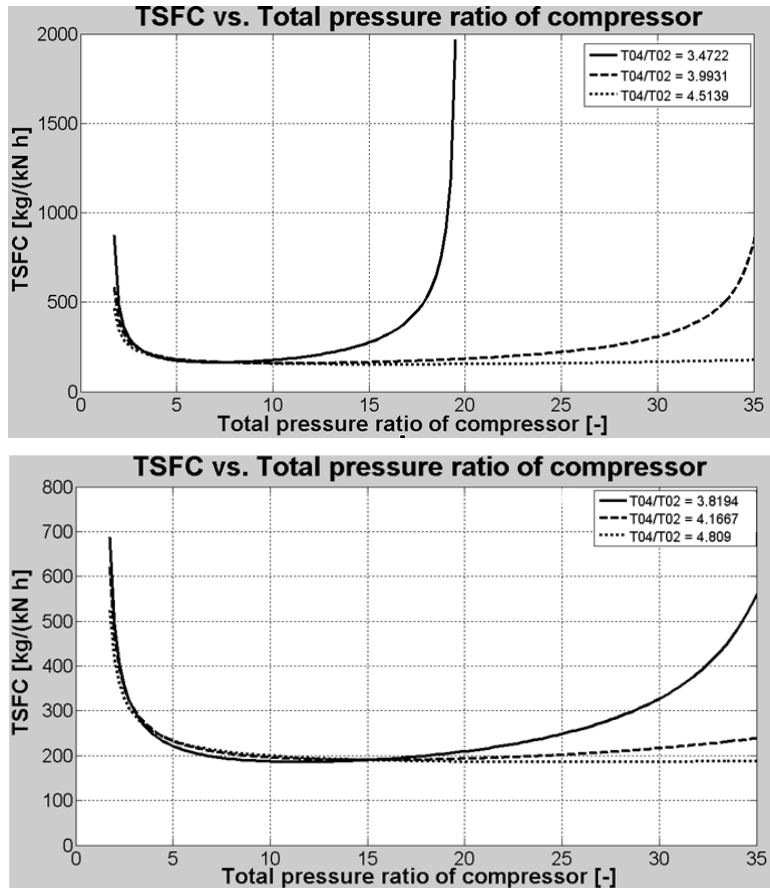


Figure 2.17 *TSFC* vs. total pressure ratio of compressor for PD-9B (above) and AL-21Φ3 (below) turbojet engines with afterburner

the viscous flow assumption, if the specific heat is defined to be constant, there is 9.52 % and 13.04 % decrease

Table 2.23 The effect of gas properties (with and without temperature and fuel to air mass flow rates ratio dependencies) and real flow conditions (pressure recovery factors and efficiencies) for the optimal pressure ratio and thrust for the PD-9B and AL-21Φ3 single spool turbojet engines

	viscous flow conditions	Gas properties	Optimum π_c by Eq. (2.21 and 2.33)		Corresponding Max. Thrust [kN]	
			PD-9B engine	AL-21Φ3 engine	PD-9B engine	AL-21Φ3 engine
Present optimization study	□	Dependent function by the fuel to air ratio of gas mixture and temperature	29	52	69.3	242.1
	□	Constant	27	47	66.4	220
	■	Dependent function by the fuel to air ratio of gas mixture and temperature	10.5	23	33.5	114
	■	Constant	9.5	20	32.9	111.3

ment in the total pressure ratio for ПД-9Б and АЛ-21Ф3 jet engines respectively. The non-real flow conditions – as inviscid and irrotational assumptions – provide unrealistic results; the thrust becomes double in comparing that with the plausible approach. The best and the most realistic test scenario for having the maximum thrust is given by case that pressure recovery rates and efficiencies are considered, and the specific heats are assumed to be dependent functions of temperatures and fuel to air mass flow rates ratios.

The condition presented in Eq. (2.18) is not sufficient to guarantee that the identified point is of the maximum thrust. The second derivative should also be checked. However, by having the similar result of the analytical method and numerical representation, it is not necessary to investigate the second derivative.

2.5. Conclusions

Today, the turbojet engines are the most relevant propulsion systems for aeronautical applications at low-speed supersonic flow regime between the low by-pass and ramjet engines and they can be considered an essential platform amongst the gas turbine engines in respect to establishing novel mathematical models. Design, development and analysis of such engines can be improved and accelerated by deriving new, simple and closed-form expressions with high accuracy for determining optimum operational conditions.

Hence, novel analytical expressions are derived and presented in subchapter 2.2, following the introduction and general remarks, to calculate the optimal compressor total pressure ratio belongs to the maximum thrust and to determine the critical pressure at the outlet of the converging nozzle for single spool turbojet engine. The new equations include viscous flow assumption by means of pressure recovery factors and efficiencies in case of relevancies and they consider technical parameters if these are available, meanwhile the specific heats are in the function of the temperature and fuel to air mass flow rates ratio.

In order to test the novel analytical expressions and to increase the coverage of thermodynamic cycle-analysis, mathematical model is developed, implemented in MATLAB environment and introduced in subchapter 2.3 for determining the characteristics of the triple-spool and dual-spool turbofan and single-spool turbojet engines w/wo afterburner at take-off/flight conditions depends on the available and considered conditions for the highest technical coverage. The mass, energy balance and the real thermo-dynamical process-equations are used in the concentrated parameter distribution-type method. Mechanical, isentropic, nozzle and burning efficiencies, pressure recovery factors, bleed air ratio for technological reasons, air ratio for blade cooling, fan and intermediate compressor pressure ratios, the afterburner temperature and power reduction rate of the auxiliary systems are considered in case of relevancies, which are not given in the technical literature [3]. Nonlinear constraint optimization method is applied for determining these data by means of fitting the resulted thrusts and thrust specific fuel consumptions to their known parameters are available in the technical specification [3]. Nevertheless, the ambient pressure and temperature, flight Mach number, incoming air mass flow rate, pressure ratio of the compressor and turbine inlet total temperature of the engines are available – if they are relevant – and they are the input parameters of the analysis. The material properties such as specific heat and the ratio of specific heats depend on the temperature and the ratio of component mass flow rates and so they are determined by iteration cycles due to the functional dependencies. HK-32 and HK-25 triple spool mixed turbofan engines at take-off (start) condition with afterburner, HK-22 and HK-144A dual spool mixed turbofan engines at take-off and at flight conditions with and without afterburning respectively, HK-8-4 and HK-86A dual spool mixed turbofan engines at take-off condition without afterburning and БД-7 and КР7-300 singles spool turbojet engines at take-off condition without afterburner are analysed by the mathematical

model to be introduced. The resulted thrusts and thrust specific fuel consumptions by parameter fitting and the available data in [3] are compared with each other. The maximum and the average relative deviation between them are 1.46 % and 0.645 % for the thrust and 0.55 % and 0.32 % for the thrust specific fuel consumptions respectively, meanwhile the identified parameters are within the plausible range.

Although the presented results provide feasible and correct technical information about the engines' operation, more analyses at different operational conditions together with applications of different types of propulsion systems should be considered, including validation, to investigate further the accuracy of the developed mathematical model.

The HK-32 and HK-25 engines have been used for determining the effect of the new equation - calculates the critical pressure - on the thrust and thrust specific fuel consumption. The results of the parameter identification for the unknown data show that the average value of the relative deviations between the resulted and the available thrust and thrust specific fuel consumption is 0.119 % by using a variant of the new equation for the critical pressure and it is 3.13 % at the conventional equation with constant gas properties (the ratio of specific heats for gas equals 1.33). The "variant" in the present context means that the true specific heats at constant pressure and at the given temperatures are considered instead of the averaged one in the total enthalpy equation. The new equation for determining the critical pressure is tested also for ПД-9Б single-spool turbojet engine with afterburning and at take-off condition. It gives higher critical pressure by 9.3 % than its original form with constant gas properties.

Finally, testing and verification of the novel analytical equation for the optimum compressor total pressure ratio is completed and presented in subchapter 2.4. ПД-9Б and АЛ-21Ф3 single-spool turbojet engines are considered for that purpose with afterburning and at take-off condition. First, similarly to the parameter identification described above, the unknown pressure recovery factors, efficiencies and the missing technical parameters are determined with MATLAB-based "fmincon" optimization algorithm. The known thrust and thrust specific fuel consumption are the goal functions of the optimization, which are aimed to be reached by modifying the unknown parameters over the given ranges. The resulted thrusts and thrust specific fuel consumptions of the optimization are close to the available data in [3]. Concerning both engines, the highest relative differences between the known and the resulted values by the parameter fitting is 0.0617 % for the thrust and 0.0245 % for the *TSFC* at ПД-9Б engine, while the unknown parameters are within the expected intervals. The plausibility of the new equation for the optimum total pressure ratio is verified by determining the extreme value of the pressure ratio-thrust functions numerically. The new equation for the optimum pressure ratio provides 3.39 % and 3.64 % thrust increments for the ПД-9Б and АЛ-21Ф3 jet engine respectively.

The presented modelling process and the new equations provide not only more accurate results for physical and technical processes but decrease the time for design, development and analysis of turbojet jet engines beside providing common platform for extending them for other type of engines too.

Based on the summary above in the paragraphs of the conclusions, the developed mathematical model and the new equations can be used in design and development processes of the engines.

3. Redesign of the Academic Turbojet Engine

3.1. Introduction

The small sized gas turbines are widely used for ground-based, vehicular applications, starter engine, APU (Auxiliary Power Unit) and research jet engine in academic applications due to low weight, easy to move and relative low cost. Furthermore, the utilization of this kind of engines has increased significantly as they are also applicable for remote-control airplanes or on unmanned aerial vehicles (UAVs) due to high thrust to weight ratio [34].

The small gas turbine includes power delivery under 5 MW. Typically, they are consisting of axial and/or centrifugal compressor, combustion chamber and axial turbine. The centrifugal compressors have several advantages in compared with axial compressors especially for small gas turbines, at which the flow paths are smaller and so the boundary layer thickness (δ) is relatively high. The centrifugal compressors are shorter, simpler and cheaper constructions and the blade numbers per stage is less than in case of axial compressors. The centrifugal compressors have higher pressure ratio per stage, they can resist better for surge and for impact of flying object. These types of compressors can fit to systems better with high pressure drop, because of the more effective energy-transfer. They have favourable isentropic efficiency below 5 kg/s mass flow rate, it is easier to balance, they are not much sensitive to the sudden variation of mass flow rate in time than the axial compressors do. The operation and the maintenance of the centrifugal compressor are cheaper; they have low power consumption at starting phase, higher reliability and longer lifetime [8].

Nowadays the demand for different calculation methods – including both design and analysis – is enhanced; significant numbers of researches are in progress with applying these approaches in the mechanical engineering ([35] and [36]). This is due to fact that high amount of cost, time and capacity can be saved by using well established and accurate methods and processes based on analytical, empirical, or numerical solutions. The frontloading product development reconfigures the conventional design processes and several sampling phases can be omitted by the virtual prototyping.

Moreover, there is another aspect, according to which the modelling and simulation is more important in case of complex systems as gas turbines for example. The development namely, in general, can be classified by the two limiting cases based on the delivered number of the products. The lower bound is called project related development, which means that the effort turns to realize only one product (as a new building, a special ship or other unique machine for example), meanwhile the upper limit, the product-based developments refer to the high number, sometimes millions of the products. The project related developments are characterised to be more costly, there are no sampling phases and there are no tests previously because the first product will be the final one in general. In contrast with that, the product-based developments involve low cost products in general and measurements are often the cases in the sampling phases. The schematic about the range between the project and product related developments are shown in Fig. 3.1. It is clear by the mentioned number of the products that the jet engines are closer to the project-based developments, so the emphasize in design and developments are rather based on reliable modelling and simulation, which makes the design and also the system cost effective and guarantees the safety and reliability.

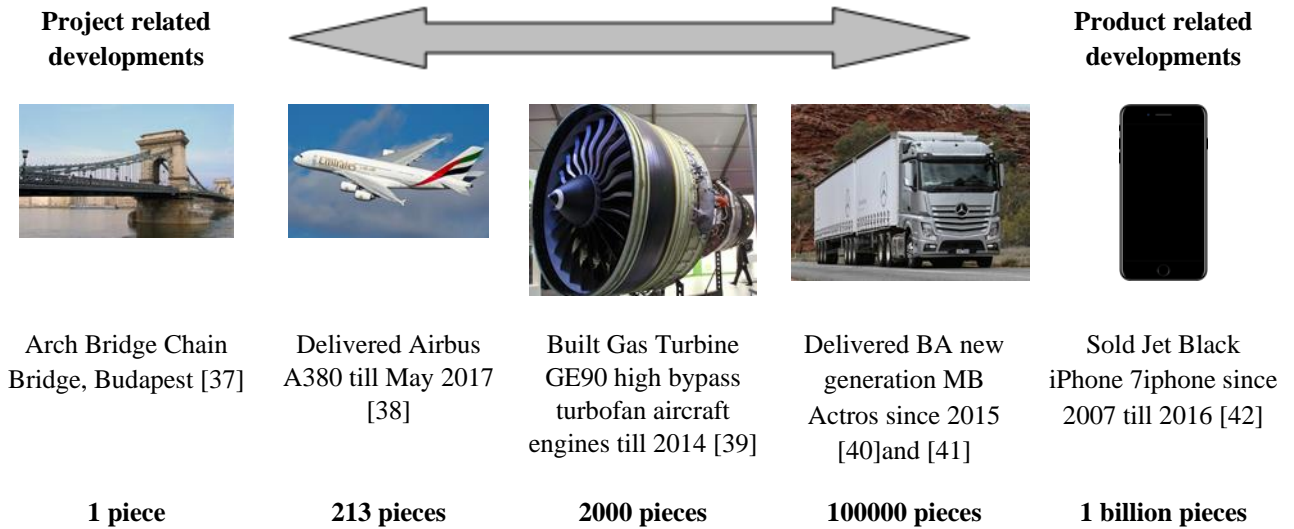


Figure 3.1 The project and product related developments

In most of the development processes, the available design variants are analysed by different calculation disciplines and design modifications are made if the characteristics are not matching with the expected specifications or other constraints are violated. The presented loop is going on till the desired structure is available. The Fig. 3.2 illustrates the impact of virtual prototyping on the time reduction and effectivity increment by using simulation driven product development. Of course, not the all design phases can be omitted by virtual prototyping. Measurements for validation purposes are strongly preferable to have at each design milestone.

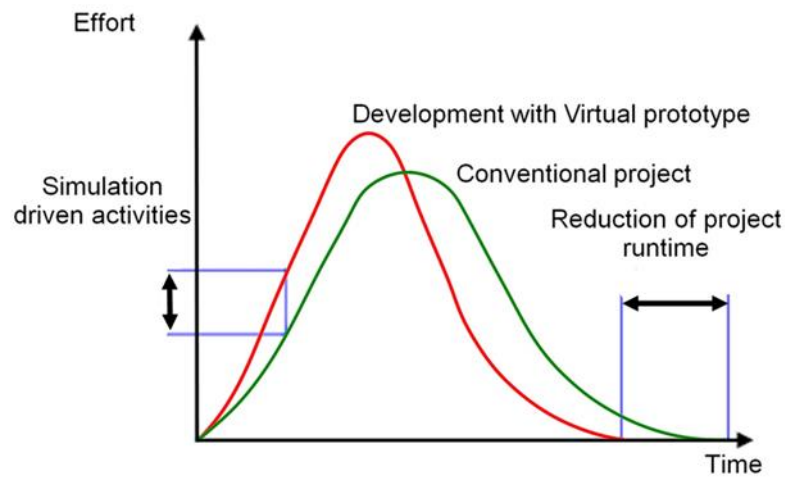


Figure 3.2 The impact of the virtual prototyping

The one of the main goals of the present research is to develop, apply, verify and validate aerodynamic development procedure for small jet engine corresponds to simulation driven product development.

3.2. Design Process of the Gas Turbine

Developing a new engine is a difficult and complex task that can be separated into numerous steps, ranging from the definition of the engine specifications to the delivery and instruction of the very first engine. Although each engine manufacturer has its own guideline for the design of a gas turbine engine, a general representation of the development process can be found in [23] and is shown in Fig. 3.3. The design process is set up to five main phases following the specification state. The first one is the preliminary studies and the second one is the determination of the thermodynamic design point. They are followed by the aerodynamic design and analyses of the gas turbine components, mechanical design, and finally the detailed design and preparation for production [23]. It is important to mention that all steps have different crosschecking and confirmation loops in order to guarantee that design goals are achieved [23].

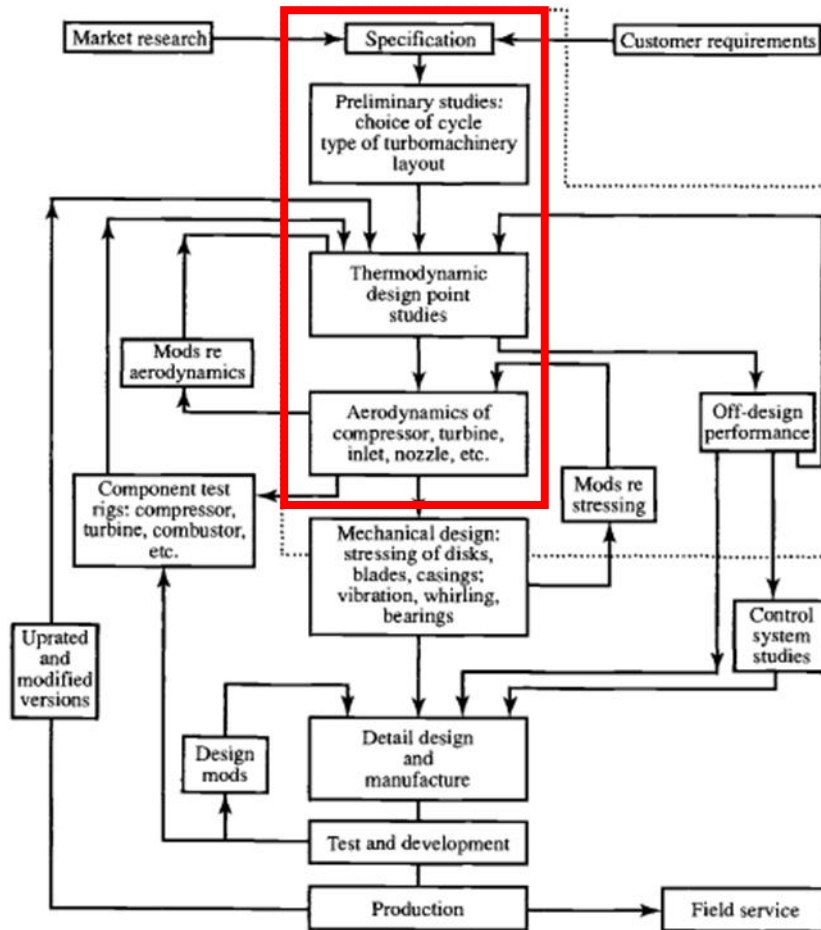


Figure 3.3 General design process for gas turbine engines [23]

Regarding the present study, the specification is given to redesign a small-sized single-spool research jet engine used for academic purposes.

The design process in the present case starts also with using mathematical model developed in the chapter 2 for the thermo-dynamical analysis by means of a concentrated parameter distribution type method in Matlab environment. This model is used to determine Thrust Specific Fuel Consumption – Specific Thrust map in the function of turbine inlet total temperature and total pressure ratio of the compressor.

The next step of the process is the mean line and 3D design of the engine components as compressor, combustion chamber, turbine and nozzle, by which the all necessary dimensions for creating the 3D geometry of the jet engine are determined. This status is found in the box of “Aerodynamics of compressor, turbine, inlet, nozzle etc.” in Fig. 3.3 and it is the last contribution of the design steps found in the red box, which contains the all design steps performed in the present work. However, the key word in the presented work is the virtual prototyping, which means that simulations (analyses) are completed following the detailed design to crosscheck the correctness of the process and initiates design modification in case of need within the frame of the front-loading design activity or design loop in other words.

3.3.General Concerns and Design Aspects

For designing the turbojet engine, it is essential to predetermine the method of calculating the characteristics in any cases for the specific values of the design variables. The design variables in this context mean the turbine inlet total temperature and the compressor total pressure ratio meanwhile the characteristics are the thrust specific fuel consumption in the function of the specific thrust at previously imposed pressure losses and efficiencies. In order to find the corresponding ranges of the design variables, the pressure losses and efficiencies are estimated based on previous literature research and/or experiences close to the expected operational condition, and for the simplicity, they are kept being constant in each point to be calculated. The turbine inlet total temperature has strong effect on the specific thrust. In general, keeping the engine as small-sized as possible for a given thrust is possible by having the highest maximum allowable value of TIT with considering the metallurgic reasons as limitation. Furthermore, the increase in total pressure ratio of the compressor will obviously cause decrease in the specific fuel consumption till the certain limit (see Fig. 2.17). At constant (allowable maximum) value of turbine inlet total temperature, the increase of compressor total pressure ratio first leads to rising specific thrust and finally decreases that. The highest specific thrust can be determined by a maximization problem. It is obvious that for any certain/smaller value of compressor total pressure ratio, the specific thrust is decreasing, and the specific fuel consumption is increasing as the optimum total pressure ratio belongs to the minimum thrust specific fuel consumption is generally higher than the total pressure ratio belongs to the maximal specific thrust for turbojet engines [23].

Regarding the turbine inlet total temperature and compressor total pressure ratio, the following aspects can be considered. High turbine inlet temperature can cause to increase the complexity of the structure and cost due to the application of cooled turbine blades and expensive alloys. Additionally, it is important to note that increasing pressure ratio enhanced engine weight, complexity and cost due to the need for more stages and multi spool configurations in extreme. These conditions are opposite with the needs, where the goal is to create a low-cost academic jet engine.

3.4.Redesign Procedure of the Turbojet Engine

The origin of the presently redesigned jet engine is TSz-21 starter gas turbine used for MiG-23 and Szu-22 Russian fighters. The TSz-21 engine has been modified to be an academic jet engine from 2005-2008 but it is still under development with especial care for control [2]. The geometrical information about the TSz-21 engine is shown in Fig. 3.4. The detailed information about the engine is found in [2].

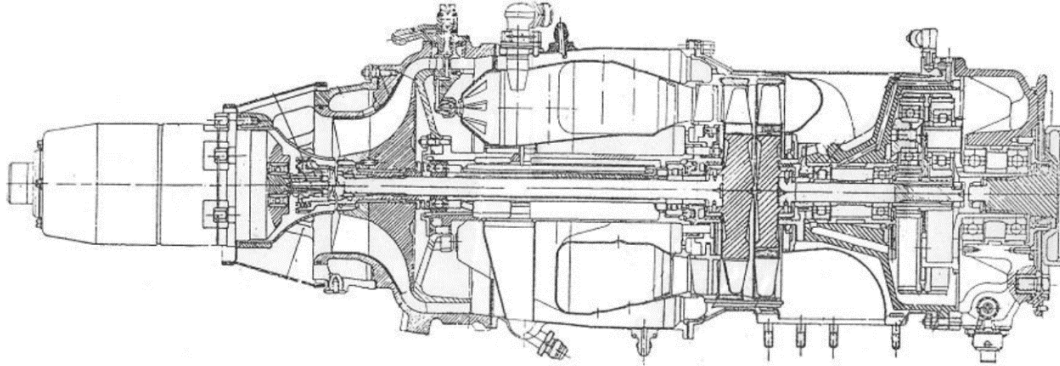


Figure 3.4 Cross sectional view of the Tsz-21 starter gas turbine geometry [43]

The of of the main goals of the present thesis is to introduce, apply and verify a design process for small-sized jet engine and analyse the results by using CFD method with plausibility check by the available measured data.

The jet engine under interest is a compact lightweight and possibly low-cost system that is adequate to create around 330 N thrust at steady state sea level ambient conditions for academic and research purposes.

The following sections introduce the applied design methods as thermo-dynamical cycle analysis with determination of the design point, mean line and 3D design of the compressor, inlet channel, combustion chamber, turbine and nozzle.

Thermodynamic analysis of the academic turbojet engine

The mathematical model is developed and used to determine the operational points and performances of the small turbojet engine. The method is introduced in detail and verified in chapter 2.

The following design criteria and assumptions are made. Ambient pressure and temperature of air are 99756 [Pa] and 299.6 [K] respectively, the fuel is assumed to be liquid kerosene with a lower heating value of 42700 kJ/kg. The considered parameters of total pressure recovery factors and efficiencies are based on the experiences and they come from chapter 2 and they are found in Table 3.1.

Table 3.1 Specified parameters of turbojet engine based on previous experiences

	Total pressure recovery factor of intake duct (r_d) and combustion chamber (r_{cc}); mechanical (η_m), nozzle (η_n) and burning (η_b) efficiencies; and compressor ($\eta_{c,s}$) and turbine ($\eta_{T,s}$) isentropic efficiencies						
Parameters	r_d	r_{cc}	η_m	η_n	η_b	$\eta_{c,s}$	$\eta_{T,s}$
Input data	0.99	0.94	0.99	0.95	0.96	0.7	0.8

The next step is to determine the expected design point of the jet engine. Hence, first, the performance map of the gas turbine has been created, where the thrust specific fuel consumption values are plotted in the function of the specific thrust, turbine inlet total temperature and total pressure ratio of the compressor. By this way, the effect of compressor pressure ratio on air mass flow rate is excluded; the variation in compressor pressure ratio does not change the mass flow rate across the engine at the same temperature. The outputs of the cycle analyses are used to determine the specific thrust (Eq. (3.1)) and thrust specific fuel consumption (Eq. (3.2)) [1]:

$$T_s = (1 + f_{cc})V_9 - V_0 + \frac{(1 + f_{cc})}{\rho_9 V_9} (p_9 - p_0) \quad (3.1)$$

$$TSFC = \frac{f_{cc}}{T_s} \quad (3.2)$$

The subscripts are based on the numbering shown in Fig. 2.9.

The performance map of the engine is shown in Fig. 3.5. For designing the jet engine, the basic thermodynamic parameters to be determined are the compressor total pressure ratio (π_c) and turbine inlet temperature (T_{04}).

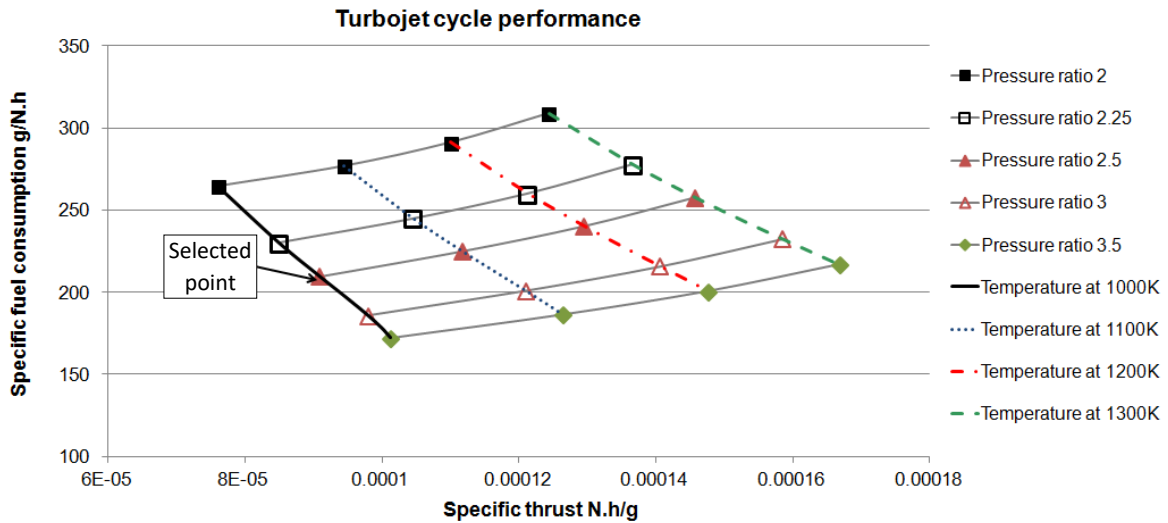


Figure 3.5 Performance characteristics of the academic jet engine

A total pressure ratio 2.5 is selected in the present case to be a reasonable compromise within the investigated range. As to achieve higher pressure ratio, it is required to consider advanced aerodynamic developments for the compressor, higher dimension, performance and state of the art production technology, which cannot be afforded by university application in the recent conditions. 1000 K turbine inlet total temperature is selected with considering that there is limited access for using high-tech cooling technology and advanced materials for the turbine blades.

The specific thrust is 327 Ns/kg (9.08E-5 Nh/g) at this point. So, by having the expected and the specific thrust of the academic jet engine, the mass flow rate of the incoming air is determined by the following way:

$$\dot{m}_{air} = \frac{T}{T_s} = \frac{330 \text{ N}}{327 \text{ N/(kg/s)}} = 1.009 \frac{\text{kg}}{\text{s}} \approx 1 \frac{\text{kg}}{\text{s}} \quad (3.3)$$

The mass flow rate of the fuel is 0.019 kg/s by Eq. (3.4) in the design point as the thrust specific fuel consumption is 209 g/Nh.

$$TSFC = \frac{\dot{m}_f}{T} \quad (3.4)$$

The real thermo-dynamical cycle of the engine in $T-s$ diagram is plotted in Fig. 3.6. The red curves (with smaller thickness) represent the constant pressures. The processes between the engine states denoted by numbers are plotted by thicker lines. This visualization effect is the reason of constant pressure lines goes below the process line in case of pressure decrement just after section “3”.

The thermodynamic parameters at the engine sections are shown in the Table 3.2

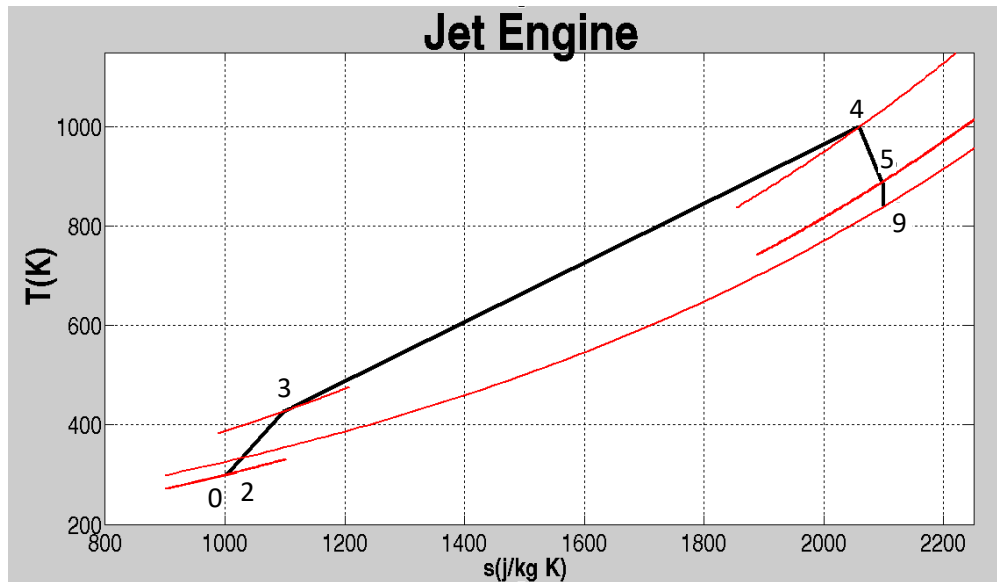


Figure 3.6 The T-s diagram of the academic jet engine

Table 3.2 Total pressure and temperature resulted by the thermodynamic cycle analysis.

Parameters	Ambient conditions	Inlet of the compressor (outlet of the diffuser)	Inlet of the combustion chamber	Inlet of the turbine	Inlet of the nozzle	Exit of the nozzle
Total pressure [Pa]	99756	98758	246896	232082	125722	124240 (static one: 99756)
Total temperature [K]	299.6	299.6	427.68	1000	887.12	887.12 (static one: 840.1)

3D design of the academic turbojet engine

After completing the thermodynamic analysis based on the required design specifications, the next step is to determine the geometrical sizes of the basic engine components as inlet diffuser, compressor, combustion chamber, turbine and exhaust nozzle [1]. As these designs are based on well established methods, the details of the component-designs are shown in Appendix A.

3.5. Conclusions

The aerodynamic redesign of a small academic jet engine has been introduced in the present part of the thesis. The considered engine was a starter gas turbine originally, which has been used for MiG-23 and Szu-22 Russian fighters. The engine was reconstructed to be a propulsion system by Dr. Beneda and Dr. Pásztor [2]. The present redesign process starts with the cycle analysis to determine the main thermodynamic parameters at the expected 330 N thrust at stationary (start) condition. The thermodynamic parameters are determined with viscous flow assumption and location dependent material properties in order to calculate the specific thrust and thrust specific fuel consumption. After making decision about operational point and having the states of the thermo-dynamical cycle, mean line design of the centrifugal compressor and axial turbine are completed. Following the 3D extension of the blades and the determination of the blade angles, chords, spacings, blade numbers and profiles, the 3D CAD models are prepared. Beside the compressor and turbine, the 3D models of the intake channel, combustion chamber and exhaust nozzle are also created. The main design criteria of these last three structures are to fit their geometrical sizes to the compressor and turbine and provide minimum pressure recovery factors. Moreover, the combustion chamber additionally should have high burning efficiency. The calculated thrust is 333.1 N, which is in line with the design specification. The aerodynamic design process of the components of the academic jet engine is introduced in Appendix A in detail.

The CFD analyses for crosschecking the correctness and the accuracy of the design are presented in chapter 4. CFD models with separated components and with complete assembly, as two approaches, have been used for that purpose.

The quantitative results of the i. thermodynamic design, ii. mean line design, iii. separated CFD analysis, iv. full model CFD analysis and v. the available measured data are shown and discussed in the chapter 5.

4. CFD Analysis of the Redesigned Academic Jet Engine

In the last decades, the benefit of CFD has been used in the design process more than before. Using that computational technology, numerous measurements can be replaced or reduced significantly, and so cost, capacity and time of developments can be saved. Many activities are available in that field [44, 45, 46]. The parameterization of the geometry provides higher reproducibility and flexibility in the model generation. The wide range of the visualization techniques get insight into the origin of the problem much deeper as ever was. Consistency, stability and convergence characteristics of the different numerical methods have been investigated and proved. The accuracy of the available methods allows designers to turn more effort on the new fields of the engineering practice called virtual prototyping, which is going to be the keyword of the next decades.

ANSYS CFX has been used for CFD analyses in the present work. The ANSYS CFX software is a state of the art, high-performance and general-purpose fluid dynamics program that has been applied to solve a wide-range of continuum-based fluid flow problems for over 25 years. The core feature of the ANSYS CFX is its advanced solver technology, the key to achieve reliable and accurate solutions quickly and robustly. The modern, highly parallelized solver is the foundation for an abundant choice of physical models to capture virtually any type of phenomena related to fluid flow. The solver and its many physical models are wrapped in a modern, intuitive and flexible GUI and user environment with extensive capabilities for customization and automation using session files, scripting and a powerful expression language [47] [48].

More information about the used CFD software is found in the Appendix B.

The all components of the academic jet engine are available in 3D CAD format till the end of the design process described in the previous chapter. The next step of the investigation is to crosscheck how the all components working separately and together, how their operation fulfil the design criteria and how their parameters fit to the parameters come from the design. Hence, 3D CFD simulations are prepared and completed.

Solid Edge software has been used for making the 3D models based on the geometry output described in chapter 3. Then Boolean operation is used to create flow fields from the solid structures. The solid domains are subtracted from the reasonable oversized volumes to get the flow field for the compressor, for the combustion chamber, for the turbine and for the nozzle. The 3D geometry of the assembly in wireframe model is shown in Fig. 4.1.

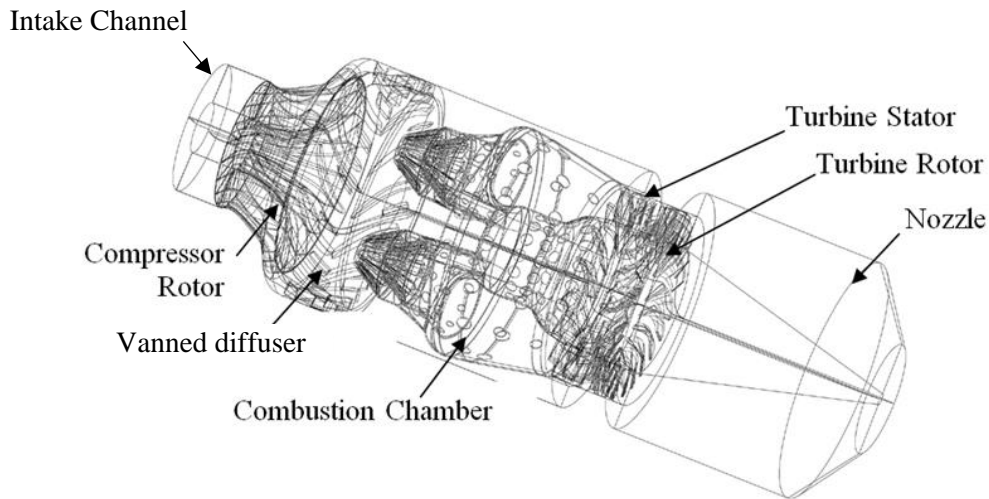


Figure 4.1 3D wireframe model of the academic jet engine

Two different modelling approach has been used for the CFD analysis of the redesigned academic jet engine: (1) separated models and (2) full model, which are discussed in the next two subchapters.

4.1.Flow Modelling of the Separated Engine Components

Separated components of the engine as the centrifugal compressor, combustion chamber, axial turbine and exhaust nozzle are considered and analysed by CFD methodology in the present part for determining the fluid- and thermodynamic parameters. The goal of this investigation is to compare them with the output of the thermodynamic cycle analysis, the design, the results of the CFD analysis for the full model and the available measured data. The intake channel (see that in Fig. 4.1) is a simple tubular section without any complexity, so homogenous and uniform upstream flow conditions are supposed. Hence, it is not considered with its 3D geometry in the present investigation. Regarding the boundary conditions, the ambient parameters are applied at the inlet of the compressor with considering the effect of the intake channel meanwhile the given mass flow rate is imposed at its exit section. The outlet total pressure and total temperature of the compressor, combustion chamber and turbine are used as the inlet boundary conditions for the combustion chamber, for the turbine and for the exhaust nozzle respectively. Their outlet boundary conditions are the given mass flow rate. Axial flow direction is considered at the inlet boundary condition of the nozzle. Hence, and due to the considered entry cross section, the results of this analysis cannot be compared with the results of the model-outputs, which consider partial entry section and non-perpendicular flow direction at the inlet of the nozzle.

4.1.1. CFD analysis of the centrifugal compressor

The geometry and the flow filed of the compressor has rotational periodicity, so one quarter of the 3D model is applied in order to reduce computational effort and use finer mesh. After preparing the flow field, the next step is the mesh generation. The boundary layer is resolved in such a way that the first cell from the wall to be fallen in the log layer region. Hence, dimensionless analytical expressions are used to determine the distance of the first cell from the wall to have y^+ between 30 and 300. The inflation layer is used with 2.4 mm total

thickness and 1.2 growth rate on the blade wall of the rotor and stator. The inflation layer is built up from 5 layers. Although the hex-dominant elements give better resolution due to the discretization method at grid aligned flow conditions, tetrahedron elements have been used due to the complexity of the geometry. The final mesh is built up from 3471912 elements and it contains 986800 nodes (see Fig. 4.2.).

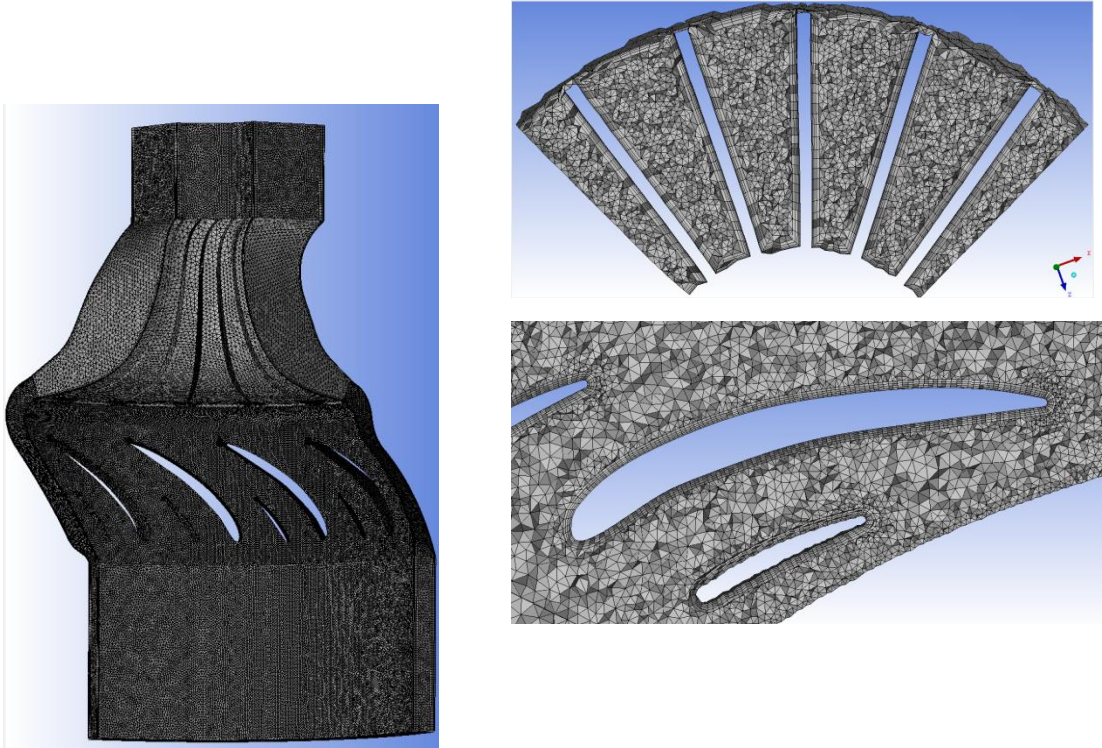


Figure 4.2 The final mesh of the centrifugal compressor passage (left) with the cut section of the rotor blade (right, top) and the stator vanes (right, bottom) meshing

Steady state continuum mechanics-based flow simulation is completed in ANSYS CFX software. 3D, compressible, turbulent and viscous air flow is considered. The operational fluid is assumed to be ideal gas. SST turbulence model is applied due to their advanced physical capabilities described in Appendix B. subchapter B.2. Frozen rotor interface has been used for rotor-stator interaction. Constant 43000 RPM is defined for the flow field of the impeller with no slip boundary condition for the relative velocity at the walls. Counter rotating wall option is set at the shroud section of the rotating flow field. Total pressure and total temperature at the inlet and mass flow rate at the outlet of the compressor unit have been defined as boundary condition. The heat transfer coefficient $8 \text{ W}/(\text{m}^2 \text{ K})$ corresponds to the stationer ambient air with 299.6 K temperature on the outer walls is applied for considering free convection, meanwhile adiabatic condition is imposed at the inner-side walls [49]. Table 4.1 shows the exact value of the boundary conditions, which are used in the simulations and Fig. 4.3 provides an overview about the locations of the used boundary conditions (excluding the solid walls).

Table 4.1 The applied boundary conditions

Inlet			Outlet
p_0 [Pa]	T_0 [K]	N [rev/min]	\dot{m} [kg/s]
98758	299.6	43000	0.25

The turbulence level is defined to be intensity value of 3.7 % is sufficient for nominal turbulence through a circular inlet and is a good estimate in case of no available measured data [50]. The global residual as 10^{-4} is taken as the convergence criterion for the simulation.

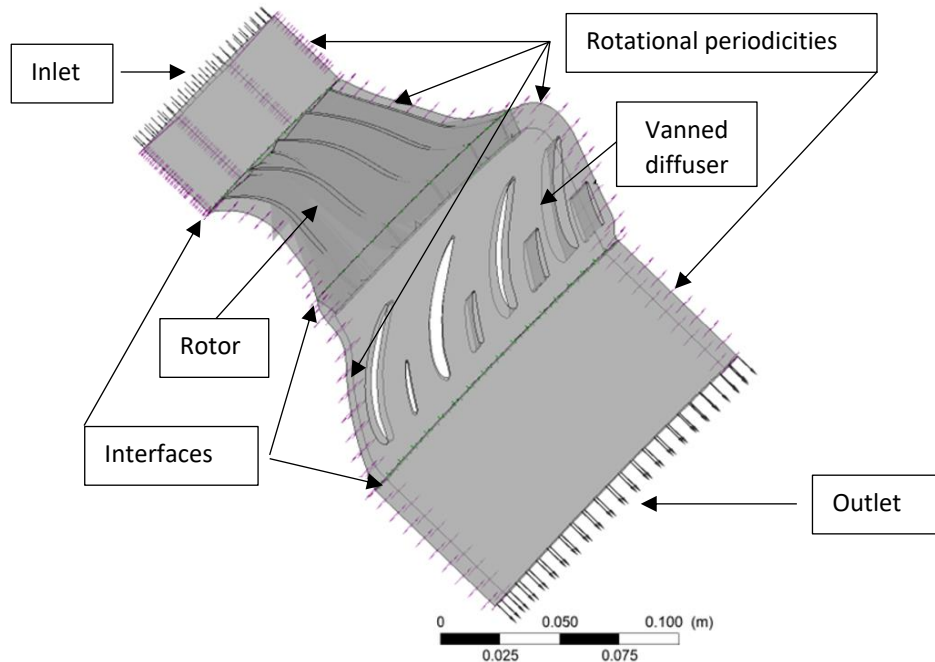


Figure 4.3 The flow field of the centrifugal compressor passage with the used boundary conditions except for the solid walls. The contact pairs of the rotational periodicities are opposite of each corresponding surface.

The imbalances converged after 1000 iteration steps under 1% and reached the convergence criteria, hence no further calculations are needed. A mesh size sensitivity analysis is completed, and it shows that the results are independent from the used spatial resolution.

The qualitative results are plotted, and they are shown in Fig. 4.4 and Fig. 4.5. Based on the streamline distribution in Fig. 4.4, the maximal velocity is reached at the exit of the rotor blades and the local Mach number exceeds the sonic speed. The outcomes of the simulation are in line with the expectations, the results are in the plausible range. The quantitative analysis of the parameters is introduced and discussed in chapter 5.

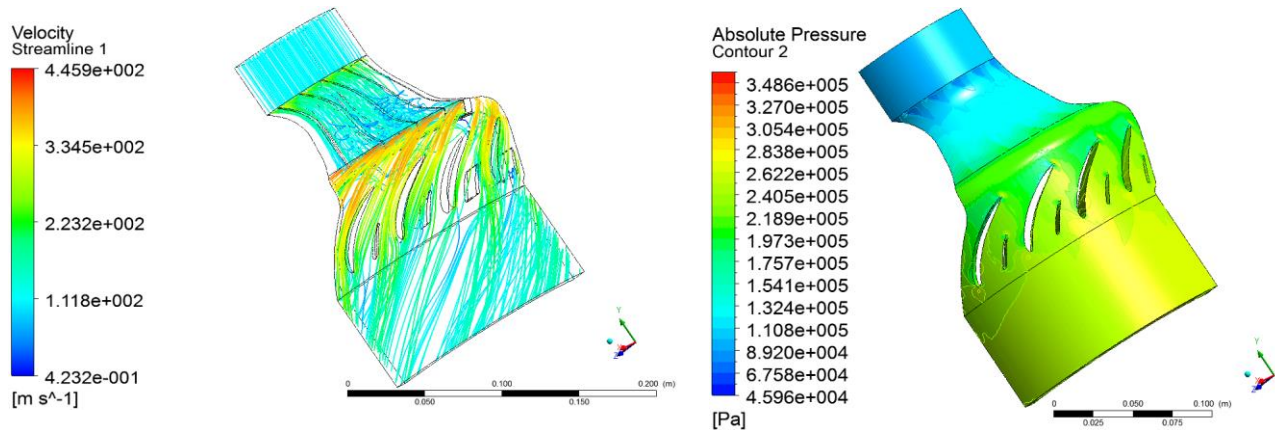


Figure 4.4 Streamlines are coloured by the velocity magnitude (left) and absolute pressure distribution on bounding walls of the centrifugal compressor unit (right)

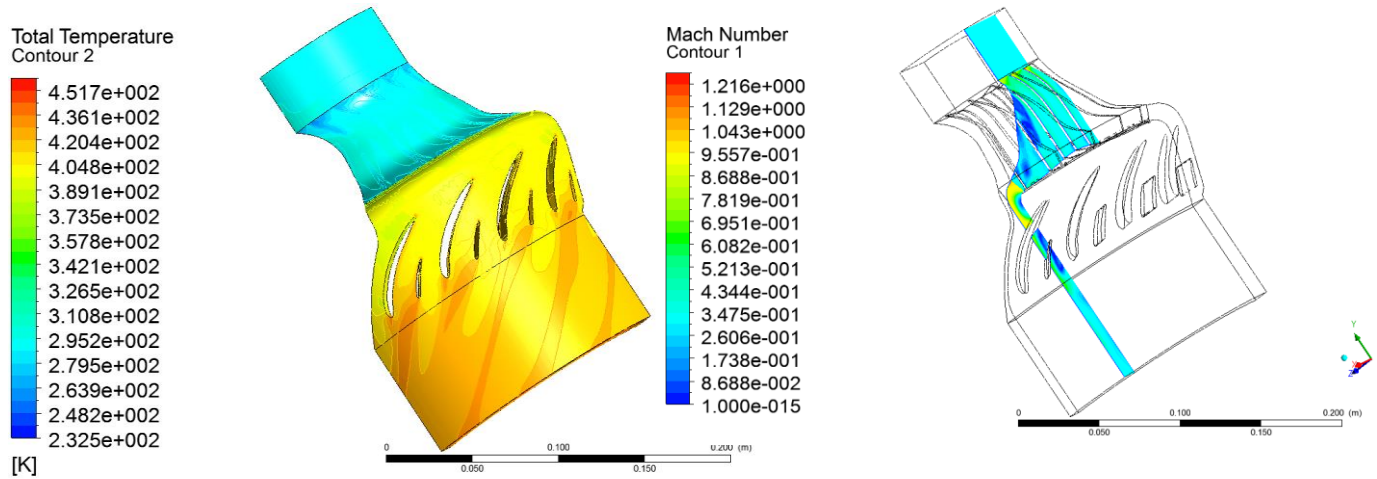


Figure 4.5 Total temperature (right) and Mach number (left figure on a selected inspection plane) distribution in the centrifugal compressor

4.1.2. CFD analysis of the combustion chamber

Similarly to the compressor unit, Solid Edge software has been used also to create the 3D model of the combustion chamber (see Fig. 4.6). One quarter part of the combustion chamber is used also for preparing the CFD flow domain due to the rotational periodicity.

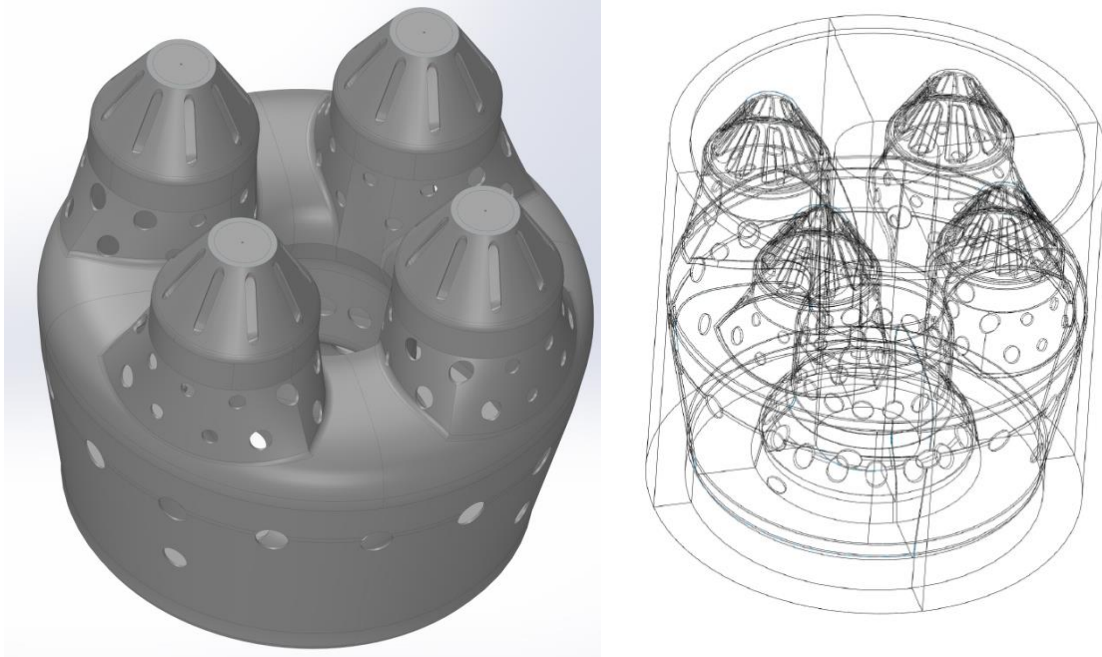


Figure 4.6 CAD model of the combustion chamber (left) and the wireframe model of the flow domain around the combustion chamber (right)

The fuel enters the combustion chamber on a 0.8 mm diameter circular surface thus the finest mesh is used here with 0.04 mm edge length. The global volume is meshed with 5 mm large elements and mesh refinement is applied on the specific walls shown in Fig. 4.7. Inflation layers are used with 2.3 mm total thickness and 1.2 growth rate. The inflation layer is built up from 10 layers. The final mesh can be seen in Fig. 4.8. which is built up from 6660546 elements and it contains 2259830 nodes.

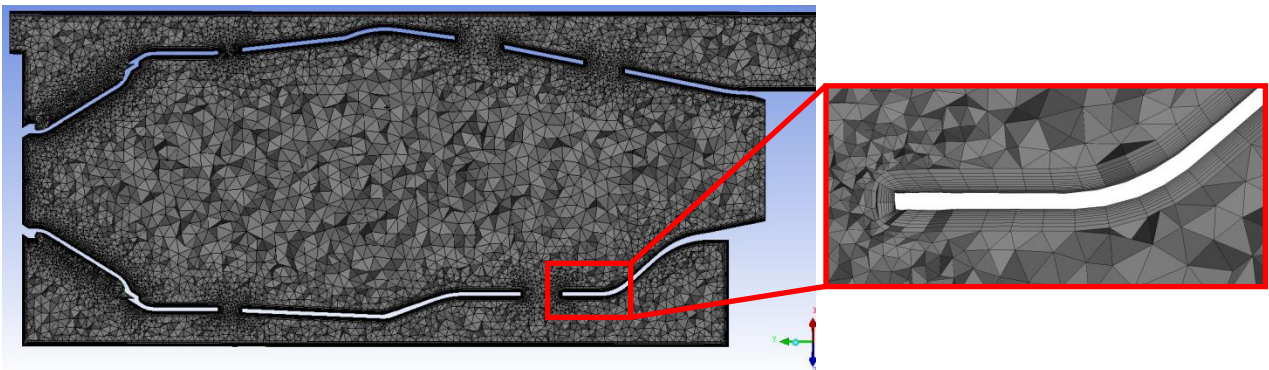


Figure 4.7 Meshing of the cross-sectional view of the combustion chamber

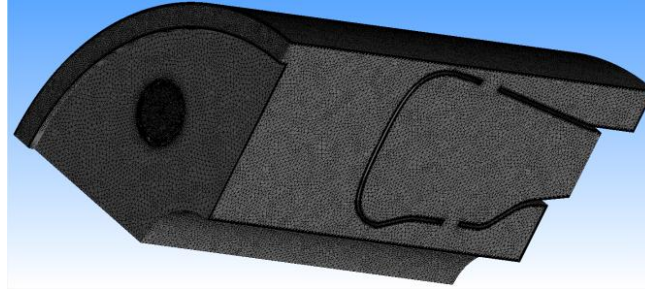


Figure 4.8 Final mesh of the combustion chamber

The fluid dynamic phenomena are turbulent, and they are combined with heat transfer processes and the reaction kinetics in the combustion chamber. So, beside the basic governing equations as mass-, momentum- and energy conservation laws, supplementary equations are needed to be solved numerically. The standard k-epsilon turbulence model and P-1 radiation model is used in this analysis. Regarding the combustion, non-premixed combustion modelling with the PDF-mixture fraction model is applied. In the non-premixed combustion, the fuel and oxidizer enter separately in the reaction zone. The PDF Flamelet combustion model is considered, it can handle chemical reactions by means of going through in a non-premixed turbulent fluid flow in a short time frame. The generated Flamelet library for Jet A is large, since it includes all the possible species that can exist in the Jet-A combustion. Simulations with this library take much computational time and computer resources, even the required time to load this library at the beginning of each simulation. In order to save time, the species of the library are reduced to H, O₂, OH, O, H₂, H₂O, CO, CO₂, n-C₁₀H₂₂, TMB-C₉H₁₂ and N₂ [51]. Table 4.2. represents the list of applied models to be used in this simulation with especial care for the combustion modelling.

Table 4.2 The applied methods and settings for modelling processes in the combustion chamber

Advection scheme	High resolution
Turbulence model discretization scheme	High resolution
Turbulence model	K-Epsilon
Liquid phase	Lagrangian Particle Tracking
Primary breakup	Blob Method
Drag Force	Schiller-Naumann
Heat transfer	Ranz-Marshall
Combustion	PDF Flamelet
Thermal radiation model	P-1

Fig. 4.9 provides an overview about the boundary conditions (excluding the solid walls), which has been considered in the simulation of the combustion and Table 4.3 shows their exact value.

Table 4.3 The applied boundary conditions for combustion chamber

Inlet air		Inlet fuel			Outlet
p_0 [Pa]	T_0 [K]	V [m/s]	T_0 [K]	\dot{m}_{fuel} [kg/s]	\dot{m} [kg/s]
267175.2	419.5	12	299.6	0.00475	0.25

The heat transfer coefficient $8 \text{ W}/(\text{m}^2 \text{ K})$ corresponds to the stationary ambient air with 299.6 K temperature on the outer walls is applied for considering free convection [49].

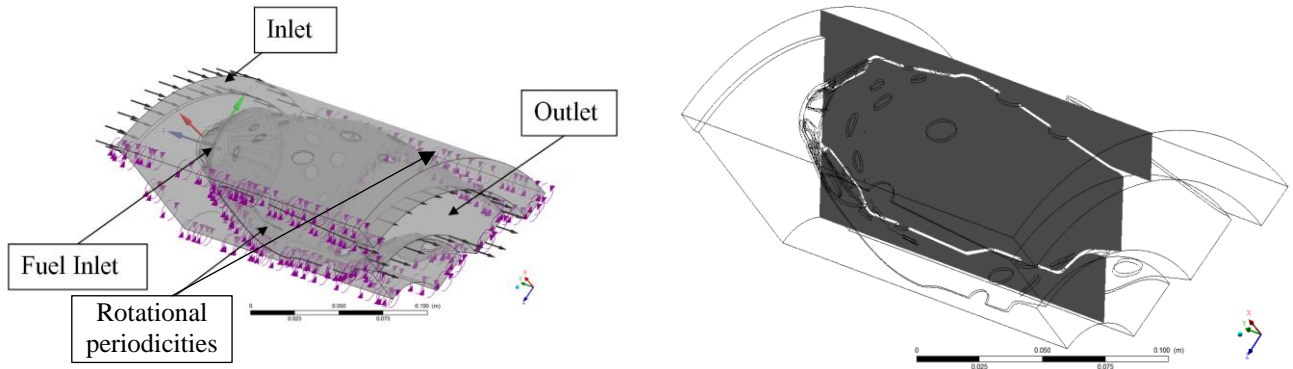


Figure 4.9 The flow field of annular type of combustion chamber with the locations of the boundary conditions (excluding the solid walls) and meridional plane for the representation of the results

The imbalances converged after 700 iteration steps under 1% and reached the convergence criteria on a cell-size independent simulation.

The qualitative results are plotted, and they are shown in Fig. 4.10-4.12.

The velocity distribution in the streamlines is found in the left side of the Fig. 4.10. It shows that velocity of air slows down enough for a stable combustion. Recirculating flows develop by means of big vortices represented in the left side of Fig. 4.11. They are in the middle of primary zone and they help to mix the air and fuel properly. However, there are other vortices in the corners and stagnation zones, due to the secondary air flow enters the combustion chamber, just cause pressure loss in the combustion chamber. The total temperature distribution is presented in the right side of Fig. 4.11. It shows high values from the inlet of fuel to the central region of the chamber, which can be considered as flame front. From this figure it also turns out, that the entering air from the secondary flow protects the inner wall against the high-heat load. The area-averaged temperature at exit of the combustion chamber is 1009 K , which is close to the design value of 1000 K . Fig. 4.12 shows the mass fractions of the $n\text{-C}_{10}\text{H}_{22}$ (on the left side) and O_2 (on the right side). They represent the expected mixing, burning and dilution processes, as n -decan appears in the primary zone of the combustion chamber while the oxygen has higher mass fraction behind the burning zone due to the high amount of incoming air for cooling purposes.

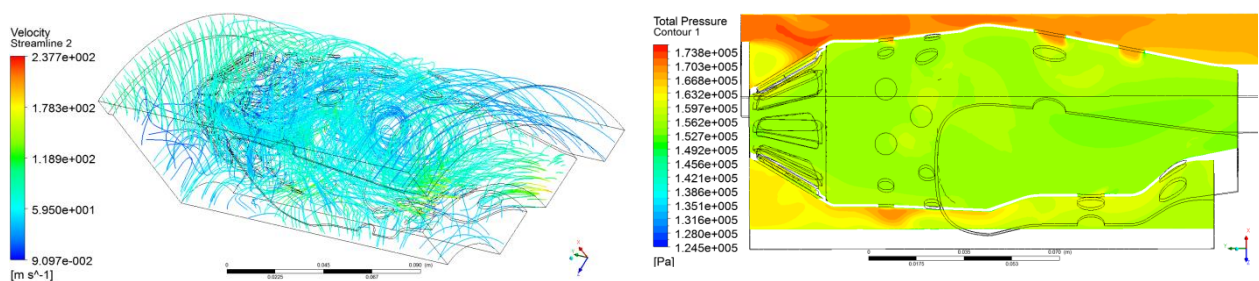


Figure 4.10 Streamlines are coloured by the velocity magnitude (left) and total pressure distribution in the meridional plane (right) of the combustion chamber

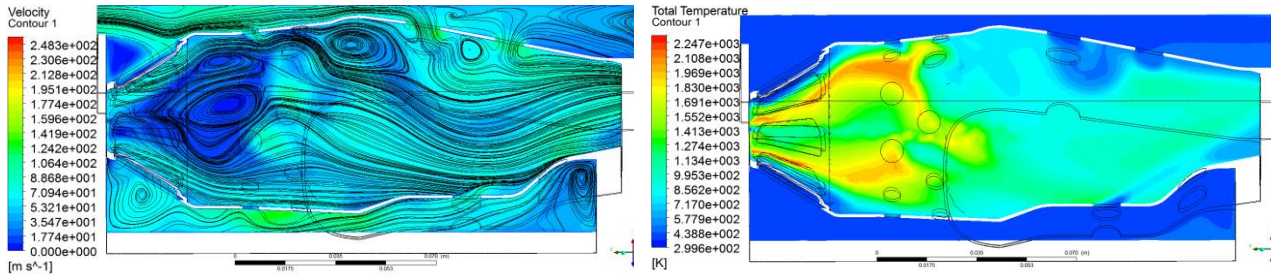


Figure 4.11 Streamlines and velocity distribution (left) and total temperature distribution (right) in the meridional plane of the combustion chamber segment

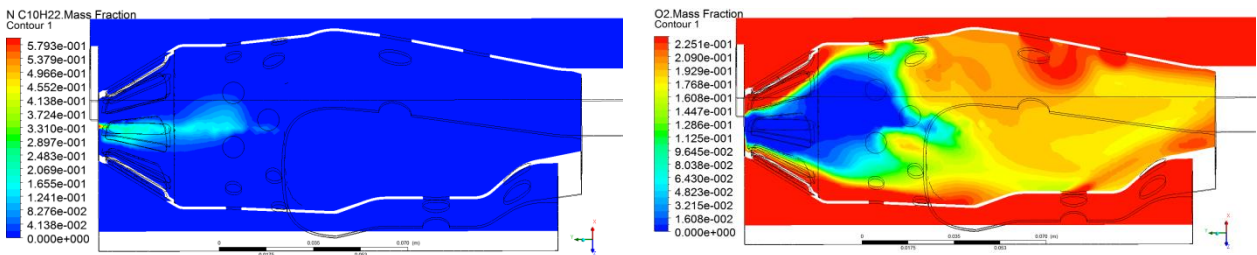


Figure 4.12 Mass fraction of the normal-decan (left) and oxygen (right) in the meridional plane of the combustion chamber segment

4.1.3. CFD analysis of the axial turbine

The 3D model of the one quarter part of the axial turbine and its flow model is created by the same CAD software as it was used for the combustion chamber. Unstructured mesh is applied for the flow domain out of the inflation layer. 2.4 mm total thickness and 1.2 growth rate of the inflation layer mesh is used on the blade wall of the rotor and stator and at the tip and hub solid bounding surfaces of the turbine section. The inflation layer is built up from 6 layers. The final mesh is shown in Fig. 4.14. It consists of 4082068 elements and 1307400 nodes.

Material properties of the combusted gas have been used in the simulation.

Table 4.4 shows the exact value of the boundary conditions, which are used in the analysis of the axial turbine. Incoming flow to be perpendicular to the inlet surface is considered.

Table 4.4 The applied boundary conditions of axial turbine

Inlet		Outlet	
p_o [Pa]	T_o [K]	N [rev/min]	\dot{m} [kg/s]
255323	1009	43000	0.25

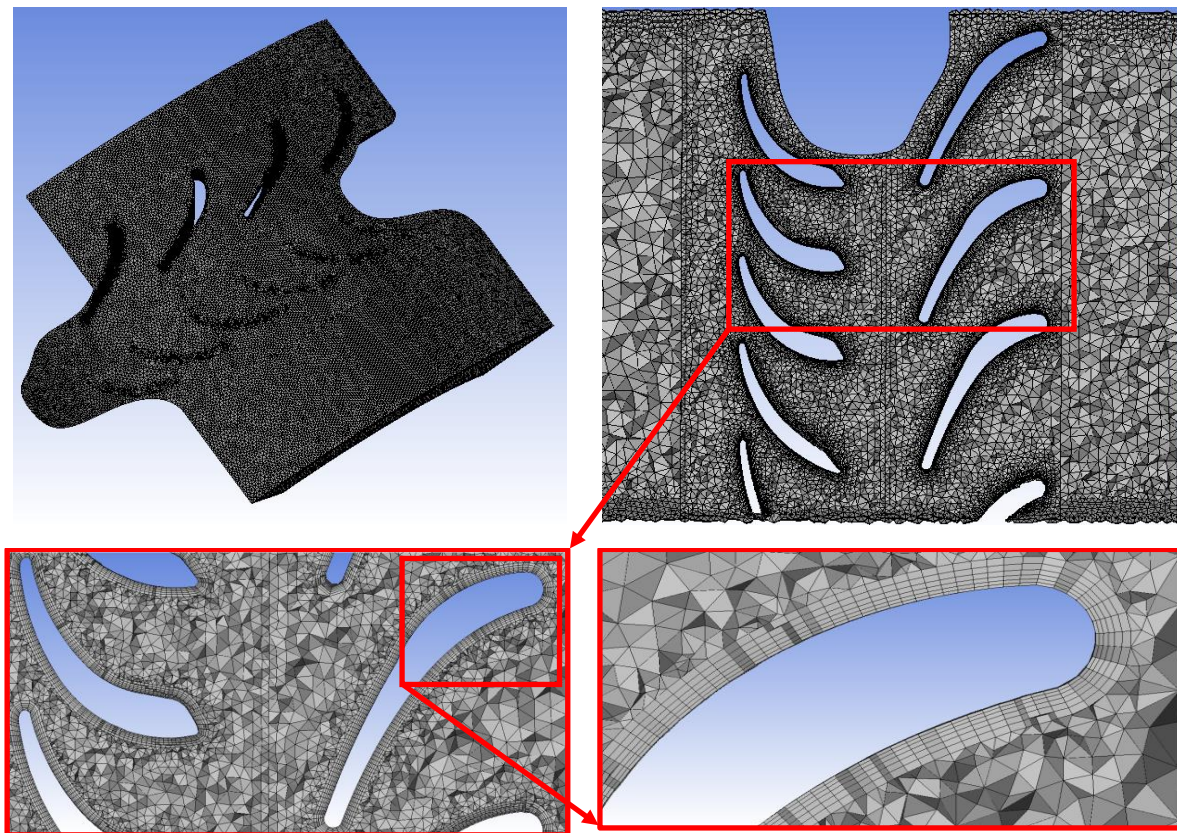


Figure 4.13 The final mesh of the axial turbine (top left) with cut section through the vanes (top right, bottom left and bottom right) including the inflation layer

Fig. 4.14 provides an overview about the flow fields, interfaces and boundary conditions (except for the solid walls and periodic surfaces), which have been used in the simulation.

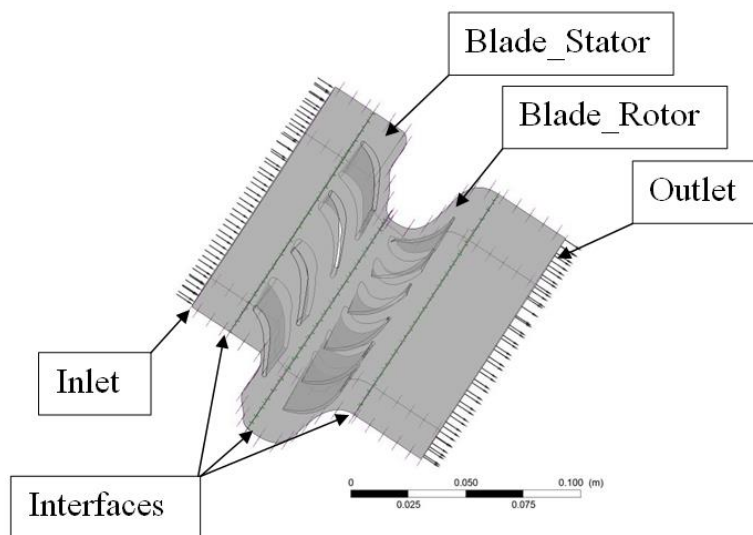


Figure 4.14 The flow fields, interfaces and the locations of the boundary conditions (except for the solid walls and periodic surfaces) of the axial turbine

The heat transfer coefficient $8 \text{ W}/(\text{m}^2 \text{ K})$ corresponds to the stationer ambient air with 299.6 K temperature on the outer walls is applied for considering free convection [49].

The residuum and the imbalances converged after 60 iteration steps in case of mash independent simulation, so no further simulation and iteration steps are required.

Qualitative results are plotted, and they are shown in Fig. 4.15-4.16. The absolute static pressure decreases through the turbine section and the total temperature drops across the turbine rotor due the work done by the expanding gases. The results are in line with the expectations, they are in the plausible range. The quantitative analyses of the parameters with comparing them with others, which come from design and analyses, are presented in chapter 5 as it was already mentioned.

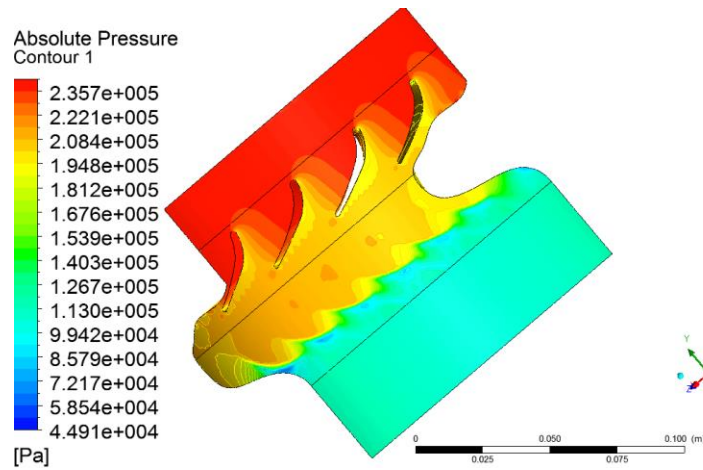


Figure 4.15 Absolute static pressure distribution on the tip section of the axial turbine

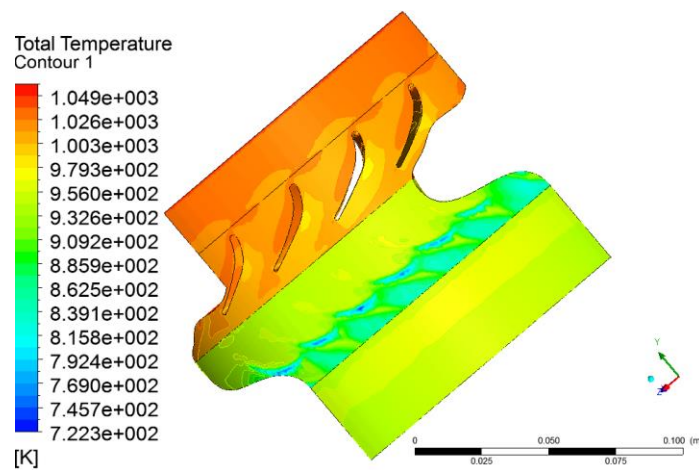


Figure 4.16 Total temperature distribution on the tip section of the axial turbine

4.1.4. CFD analysis of the exhaust nozzle

Solid Edge software has been used also to create the 3D model of the exhaust nozzle and its flow field. Similarly to the previous cases, the one quarter part of the full model is used due to the rotational periodicity. The unstructured mesh is applied for this model out of the inflation layer. The inflation layer has 2.4 mm total thickness, 1.2 growth rate and it is made of 10 layers. The final mesh is shown in Fig. 4.17. It contains 4789013 elements and 1248789 nodes.

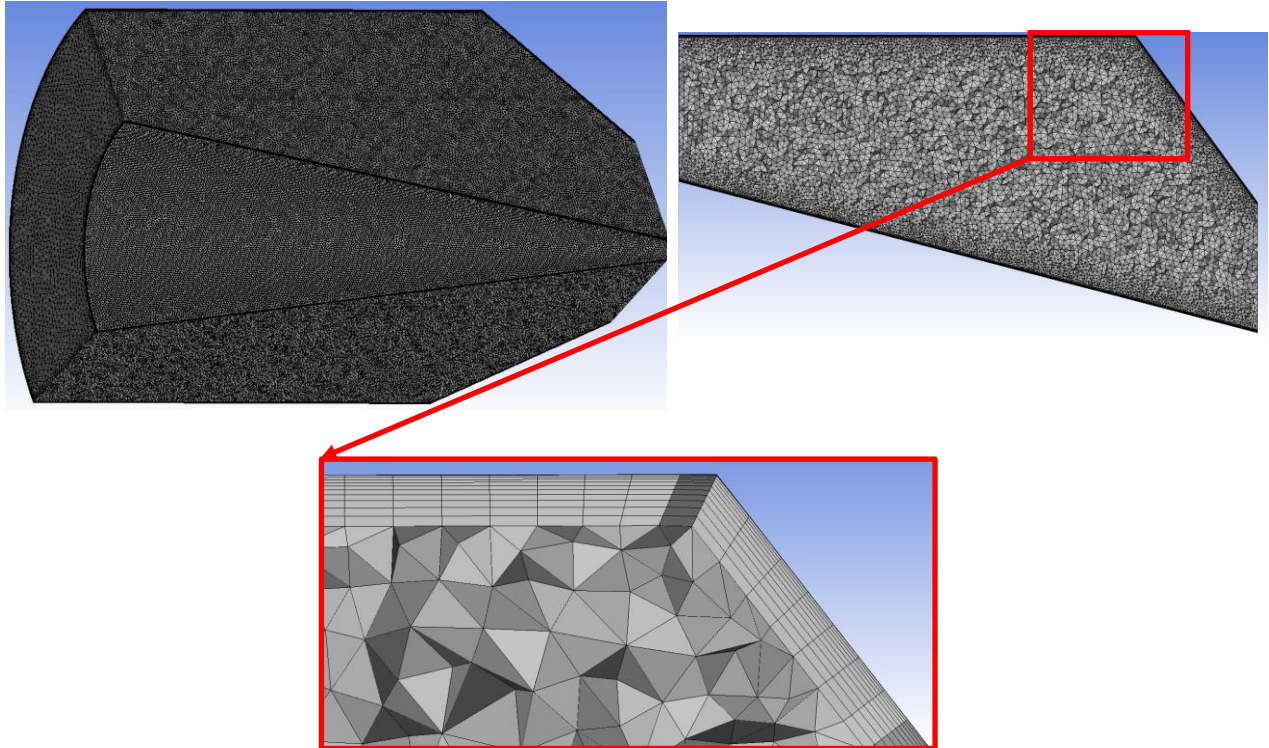


Figure 4.17 The final meshing of the exhaust nozzle flow domain (top left) and meridional cut-section of the nozzle mesh (top right and bottom)

Table 4.5 shows the exact value of the boundary conditions, which are used in the simulation of exhaust nozzle. The heat transfer coefficient $8 \text{ W}/(\text{m}^2 \text{ K})$ corresponds to the stationer ambient air with 299.6 K temperature on the outer walls is applied for considering free convection [49].

Although the flow leaves the turbine section has tangential component, only axial flow direction is considered in the present simulation. The full front section of the nozzle is considered as inlet section due to the general application. Hence, these data cannot be compared with the data resulted by the full CFD approach.

Table 4.5 The applied boundary conditions of the nozzle

Inlet		Outlet
p_0 [Pa]	T_0 [K]	\dot{m} [kg/s]
129625.6	900.32	0.25

Fig. 4.18 provides an overview about the boundary conditions, which has been used in the simulation.

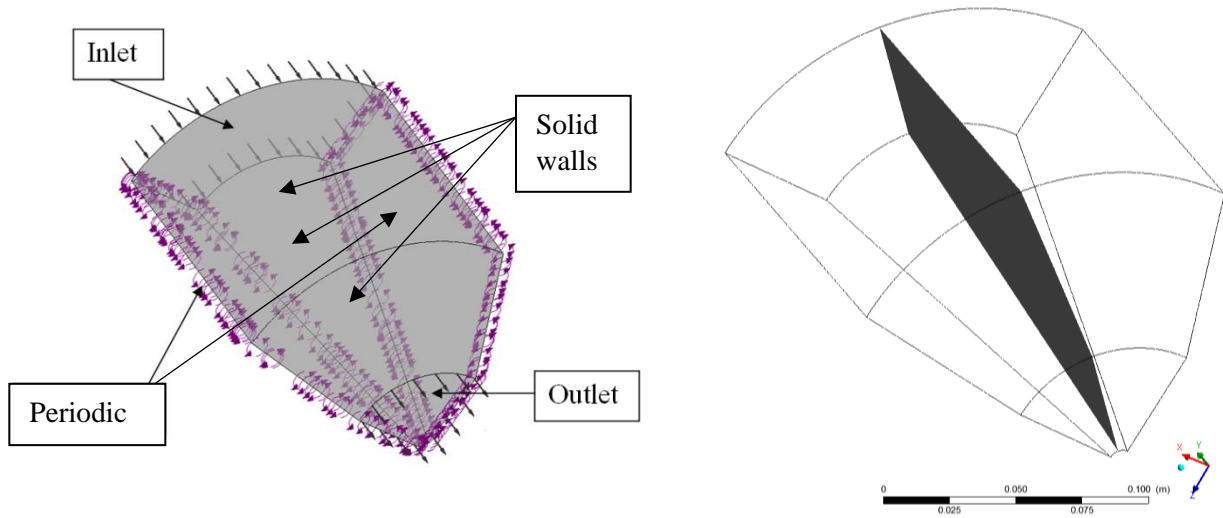


Figure 4.18 Flow field of the exhaust nozzle with the used boundary conditions (left) and the cut section for displaying the results (right)

The residuum and imbalances are converged after 15 iteration steps. The results are mesh independent.

The qualitative outcomes of the simulation are shown in Fig. 4.19 and 4.20. The static pressure and temperature reduce, and the velocity increases during the expansion process. The results are plausible, the parameters are in the expected ranges.

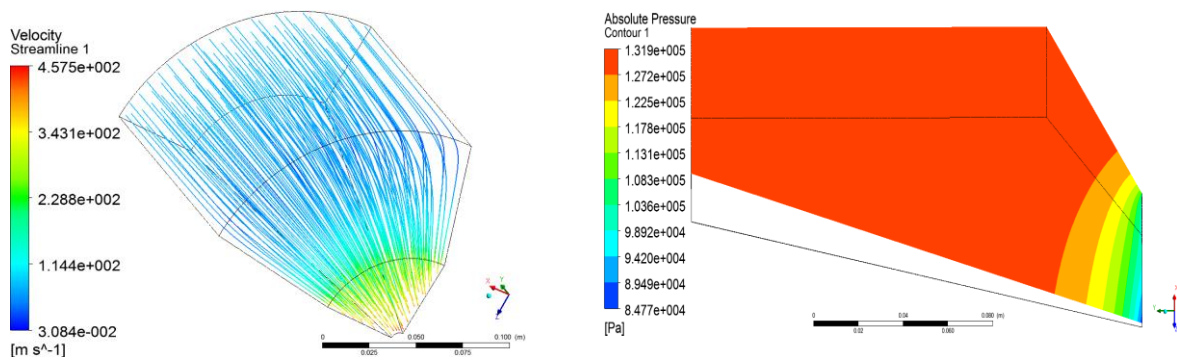


Figure 4.19 Streamlines are coloured by the velocity magnitude in the flow domain (left) and absolute static pressure distribution in the cut section of the nozzle (right)

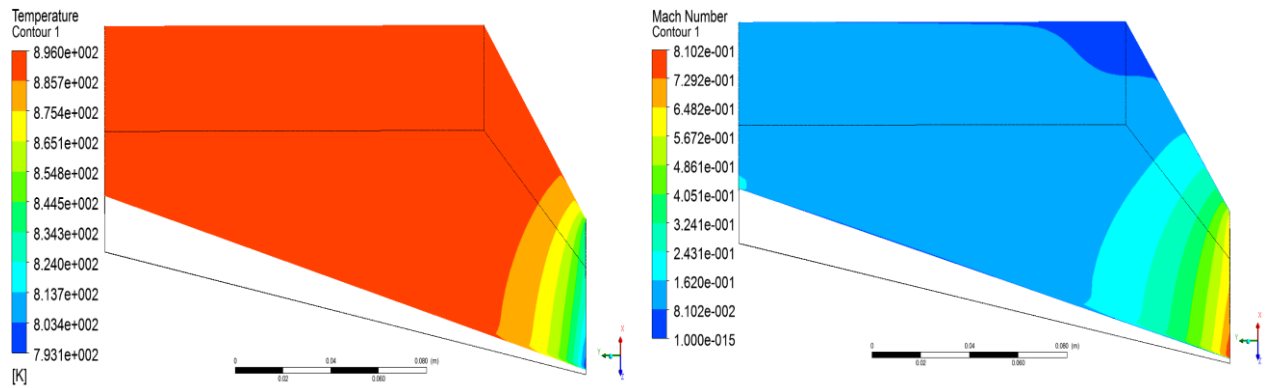


Figure 4.20 Static temperature (left) and Mach number (right) distribution in the cut section of the exhaust nozzle

4.2.CFD Analysis of the Full Model

Flow field of the inlet channel, centrifugal compressor, combustion chamber, axial turbine and exhaust nozzle are assembled to form the 3D flow field of the full model. Here, as it was the case before, in the all separated models, only the one quarter part of the geometry is used, and rotational periodicity boundary condition is applied at the corresponding surfaces. The used flow domain is shown in Fig. 4.21. Fig. 4.22 represents the plane, in which the simulation results are shown.

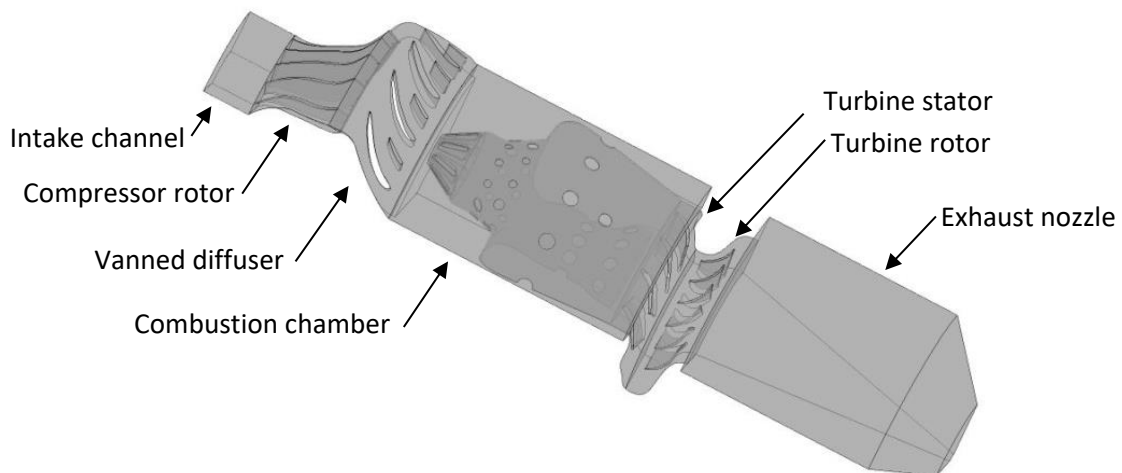


Figure 4.21 One quarter part of the flow field of the academic jet engine with the main components

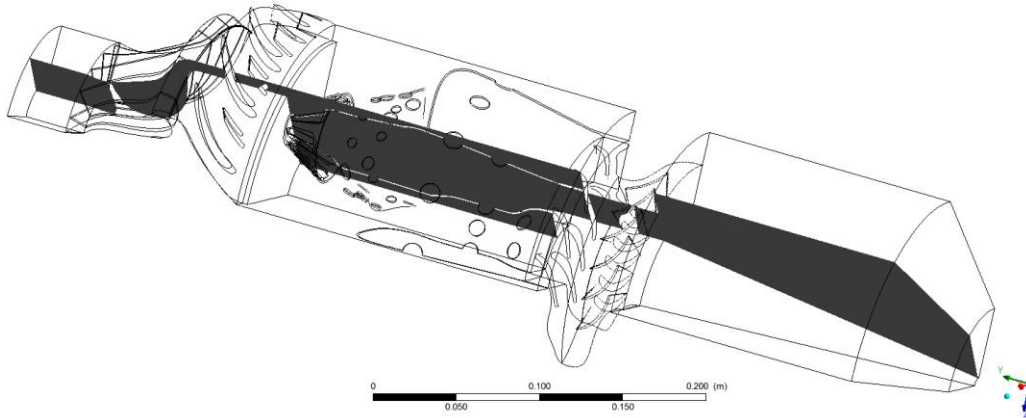


Figure 4.22 Flow field of a quarter academic jet engine by wire frame and the meridional plane for showing the results

The numerical mesh is designed to apply local mesh refinement at the high gradient flow conditions and to guarantee the completeness of y^+ to be 30-300. The expectation is that results should be mesh independent by maximum 5 % allowing differences in the thrust. The final mesh is built up from 4799728 elements and it contains 2067312 nodes. The final mesh configuration is shown in Fig. 4.23.

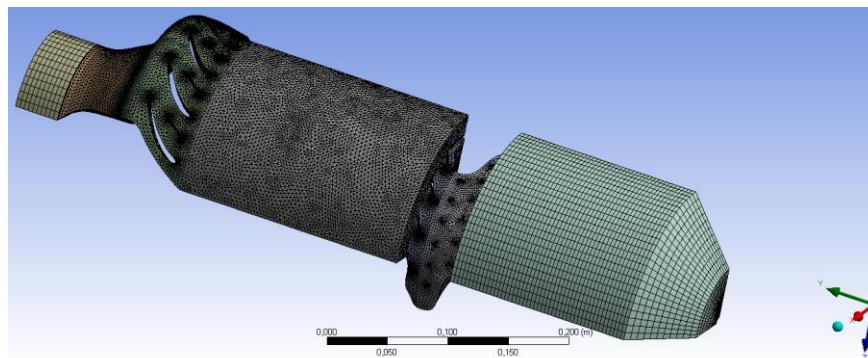


Figure 4.23 The final mesh for the one quarter flow field of the academic jet engine

The material properties of the incoming air as ideal gas are $\gamma = 1.4$ and $R = 287.058 \text{ J}/(\text{kg K})$. The reference pressure of the domains is 99756 Pa. The ambient air enters in the jet engine and the hot gases expand in the environments. Hence 99756 Pa total pressure and 299.6 K total temperature with normal flow direction into the inlet surface of the intake flow channel is defined as inlet boundary condition. 99756 Pa static pressure is defined as outlet boundary condition. 43000 RPM rotational speed is defined for the rotating flow domain of the compressor and turbine. Table 4.6 shows the used boundary conditions.

The list of applied models for the combustion chamber is found in Table 4.2.

Fig. 4.24 provides an overview about the type and the location of the used boundary conditions.

The heat transfer coefficient is $8 \text{ W}/(\text{m}^2 \text{ K})$ corresponding to the stationer ambient air with 299.6 K temperature on the outer walls is applied for considering the free convection [49].

Table 4.6 The applied boundary conditions

Inlet (air)			Inlet (fuel)		Outlet
p_0 [Pa]	T_0 [K]	N [rev/min]	V [m/s]	T_0 [K]	Opening pressure [Pa]
99756	299.6	43000	12	299.6	99756

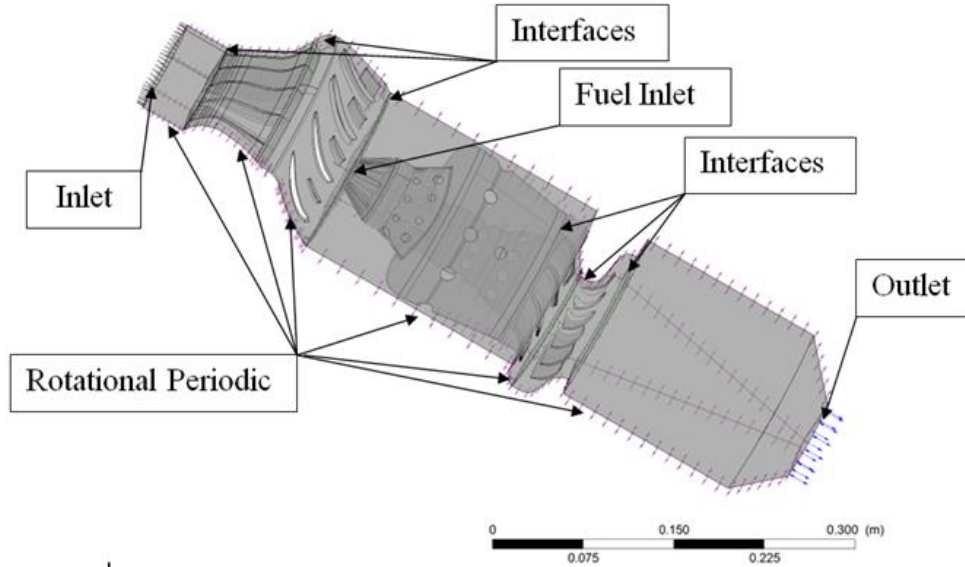


Figure 4.24 The used boundary conditions and interfaces in the CFD simulation in case of the full engine model

The results are mesh independent in line with the present expectation.

The residuum and imbalances are converged after 1000 iteration steps.

The simulation results are plotted on the plane denoted in Fig. 4.22 and they are shown in Fig. 4.25-4.27. The presented velocity, pressure, total temperature and mass fraction distributions are plausible. The flow leaves the turbine has tangential component, which can be seen clearly in the streamlines in Fig. 4.25 (left). This is not the case in the separated models, where only the axial velocity components are considered at the inlet sections of the nozzle. This together with the reduced inlet segment of the nozzle result higher pressure-drop at the full model and explain the differences between the separated and full modelling approaches.

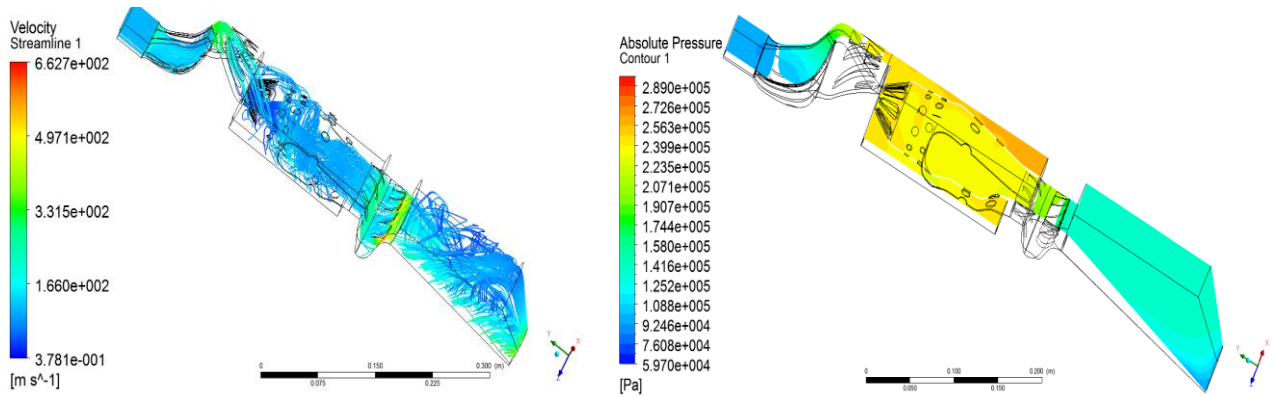


Figure 4.25 Streamlines coloured by the velocity magnitude (left) and absolute static pressure distributions in the meridional plane (right) of the academic jet engine

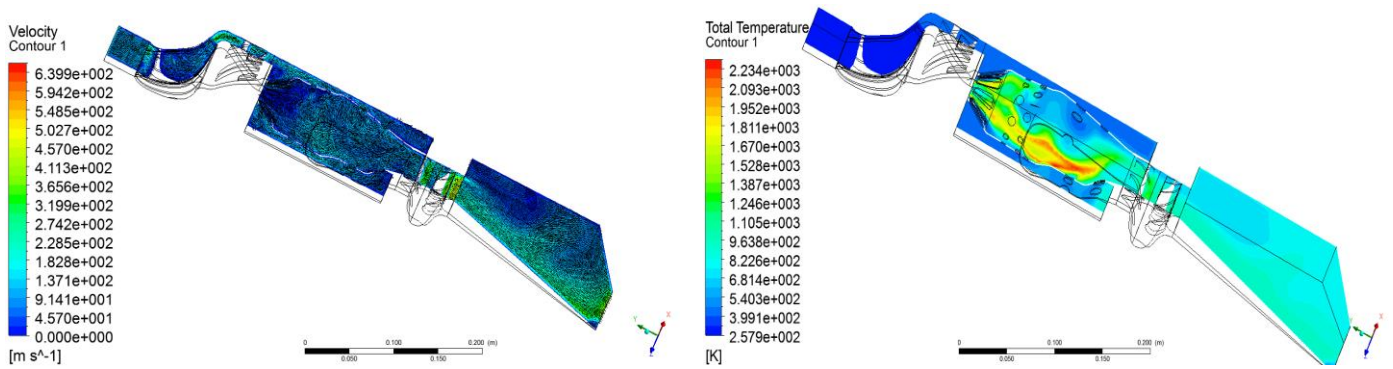


Figure 4.26 Velocity vectors and velocity distribution (left) and total temperature distribution in the meridional plane of the academic jet engine

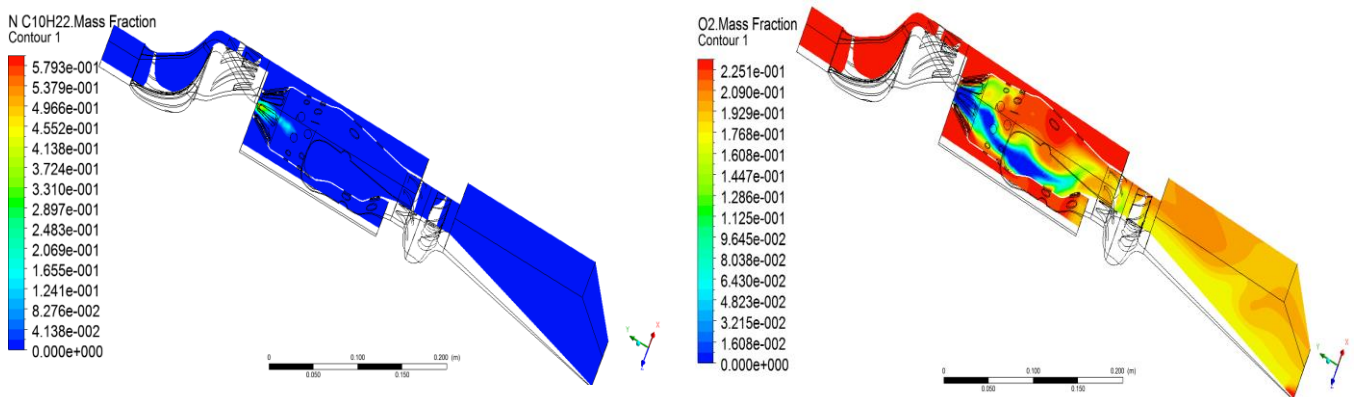


Figure 4.27 Mass fraction of the normal-decan (left) and oxygen (right) in the meridional plane of the academic jet engine

4.3. Conclusions

The goal of the present chapter of the thesis is to complete CFD analyses for the separated and for the full models of the academic jet engine under investigation. The outcomes of these computations can be used to determine and evaluate the accuracy of the analysis, design and to compare them with the available measured data. The qualitative results of the analyses are plausible, and the two CFD approaches (for separated and full models) provide parameters in the same ranges except for the exhaust nozzle, where the tangential flow components are not considered and its entire inlet surface is applied as inlet boundary condition in case of the separated modelling approach.

The quantitative results of the i. thermodynamic design, ii. mean line design, iii. separated and iv. full CFD analyses and v. measurement are shown and discuss in the next chapter, in the chapter 5 in detail.

5. Discussion, Conclusion and Verification of the Results

There are two goals of the present chapter. The one of them is to compare the target specifications and the parameters, which are calculated by the engine design, with the results of the CFD analyses for the full and for the separated models. The second one is to compare the all previously mentioned data with the results of the available measured values [4]. The thermodynamic parameters - if they are available by measurement or calculations - as total temperature, static temperature, total pressure and static pressure are presented along the engine length for the results of the thermodynamic cycle analysis, for the mean line design, for the CFD simulations (for separated model and for the full model) and last but not least for the available measurements in Fig. 5.1-5.4. The results of the thermodynamic cycle analysis and mean line design are compared with the outcomes of the CFD analysis and then the results of the CFD computations with the measured data in quantitative manner. This sequence is because the measured data are not always available and their accuracy is not verified statistically, they may have uncertainties [4].

The numerical value of the thermodynamic parameters at each engine section and the exhaust velocities at design and different analysis methods are shown in Table 5.1 and 5.2 respectively.

5.1. Verification of the results

The total temperatures provided by cycle analysis, mean line design, CFD analyses (separated and full models) and measurement at the sections of the academic jet engine are shown by empty blue circle, black star, filled brown circle, empty red square and empty green triangle symbols respectively (see Fig. 5.1). As expected, the total temperature at the inlet section of the diffuser and at the compressor inlet is the same and equal to ambient total temperature. Then, it becomes slightly higher, quite above 400 K at the compressor exit. The total temperature increases dramatically to about 1000 K in the combustion chamber and finally it declines at the end of the turbine and the nozzle section. The maximum relative differences between the results of the cycle analysis and CFD simulations (first for the separated and secondly for the full model) are 1.95 % and 3.61 % and the average relative deviation between the investigated parameters are 0.81 % and 1.05 %. The maximum

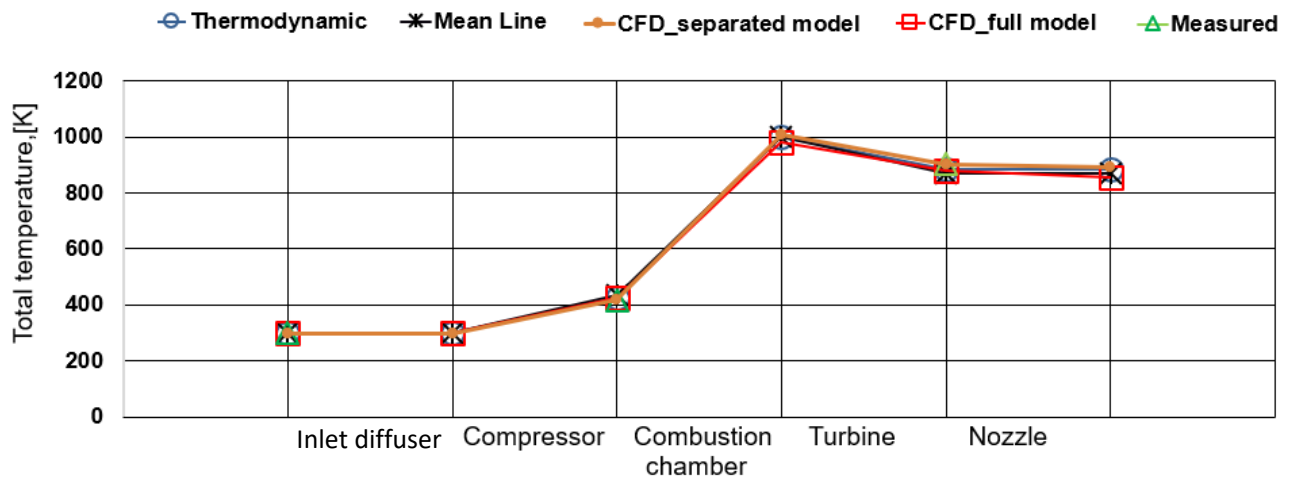


Figure 5.1 Total temperatures - if they are available - in the function of engine segments by thermodynamic cycle-analysis, mean line design, CFD analyses (separated and full models) and available measurement [4]

relative differences between the mean line design and CFD data (first for the separated and secondly for the full model) are 4.10 % and 2.22 % meanwhile the average relative deviations between the investigated parameters are 1.75 % and 1.13 %. Concerning the CFD (first the separated and secondly the full model) and measured total temperatures, the maximum relative deviations between them are 1.26 % and 3.04 % and the average relative deviation between their values are 0.61 % and 1.98 %, respectively.

Fig. 5.2 shows the calculated and measured static temperatures in the function of the engine length similarly than it was mentioned in the previous paragraph except for the data from the thermodynamic cycle analysis, because only the total quantities are considered in it omitting the nozzle exit. The calculated mean line design and CFD results match well with each other similarly than it was before at the total temperature. The maximum relative difference between the outputs of the mean line design and CFD simulations (first for the separated and secondly for the full model) are 4.58 % and 3.04% and the average relative deviation between the investigated values are 1.59 % and 1.56 %. The highest relative differences between the available measured and CFD data (first for the separated and secondly for the full model) are 4.25 % and 3.89 % meanwhile the average relative deviations between the investigated static temperatures are 3.03 % and 2.11 %. The separated CFD model gives the highest static temperature at the inlet of the nozzle (see Fig. 5.2). This is caused by the low Mach number and so the low flow speed, which is the consequence of the inlet and outlet boundary conditions. Namely the flow has higher inlet area at the nozzle, and it is imposed to be perpendicular to the inlet surface of the nozzle, which provides low axial velocity corresponds to the inlet total pressure, total temperature and exit mass flow rate. However, in the other cases, beside the axial velocity, there is a tangential component of the flow also together with smaller inlet cross section of the nozzle, which results higher absolute velocity. This higher absolute velocity provides less static temperature and pressure at the same or similar total temperature and pressure respectively. Hence, due to the used boundary conditions, the results of the separated CFD model in case of the nozzle cannot be reasonably compared directly with the parameters provided by the other approaches.

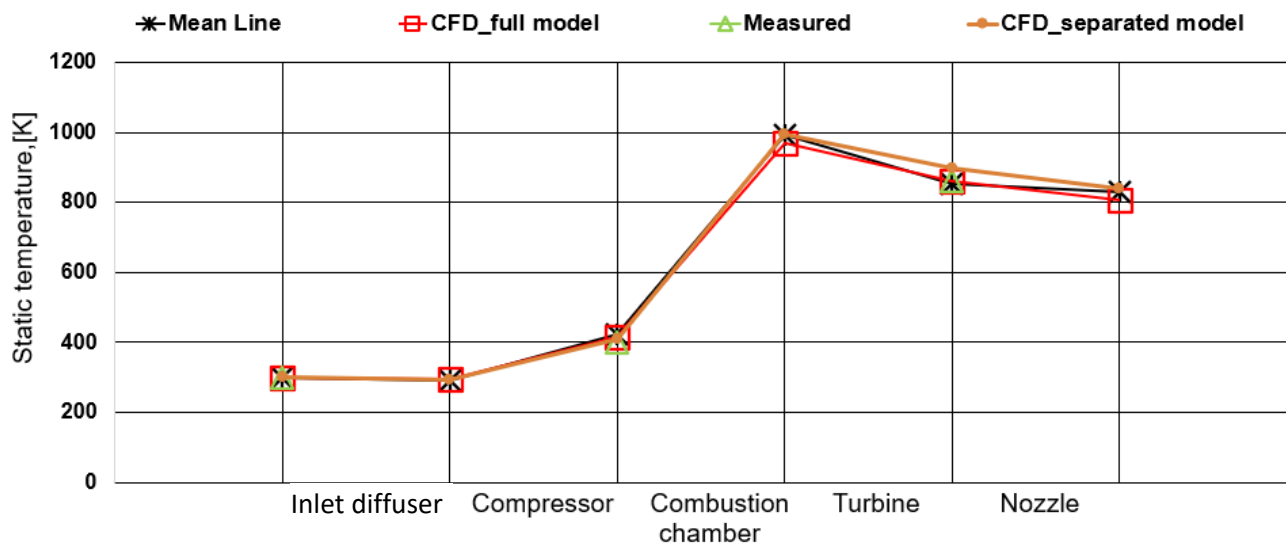


Figure 5.2 Static temperatures - if they are available - in the function of the engine segments by mean line design, CFD analyses (separated and full models) and available measurement [4]

The total pressure at the compressor inlet is 99756 Pa. It is boosted by the compressor to around 250 kPa before the combustion chamber (see Fig. 5.3). Afterwards, it expands to the atmospheric pressure in three

steps. First, it decreases slightly going through the combustion chamber. Then the flow enters the turbine and the pressure drops to around 130 kPa. Afterwards, the pressure decreases until the end of the nozzle as it is shown in the figure. The CFD models give the highest total pressure in the compressor, in the combustion chamber and in the turbine sections. Although this is due to the fact, that losses are overestimated in the thermodynamic and mean line design, the results of these approaches are closer to the measured values. The maximum relative differences between the results of the thermodynamic cycle and CFD simulations (first for the separated and secondly for the full model) are 9.10 % and 13.53 % and the average relative deviations between the investigated parameters in the entire range are 3.42 % and 4.71 %. Similarly, the maximum relative differences between the results of the mean line design and CFD total pressure values (first for the separated and secondly for the full model) are 9.09 % and 12.41 %, meanwhile the average relative deviations between the compared data are 3.13 % and 4.59 %. Concerning the CFD and measured total pressures, the maximum relative differences, first between the separated and secondly for the full model, are 13.27 % and 27.04 % respectively. The average relative deviations between their values are 5.75 % and 10.65 % for the separated and for the full models.

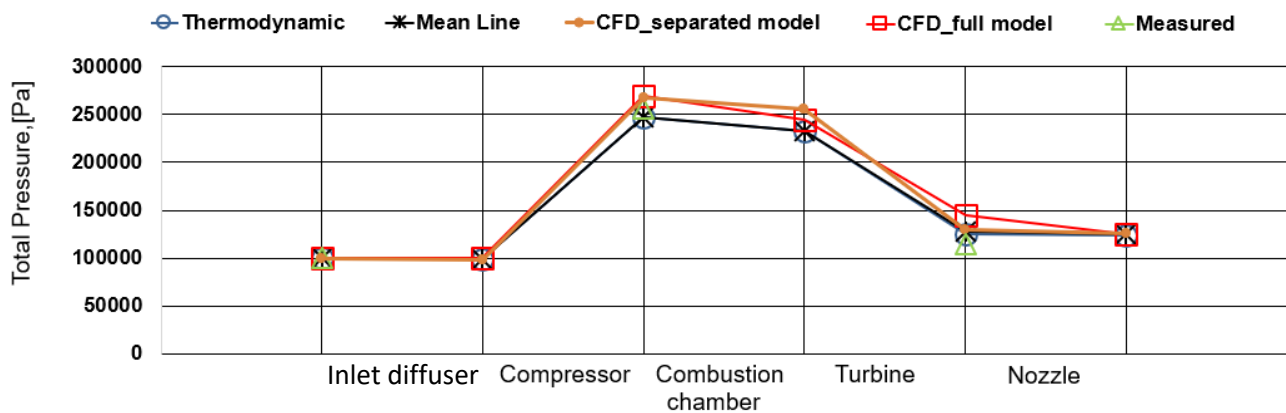


Figure 5.3 Total pressure values - if they are available - in the function of engine segments by thermodynamic analysis, mean line design, CFD analyses (separated and full models) and available measurement [4]

The results of the static pressure along the length of the engine, as it is shown in Fig. 5.4, provides information also about the usability and the accuracy of the design and analyses models. The thermodynamic cycle analysis has no static parameters except for the nozzle outlet, because it uses total quantities. The maximum relative differences between the results of the mean line design and CFD analyses (first for the separated and secondly for the full model) are 9.77 % and 12.60 %, meanwhile the average relative deviations between their investigated values are 3.18 % and 5.01 %. The highest relative differences between the results of the available measurement and CFD analyses (first for the separated and secondly for the full model) are 9.75 % and 6.85 %. The average relative deviations are 4.87 % and 3.43 % between the investigated static pressures of the measured and CFD resulted data (first for the separated and secondly for the full model).

330 N thrust was imposed as goal function of the design, which corresponds to 330 m/s exit velocity at flight speed is equal to zero and mass flow rate is 1 kg/s. Concerning the design and analyses, the resulted exhaust velocities – provided by the thermodynamic cycle analysis, mean line design and the CFD simulations for the separated and for the full models – are shown in Table 5.2. The highest relative difference between the expected design value and the calculated ones, except for the CFD analysis in case of the separated model, is 1.46 % and it is in the case of CFD analysis at full model. The average of the relative deviations between the

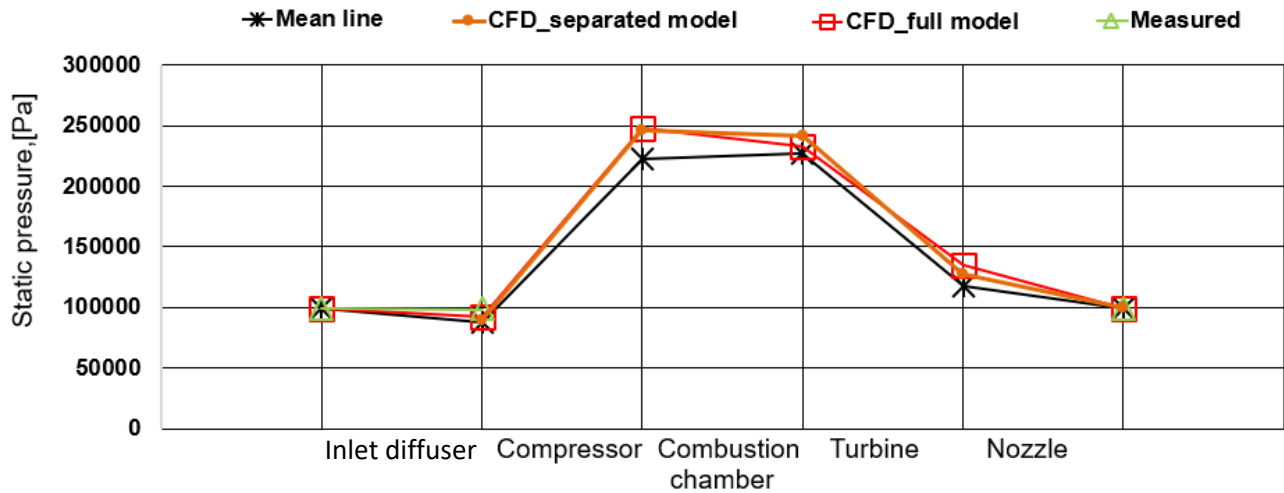


Figure 5.4 Static pressures - if they are available - in the function of engine segments by mean line design, CFD analyses (separated and full models) and available measurement [4]

Table 5.1 Thermodynamic parameters of thermodynamic cycle analysis, mean line design, CFD analyses (separated and full models) and measurement [4] – if they are available – at the consecutive sections of the academic jet engine

Parameter	Methodology	Upstream of the engine	Inlet of the compressor	Inlet of the combustion chamber	Inlet of the turbine	Inlet of the nozzle	Exit of the nozzle
Total temperature [K]	Thermodynamics	299.6	299.6	427.68	1000	887.12	887.12
	Mean line design	299.6	299.6	436.7	1000	871.49	871.49
	CFD (separated model)	299.6	299.6	419.5	1009	900.32	892.12
	CFD (full model)	299.6	299.6	427.2	982.4	880	856.24
	Measurement	299.6	-	414.2	-	905.4	-
Static temperature [K]	Thermodynamics	299.6	-	-	-	-	840.1
	Mean line design	299.6	289.84	423.79	994.7	855	831.15
	CFD (separated model)	299.6	291.5	409.9	994.37	896	839.4
	CFD (full model)	299.6	293.34	416.9	969.6	862.6	806.6
	Measurement	299.6	-	401.3	n/a	859.5	n/a
Total pressure [Pa]	Thermodynamics	99756	98758	246896	232082	125722	124240
	Mean line design	99756	98758	246927	232112	127342	125752.8
	CFD (separated model)	99756	98758	267175.2	255323	129625.6	125280.5
	CFD (full model)	99756	99698.7	269532	244250.4	145386.4	124722.4
	Measurement	99756	-	256910	-	114442	-
Static pressure [Pa]	Thermodynamics	99756	-	-	-	-	99756
	Mean line design	99756	87953	222312	227187	117928	99756
	CFD (separated model)	99756	89719.8	246382.5	241748.4	127312.3	99756
	CFD (full model)	99756	92599.4	247400	232559	134923	99756
	Measurement	99756	99410	-	-	-	99756

computed ones is 1.23 %. The used design process is acceptable in engineering point of view. The measured thrust is not used in the present assessment because of uncertainty communicated by the authors [4].

Table 5.2 Exhaust velocity of the academic jet engine in case of thermodynamic cycle analysis, mean line design and CFD analyses (separated and full models)

Methodology	Exhaust velocity, (m/s)
Thermodynamic cycle analysis	330
Mean line design	333.1
CFD (separated model)	337.2
CFD (full model)	325.2

5.2. Conclusions

The correctness of the procedure about the virtual prototyping (aerodynamic redesign) of the academic jet engine is revised in the present chapter quantitatively. There are two ways for investigating the plausibility and the accuracy of the outcomes of the design and analyses in the present case. The one of them is to compare the engine design parameters (given by thermodynamic cycle analysis and mean line design) with the results of the CFD analyses (separated and full modelling approaches) and the second one is to evaluate the results of the CFD analyses with the available measured data even though the accuracy of these measured data are not verified statistically [4]. The outcomes of these investigations are the following. The average relative deviations between the results of the thermodynamic cycle analysis and CFD simulations are 0.81 % (for the separated model) and 1.05 % (for the full model) in case of the total temperature, meanwhile they are 3.42 % (separated model) and 4.71 % (full model) for the total pressure. The average relative deviations between the results of the mean line design and the CFD analyses are 1.75 % (separated model) and 1.13 % (full model) for the total temperature, meanwhile it is 1.59 % (separated model) and 1.56 % (full model) for the static temperature. Similarly, the average relative deviations between the mean line design and CFD analyses are 3.13 % (separated model) and 4.59 % (full model) for the total pressure and they are 3.18 % (separated model) and 5.01 % (full model) for the static pressure. Although the accuracy is not verified statistically, available measured data are used for the plausibility checking of the outcomes of the academic jet engine design. The average relative deviations between the available measured data and the results of the CFD analyses in case of the total temperature are 0.61 % (separated model) and 1.98 % (full model) and they are 3.03 % (separated model) and 2.11 % (full model) for the static temperature. The average relative deviations between the available measured data and the result of the CFD analyses in case of the total pressure are 5.75 % and 10.65 % for the separated and for the full model respectively, meanwhile they are 4.87 % and 3.43 % for the static pressure.

The results of the thrusts for the academic jet engine are 333.1 N by the mean line design and 325.2 by the full-model CFD analysis. The expected target thrust is 330 N. The maximum relative deviation between the computed and expected value is 1.46 %. It is at the case of the full-model CFD analysis.

Based on the all results discussed above, the design process is acceptable in engineering point of view.

6. Novel Application of Inverse Design Method by Means of Redesigning Compressor Stator Vanes in the Redesigned Jet Engine

The main goal of this chapter is to introduce the adaption of a new method for redesigning compressor vanned diffuser in the academic jet engine redesigned in chapter 3. The applied inverse design method is based on a finite volume and explicit time marching solution of the compressible Euler equations. Stratford's separation prediction method is used for determining the expected pressure distribution along the suction side of the profile on such a way that the cost effective and highly utilized vane geometry – which will belong to the expected pressure distribution: close but certain distances far from the separation – will provide less total pressure drop, higher static pressurize, greater mass flow rate and more axial flow turning than the baseline design. Following the inverse design procedure for determining the new profile and verification of the result by ANSYS CFX inviscid and viscous flow simulations, the viscous module of the CFX software has been used to compare the results of the new and the original vanes with each other. Although the purpose of this section is to introduce a design technique for compressor vanned diffuser, the procedure can be extended and applied for other wall bounded flows at strong adverse pressure gradient flow conditions.

6.1. Introduction of Optimization Methods for CFD in General

As it is already mentioned before in the subchapter 1.4, the benefit of Computational Fluid Dynamics (CFD) has been used in the design process more than before. Using CFD techniques, the numerous experiments can be replaced or reduced significantly, and the cost, capacity and time of developments can be saved. The parameterization of the geometry provides higher reproducibility and flexibility in the model generation. Different computational techniques are widely used in the aerospace engineering also. Their consistency, stability and convergence characteristics have been investigated and proved. The accuracy of the available techniques allows designers to turn more effort on the new fields of the engineering practice called virtual prototyping, which is the keyword of the next decades. Additionally, in case of applying optimization methods, not only the development process, but the overall efficiency of the new products can also be increased significantly.

Beside the developments of the central core of the fluid dynamics solvers, the different optimization techniques, coupled with CFD, are also under intensive research [52]. In case of direct optimization techniques, an attempt has been made to find the optimal solution. They typically utilize some sort of search technique (gradient-based optimizer), stochastic based algorithms (e.g. evolutionary strategies, genetic algorithms) and artificial neural networks for example. These procedures can be computationally expensive because several flow solutions must be completed to specify for example the direction of deepest descent, fitness of individuals in the population in order to determine the shape changes. Furthermore, the required number of flow solutions increases dramatically with the number of design variables.

Several optimization methods have been developed so far, but the optimal shapes for practical CFD design have been the subject of limited methods.

6.1.1 Evolutionary algorithms [53]

One group of the optimization methods is the evolutionary algorithms (EA), which are used in order to find the optimal configurations. The EA relies on the wide number of simulations, which may result in an appreciable computational effort. These optimization algorithms apply mechanisms inspired by nature, such as mutation, crossover, natural selection and survival of the appropriate in order to simplify a set of solution

candidates by using repeated analyses. The most important idea for evolution algorithms is to find the optimal solution by using the analogy to estimate the theory. Evolutionary algorithms can be coupled with CFD methods. The basic cycle of evolutionary algorithms is depicted in Fig. 6.1.

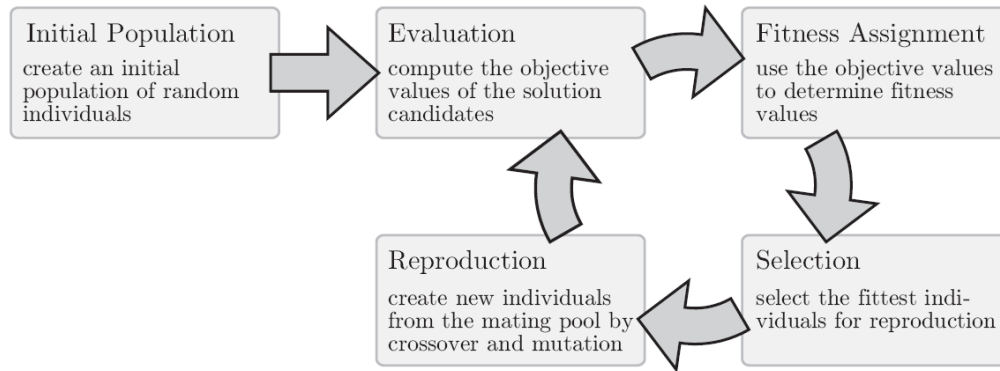


Figure 6.1 The basic cycle of evolutionary algorithms [53]

If the final criterion is satisfied, the evolution stops. Otherwise, the algorithm continues with next cycle. The group of genetic algorithms (GA) is a part of the group of evolutionary algorithms. The GA proceeds to initialize a function of solutions haphazardly, and then refine it through several applications of mutation, crossover, inversion and selection operators. Crossover and mutation are identified as essential genetic operators. This formation process is repeated until an ending condition has been reached. There are many disadvantages of the use of genetic algorithms as compared to the other optimization algorithms:

1. One single function evaluation may need many hours of complete simulation. Then optimization methods cannot work with this type of problem because it is a very expensive fitness function evaluation. Thus, it is required to use an approximated fitness that is computationally efficient.
2. In many problems, GAs may have a trend to converge to local optima rather than the global optimum of the problem. GAs is unacquainted with the abnegation of short-term capability in order to get longer-term capability.
3. If the capability measure is only a single right/wrong criterion then GAs cannot be adopted to solve the problem and there is no way to converge on the solution. In this case a random search can solve the problem fast as a GA.
4. For certain optimization problems and problem cases other optimization algorithms may find better solutions than genetic algorithms (given the same computational capacity).

6.1.2 Genetic programming [53]

The goal of genetic programming (GP) is to determine the connection between the inputs and output before the simulation. The aim of this process is to find system operator that connects the given input and response, as sketched in Fig. 6.2. Meanwhile the GA determines the set of input data which, when transformed by a known system dynamics algorithm, most closely matches a set of known output data, the GP determines the system dynamics algorithm, which most closely transforms a set of known input data into a set of known output data. The GA/GP applied to problems in many different disciplines: engineering design (e.g.: air foil

optimization, control system tuning, artificial vision systems), financial forecasting and biological system modelling.

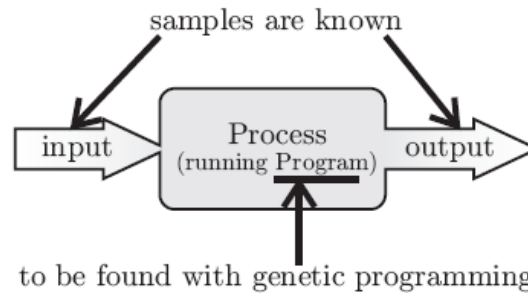


Figure 6.2 Relation between input and output [53]

6.1.3 Simulated annealing [53]

The starting point is an analogy with the thermodynamics of equilibrium. Condensed matter consists of a very large number of molecules, whose energy is described by the Boltzmann probability distribution: $P(E) = \exp(-E/kT)$, where E is the energy of the configuration, T the temperature and k the Boltzmann constant. The simulated annealing (SA) is a multi-dimensional optimization technique based on following local gradients to a minima/maximum. The SA requires the user to choose some optimization parameters (e.g. transition probability function, transition step size) meanwhile GA requires less explicit input by the user. The GA may be less efficient than SA for well-behaved optimization problems but may be better suited to complex parameter spaces.

6.1.4 Evolutionary programming [53]

Evolutionary Programming (EP) was used first in 1960's in order to use simulated evolution as a learning process aiming to generate artificial intelligence. Currently, evolutionary programming is a wide evolutionary computing dialect with no fixed structure or (representation), in contrast with some of the other dialects. It is becoming harder to distinguish between evolutionary strategies. Some of its original variants are quite similar to the later genetic programming, except that the program structure is fixed and its numerical parameters are allowed to evolve. Different from genetic algorithm, evolutionary programming mimics the evolution of species not the genes, so in evolutionary programming emphasize the linking of species behaviour. The evolutionary programming emphasize is on the behaviour evolution of species and establishes the behaviour chain between parent and offspring, that is to say, the good offspring can be existed and not consider its parent. So, in evolutionary programming the fitness value is applied to select offspring.

6.1.5 Learning classifier system [53]

A Learning Classifier System, or LCS, is an automatic learning system with close links to genetic algorithms. Learning classifier systems can be divided into two types depending on when the genetic algorithm acts. One of them is the Pittsburgh-type LCS which has a well-known set up of rules, where the genetic algorithm recombines and copy the best of these rule sets. In a Michigan-style LCS there is only a single well-known rule and the algorithm's action focuses on selecting the best classifiers within that rule set. Michigan-style LCSs have two main types of fitness definitions, strength-based and accuracy-based. The term "learning classifier system" most often refers to Michigan-style LCSs.

Initially the classifiers or rules were binary, but nowadays research has developed this reflection to include real-valued, neural network, and functional (S-expression) conditions. An LCS is "adaptive" in the sense that its ability to choose the best action improves with experience. The advantage of a Learning Classifier System is that it is able to learn during its running and working processes.

6.1.6 Turbulence model based on the optimization of CFD [53]

In case of turbulence, the model parameters of the engineering turbulence modelling from Wilcox are considered as Reynolds Averaged Navier-Stokes equations (RANS). The purpose of this modelling is to suit the parameters of the model using optimization in order to better predict the time averaged turbulence velocity profiles in channel flows. In the RANS modelling, the balance equations are averaged in time with respect to the turbulent variation of the flow variables.

6.1.7 Adjoint methods for shape optimization [53]

Adjoint methods are gradient-based methods, commonly utilized in aerodynamic optimization. These methods are based on the estimation of the gradient of an objective function. This is the way of finding the most efficient solution candidates. This topic concentrates on the optimization of 2D or 3D shapes (air foils, blades, wings, etc.). The objective function is expressed in terms of flow variables computed by numerically solving the flow equations in the consequent domain, with problem-specific boundary conditions. The adjoint approach is based on control theory, and the gradient can be estimated obligatory by a gradient-based optimization method.

The reason for the advantage of the adjoint method is that the gradient points towards a better solution while the evolutionary algorithms are usually not capable to employ limited information during the solution modification.

In the aerodynamics, the problems typically contain huge number of design variables so the estimation of gradient by means of deterministic algorithms is very time consuming, when compared to other methods for example direct analysis (in direct analysis the computation and the gradient flow variable is contained) or inverse design method. The adjoint approach can estimate the gradient of the objective function. For the gradient computation the cost does not depend on the number of design variables and is equivalent for solving the flow equation.

Two types of adjoint methods have been developed the continuous and discrete. Relating to their supplies at the enlargement stage, both approaches have got advantages and disadvantages, though according to the experience both approaches result in the same accuracy.

6.1.8 Ant colony optimization Genetic programming [53]

In computer science and operations research, the ant colony optimization algorithm (ACO) is a probabilistic technique for solving computational problems, which can be reduced to finding good paths through graphs. This algorithm is a member of ant colony algorithms family, in swarm intelligence methods, and it constitutes some metaheuristic optimizations. The first algorithm was aiming to search for an optimal path in a graph, based on the behaviour of ants seeking a path between their colony and a source of food. The original idea has since diversified to solve a wider class of numerical problems, and as a result, several problems have emerged, drawing on various aspects of the behaviour of ants. There are several applications also for coupling with CFD.

6.2. Inverse Design Based Optimization

In case of the inverse design-type methods, the geometry modification is based on the prescribed set of the pre-defined variables at the wall by simple, fast and robust algorithms, which make them especially attractive amongst other optimization techniques. The wall modification can be completed within much less flow solutions for inverse design techniques than for direct optimization methods. Hence, the inverse design methods typically being much more computationally efficient, and they are very innovative to be used in practice. The main drawback of the inverse design methods is that the designer should create target (optimum in a specific sense) pressure or velocity distributions that should correspond to the design goals and meet the required aerodynamic characteristics. It can be difficult to specify the required pressure or velocity distribution that satisfies all the design goals. Also, one cannot guarantee that the prescribed pressure/velocity distribution will provide mechanically correct air foils without trailing edge open or cross over [54]. These drawbacks are solved within the frame of the present research. The optimum pressure distribution is found, and the trailing edge is closed in the all investigated cases.

Without high performance computing, the earliest methods of inverse design were analytical. Jacobs, Theodorsen, Mangler and Lighthill [55] can be considered as pioneer in this field by developing an inverse design method for 2D incompressible flow past air foils, making use of conformal mapping and potential flow solution. These methods are limited to the shock-free irrotational flows and difficult to extend to 3D. At the last decades of the twentieth century, the inverse methods are rather based on an iterative solution and they are generally developed together with the newly developed CFD solvers mostly based on the theory of characteristics. The governing equations of those methods are generally the Euler and Navier-Stokes equations. The solid wall modification algorithm is performed by means of transpiration technique (Giles and Drela [56], Demeulenaere [57] and De Vito [58]). These methods are primarily dedicated to the design of air foils, wings and turbomachinery cascades, but it has also been applied for design of duct geometries (Cabuk and Modi [59]) [54].

The general procedure of the iterative type inverse design methods requires an initial geometry and optimal pressure or velocity distribution over the wall to be modified. These prescribed distributions generally come from the industrial experiences and/or theory. The iterative cycle starts with the direct solution of a CFD solver. Completing the convergence criteria, a new boundary condition is applied at the solid boundary to be optimized, by which the wall become locally opening as inlet or outlet, depends upon the evolved pressure distribution between the boundary and computational domain. The outcome of this analysis is a velocity distribution along the wall, which is not necessarily parallel with it. The final step of the cycle is the wall modification. The wall becomes parallel with the local velocity vector corresponds to a new streamline of the flow field. The mentioned procedure is repeated until the target distribution is reached by the direct analysis and so the new geometry is available [54].

Two-dimensional inviscid inverse design-based optimization method has been adopted, modified, tested and verified by using ANSYS CFX commercial software in the present work. The vanned diffuser of the academic jet engine is redesigned by the inverse design tool. The detailed description of the used numerical method is found in the Appendix C. The introduction and implementation of the Stratford's separation prediction method with the goal of having the optimum pressure distribution - as an input for the inverse design tool - is described in the Appendix D. The redesign process of the vanned diffuser by the inverse design method is introduced in the next subchapter. The outcome of this step is the expected vane geometry. Finally, the plausibility analyses of the results are presented by using ANSYS CFX software in inviscid and viscous flow assumptions at the same geometry, boundary conditions, material properties and physical settings, if they are relevant by means of the used level of the approximation.

6.3. Redesign and Optimization of the Compressor Vanned Diffuser for the Academic Jet Engine

As it is discussed previously, the used inverse design method requires optimal pressure distributions along the suction and pressure sides of the blade or vane to determine the adherent geometry. The flowchart of the whole optimization process with the inverse design method is found in Fig. 6.3.

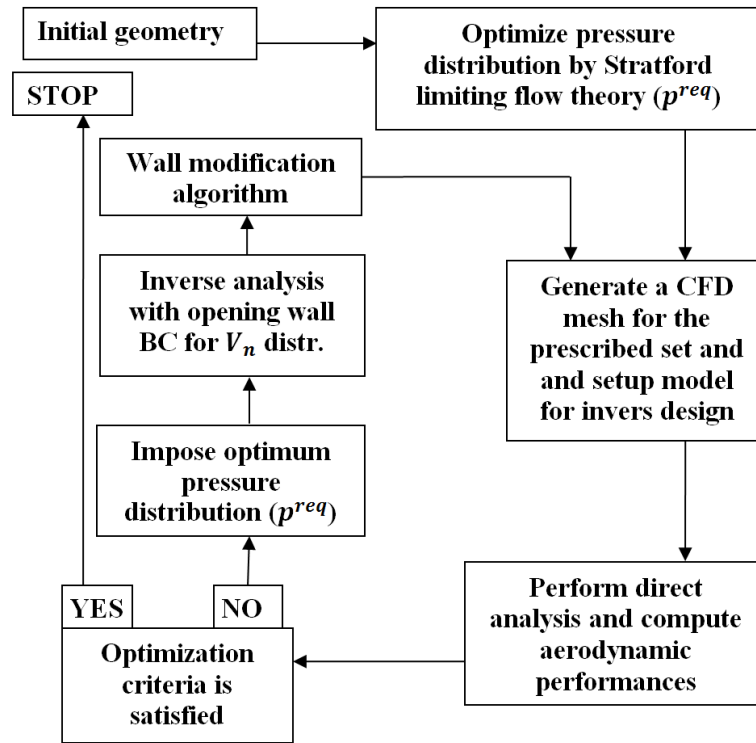


Figure 6.3 Flowchart of the inverse design-based optimization process

The first step of the optimization is to establish an initial geometry. The vanned diffuser of the academic jet engine is considered for this purpose with the following considerations. The 2D projection of the cut section at mean diameter is applied and the splitter vanes are removed with the goal of (i) increasing the cross sectional area, (ii) decreasing weight, (iii) minimizing the drag and losses and (iv) keeping production cost as low as possible by means of using as close configuration to the base line design as possible.

In line with flow chart shown in Fig. 6.3, the next step of the process is to create the optimal required static pressure distribution along the suction surface of vane. The procedure about the constrained optimization described in Appendix D is used for that purpose: the required pressure distribution for the inverse design method is determined by the application of Stratford's separation prediction method. The calculation is implemented in Microsoft Excel environment. The reason of the selected computer program is its widespread availability, the fast and efficient data handling and management, calculation, visualisation and data transfer.

After completing the calculations, the array of the pressure coefficient distribution curves at the inlet total pressure 270000 Pa, inlet total temperature 436 K and static outlet (trailing edge) pressure 240184 Pa is shown in Fig. 6.4. These parameters are determined to be in the same range as they are in the design and analysis part

of the academic jet engine at the location of vanned diffuser. The minimum pressure coefficients (rooftops) are in the range of $[-2.8, -0.5]$. The denoted (red) curve means the variant with the maximum closed surface area, which is belongs to the rooftop pressure coefficient $C_p=-1.8$.

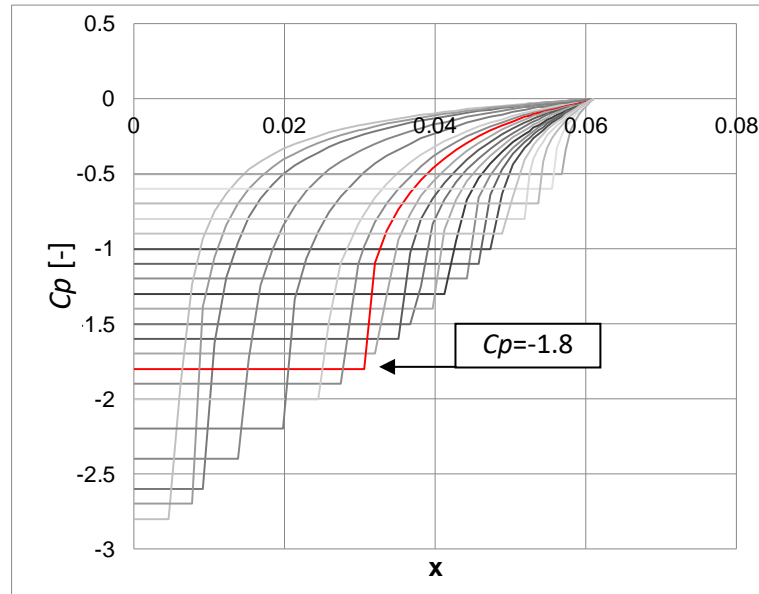


Figure 6.4 Distribution of pressure coefficients for different rooftop pressure coefficients

Four different curves belong to rooftop pressure coefficients $C_p=-1.8$, $C_p=-2.2$, $C_p=-2.6$ and $C_p=-1.6$ are selected and used to compute the required pressure distribution on the suction side of the vanes for the inverse design software. The blade walls belong to these imposed pressure distributions are generated by the methodology to test the inverse design method and to determine their effects on the 3 design parameters as follows.

- i. Static pressurise (see Fig. 6.5 and 6.7), which should be as much as possible in the vanned diffuser without separation and high loss to provide the expected flow direction and velocity magnitude.
- ii. Flow axiality; flow angle from horizontal direction at the exit of the vanned diffuser. The static pressure is expected to increase as it is mentioned above as the flow goes through the diffuser. Hence, the flow turning should be maximised without separation and axial flow is expected for the combustion chamber to have low pressure loss. It means that the flow angle measured from horizontal (axial) direction should be minimal at the downstream of the vanned diffuser.
- iii. Mass flow rate per unit length. The blockage effect of the vanned diffuser should be minimised, which means that the mass flow rate should be as much as possible for the highest performance of the academic jet engine.

The static pressure distributions correspond to the rooftop pressure coefficients $C_p=-1.8$, $C_p=-2.2$, $C_p=-2.6$ and $C_p=-1.6$ are determined by the definition of the pressure coefficient and these pressure distributions are shown in Fig. 6.5. The pressure distributions are mostly linear along the pressure side of the vanes.

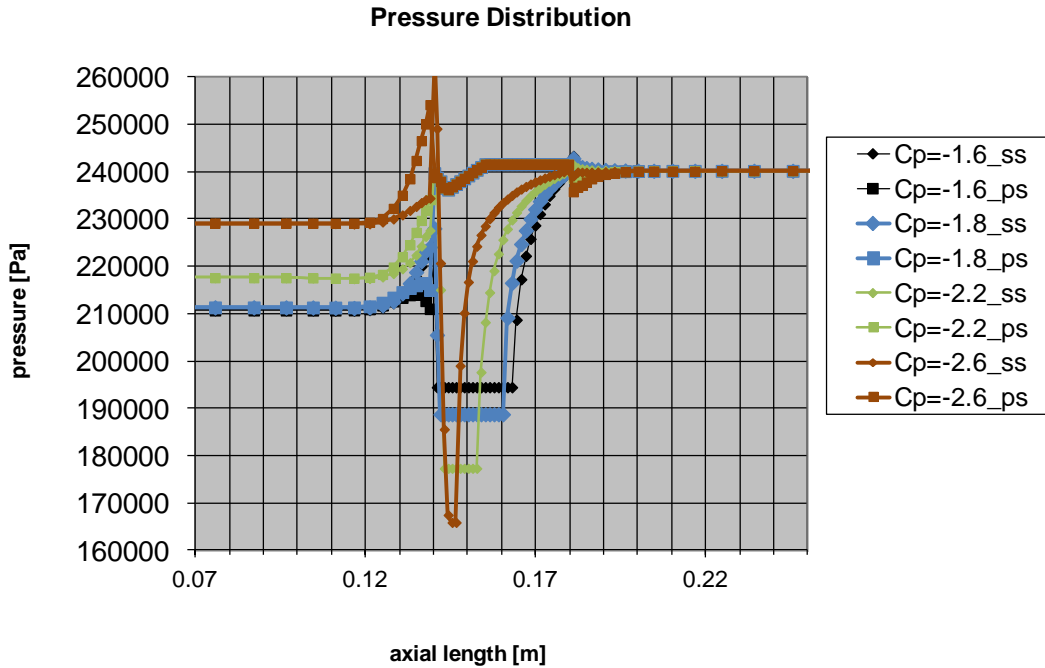


Figure 6.5 Pressure distribution for the considered rooftop pressure coefficients

As the initial geometry and the optimized pressure distributions are available, the next step, before the inverse design loop is to complete direct inviscid CFD simulation for the initial geometry (see Fig. 6.3). Physical and computational settings with the applied mesh and convergence characteristics are introduced in the next paragraphs.

The boundary conditions for the both direct and inverse mode of the software are next: inlet total pressure: $p_{tot,in}=270000$ [Pa]; inlet total temperature: $T_{tot,in}=436$ [K]; inlet flow angle: 45° and outlet static pressure: $p_{stat,out}=240184$ [Pa]. Of course, the thermodynamic parameters are the same that are used for generating the curves for the target pressure coefficients and pressure distributions, and they are in the range of the redesigned academic jet engine.

Free slip boundary condition is applied for solid surfaces and translational periodicity is considered at the boundaries of the cascade, out of the solid walls, are opposed with each other.

Air as ideal gas is applied for the operational medium.

110×60 H-type mesh is used in the all cases resulted by the mesh sensitivity analysis.

The simulations are converged; the residua are below 10^{-7} in the all investigated scenarios and the results are mesh independent.

The simulation for the initial geometry is completed and the Mach number, static pressure and static temperature distributions are plotted in Fig. 6.6, Fig. 6.7 and Fig. 6.8. The results are plausible; they are within the expected and suitable interval according to preliminary study [4], so they are accepted in physical point of view. The peaks in the flow field at the leading and at the trailing edges are due to the spatial discretization; sudden change of mesh.

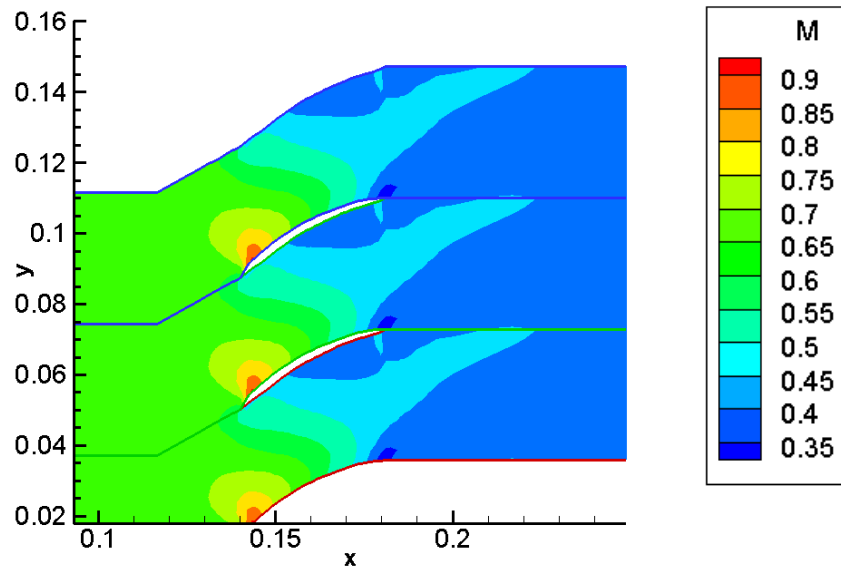


Figure 6.6 Mach number [-] distribution in case of initial geometry [m]

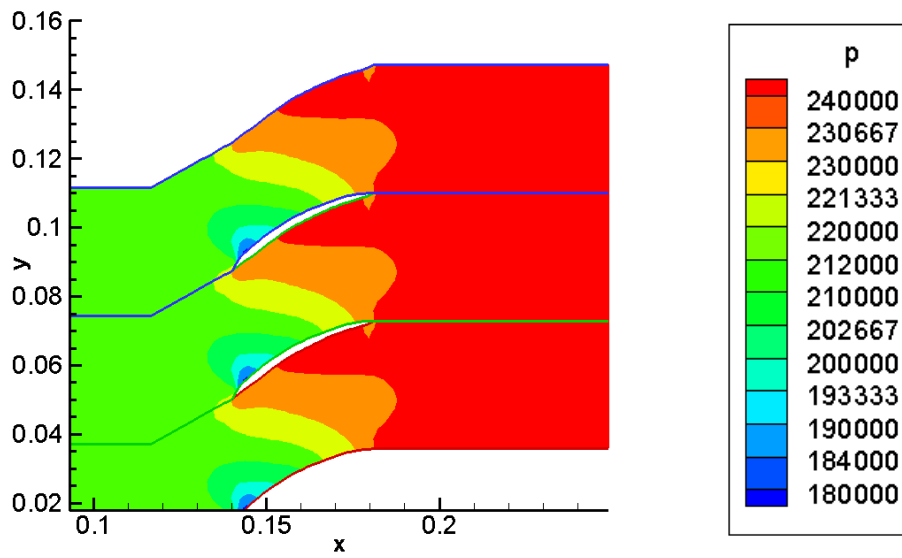


Figure 6.7 Static pressure [Pa] distribution in case of initial geometry [m]

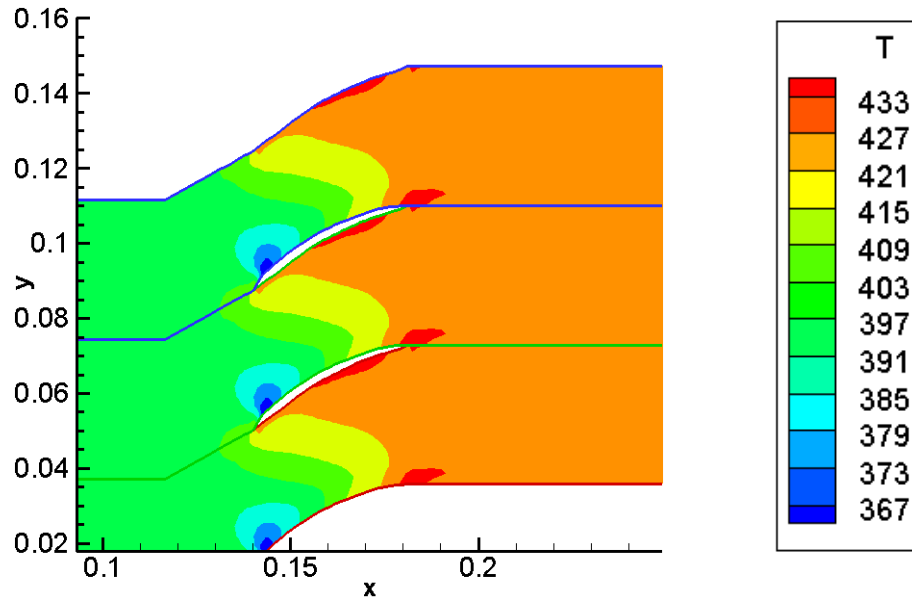


Figure 6.8 Static temperature [K] distribution in case of initial geometry [m]

The next step is to apply the required pressure distributions belong to the rooftop pressure coefficients $C_p = -1.6$, $C_p = -1.8$, $C_p = -2.2$ and $C_p = -2.6$ (see Fig. 6.5) in the inverse design method.

It is worth to mention that during the practical completeness of inverse design task, several points of the target pressures near to the leading edge of the suction side are modified to make the high pressure gradient smoother (see Fig. 6.5). Moreover, an arbitrary (optimal in this sense) target pressure distribution often causes non-realistic geometry as negative thickness, trailing edge opening or cross over. Based on several theoretical investigation and computational tests, it can be noticed, that the expected (target) pressure distribution cannot be arbitrary in case of subsonic flow due to the information propagation into the upstream (leading edge) direction along the streamline bounded by the wall. If the required pressure is differed from the initial one at the certain representative part of the near wall region, the flow can be retarded or sucked depends on the local conditions. This effect has an influence on the flow evolution starting from the leading edge and the pressure should be redistributed by considering higher or lower local kinetic energy along the stream line especially at the first couple mesh points of the leading edge [54].

The inverse design iteration loop of the inverse, wall modification and direct modes - shown in Fig. 6.3 - is generally converged after 10 iteration cycles. The normal velocity distribution across the solid wall is near to zero at the 10th iteration of the inverse subroutine, which represents that there is no need for further steps, the pressure gradient is infinitesimally small (no flow) across the solid boundary.

After completing the inverse design calculations, the corresponding vane shapes are shown in Fig. 6.9. The geometries belong to different rooftop pressure coefficients are denoted by different colours.

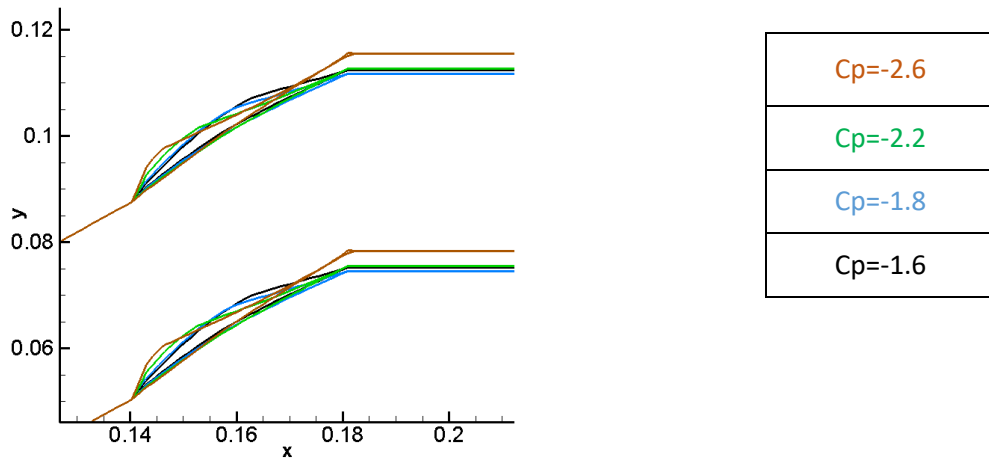


Figure 6.9 Geometrical configurations of the all redesigned vanes in one graph

The design parameters of the initial and the redesigned vanes by the inverse method at the applied rooftop pressure coefficients are found in Table 6.1.

Table 6.1 Design parameters of the initial and the redesigned vane geometries at the investigated rooftop pressure coefficients

	Initial geometry	$C_p=-1.6$		$C_p=-1.8$		$C_p=-2.2$		$C_p=-2.6$	
		value	%	value	%	value	%	value	%
Flow angle from axial direction at downstream location (deg.)	26	23	-11.5	22	-15.4	28	7.69	32	23.08
Static pressurise: $p_{stat,out}/p_{stat,in}$ (-)	1.119	1.136	1.52	1.14	1.88	1.103	-1.43	1.05	-6.17
Mass flow rate per unit length (kg/(s m))	15.5	16	3.23	16.5	6.45	15.7	1.29	14.2	-8.39

As it is shown, the variant with $C_p=-1.8$ (belongs to the optimal pressure distribution) has the maximum flow turning in axial (x) direction, static pressure-rise and mass flow rate per unit length. The corresponding results of the optimization procedure are found in Fig. 6.10. The target and optimised (result) pressure distribution are compared with each other and the deviation between them is negligible. The average normalized differences between the suction side and pressure side pressure distributions are 0.42 % and 0.34 % respectively. The “init” is the pressure distribution of the initial vane geometry.

The optimized (redesigned) geometry with the resulted Mach number and pressure distribution are found in Fig. 6.11 and Fig. 6.12. The both Mach number and pressure distributions show more homogenous and uniform transition along the blade channel compared to the initial profile. The baseline and the optimized blade profiles are shown together in Figure 6.13 for comparison.

Based on the results above, the existence of a unique optimum pressure distribution on the suction side of the blade - belongs to rooftop $C_p=-1.8$ - in adverse pressure gradient flow condition from the location of the highest velocity - determined by the Stratford’s separation prediction method - is proven and this pressure distribution has (i) the highest closed surface area and the cascade corresponds to this pressure distribution provides (ii) the maximum flow turning in axial direction, (iii) the maximum static pressure-rise and (iv)

maximum mass flow rate per unit length, (\dot{v}) beside close, but certain distance far from the separation. The all parameters are improved by 7.9 % in average. This pressure distribution is going to be used in the next chapter of the present work for the verification of the results.

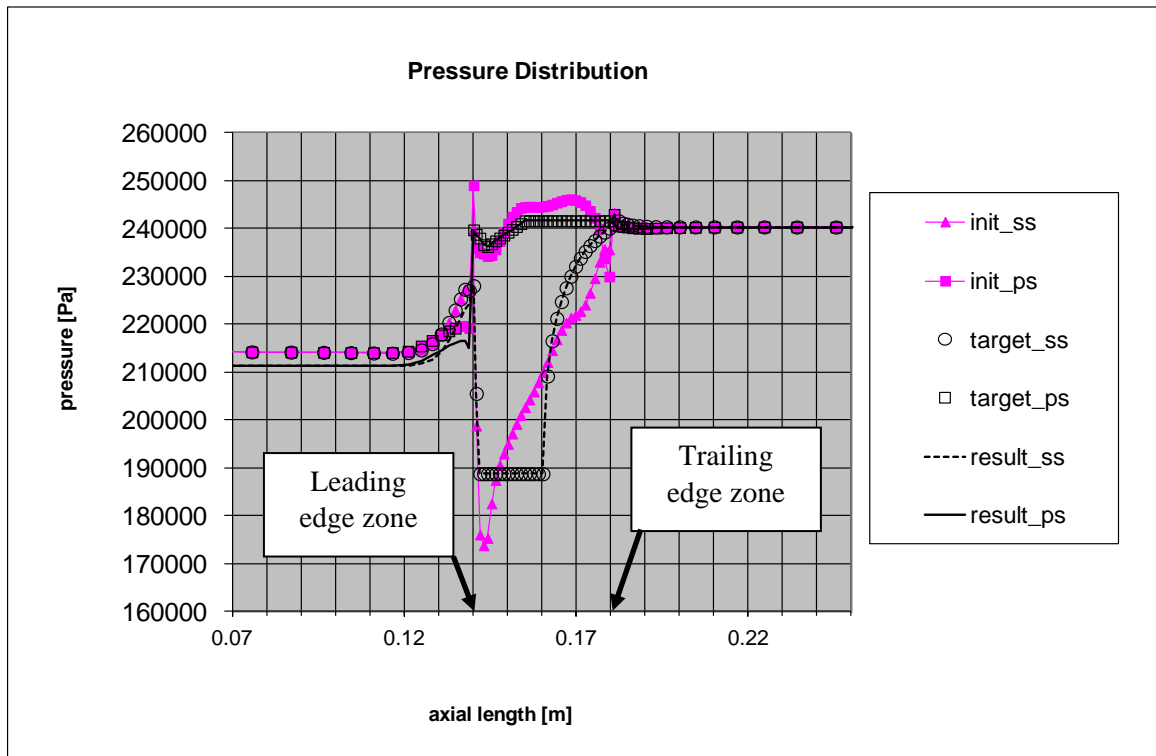


Figure 6.10 Comparison of the initial, target (at rooftop $C_p = -1.8$) and the resulted static pressure distributions along the suction and pressure side of the profile (ss: suction side, ps: pressure side)

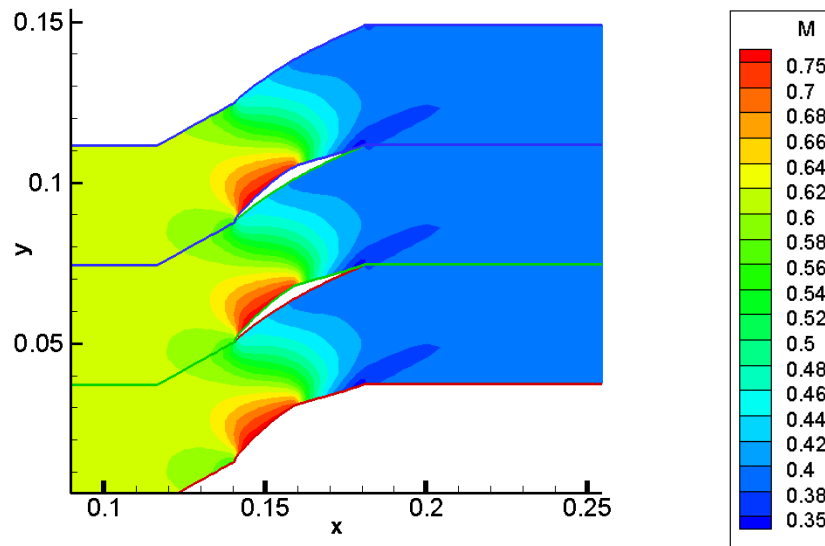


Figure 6.11 Mach number [-] distribution in case of redesigned (optimal) vane geometry [m] (at rooftop $C_p = -1.8$)

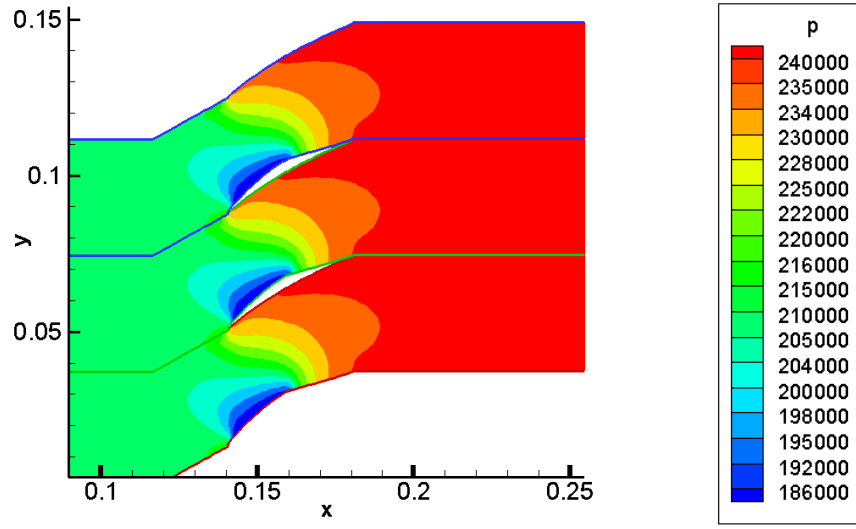


Figure 6.12 Static pressure [Pa] distribution in case of redesigned (optimal) vane geometry [m] (at rooftop $C_p=-1.8$)

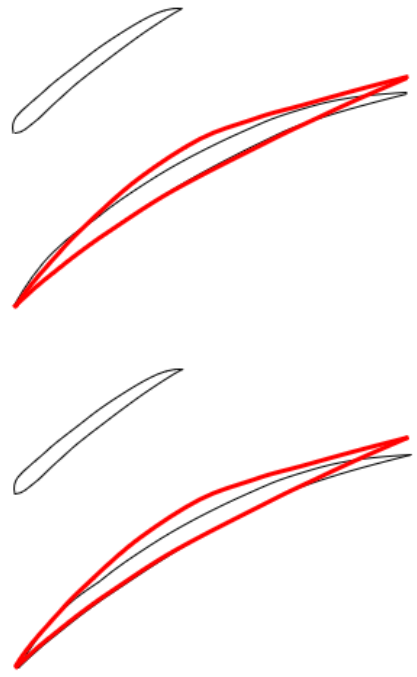


Figure 6.13 Vane configurations in case of baseline (black) and redesigned (optimal at rooftop $C_p=-1.8$) (red) variants

6.4. Verification of the Results by ANSYS CFX

The verification in this context means that the results of the output geometry of the optimization process (at rooftop $C_p=-1.8$) are compared with the results of a highly validated commercial CFD code to crosscheck the correct and accurate operation of the inverse design tool. ANSYS CFX is used for that purpose at the similar mesh, the same boundary conditions and material properties. The simulations in the ANSYS CFX are performed by two different ways as inviscid and viscous flow assumptions to see the differences between them and the (inviscid) in-house code.

6.4.1. Inviscid analysis of the optimized vane (at Rooftop $C_p=-1.8$) by CFX

The Design Modeller, which is part of ANSYS Workbench, is used for creating the flow field. The 2D coordinates of the points are imported from the Tecplot_21_10.dat file into the Design Modeller. Concerning the numerical mesh, similar configuration is created in the present case also than in the direct mode of the inverse design method to minimize the differences between the two simulation approaches. The numbers of the elements and nodes to be used in the simulation are 7448 and 6494, respectively.

In CFX-Pre sub module, the properties of the operational fluid through the domain are defined. Air as an ideal gas with zero viscosity is used. The option of heat transfer corresponds to 'Total Energy'. Free slip boundary condition is applied for solid surfaces. Translational periodicity is considered at the boundaries next to the vane-walls in the cascade, out of the solid walls, are opposed with each other. The boundary conditions are

the following: inlet total pressure: $p_{tot,in}=270000$ [Pa]; inlet total temperature: $T_{tot,in}=436$ [K]; inlet flow angle: 45° and the outlet static pressure: $p_{stat,out}=240184$ [Pa]. After reaching the convergence criterion ($10E-4$), the results of the CFX analysis are evaluated. First, the pressure distributions, as quantitative results, are shown in the upstream, downstream of the periodic pairs and at the vane segments along the suction and pressure side of the profile (see Fig. 6.14). The initial, the target and the resulted pressure distributions of the inverse design method are also shown beside the inviscid result of the CFX at the pressure side (Ansys_inviscid_ps) and at the suction side (Ansys_inviscid_ss).

The average relative deviations between the results of the inverse design code and ANSYS inviscid approach are 2 % at suction side and 0.29 % at the pressure side. These data ($< 5\%$) confirm that the inverse design optimization method works correctly and provides plausible and accurate results in engineering point of view.

The differences between the direct solver of the inverse design method and ANSYS CFX are mostly due to the different treatments of the boundary conditions and averaging techniques over the cells. Additionally, the used discretization methods could also contribute to have slightly different results based on the different inherent mechanism. This can be seen mostly at the inlet stagnation point of the vane, where one has the highest difference between the two approaches.

The qualitative results are also presented in case of CFX for comparison (see Fig. 6.15 and Fig. 6.16), which are agreed with results of the in-house code at acceptable level.

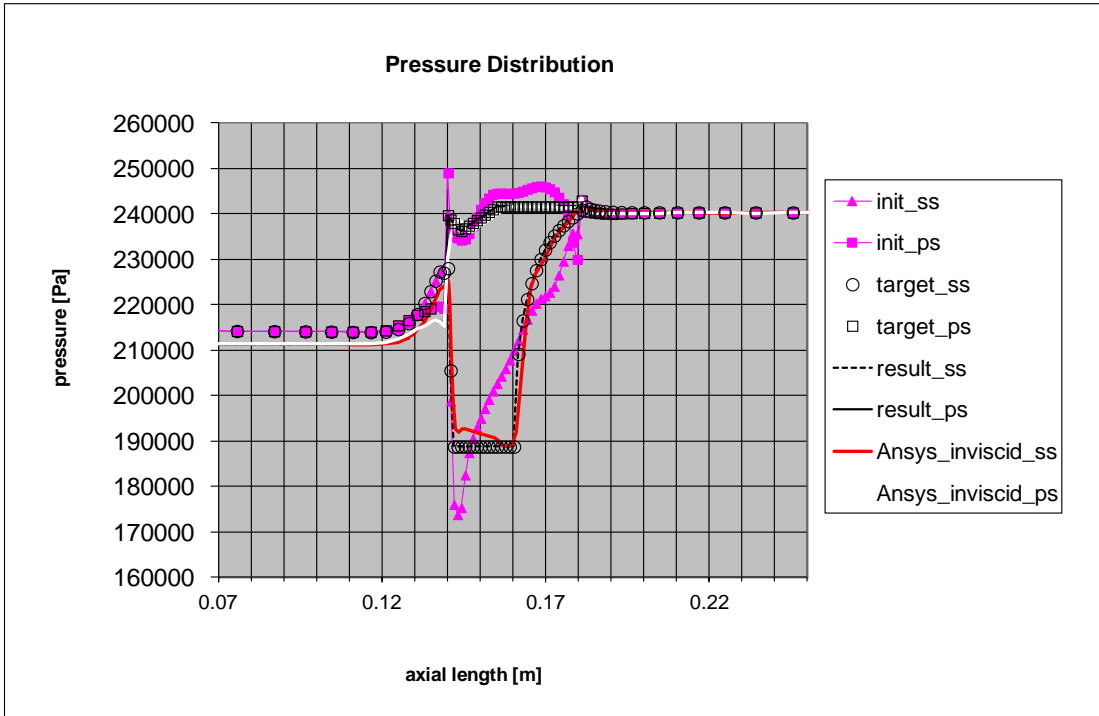


Figure 6.14 Pressure distributions of the initial (init), target (at rooftop $C_p=-1.8$) and redesigned (result) vane configurations in case of inviscid flow analysis by the direct solver of inverse design tool and ANSYS CFX (Ansys) inviscid solution (ss=suction side, ps=pressure side)

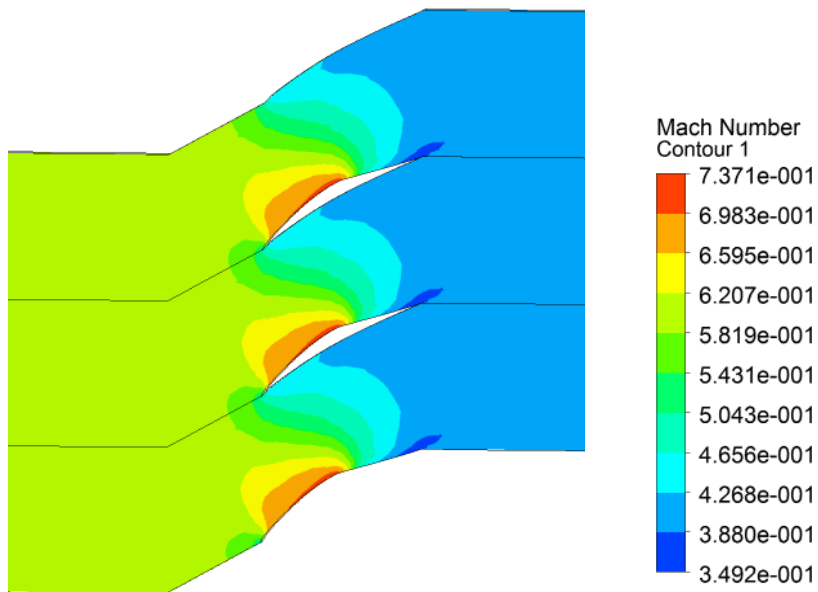


Figure 6.15 Mach number [-] distribution of the redesigned vane (at rooftop $C_p=-1.8$) in case of ANSYS CFX (inviscid flow analysis)

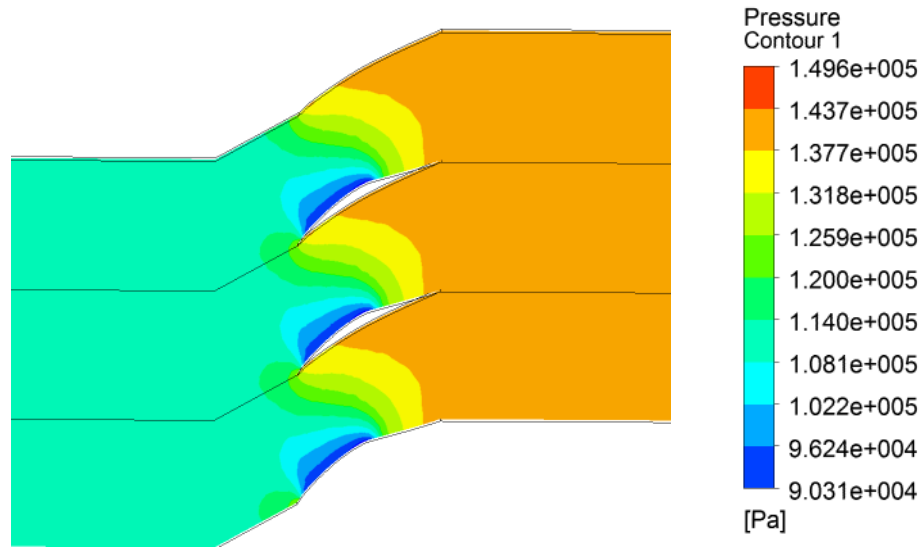


Figure 6.16 Pressure distribution [Pa] of the redesigned vane (at rooftop $C_p=-1.8$) in case of ANSYS CFX (inviscid flow analysis)

6.4.2. Viscous analysis of the optimized (at Rooftop $C_p=-1.8$) vane by CFX

The same procedure is followed in case of viscous flow than in case of inviscid analysis. However, due to the more complex treatment of the physics, there are some specific differences between the two approaches. The boundary layer is resolved on such a way that the first cell from the wall to be fallen in the log layer region. Hence, dimensionless analytical expressions derived over the flat plate flow are used to determine the distance of the first cell from the solid wall to have $y^+=40$. The inflation layer is built up from 20 layers. The numbers of elements and nodes to be used in the simulation are 87221 and 36756 respectively.

Air is considered as an ideal gas for the operational fluid. The value of the dynamic viscosity is set to be $1.831e-05$ Pas. Total energy is used for the heat transfer. Shear Stress Transport (SST) turbulence model has been applied.

The boundary conditions are the following: inlet total pressure: $p_{tot,in}=270000$ [Pa]; inlet total temperature: $T_{tot,in}=436$ [K]; inlet flow angle: 45° and the outlet static pressure: $p_{stat,out}=240184$ [Pa]. No slip boundary condition is used for the wall boundary conditions and translational periodicity is considered at the boundaries of the cascade, out of the solid walls, are opposed with each other.

After having mesh independent and converged solution, the initial, the target and the resulted pressure distributions of the inverse design tool are plotted in a same diagram with the inviscid (Ansys_inviscid_ss and Ansys_inviscid_ps) and viscous (Ansys_viscous_ss and Ansys_viscous_ps) flow result of the CFX software (ss=suction side and ps=pressure side) as it is shown in Fig. 6.17. The maximum differences between the in-house and ANSYS viscous wall pressure results are 8 %, and the relative average differences between the

results of the direct mode of the in-house code and Ansys viscous flow analysis are 3.04 % on the suction side and 0.3 % at pressure side. The highest difference is arisen around the leading-edge stagnation point, similarly to the inviscid flow analyses discussed in the previous subchapter.

The qualitative results are also presented in case of viscous CFX simulations for comparison. The relative static and total pressure distributions are plotted in Fig. 6.18 and Fig. 6.19 respectively. These distributions are in line with the results of the CFX inviscid analysis and with the results of the direct solver of the inverse design method.

Both, the viscous and inviscid analyses confirm that the adopted and applied inverse design optimization method provides plausible and accurate results for the presented case, which is acceptable in engineering point of view as the average difference between the different approaches is less than 5 % at the investigated quantitative results. Hence, the introduced inverse design-based optimization method - after further sensitivity analyses and validations by measurements - can be used in design and developments in the other field of the engineering science, too.

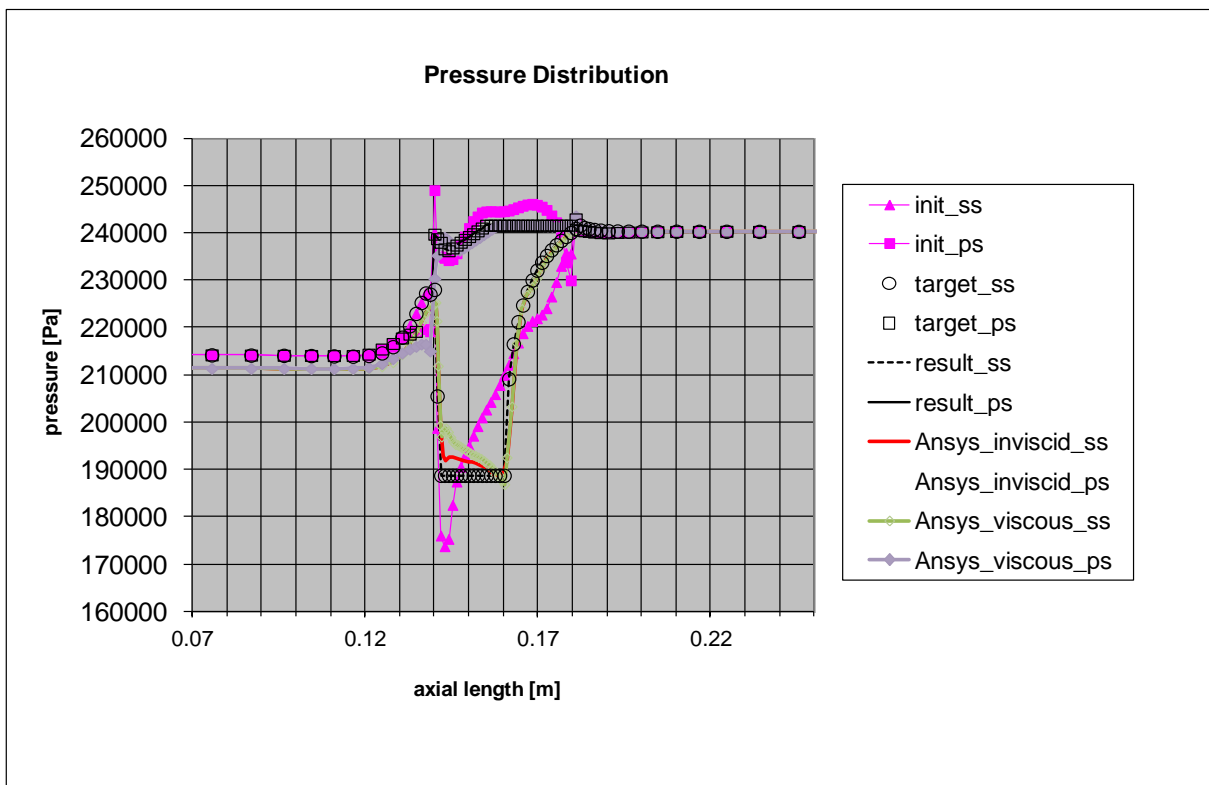


Figure 6.17 Pressure distributions of the initial (init), target and redesigned (result) vane configurations in case of inviscid flow analyses by the direct mode of the in-house invers design code and inviscid and viscous flow analyses by the ANSYS CFX (Ansys) (ss=suction side, ps=pressure side)

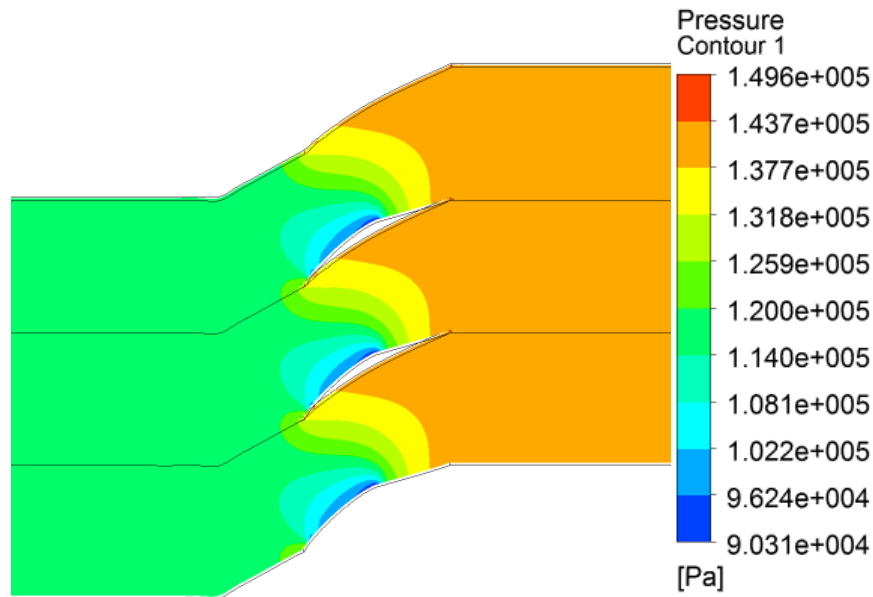


Figure 6.18 Pressure distribution of the redesigned vane (at rooftop $C_p=-1.8$) in case of ANSYS CFX (viscous flow analysis)

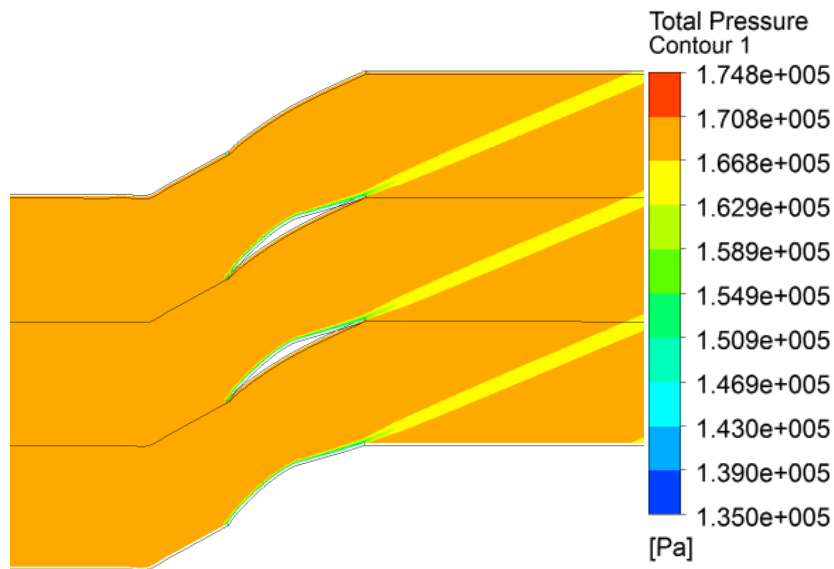


Figure 6.19 Total pressure distribution of the redesigned vane (at rooftop $C_p=-1.8$) in case of ANSYS CFX (viscous flow analysis)

Finally, the performance of the original vanned diffuser with splitter vanes and the optimized geometry is compared with each other by using ANSYS CFX viscous flow solver. The mesh, the boundary conditions, the physical and numerical settings are the same as before for the viscous flow analysis. After having convergent status for the execution, the qualitative results of the original vanned diffuser with splitter vanes are presented in Fig. 6.20 and 6.21.

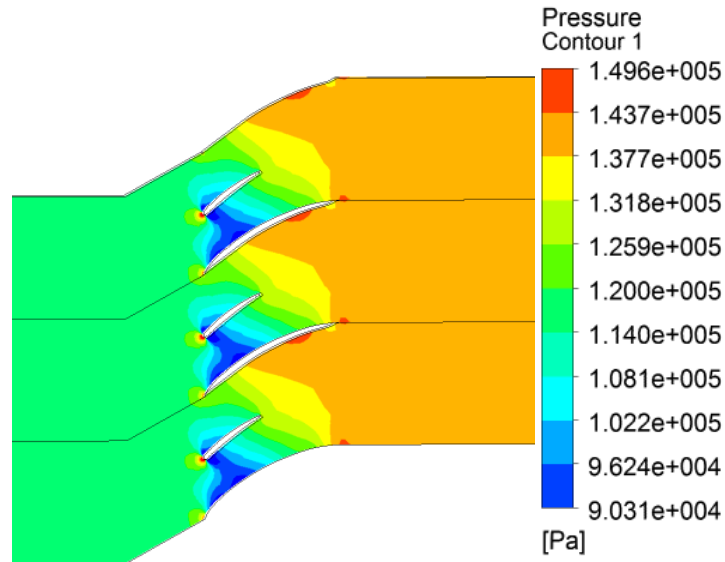


Figure 6.20 Pressure distribution of the baseline vanned diffuser in case of ANSYS CFX (viscous flow analysis)

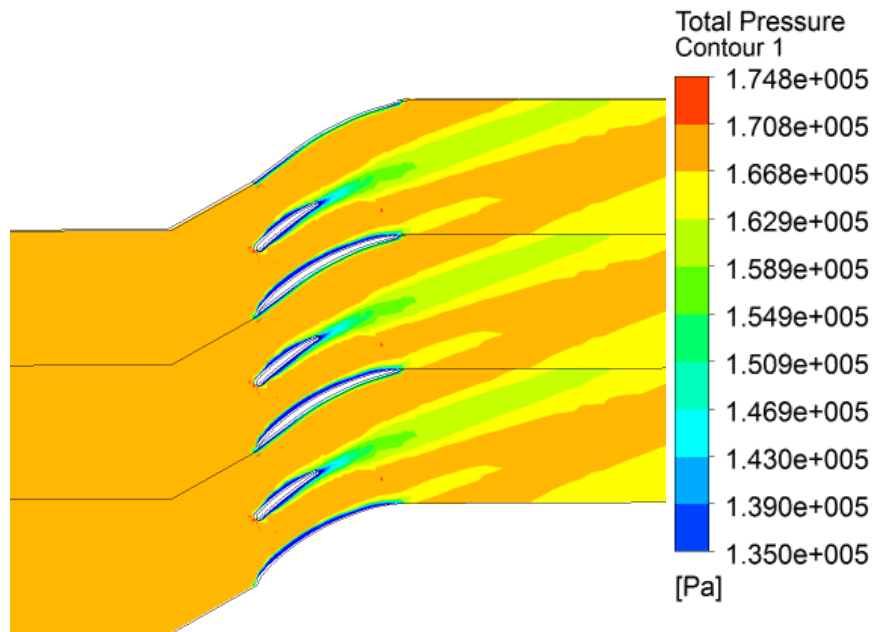


Figure 6.21 Total pressure distribution of the baseline vanned diffuser in case of ANSYS CFX (viscous flow analysis)

Following the qualitative results, the quantitative comparison is completed between the original (baseline) geometry with splitter vanes and the optimized geometry (at rooftop $C_p = -1.8$) in order to evaluate the relevancies of the design. The total pressure recovery factor, the static pressure, the flow turning in axial direction and the mass flow rate are shown in the Table 6.2.

Table 6.2 Improvements of design parameters with respect to the baseline design

	Baseline configuration	Optimized vanned diffuser	Improvements
Total pressure recovery factor (-)	0.96	0.99	3.13%
Static pressure-rise (-)	1.1	1.12	1.81%
Flow angle from horizontal at downstream (degrees)	26	22	-15.38%
Mass flow rate per unit length (kg/(m s))	15.5	16	3.2%

It is shown that the newly redesigned optimum vane configuration provides better performance than the original vane configuration in the all investigated design parameters. The average relative improvements are 5.88 %.

The combination of the optimum pressure distribution by means of the maximum closed surface area created by Stratford's separation prediction method and the presented inverse design method provides a suitable tool for determining the best design variant at given operational condition for vanned diffuser of centrifugal compressors.

6.5. Conclusions

The adoption and the new application of the inversed design optimization method have been completed in the present research for redesigning the vanned diffuser in an academic jet engine with verification. The goal function of the optimization is to keep the (i) original geometrical configuration and dimensions as much as possible, meanwhile (ii) the maximum flow turning (the maximum blade loading and so the maximal closed area of pressure distribution around the vane), (iii) the maximum static pressurize, (iv) the maximum mass flow rate and (v) the maximal pressure recovery factor are expected on such a way that (vi) the flow stream to be close but certain distance far from the separation.

Compressible Euler equations are considered as governing equations in the used academic code and a specific finite volume method has been applied to solve the system of the nonlinear partial differential equations. Stratford's separation prediction method has been used to determine and then select the optimum pressure distribution at given boundary conditions along the suction side in adverse pressure gradient flow condition.

The outcomes of the recent investigations are the following:

- (i) The initial geometry for the inverse design tool is determined to 1. increase the cross-sectional area, 2. decrease the weight, 3. minimize the drag and losses and 4. keep production cost as low as possible, so
 - a. the splitter vanes are removed and
 - b. only the longer vanes are kept and used as initial geometry.

- (ii) The combination of
 - a. the Stratford's separation prediction method with the maximum closed surface area of the pressure distribution
 - b. and inverse design method
has provided the optimum vane configuration by means of
 - c. the highest static pressure-rise,
 - d. the highest flow turning in axial direction,
 - e. the highest mass flow rate and
 - f. the maximal pressure recovery factor between the investigated cases meanwhile
 - g. the flow is close but certain distance far from the separation.

The relative average difference between the target and the resulted pressure distribution is 0.42% at suction side and 0.34 % at pressure side.

- (iii) Ansys CFX commercial code has been used for verification, for crosschecking that the outcomes of inverse design method are plausible, correct and accurate.
 - a. The inviscid-type verification has provided 2 % and 0.29 % relative average deviations in case of the resulted pressure distribution between the commercial and the direct solver of the in-house code at suction side and pressure side of the vane respectively.
 - b. The average relative difference at the pressure distributions between the results of CFX at viscous and the direct mode of the inviscid inverse design tool is 3.04 % at suction side and 0.3 % at pressure side of the vane.

- (iv) The aerodynamic performance of the base line design and the optimized vanned diffuser has been compared with each other by means of viscous flow analyses. The optimized version has
 - a. higher total pressure recovery factor by 3.13 %,
 - b. higher static pressure-rise by 1.81 %,
 - c. flow angle decrement measured from the axial (x) direction by 15.38 % and
 - d. higher mass flow rate per unit length by 3.2 %
than the original vane configuration.

Based on the all paragraphs mentioned above, the presented inverse design tool with Stratford's separation prediction method is verified, it can be used successfully in the developments of vanned diffusers of centrifugal compressors. However, measurement-based validation would be indispensable to complete before the introduction that into the R&D processes. Additionally, there are several features to improve its capability as follows: (i) extension in 3D and (ii) viscous flow conditions, (iii) automatic target pressure distribution at the leading edge for guarantying the existence (structural integrity) of the blade geometry (iv) investigate the effect and/or develop other separation prediction methods to increase the overall accuracy and (v) to be suitable with other range of Re and highly compressible flow regime.

7. Conclusions

Aero- and thermodynamic redesign and analyses of the TSz-21 academic jet engine is completed in the present thesis. The origin of the single spool engine is a starter gas turbine, which was used originally for MiG-23 and Szu-22 Russian fighters. This engine has been modified to be an academic jet propulsion system by Dr. Beneda and Dr. Pásztor from 2005-2008 and it is still under development with especial care for control systems [2].

The virtual prototyping of the jet engine components consists of four different steps in the present case as follows:

1. Thermo-dynamic cycle analysis for determining the design (operational) point,
2. Mean line and 3D design of the engine for having geometrical sizes and CAD models,
3. Computational Fluid Dynamics (CFD) analysis for verification of the design and plausibility check by the available data and
4. Inverse design of the vanned diffuser.

Thermo-dynamic cycle analysis for determining the design (operational) point

The redesign process starts with thermodynamic cycle analysis for determining the expected operational condition. Hence, first, improved mathematical models have been developed for cycle analysis, for determining the critical pressure at converging nozzle and for determining the optimum total pressure ratio of the compressor belongs to the maximum thrust. These models are based on the mass and energy balance, they consider viscous flow conditions meanwhile the specific heats at constant pressure and the ratios of specific heats depend on the total temperature and fuel to air mass flow rates ratio. The model for cycle analysis is adapted for triple-, dual- and single-spool turbojet engines for the shake of the complexity and the expression for the optimum total pressure ratio is developed for single spool turbojet engines.

HK-32 and HK-25 triple spool mixed turbofan engines at take-off (start) condition with afterburner, HK-22 and HK-144A dual spool mixed turbofan engines at take-off and at flight conditions with and without afterburning respectively, HK-8-4 and HK-86A dual spool mixed turbofan engines at take-off condition without afterburning and BД-7 and KP7-300 singles spool turbojet engines at take-off condition without afterburner are considered for verification and plausibility check of the thermodynamic cycle analysis. Constrained nonlinear optimisation is applied at these cases for determining the unknown parameters as efficiencies, losses, power reduction rates of the auxiliary systems, bleed air ratios for technological reasons, air income ratios due to blade cooling and total temperatures in the afterburner (if it is the case) by means of having parameter-state, which provides the closest results to the available thrusts [3] and thrust specific fuel consumptions. The maximum and the average relative deviations between the resulted and available thrusts and thrust specific fuel consumptions are 1.46 % and 0.645 % (for the thrusts) and 0.55 % and 0.32 % (for the thrust specific fuel consumptions) respectively, meanwhile the identified parameters are within the plausible range.

HK-32 and HK-25 engines have been used for determining the effect of the new equation - calculates the critical pressure - on the thrust and thrust specific fuel consumption. The results of the parameter identification for the unknown data show that the average value of the relative deviations between the resulted and the available thrusts and thrust specific fuel consumptions is 0.119 % by using a variant of the new equation for the critical pressure and it is 3.13 % at the conventional equation with constant gas properties (the ratio of specific heats for gas equals 1.33). The “variant” in the present context means that the true specific heat is considered instead of the average one at the given temperature range in the total enthalpy equation. The new equation for determining the critical pressure is tested also for PД-9Б single-spool turbojet engine with

afterburning and at take-off condition. It gives higher critical pressure by 9.3 % than its original form with constant gas properties.

Finally, the last section in the thermodynamic cycle-analyses is the test and the verification of the novel analytical equation for the optimum compressor total pressure ratio. ПД-9Б and АЛ-21Ф3 single-spool turbojet engines are considered for that purpose with afterburning and at take-off condition. First, similarly to the parameter identification described above, the unknown pressure recovery factors, efficiencies and the missing technical parameters are determined by constraint optimisation. Concerning the both engines, the highest relative differences between the known and the resulted thrusts and thrust specific fuel consumptions are 0.0617 % and 0.0245 % respectively for the *TSFC* at ПД-9Б engine, while the unknown parameters are within the expected intervals. The plausibility of the new equation for the optimum total pressure ratio is verified by determining the extreme value of the pressure ratio-thrust functions numerically. The new equation for the optimum pressure ratio provides 3.39 % and 3.64 % thrust increments for the ПД-9Б and АЛ-21Ф3 jet engine respectively.

Based on the intensive verification and plausibility check, the developed mathematical model and the new equations are suitable. So, they are used for determining the operational point of the academic jet engine, which belongs to expected thrust 330 N at start and sea level conditions.

Mean line and 3D design of the engine for the geometrical sizes and CAD models

After making decision about operational point and having the states of the thermo-dynamical cycle, mean line design of the centrifugal compressor and axial turbine are completed. The design processes for the compressor and turbine are based on the standard procedure found in [60] and [1] respectively. Constant nozzle outlet angle blade twisting method is used due to favourable production cost. Following the 3D extension of the and the determination of the blade angles, chords, spacings, blade numbers and profiles, the 3D CAD models are prepared. Beside the turbine, the 3D models of the compressor, inlet channel, combustion chamber and exhaust nozzle are also created. The main design criteria of these last three structures are to fit their geometrical sizes to the compressor and turbine and provide minimum pressure recovery factors. The combustion chamber additionally has high burning efficiency. The calculated thrust is 333.1 N in the mean line design, which is in line with the design specification. As the 3D models of the structures are available, the preparations of the flow fields are also completed.

CFD analysis for verification of the design and plausibility check by the available data

CFD analyses are performed and introduced in the next steps of the present work by means of separated and full components as two different approaches for crosschecking the correctness and the plausibility of the results of the design. The qualitative results of these simulations are plausible, the thermodynamic parameters are in the same intervals. Concerning the quantitative results, there are two ways for investigating the plausibility and the accuracy of the outcomes of the design and the analyses in the present case. The one of them is to compare the engine design parameters (given by thermodynamic cycle analysis and mean line design) with the results of the CFD analyses (separated and full modelling approaches) and the second one is to evaluate the results of the CFD analyses with the available measured data even though the accuracy of these measured data are not verified statistically [4]. The outputs of these investigations are the following. The average relative deviations between the results of the thermodynamic cycle analysis and CFD simulations are 0.81 % (for the separated model) and 1.05 % (for the full model) in case of the total temperature, meanwhile they are 3.42 % (separated model) and 4.71 % (full model) for the total pressure. The average relative deviations between the results of the mean line design and the CFD analyses are 1.75 % (separated model) and 1.13 % (full model)

for the total temperature, meanwhile it is 1.59 % (separated model) and 1.56 % (full model) for the static temperature. Similarly, the average relative deviations between the mean line design and CFD analyses are 3.13 % (separated model) and 4.59 % (full model) for the total pressure and they are 3.18 % (separated model) and 5.01 % (full model) for the static pressure. Although the accuracy is not verified statistically, available measured data are used for the plausibility checking of the outcomes of the academic jet engine design. The average relative deviations between the available measured data and the results of the CFD analyses in case of the total temperature are 0.61 % (separated model) and 1.98 % (full model) and they are 3.03 % (separated model) and 2.11 % (full model) for the static temperature. The average relative deviations between the available measured data and the result of the CFD analyses in case of the total pressure are 5.75 % and 10.65 % for the separated and for the full model respectively, meanwhile they are 4.87 % and 3.43 % for the static pressure.

The results of the thrusts for the academic jet engine are 333.1 N by the mean line design and 325.2 by the full-model CFD analysis. The expected target thrust is 330 N. The maximum relative deviation between the computed and expected value is 1.46 %. It is at the case of the full-model CFD analysis.

Based on the discussed results above, the presented methodology till that section by means of virtual prototyping of the academic jet engine components is suitable, the provided results are acceptable in engineering point of view.

Inverse design of the vanned diffuser

Inverse design optimization technology is adopted and developed in the last part of the present research for redesigning the vanned diffuser in the academic jet engine with verification. Compressible Euler equations are considered as governing equations in the used academic code and a specific finite volume method has been applied to solve the system of the nonlinear partial differential equations. Stratford's separation prediction method has been used to determine and then select the optimum pressure distribution at given boundary conditions along the suction side of the vane in adverse pressure gradient flow condition.

The outcomes of the inverse design optimisation are the following:

- (i) The initial geometry for the inverse design tool is determined to 1. increase the cross-sectional area, 2. decrease the weight, 3. minimize the drag and losses and 4. keep production cost as low as possible, so
 - a. the splitter vanes are removed and
 - b. only the longer vanes are kept and used as initial geometry.
- (ii) The combination of
 - a. the Stratford's separation prediction method with the maximum closed surface area of the pressure distribution
 - b. and inverse design methodhas provided the optimum vane configuration by means of
 - c. the highest static pressure-rise,
 - d. the highest flow turning in axial direction,
 - e. the highest mass flow rate and
 - f. the maximal pressure recovery factor between the investigated cases meanwhile
 - g. the flow is close but certain distance far from the separation.

The relative average difference between the target and the resulted pressure distribution is 0.42 % at suction side and 0.34 % at pressure side.

- (iii) Ansys CFX commercial code has been used for verification, for crosschecking that the outcomes of inverse design method are plausible, correct and accurate.
 - a. The inviscid-type verification has provided 2 % and 0.29 % relative average deviations in case of the resulted pressure distribution between the commercial and the direct solver of the in-house code at suction side and pressure side of the vane respectively.
 - b. The average relative difference at the pressure distributions between the results of CFX at viscous and the direct mode of the inviscid inverse design tool is 3.04 % at suction side and 0.3 % at pressure side of the vane.
- (iv) The aerodynamic performance of the base line design and the optimized vanned diffuser has been compared with each other by means of viscous flow analyses. The optimized version has
 - a. higher total pressure recovery factor by 3.13 %,
 - b. higher static pressure-rise by 1.81 %,
 - c. flow angle decrement measured from the axial (x) direction by 15.38 % and
 - d. higher mass flow rate per unit length by 3.2 %
than the original vane configuration.

Based on the results mentioned above, the presented inverse design tool with Stratford's separation prediction method is verified, it can be used successfully in the developments of vanned diffusers of centrifugal compressors. However, measurement-based validation would be indispensable to complete before the introduction that into the R&D processes.

8. List and Summary of the Thesis

Advanced aerodynamic design process has been developed and applied for a turbojet engine with especial care i. for deriving new equations and procedures to increase the accuracy of thermo-dynamic cycle analyses and ii. for introducing inverse design methodology for redesign vanned diffuser in order to optimize design specifications. Jet engines with available technical parameters in the open literature are used for the verification and plausibility check of the thermodynamic models, meanwhile an in-house academic turbo jet engine has been considered for design, design-verification and plausibility check.

Thesis 1:

The accuracy of the critical pressure at the exit of the converging nozzle of jet engines is increased by considering specific heats at constant pressure and ratios of specific heats are the functions of temperatures and fuel to air mass flow rates ratio. Hence, the following equation has to be used for determining critical static pressure at the outlet of the converging nozzle:

$$p_c = p_{07} \left[1 - \frac{1}{\eta_n} \left(1 - \frac{2\bar{c}_{pmix}(T_{09}, T_c, f)}{2\bar{c}_{pmix}(T_{09}, T_c, f) + \gamma_{mix}(T_c, f) R_{mix}} \right) \frac{\bar{c}_{pmix}(T_{09}, T_c, f)}{2\bar{c}_{pmix}(T_{09}, T_c, f)} \right]^{\frac{\bar{\gamma}_{mix}(T_{09}, T_{9s}, f)}{\bar{\gamma}_{mix}(T_{09}, T_{9s}, f) - 1}}, \quad (8.1)$$

where p_{07} is the total pressure [Pa] at the upstream of the nozzle, η_n is the isentropic efficiency of the nozzle [-], \bar{c}_{pmix} is the average specific heat [J/(kg K)], T_0 and T is the total and static temperatures respectively [K], f is the fuel to air mass flow rates ratio [-], R_{mix} is the specific gas constant of the gas mixture [J/(kg K)], $\bar{\gamma}_{mix}$ is the average ratio of the specific heats [-] and “C” in subscript means critical. The standalone parameters are valid at the given nozzle sections meanwhile the averaged ones are at the given temperature ranges and fuel to air ratios.

The Eq. (8.1) gives higher critical pressure by 9.3 % for the ПД-9Б single spool turbojet engine than its original form shown by Eq. (8.2) with constant gas parameters (the ratio of specific heats for the gas is 1.33).

$$p_c = p_{07} \left(1 - \frac{1}{\eta_n} \left(\frac{\gamma_{gas} - 1}{\gamma_{gas} + 1} \right)^{\frac{\gamma_{gas}}{\gamma_{gas} - 1}} \right) \quad (8.2)$$

The thermodynamic analyses of the HK-32 and HK-25 triple spool jet engines are also completed including the determination of the critical pressure at the exit of the converging nozzle by using a variant of (8.1) and (8.2). The average deviation between the resulted (by the parameter fitting) and the available thrust and thrust specific fuel consumption [3] is 0.119 % by using a variant of (8.1) and 3.13 % at the conventional equation (8.2) at the same other conditions. The “variant” in the present context means that the true specific heats at constant pressure and at the given temperatures are considered instead of the averaged one in the total enthalpy equation.

Related publications: [117, 118 and 121]

Thesis 2:

The accuracy of the optimum total pressure ratio of the turbojet engines pertaining at maximum specific thrust is improved by applying frictional (viscous) flow assumptions beside the temperature and mass fraction dependencies of the relevant properties of the gas mixture. Therefore, the following expression has to be used for determining the optimum total pressure ratio of turbojet engines at maximum specific thrust:

$$\pi_{C_opt} = \sqrt[\beta]{\frac{\varepsilon(1+\phi)}{\phi(\varepsilon+\beta)'}} \quad (8.3)$$

where

$$\beta = \frac{\bar{\gamma}_{mix}(T_{02}, T_{03s}, f=0) - 1}{\bar{\gamma}_{mix}(T_{02}, T_{03s}, f=0)}, \quad (8.4)$$

$$\varepsilon = \frac{\bar{\gamma}_{mix}(T_{04}, T_{05s}, f_T) - 1}{\bar{\gamma}_{mix}(T_{04}, T_{05s}, f_T)}, \quad (8.5)$$

$$\phi = \frac{\bar{c}_{pmix}(T_{02}, T_{03}, f=0) T_{02}}{\bar{c}_{pmix}(T_{04}, T_{03}, f_{cc}) T_{04} \eta_m \eta_{C,s} \eta_{T,s} (1 - \delta_{tech}) (1 + \delta_{bc}) (1 + f_{cc}) (1 - \xi)}, \quad (8.6)$$

$\bar{\gamma}_{mix}$ is the average ratio of the specific heats of gas mixture [-], T_0 is the total temperature [K], f is the fuel to air mass flow rates ratio [-] (cc : combustion chamber), \bar{c}_{pmix} is the average specific heat at constant pressure for the gas mixture [J/(kg K)], η is the efficiency [-] (s : isentropic, m : mechanical, τ : turbine and c : compressor), δ_{tech} is the bleed air ratio for technological reasons [-], δ_{bc} is the ratio of the incoming air due to blade cooling [-] and ξ is the power reduction rate of the auxiliary systems [-]. The standalone parameters are valid at the specified engine sections meanwhile the averaged ones are at the given temperature ranges and fuel to air ratios.

In case of viscous (frictional) flow conditions and variable specific heats, which are included in Eq. (8.3), the calculated optimum total pressure ratio is higher by 40 % and 53.3 % for the ПД-9Б and АЛ-21Ф3 jet engines respectively than their total pressure ratios found in the technical specification [3]. These newly calculated optimum total pressure ratios correspond to 3.39 % and 3.64 % thrust increments consistently. In addition, besides keeping the viscous flow assumption, if the specific heats (and so the ratios of specific heats) are defined to be constant, there are 9.52 % and 13.04 % decrements in the total pressure ratios for ПД-9Б and АЛ-21Ф3 jet engines respectively.

Related publication: [117]

Thesis 3:

The thermo-dynamical model for design and analysis jet engines including single-, dual-, and triple spool configurations has to be established by the following way:

- i. Mass and energy balance have to be applied,*
- ii. Frictional (viscous) flow assumption has to be considered in the processes of the thermo-dynamical cycles,*
- iii. The specific heats and the ratio of specific heats are the functions of the temperature and the fuel to air mass flow rates ratios. Iteration cycles have to be used for evaluating the temperatures and component mass fractions if they are the variables of the gas parameters.*
- iv. The non-available technical data as efficiencies (e.g.: mechanical, isentropic of fan, compressor and turbine, burning and exhaust nozzle), total pressure recovery factors (e.g.: inlet diffuser, combustion chamber and afterburner or turbine exhaust pipe), total pressure ratio of the fan and intermediate pressure compressor, power reduction rate of the auxiliary systems, bleed air ratio for technological reasons, air income ratio due to blade cooling and total temperature of the afterburner, if these are relevant – have to be determined either by*
 - a) well known and established (practical) experiences,*
 - b) measurements,*
 - c) simulations (e.g.: CFD simulations for efficiencies and total pressure recovery factors) and*
 - d) parameter identification, in which the goal function of the optimization is to minimize the differences between the calculated and available thrust and thrust specific fuel consumption.*

- v. *Equation (8.1) has to be used for determining critical static pressure at the exit of the converging nozzle.*
- vi. *Equation (8.3) has to be used for determining the optimum compressor total pressure ratio at maximum specific thrust for turbojet engines.*

4 single spool (at one operational condition), 4 dual spool (two is at two and two is at one operational conditions) and 2 triple spool (at one operational condition) jet engines are analysed by the mathematical models introduced in the present thesis. The resulted thrusts and thrust specific fuel consumptions by constraint nonlinear optimisation - in order to find the unknown parameters – are compared with available data in [3] for verification. The maximum and the average relative deviation between them are 1.46 % and 0.645 % for the thrust and 0.55 % and 0.32 % for the thrust specific fuel consumptions respectively, meanwhile the identified parameters are within the plausible range.

Related publications: [117-119, 121, 122, 125 and 126]

Thesis 4:

The combination of the Stratford's separation prediction method – for providing the maximum closed surface area of the pressure distribution – and inviscid inverse design method – for creating the blade geometry belongs to this pressure distribution – have to be used in design, re-design and developments of vanned diffusers in centrifugal compressor units for providing the optimum vane configurations by means of having:

- i. *the minimal design changes with respect to the baseline configuration, if it is applicable, and in the present case:*
 - a. *the splitter vanes are removed, and*
 - b. *only the vanes with higher chord-length are kept and used as initial geometry for the inverse design method,*
 - ii. *the maximum static pressure-rise,*
 - iii. *the highest flow turning in axial direction,*
 - iv. *the largest mass flow rate*
 - v. *and the greatest total pressure recovery factor ($p_{total_downstream}/p_{total_upstream}$),*
- meanwhile the flow is close but certain safe distance far from the separation as it is guaranteed by the Stratford's separation prediction method.*

Regarding the redesigned (optimized) blade configuration, the average relative difference of the pressure distributions between the results of the CFX at viscous flow condition and the inviscid in-house code is 3.04 % at suction side and 0.3 % at pressure side.

The aerodynamic performance of the base line design and the optimized vanned diffuser has been compared with each other by means of viscous flow analyses. The optimized version has

- i. higher total pressure recovery factor by 3.13 %,
- ii. higher static pressure-rise by 1.81 %,
- iii. flow angle decrement measured from the axial (x) direction by 15.38 %, and
- iv. higher mass flow rate per unit length by 3.2 %

than the original vane configuration has. 2D planar approach has been considered in the present methodology.

Related publications: [119, 120 and 123]

Thesis 5:

The following process has to be used for aerodynamic design of jet engines:

- i. *thermo-dynamic cycle analyses according to Thesis 1. 2. and 3. for determining the design (operational) point,*

- ii. *establishment of the main geometrical sizes and the necessary RPM, if they are relevant* [1],
- iii. *mean line and 3D design with geometry preparation and CAD modelling,*
- iv. *CFD analyses for verification of the design and plausibility check by the available data and*
- v. *inverse design of the solid walls, vanned diffuser in the present case according to Thesis 4.*

After completing the aerodynamic redesign of the academic jet engine in line with the above defined process, excluding the last steps, the conclusions are next. The average relative deviation – using data at engine unit sections – between the results of the thermodynamic cycle analysis and the CFD analysis in case of the full model is 1.05 % for the total temperature and it is 4.71 % for the total pressure. The average relative deviation between the results of the mean line design and CFD analysis in case of the full model also is 1.13 % for the total temperature and it is 1.56 % for the static temperature. Similarly, it is 4.59 % for the total pressure and it is 5.01 % for the static pressure. Although its accuracy is not verified statistically, available measured data [4] is used for plausibility checking of the computed results. The average relative deviation between the available measured data and the results of the CFD analysis in case of full model is 1.98 % for the total temperature and it is 2.11 % for the static temperature. Similarly, it is 10.56 % for the total pressure and it is 3.43 % for the static pressure. The thrust of the academic jet engine is 333.1 N by the mean line design and 325.2 by the full-model CFD analysis. The expected target thrust is 330 N. The maximum relative deviation between these computed and the expected value is 1.46 % and it is at the full-model CFD analysis.

Related publications: [117-128]

Berlin, 31. 12. 2020.

.....
Foroozan Zare

Bibliography

- [1] Sánta, I., *Tervezési Segédlet - Gázturbinás Repülőgép Hajtóművek (Design Guide Line - Aircraft Engines with Gas Turbines)*, Budapest: BME Vasúti Járművek, Repülőgépek és Hajók Tanszék (BME, Department of Aeronautics, Naval Architecture and Railway Vehicles), 2008.
- [2] Beneda, K., Pásztor, E., “A TKT-1 Kisméretű, Oktatási és Kutatási Célú Gázturbinás Sugárhajtómű Első Tíz Éve (The First Ten Years of the TKT-1 Small-Sized Academic and Research Turbo Jet Engine),” *Repüléstudományi Közlemények (Aeronautical Science Bulletins - online scientific journal)*, vol. 3, pp. 117-132, 2015.
- [3] Кулагин, В.В., *Теория расчёт и проектирование авиационных двигателей и энергетических установок, Книга 1, 2*, ISBN 5-217-03269-3, Moscow: Москва, Машиностроение, 2005.
- [4] Pallag, N., “A TKT-1 gázturbinás sugárhajtómű áramlástan vizsgálat (Numerical Analysis of Flow Conditions in TKT-1 Jet Engine), MSc Thesis,” Budapest University of Technology and Economics, Budapest, 2013.
- [5] Gáti, B., Drouin, A., “Open Source Autopilot for Academic Research-The Paparazzi System,” in *IEEE*, Washington, DC, USA, 2013.
- [6] Voskuilj, M., Rohács, D., Rohács, J., Schoustra, R-J.,, “Preliminary Evaluation of the Environmental Impact Related to Take-off and Landings Supported with Ground-Based (MAGLEV) Power,” *Journal of Aerospace Operations*, vol. 2, no. 3-4, pp. 161-180, 2013.
- [7] Beneda, K., Rohács, J., “Dynamic Model of Variable Inducer Shroud Bleed for Centrifugal Compressor Surge Suppression,” *International Review of Aerospace Engineering*, vol. 6(3), pp. 163-173, 2013.
- [8] Beneda, K., Simongáti, Gy., Veress, Á., *Járművek hő- és áramlástechnikai berendezései I. (Turbomachinery and Heat Engines in Vehicles I.)*, Budapest: Typotex Kiadó, URL: https://www.tankonyvtar.hu/hu/tartalom/tamop412A/0018_Jarmuvek_ho-es_aramlastechnikai_berendezesei_1/adatok.html [Accessed: 02.10.2019.], 2014.
- [9] [Online]. Available: http://www.leteckemotory.cz/motory/r-29b/r-29b-300_rez.jpg and <http://www.leteckemotory.cz/motory/f100/>. [Accessed 02. 10. 2019.].
- [10] Koff, B., “Spanning the Globe with Jet Propulsion,” *American Institute of Aeronautics & Astronautics*, no. <https://doi.org/10.2514/6.1991-2987>, 2012.
- [11] Rolls-Royce, “Civil Aerospace, Future product, UltraFan,” Rolls-Royce, [Online]. Available: <https://www.rolls-royce.com/products-and-services/civil-aerospace/future-products.aspx#section-overview>. [Accessed 31 12 2020].
- [12] Han, P., “Additive Design and Manufacturing of Jet Engine Parts,” *Engineering*, vol. 3, no. 5, pp. 648-652, 2017.
- [13] Homaifar, A., Lai, Y. H., McCormick, E., “System Optimization of Turbofan Engines Using Genetic Algorithms,” *Applied Mathematical Modelling*, vol. 18, no. 2, pp. 72-83, 1994.
- [14] Guha, A., “Optimum Fan Pressure Ratio for Bypass Engines with Separate or Mixed Exhaust Streams,” *Journal of Propulsion and Power*, vol. 17, no. 5, pp. 1117-1122, 2001.

- [15] Silva, V.V.R., Khatib, W., Fleming, P.J., "Performance Optimization of Gas Turbine Engine," *Engineering Applications of Artificial Intelligence*, vol. 18, no. 5, pp. 575-583, 2005.
- [16] Al-Hamdan, Q., Ebaid, M., "Modeling and Simulation of a Gas Turbine Engine for Power Generation," *Journal of Engineering for Gas Turbine and Power*, vol. 128, no. 2, 2006.
- [17] Henriksson, M., Grönstedt, T., Breitholtz, C., "Model-Based on-Board Turbofan Thrust Estimation," *Journal of Control Engineering Practice*, vol. 19, no. 6, pp. 602-610, 2011.
- [18] Turan, O., "Exergetic Effects of Some Design Parameters on the Small Turbojet Engine for Unmanned Air Vehicle Applications," *Energy*, vol. 46, no. 1, pp. 51-61, 2012.
- [19] Khaliq, A., Kaushik, S.C., "Thermodynamic Performance Evaluation of Combustion Gas Turbine Cogeneration System with Reheat," *Applied Thermal Engineering*, vol. 24, no. 13, pp. 1785-1795, 2004.
- [20] Sanjay, "Investigation of Effect of Variation of Cycle Parameters on Thermodynamic Performance of Gas-Steam Combined Cycle," *Energy*, vol. 36, no. 1, pp. 157-167, 2010.
- [21] Atashkari, K., Nariman-Zadeh, N., Pilechi, A., Jamali, A., Yao, X., "Thermodynamic Pareto Optimization of Turbojet Engines Using Multi-Objective Genetic Algorithms," *International Journal of Thermal Science*, vol. 44, no. 11, pp. 1061-1071, 2005.
- [22] Lazzaretto, A., Toffolo, A., "Analytical and Neural Network Models for Gas Turbine Design and Off-Design Simulation," *International Journal of Thermodynamics*, vol. 4, pp. 173-182, 2001.
- [23] Mattingly, J. D., *Elements of Propulsion: Gas Turbines and Rockets*, 1801 Alexander Bell Drive, Reston, Virginia 20191-4344: American Institute of Aeronautics and Astronautics, Inc., 2006.
- [24] El-Sayed, A. F., *Aircraft Propulsion and Gas Turbine Engines*, United States of America: Taylor & Francis Group, LLC, ISBN 9781466595163, 2008.
- [25] Sánta, I., *Repülőgép Hajtóművek Elmélete I. (Theory of Aircraft Engines I.) (Gázturbinás Hajtóművek (Engines with Gas Turbines))*, Budapest: BME, Department of Aeronautics, Naval Architecture and Railway Vehicles, lecture note, 2008.
- [26] Kurzke, J., "The GasTurb Program - Commercial Computer Program, GasTurb12," [Online]. Available: <http://www.gasturb.de>. [Accessed 03 03 2016].
- [27] Kuznetsov, "Wikipedia," Kuznetsov Design Bureau, [Online]. Available: https://en.wikipedia.org/wiki/Kuznetsov_NK-32. [Accessed 17. 11. 2019.].
- [28] Kuznetsov, "Wikipedia," Kuznetsov Design Bureau, [Online]. Available: https://en.wikipedia.org/wiki/Kuznetsov_NK-25. [Accessed 17. 11. 2019.].
- [29] Russian Aviation, "Russian Aviation (News)," Kuznetsov, [Online]. Available: <https://www.ruaviation.com/news/2016/8/15/6454/?h>. [Accessed 17. 11. 2019.].
- [30] I. 2. International Organization for Standardization, "International Standard Atmosphere," Wikipedia, 1975. [Online]. Available: https://en.wikipedia.org/wiki/International_Standard_Atmosphere. [Accessed 02 02 2020].
- [31] Beneda, K., "Development of Active Surge Control Devices for Centrifugal Compressors, PhD Thesis," BME, Department of Aeronautics, Naval Architecture and Railway Vehicles, Budapest, 2013.

- [32] MathWorks, “MATLAB, Constrained Nonlinear Optimization Algorithms,” MathWorks, Inc., [Online]. Available: <https://uk.mathworks.com/help/optim/ug/constrained-nonlinear-optimization-algorithms.html#brnox0o>. [Accessed 28 12 2020].
- [33] Mathworks, “Matlab R2017b Documentation (Optimization Toolbox; "fmincon" function),” 2017. [Online]. Available: <https://uk.mathworks.com/help/optim/ug/fmincon.html>. [Accessed 30 09 2017].
- [34] Chu, H. H., Hsiao-Wei, C., “Aerospace Technology Development – Small Gas-Turbine development,” *ROC: Aerospace Development Planning*, pp. 4-22, 1996.
- [35] Beneda, K., “Dynamic Nonlinear Mathematical Model of Active Compressor Surge Control Devices,” in *Proceedings of the 11th Mini Conference on Vehicle System Dynamics, Identification and Anomalies (VSDIA)*, Budapest, 2008.
- [36] Hargitai, C., “Effect of Parameters of Inland Vessel Semi Empirical Motion Equations on Transient Motion Phenomena,” in *Proceedings of the TVL: Second Scientific Workshop on Transport, Vehicle and Logistics organized by the PhD Schools of the Faculty of transportation engineering and vehicle engineering*, Budapest, 2012.
- [37] “The bridges of Budapest,” [Online]. Available: http://www.bridgesofbudapest.com/bridge/chain_bridge. [Accessed 24 06 2017].
- [38] “Airbus A380,” Wikipedia, [Online]. Available: https://en.wikipedia.org/wiki/Airbus_A380. [Accessed 24 06 2017].
- [39] [Online]. Available: https://en.wikipedia.org/wiki/General_Electric_GE90. [Accessed 24. 06. 2017.].
- [40] Mercedes-Benz, “Mercedes-Benz Actros,” Mercedes-Benz, [Online]. Available: <http://media.daimler.com/marsMediaSite/en/instance/ko/Mercedes-Benz-Actros.xhtml?oid=9904742>. [Accessed 24. 06. 2017.].
- [41] [Online]. Available: <http://behindthewheel.com.au/next-gen-mercedes-benz-actros-launched-australia/2017-mercedes-benz-actros>. [Accessed 24. 06. 2017.].
- [42] [Online]. Available: <https://en.wikipedia.org/wiki/IPhones>. [Accessed 24. 06. 2017.].
- [43] “Re/872. Az 55 típusú hajtómű műszaki üzembentartási szakutasítás 2. könyv. (Operational and maintenance manual of engine Type 55, second book),” Honvédelmi Minisztérium (Ministry of National Defense), 1980.
- [44] Beneda, K., “CFD Simulation of Blade Load Distribution Control as Active Centrifugal Compressor Surge Suppression,” *ACTA AVIONICA*, vol. 15, no. 25, pp. 13-20, 2013.
- [45] Beneda, K., “Numerical Simulation of MEMS-based Blade Load Distribution Control in Centrifugal Compressor Surge Suppression,” in *ICNPAA 2012 Congress: Mathematical Problems in Engineering, Aerospace and Sciences*, Vienna, Austria, 2012.
- [46] Nagy, A., Rohács, J., Régert, T., “Investigation on the Effect of Hydrodynamic MEMS on Airfoil,” in *26th International Congress of the Aeronautical Sciences (ICAS)*, Optimage Ltd., Anchorage, USA, 2008.
- [47] swMATH, “ANSYS-CFX,” swMATH - an Information Service for Mathematical Software, [Online]. Available: <http://swmath.org/software/6391>. [Accessed 30. 12. 2020.].

- [48] ANSYS, *ANSYS CFX-Solver Theory Guide, Release 14.5*, Southpointe, 275 Technology Drive, Canonsburg, PA 15317, 2012.
- [49] Robert Bosch GmbH, *Automotive Handbook*, John Wiley & Sons, 2018.
- [50] ANSYS Inc., “CFX Inlet Turbulence Conditions,” Introduction to ANSYS CFX, Lecture 07 - Turbulence, CFX-Intro_14.0_L07_Turbulence .pdf , 2013.
- [51] Khayamyan, S., *Flow Field in a Gas Turbine Burner*, MSc Thesis, Lulea, Sweden: Lulea University of Technology, <http://www.diva-portal.org/smash/get/diva2:1017888/FULLTEXT01.pdf>, 2010 [Accessed: 23.10.2019].
- [52] Thévenin, D. Janiga, G., *Optimization and Computational Fluid Dynamics*, Hardcover, Berlin: Springer, 2008.
- [53] Weise, T., *Global Optimization Algorithms - Theory and Application*, ebook: <http://www.it-weise.de/>, 2011.
- [54] Veress, Á., Felföldi, A., Gausz, T., Palkovics, L., “Coupled Problem of the Inverse Design and Constraint Optimization,” *Applied Mathematics and Computation*, vol. 219 , no. 13, pp. 7115-7126, 2013.
- [55] Lighthill, M.J., “A new Method of Two-dimensional Aerodynamic Design,” in *Aeronautical Research Council*, London,, 1945.
- [56] Giles, M. B., Drela, M., “Two-Dimensional Transonic Aerodynamic Design Method,” *Journal of AIAA*, vol. 25, no. 9, pp. 1199-1206, 1987.
- [57] Demeulenaere, A., “An Euler/Navier-Stokes Inverse Method for Compressor and Turbine Blade Design,” Von Kármán Institute for Fluid Dynamics, *Inverse Design and Optimisation Methods*, 1997.
- [58] De Vito, L., Van den Braembussche, R. A. , Deconinck, H., “A Novel Two-dimensional Viscous Inverse Design Method for Turbomachinery Blading,” in *International Gas Turbine and Aeroengine Congress and Exhibition*, Amsterdam, PAYS-BAS, 03/06/2002.
- [59] Cabuk, H., Modi, V., “Optimum Plane Diffusers In Laminar Flow,” *Journal of Fluid Mechanics*, vol. 237, pp. 373-393, 1992.
- [60] Japikse, D., *Centrifugal Compressor Design and Performance*, Wilder, Vermont: Concepts ETI, Inc. Printed in the United States of America by Thomson-Shore, Inc., 1996.
- [61] Andronenko, S., Stiharu, I., Packirisamy, M., Moustapha, H. Dionne, P., “The Use of Microelectromechanical Systems for Surge Detection in Gas Turbine Engines,” in *Proceedings of the 2005 International Conference on MEMS, NANO and Smart Systems (ICMENS'05)*, 2005.
- [62] Шустов, И. Г., *Двигатели 1944-2000: авиационные, ракетные, морские, промышленные. Иллюстрированный каталог авиадвигателей с их характеристиками, описанием, АКС-Конверсалт*, 2000.
- [63] Ailer, P., “Kisteljesítményű gázturbina modellezése és nemlineáris irányítása, PhD értekezés (Modelling and Nonlinear Control of a Low-Power Gas Turbine, PhD thesis),” BME Repülőgépek és Hajók Tanszék (BME Department of Aircraft and Ships), Budapest, 2002.
- [64] Al-Hamdan, Q. Z., Ebaid, M. S. Y., “Modeling and Simulation of a Gas Turbine Engine for Power Generation,” *ASME Journal of Engineering for Gas Turbines and Power*, vol. 128, no. 2, pp. 302-311, April 2006.

- [65] Bartolini, G., Muntoni, A., Pisano, A., and Usai, E., “Compressor Surge Active Control via Throttle and CCV Actuators. A Second-Order Sliding-Mode Approach,” in *International Workshop on Variable Structure Systems*, Antalya, Turkey, 2008.
- [66] Schleer, M. W., “Flow Structure and Stability of a Turbocharger Centrifugal Compressor,” PhD Dissertation, Eidgenössischen Technische Hochschule, Zürich, 2006.
- [67] Yoon, S. Y., Lin, Z., Goynes, C., Allaire, P. E., “An Enhanced Greitzer Compressor Model Including Pipeline Dynamics and Surge,” *ASME Journal of Vibration and Acoustics*, vol. 133, no. 5, October 2011.
- [68] Boinov, K. O., Lomonova, E. A., Vandenput, A. J. A., Tyagunov, A., “Surge Control of the Electrically Driven Centrifugal Compressor,” vol. 42, no. 6, pp. 1523-1531, 2006.
- [69] Ferrari, M. L., Pascenti, M., Magistri, L., Massardo, A. F., “Hybrid System Test Rig: Start-up and Shutdown Physical Emulation,” *ASME Journal of Fuel Cell Science and Technology*, vol. 7, no. 2: 021005, 2010.
- [70] Veress, Á., “Axial Compressors (Aircraft Engines II., lecture note at BME University),” Budapest University of Technology and Economics (BME), Department of Aeronautics, Naval Architecture and Railway Vehicles, Budapest, 2018.
- [71] Boyce, M. P., “Principles of Operation and Performance Estimation of Centrifugal Compressors,” *Proceedings of the 22nd Turbomachinery Symposium*, pp. 161-177, 1993.
- [72] “Turbine Engines of the World. In: Flight International Weekly,” 10 January 1974. [Online]. Available: <http://www.flightglobal.com/pdfarchive/view/1974/1974%20-%2000043.html>. [Accessed 15 02 2013].
- [73] Ballal, D. R., Zelina, J., “Progress in Aero Engine Technology (1939 – 2003),” [Online]. Available: http://soliton.ae.gatech.edu/people/jseitzma/classes/ae4451/AeroEngineTechnology1939_2003AE4451.pdf. [Accessed 15 03 2013].
- [74] [Online]. Available: Sources: https://www.reddit.com/r/ThingsCutInHalfPorn/comments/et58le/lycoming_alf_502/ and <http://www.seattleturbine.com/index2.shtml>, both are accessed on 13.09.2020.
- [75] Bauer, P., Bokor, J., “Infinite Horizon LQ Optimal Output Tracking – From Development to Real Flight Tests,” in *In Proc. of 12th IEEE International Symposium on Computational Intelligence and Informatics*, Budapest, November 2, 2011.
- [76] Gáti, B., “Unmanned Aerial Systems for Educational Purpose,” in *13th Mini Conference on Vehicle System Dynamics, Identification and Anomalies*, Budapest, 2012.
- [77] Szabolcsi, R., “UAV automatikus repülésszabályozó rendszer számítógépes tervezése (Computational Design of UAV's Automatic Flight Control System),” *Hadmérnök (Military Engineer)*, vol. 1, pp. 222-237, March 2012.
- [78] Koncz, M. T., “Automatikus irányítású célrepülőgépek pályatervezése (Flight Path Design of Targeted Aircraft with Automatic Control),” in *Új évezred, új technológia – Gripenek a magyar légierőben, Szolnoki Repüléstudományi Konferencia (Grippens are in the Hungarian Air Force, Conference on Aeronautical Sciences in Szolnok)*, Szolnok, 2006.
- [79] Helvoirt, van, J., “Centrifugal compressor surge: modeling and identification for control, PhD Thesis, <https://doi.org/10.6100/IR629084>,” Technische Universiteit Eindhoven, 2007.

- [80] Eckert, B., Schnell, E., Axial- und Radialkompressoren: Anwendung, Theorie, Berechnung, Berlin: Springer, 1980.
- [81] Csató, J., “Előperdítés hatása turbófeltöltő centrifugálkompresszorának karakterisztikájára (Effect of prerotation on the characteristics of centrifugal compressor in turbocharger),” BME Közlekedésmérnöki Kar (Budapest University of Technology and Economics, Faculty of Transportation Engineering), Budapest, 1994.
- [82] Veress, Á., “Centrifugal Compressors (Aircraft Engines II., lecture note at BME University),” Budapest University of Technology and Economics (BME), Department of Aeronautics, Naval Architecture and Railway Vehicles, Budapest, 2013.
- [83] Osborne, C., Runstadler, P. W., Dodd Stacy, W., “Aerodynamic and Mechanical Design of an 8:1 Pressure Ratio Centrifugal Compressor,” NASA Lewis Research Center, Cleveland, 1975.
- [84] Rolls-Royce, The Jet Engine, Hoboken, United States: John Wiley and Sons Ltd., 2015.
- [85] ANSYS, “ANSYS CFX-Solver Modeling Guide, Release 14.5,” ANSYS, Inc., Southpointe 275 Technology Drive Canonsburg, PA 15317, ansysinfo@ansys.com, <http://www.ansys.com>, October 2012.
- [86] Lentini, J. J., Scientific Protocols for Fire Investigation, New York: CRC Press, Taylor and Francis Group, 2013.
- [87] Montgomery, J. H., Crompton, T. R., Environmental Chemicals Desk Reference, New York: CRC Press, Taylor and Francis Group, 2017.
- [88] Chen, L., Gao, K., Zhang, C., Lang, W., “Advanced Biofuels: Chapter 2 - Alternative Fuels for IC Engines and Jet Engines and Comparison of Their Gaseous and Particulate Matter Emissions,” Woodhead Publishing Series in Energy, 2019.
- [89] Cyrus, B. M. H., “The Historical Evolution of Turbomachinery,” in *Proceeding of the 29 Turbomachinery Symposium, Mee Industries Inc.*, Monrovia, california, 2000.
- [90] Masanori, Y., Junichiro, M., Keizo, T., Eisaku, I., Satoshi, H., “Development of 1600°C - Class High-Efficiency Gas Turbine for Power Generation Applying J-Type Technology,” *Mitsubishi Heavy Industries Technical Review*, vol. 50, no. 3, 2013.
- [91] Nageswara, R. M., Advances in Gas Turbine Technology, Materials for gas turbines - An Overview, India: VIT University, 2011.
- [92] Gorla, R. S. R., Khan, A., A., Turbomachinery - Design and Theory, Karachi, Pakistan: Marcel Dekker, 2003.
- [93] Tournier, J. Michel. El-Genk, S. Mohamed., “Axial flow, multi-stage turbine and compressor models,” *Energy Conversion and Management*, no. 51, pp. 16-29, 29 September 2009.
- [94] Da Lio, L., Manente, G., Lazzaretto, A., “New efficiency charts for the optimum design of axial flow turbines,” *Energy*, no. 77, pp. 447-459, 2014.
- [95] Moustapha, H., Zelesky, M.F., Baines, N.C., Japikse, D., Axial and Radial Turbines, 3rd ed., Concepts ETI, Inc., 2003.
- [96] Beneda, K., Repülőgép-hajtóművek elmélete 2. (Theory of Aircraft Engines II.), Budapest: Akadémiai Kiadó, 2018.

- [97] Sánta, I., “Repülőgép Hajtóművek Tervezése - Axiális Kompresszorok Aero- Termodinamikai Számítása (Design of Aircraft Engines - Aero- and Thermodynamic Calculations of Axial Compressors),” Budapest University of Technology and Economics, Department of Aeronautics Naval Architecture and Railway Vehicles, Budapest, 2009.
- [98] Menter, F. R., “Two-Equation Eddy-Viscosity Turbulence Models for Engineering Applications,” *AIAA Journal*, vol. 32, no. 8, p. 1598–1605, 1994.
- [99] “SST k-omega model,” CFD Online, 28 02 2011. [Online]. Available: http://www.cfd-online.com/Wiki/SST_k-omega_model. [Accessed 11 10 2019].
- [100] Menter, F. R., “Zonal Two Equation k- ω Turbulence Models for Aerodynamic Flows,” *AIAA Paper*, Vols. 93-2906, 1993.
- [101] Stiesch, G., Modeling Engine Spray and Combustion Processes, Berlin Heidelberg: Springer-Verlag, ISBN 978-3-642-05629-1, 2003.
- [102] Herrmann, M., “Modeling Primary Breakup: A Three-Dimensional Eulerian Level Set/Vortex Sheet Method for Two-Phase Interface Dynamics,” *Center for Turbulence Research, Annual Research Briefs*, pp. 185-196, 2003.
- [103] Edwards, J. T., “Reference Jet Fuels for Combustion Testing,” in *55th AIAA Aerospace Sciences Meeting, Session: Alternate Aviation Fuels I*, Grapevine, Texas, 2017.
- [104] Bacchi, R., D., A. , “Best Practice Guidelines for Combustion Modeling (ANSYS),” [Online]. Available: http://www.esss.com.br/events/ansys2013/brazil/pdf/24_5_1450.pdf. [Accessed 23 10 2019].
- [105] Marchello, M., “A Three Dimensional High Resolution Compressible Flow Solver,” PhD thesis, Catholic University of Leuven, 1992.
- [106] Roe, P.L., “Approximate Riemann Solvers, Parameter Vectors, and Difference Schemes,” *Journal of Computational Physics*, vol. 43, pp. 357-372, 1981.
- [107] Yee, H.C., “A class of high-resolution explicit and implicit shock-capturing methods,” NASA TM-101088, 1989.
- [108] Hirsch, C., Numerical Computation of Internal and External Flows, vol. II, John Wiley & Sons, 1990.
- [109] Lefebvre, M., Antwerp, T.S., “Arts Numerical Aero-thermal Prediction of Laminar/Turbulent Flows in a Two-dimensional High Pressure Turbine Linear Cascade,” in *Second European Conference on Turbomachinery - Fluid Dynamics and Thermodynamic*, Belgium, 1997.
- [110] Laney, C. B., Computational Gas dynamics, Cambridge University Press, ISBN-13: 978-0521625586, 1998.
- [111] Stein, E., Borst, R. Hughes, T, Finite volume methods, foundation and analysis, L. c. Edited by John Wiley & Sons, Ed., 2004.
- [112] Kuzmin, D., Möller, M. , “Algebraic Flux Correction II. Compressible Euler Equations,” *Springer*, pp. 207-250, 1990.
- [113] Smith, A. M. O., “High-Lift Aerodynamics,” *Journal of Aircraft*, vol. 12, no. 6, pp. 501-530, 1975.
- [114] Stratford, B. S., “The Prediction of Separation of the Turbulent Boundary Layer,” *Journal of Fluid Mechanics*, vol. 5, pp. 1-16, 1959.

- [115] Molnár, D., “Investigation of Inverse Design Utilization for Static Pressurize of a Cascade,” Budapest university of technology and economics, Budapest, 2016.
- [116] Ochkov, V. F. , “Теплотехника и теплоэнергетика,” National Research University Moscow Power Engineering Institute (Technical University), Dept. Theoretical basics of thermal engineering, 27 06 2016. [Online]. Available: <http://tw.t.mpei.ac.ru/TTHB/2/KiSyShe/eng/Chapter1/1-6-Concept-of-heat-capacity.html>. [Accessed 01 02 2020].

Author’s Publications

- [117] Zare, F., Veress, Á., “Novel Closed-Form Equation for Critical Pressure and Optimum Pressure Ratio for Turbojet Engines,” *International Journal of Turbo & Jet-Engines*, *IF: 0.733, Q3, (2019/2020)*, accepted for publication, <https://www.degruyter.com/view/j/tjj.ahead-of-print/tjj-2019-0039/tjj-2019-0039.xml>, published online: 2019-11-30, DOI: <https://doi.org/10.1515/tjj-2019-0039>, 2019.
- [118] Zare, F., Veress, Á., “Derivation and Application of a New Equation for Design and Analysis of Triple Spool Mixed Turbofan Jet Engines with Verification,” *Acta Polytechnica Hungarica*, *IF: 0.745, Q2 (2016)*, vol. 13, No. 6, 2016 pp. 147-162, http://www.uni-obuda.hu/journal/Zare_Veress_70.pdf, 2016.
- [119] Zare, F., Veress, Á., “Preliminary Introduction to Virtual Prototyping of Jet Engine Components by Means of Aerodynamic Design,” *Repüléstudományi Közlemények, on-line tudományos folyóirat (Aeronautical Science Bulletins - online scientific journal)*, number: XXIX. vol.: 2017/3., pp. 141-148, 2017.
- [120] Zare, F., Veress, Á., “Plausibility Check of the Inverse Design and Optimization Method for Cascade Flow by Means of ANSYS CFX Software,” *Repüléstudományi Közlemények, on-line tudományos folyóirat (Aeronautical Science Bulletins - online scientific journal)*, number: XXVII., vol.: 2015/2., HU ISSN 1789-770X, pp. 182-206. 2015.
- [121] Zare, F., Veress, Á., “Development and Verification of an Improved Thermo-Dynamical Model for Single Spool Jet Engines,” *Repüléstudományi Közlemények, on-line tudományos folyóirat (Aeronautical Science Bulletins - online scientific journal)*, number: XXVI. vol.: 2014/2., pp. 539-551. 2014
- [122] Zare, F., Veress, Á., “Aerodynamic Redesign and Analysis of Gas Turbine Components - Virtual prototyping of Jet engine,” *XIX. Magyar Repüléstudományi Napok 2017. (XIX. Hungarian Days of Aeronautical Sciences 2017.) 15-16. November 2017. HungaroControl (Hungarian Air Navigation Services Pte. Ltd. Co. 1185. Budapest Igló u. 33-35.) Repüléstudományi Közlemények, on-line tudományos folyóirat (Aeronautical Science Bulletins - online scientific journal)*, number: XXIX., vol.: 2017/2., pp. 309-330. 2017.
- [123] Zare, F., Veress, Á., “Novel Application of Inverse Design Method by Means of Redesigning Compressor Stator Vanes in a Research Jet Engine,” *in the Proceedings of 15th mini Conference on Vehicle System Dynamics, Identification and Anomalies*, Budapest, 7-9. November 2016, ISBN 978-963-313-266-1, pp. 261-280. 2016.

- [124] Zare, F., Veress, Á., “Numerical Modelling and Simulation of a Centrifugal Compressor Passage with Plausibility Check,” *14th mini Conference on Vehicle System Dynamics, Identification and Anomalies*, Budapest, November. 10-12, 2014, Conference Proceedings, ISBN 978-963-313-186-2, pp. 367-378. 2014.
- [125] Zare, F., Veress, Á., “Mathematical Model Development and Thermo-dynamical Cycle Analyses of a Dual Spool no By-pass and a Dual Spool Mixed Turbofan Engine,” *International Conference on Innovative Technologies, IN-TECH 2013*, Budapest, 10. - 12. 09. 2013, ISBN 978-953-6326-88-4, pp. 41-44, 2013.
- [126] Zare, F., Veress, Á., Beneda, K., “Simplified Mathematical Model for a Single Spool and no Bypass Jet Engines,” *Repüléstudományi Konferencia (Conference on Aeronautical Sciences) 11.04.2013.*, Szolnok, Hungary, *Repüléstudományi Közlemények (Aeronautical Science Bulletins - online scientific journal)*, number: XXV., vol.: 2013/2 (special issue), HU ISSN 1789-770X, pp. 39-52, 2013.
- [127] Bicsák, Gy., Zare, F., Veress, Á., “Gázturbina égésfolyamatának vizsgálata különböző égésmodellekkel (Analysing of Combustion Processes in Gas Turbine with Using Different Combustion Models),” *Jövő Járműve folyóirat (Journal of Future Vehicles)*, HU ISSN 1788-2699, vol.: 2012-3/4, pp. 46-51, 2012.
- [128] Bicsák, Gy., Zare, F., Veress, Á., “Numerical Modelling of Heat Transfer Processes in the Solar Taurus T60 Gas Turbine Combustion Chamber,” *VSDIA 2012 Conference (13th MINI Conference on Vehicle System Dynamics, Identification and Anomalies)*, Budapest, November 5-7, 2012, Conference Proceedings, ISBN 978-963-313-102-2, pp. 555-574. 2012.

APPENDIX A – Aerodynamic Redesign of the Academic Jet Engine’s Components

A.1 Compressor Design and Analysis

The design process of the academic jet engine is started with calculating the dimensions of the compressor because the geometry of the inlet diffuser and the combustion chamber can be determined after knowing the inlet and outlet sizes of the compressor unit.

Centrifugal compressor is selected for increasing the total pressure of the air in the present case due to its favourable characteristics described below at the expected compressor total pressure ratio 2.5 and mass flow rate 1 kg/s.

Introduction and main application of centrifugal compressors [31]

Turbo machines are designed and applied to transfer and convert energy between working fluid and structural parts such as blades and shafts. There are two main types, turbines and compressors [31]. Dynamic compressors operate according to the principle of Euler turbine equation and they form subspecies of the above-mentioned machines are used to provide high pressure working medium for various systems. Gas turbines are the most prevalent and important application of dynamic compressors that are for vehicle propulsion [61], [62], power generation in transportation as well as in ground application [63], [64] and turbochargers in reciprocating engines [65], [66]. The centrifugal compressors are found in other segment of the industry like compressor stations in natural gas transportation [67] or in applications, which require moderate amount of mass flow rate pushing through that against relatively high discharge pressure. The one of the most promising application of the centrifugal compressors is in fuel cell power systems for electric drive [68], [69].

Beside the centrifugal one, the dynamic compressors are categorised to be axial one, meanwhile the third variant is called mixed flow compressor, which is less frequent.

The axial arrangement results in relatively high mass flow rates; however, it causes to supply lower pressure ratio in one stage, because the inlet and outlet blade speeds, u_1 and u_2 , are the same in general, if they are at the same radius. However, to prevent flow separation in the device, the difference between tangential components of absolute velocities must also be kept at moderate levels. Typical pressure ratio range for axial compressor stages is 1.2...1.3 [31]. However, this value can be enhanced up to 2.2 with up-to-date technologies, using supersonic flow, when oblique shock wave contributes to compression [70]. Since axial compressors are sensitive to manufacturing tolerances and clearances, the number of stages must be increased in order to get the required output pressure, which lead to high number of components, unit complexity as well as rising costs. A typical axial flow compressor is shown on the left side of Fig. A.1.



Figure A.1 Axial (left) and centrifugal (right) compressor designs [31]

The efficiency of the unit is adversely affected as the quantity of working medium, which must be handled by the device, decreases (practical limit lies between 10-20 kg/s mass flow rate based on the overall pressure ratio [71]), and the relative clearances start to rise [31]. The noticeable amount of working medium bypassing from the compressor discharge back to the inlet through the gap between the rotor blade tip and casing after having received substantial work input accounts for the drop of efficiency, which is a main factor for economical operation of a unit [31]. As a result, it is natural to find centrifugal flow compressor (see the right side in Fig. A.1) in the place of axial devices in low mass flow rate applications. One can find another advantage in applying higher pressure ratio as it has capability for it. This in turn will lead to the smaller number of stages in order to achieve a specified output. As far as aviation industry applications are concerned, the moderate weight of the unit, which is resulted by the decreasing number of components causes improved system reliability and robustness, which is considered to be an important feature. Furthermore, the peripheral speed, as opposed to the axial devices, change dramatically from the inlet of the unit to its discharge cross section, which makes it possible for the product to be higher. By using transonic flow, the typical pressure ratio of a conventional centrifugal compressor, which normally stands at about 3...5, can be increased to 8...10 [31]. On the contrary, it is worth mentioning that the increasing mass flow rate leads to the growth of the frontal area because of excessive diffuser diameters which causes the centrifugal compressor to be impractical to the aerospace applications at higher nominal deliveries [31]. Moreover, the flow turning from axial to radial and finally back to axial one at high speed flow increases the losses significantly.

The thermal efficiency of a work production energetic system, which is defined by differences in heat added and removed (the energy converted into technical work) divided by the heat added is considered as one of the most important parameters in thermodynamics. Thermal efficiency in general and substituted for the idealized Brayton cycle is shown in Eq. (A.1) [31] and in Fig. A.2. Because of monotonic nature of the exponent function, the thermal efficiency will increase if the pressure ratio increases [31]. The intensity of this monotonic behaviour reduces when the pressure ratio increases at high pressure ratio range, especially over pressure ratio 10, 20 [31]. This, in fact explains the reason of small, simple compressor designs with pressure ratios of about 2 to 10, medium complexity units at about 20, and cutting-edge technology with pressure ratio over 40 and this explains the need for centrifugal compressor in the present case also.

$$\eta_{th,id} = \frac{Q_{in} - |Q_{out}|}{Q_{in}} = 1 - \frac{|Q_{out}|}{Q_{in}} = 1 - \frac{C_p(T_4 - T_1)}{C_p(T_3 - T_2)} = 1 - \frac{1}{\pi_c^{\frac{\gamma-1}{\gamma}}} \quad (A.1)$$

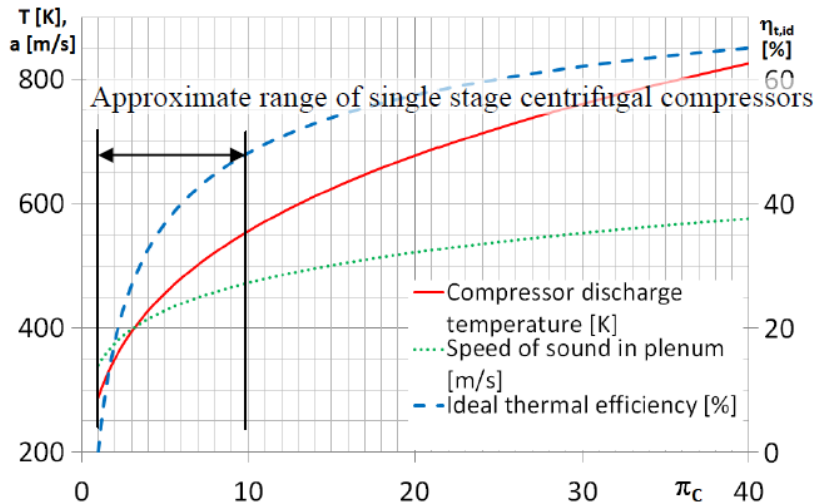


Figure A.2 Thermal efficiency of the ideal Brayton cycle versus pressure ratio ($\gamma = 1.4$) [31]

The tendency of total pressure ratio rise of the newer gas turbines are in line with the previous explanation about the thermal efficiency in ideal case: higher pressure ratio gives higher thermal efficiency as it is shown in Fig. A.2. This results higher total pressure ratio as function of year of introduction for different engines (see Fig. A.3). Although most of these engines have high mass flow rate belongs to the range over 100 kg/s, there are some of them are falling into the medium mass flow rate class [31]. The Lycoming ALF 502 bypass engine which is utilized on BAe 146 (currently called as Avro RJ85/100), a medium sized commercial airliner, can be described as a typical representative of this medium size class [31]. In that design and many other similar engines, the comparably small mass flow rate in the core engine (roughly 15-20 kg/s) and the high overall pressure ratio (over 13:1) would lead to a very short and thus inefficient blades in the last compressor stages (information from [72]) [31]. Replacing the last axial stages with one centrifugal stage to prevent the low volumetric efficiency generated by relatively high clearances seems to be a good solution. This is an important possibility for the utilization of centrifugal compressors in modern gas turbine engines. Fig. A.4 illustrates a

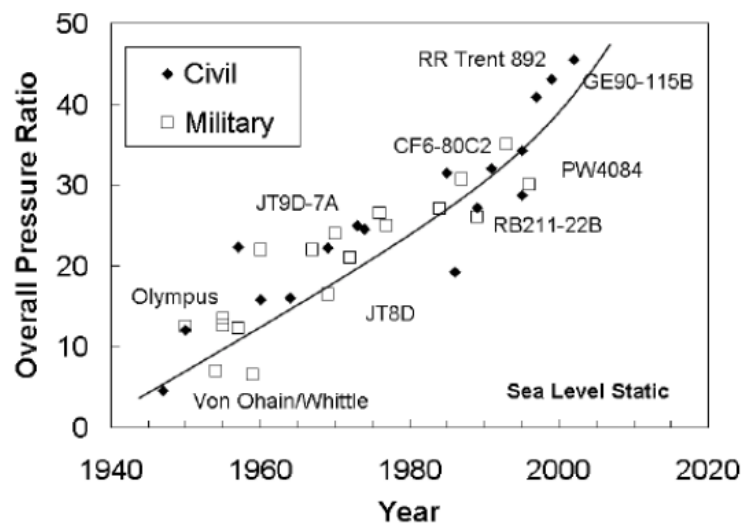


Figure A.3 Change of overall pressure ratio of various gas turbine engines [73]

section view of the gas turbine along with two comparable designs using centrifugal compressors. The number of stages of axial compressor can be reduced further at lower mass flow rates. Axial compressor with 2-3 sta-

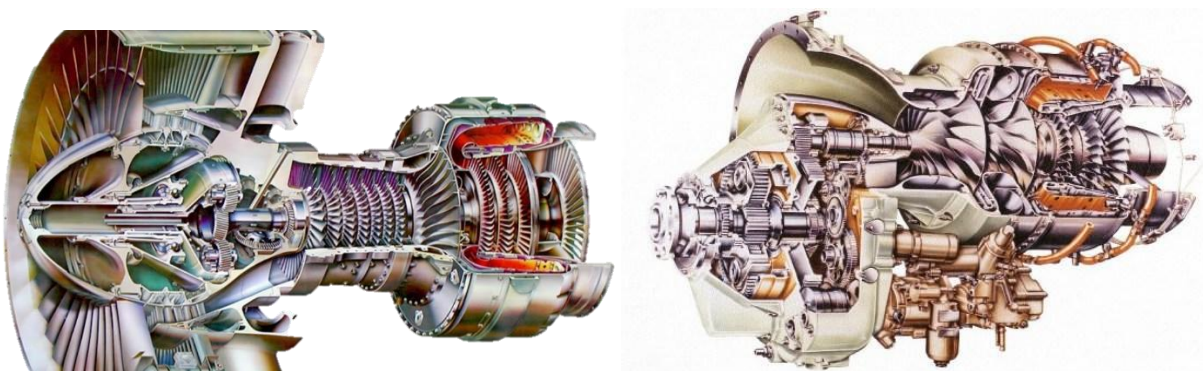


Figure A.4 Section views of ALF 502 high bypass ratio turbofan engine and TPE331 turboprop including centrifugal compressors [74]

ges are used in the lower range of medium sized airlines (e.g. Bombardier Dash 8 Q400), in which the nominal mass flow rate of the gas turbine is about 10 kg/s [31]. The other solution – instead of applying 2-3 stages axial compressor – is using double stage centrifugal compressor (see TPE331 engine in Fig. A.4).

A single stage centrifugal compressor, which uses transonic inlet flow regime in most of the cases can be found in mini or micro gas turbines, such as auxiliary power units (APU's) and engines of unmanned aerial vehicles (UAV's).

The one of the most actual application fields of the centrifugal compressor is in the engine of UAVs, for which a flexible platform is under development to be able to fulfil both civil and military purposes. Noticeable results have been obtained regarding the optimal tracking of the vehicle [75], application for educational purpose [76] or utilization in the field of military intelligence services [77] and target drone for practice-firing [78]. Although these applications may not be in a tight relationship with the main issue of the current subchapter, it has been emphasized because they are often equipped with turbojet engines in which, due to their performance needs, just centrifugal compressors are affordable [31].

Operation principle of centrifugal compressors [31]

Both axial and centrifugal compressor types work on the same basic principle; one stage of a compressor is composed of a rotor and a stator. The compression process takes place as fluid momentum change in the rotor followed by diffusion in the stator to convert kinetic energy into static pressure [79]. The designation stator in the case of centrifugal compressors can stand for a vaneless or a vanned diffuser and a volute. The section view of a centrifugal compressor is depicted in Fig. A.5.

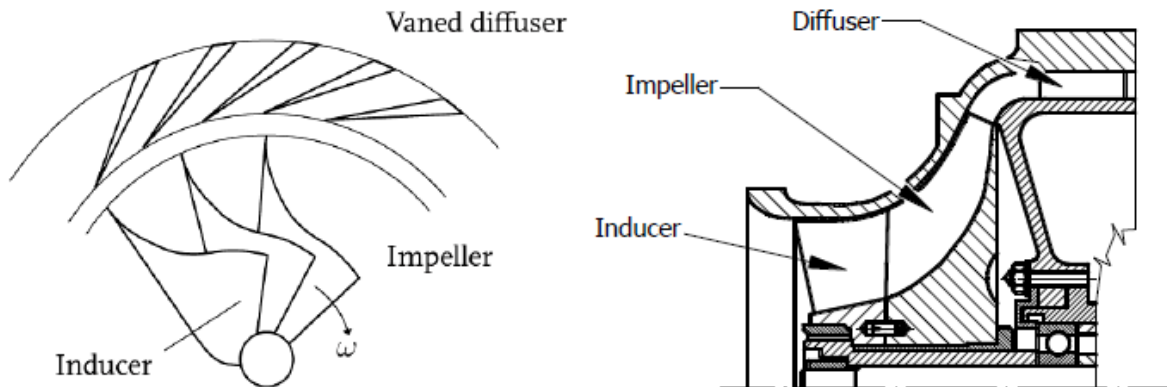


Figure A.5 Front view [79] and a meridional section [31] of centrifugal compressor

The energy transfer, which is done by the impeller, can be demonstrated by the Euler's turbine equation that can be derived from the impulse moment equation:

$$M = \dot{m} (r_2 c_{2u} - r_1 c_{1u}) \quad (A.2)$$

This equation can be used to calculate the power related to the operation of a turbo machine. As the power is simply the product of moment and angular velocity, the equation yields:

$$P = M\omega = \dot{m}(r_2c_{2u} - r_1c_{1u})\omega = \dot{m}(u_2c_{2u} - u_1c_{1u}) \quad (\text{A.3})$$

Based on Eq. (A.3) it is obvious that the velocities play an essential role in the operation of a compressor. The generated speeds depend on blade geometry, so the evaluation is possible using the known velocity triangles. The outlet velocity triangles at the impeller exit are shown in Fig. A.6 with the three-blade curvature/twist configurations.

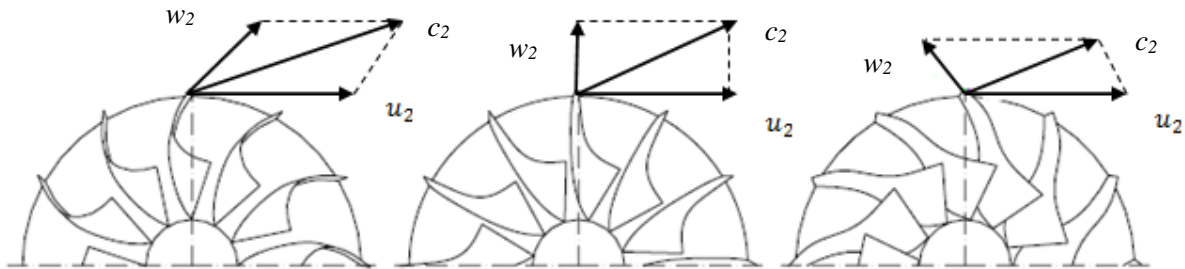


Figure A.6 Velocity triangles of forward curved, radial and backward curved blades (based on [80])

The centrifugal compressor has several parameters. The most important ones are the delivered mass flow rate, the realized discharge pressure and the rotational speed at which these are obtained. The physical values are subject to change due to variation in ambient conditions. This can change the operation of ground-based applications; however, it is essential to carefully consider their influence in aviation where ambient temperature and pressure have an extremely wide range.

Design of centrifugal compressor

The design of the centrifugal compressor has three main parts in the present case in line with [60]. The first one is the inducer, the second one is the impeller design and the third one is the diffuser design. The inducer design can be performed independently of the impeller since it is not strongly coupled to the subsequent components [60].

The inducer is found in the first part of the compressor and a sketch about it is shown in Fig. A.7. This component is responsible for guiding the flow to the impeller smoothly. The inducer is in front of impeller section where the axial motion of the fluid is changed in the radial direction. Without inducers, the rotor operation would suffer from flow separation and high noise. In the first assumption, the air which arrives at impeller assumed to be in axial direction, so the angular momentum of air is zero. In case of having smoothly guided air, the axial portion of the vanes must be curved. The angle between the relative velocity and axial direction is indicated as β_1 as it is shown in Fig. A.7.

The most essential part of the inducer design is to obtain the minimum value of the tip relative Mach number necessary to pass the flow while meeting any structural conditions [60]. The requirement for having minimum local Mach number is to find geometry structure for hub to tip ratio and hence approach absolute velocity

which gives the minimum relative velocity. Generally, the hub to tip ratio is set from structural requirement and is frequently changed between the 0.3 to 0.4 for simply overhung rotors [60].

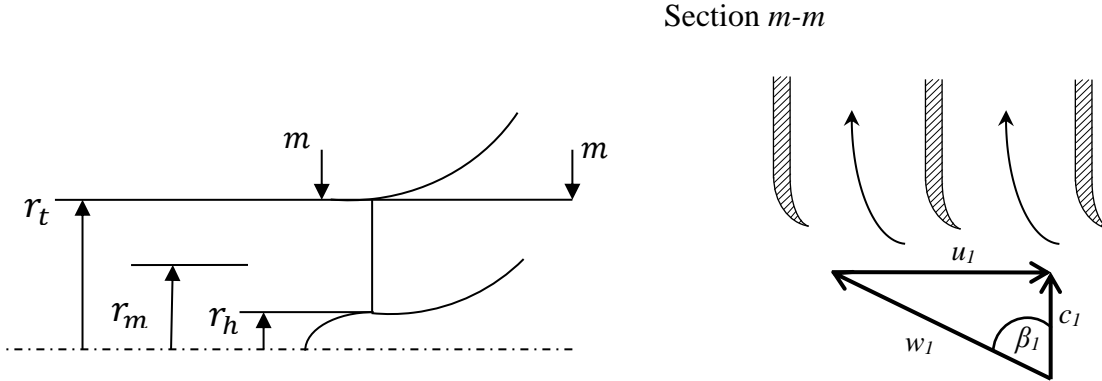


Figure A.7 Meridional view of an inducer with the velocity triangle

The process for having the minimum relative Mach number and the inducer geometry of the centrifugal compressor is accomplished by simple handmade calculation which is found here in line with [60]. The predefined data of the design is the inlet total pressure, total temperature and the mass flow rate. The RPM, the absolute inlet flow angle (measured from the meridional direction) and the radius of the hub is given by designer's choice. The material properties of the gas (specific heat at constant pressure and the ratio of specific heats) are not a function of the temperature in the whole compressor design because it has negligible effect for the final outcomes as it was shown in subchapter 2.4.2. The boundary layer blockage is defined as an empirical data and the axial component of the absolute velocity is defined as a starting estimate of the iteration process. The calculation process is the following.

The tangential component of the absolute velocity and the absolute velocity at the inlet section is determined based on the next relations [60]:

$$c_{\theta 1} = c_{m1} \tan \alpha_1 \quad (\text{A.4})$$

$$c_1 = (c_{m1}^2 + c_{\theta 1}^2)^{1/2} \quad (\text{A.5})$$

Then by having the absolute velocity, the static temperature and pressure, the Mach number and the density can be calculated by Eq. (A.6)-Eq. (A.9) [60].

$$T_1 = T_{01} - c_1^2 / (2C_p) \quad (\text{A.6})$$

$$M_1 = c_1 / \sqrt{\gamma R T_1} \quad (\text{A.7})$$

$$p_1 = p_{01} (T_1 / T_{01})^{\gamma / (\gamma - 1)} \quad (\text{A.8})$$

$$\rho_1 = p_1 / (RT_1) \quad (\text{A.9})$$

Afterwards, the mass flow rate, the density, the axial component of the absolute velocity and the parameter for boundary layer blockage are used to calculate flow area and the radius of the tip as follow [60]:

$$A_f = \frac{\dot{m}}{[\rho_1 c_{m1}(1 - B_1)]} \quad (\text{A.10})$$

$$r_{1t} = \left\{ \frac{A_f}{\pi} + r_{1h}^2 \right\}^{1/2} \quad (\text{A.11})$$

So, by knowing the tip radius, the tangential speed at the tip section can be determined as next:

$$u_{1t} = \frac{2\pi r_{1t} N}{60} \quad (\text{A.12})$$

Relative velocity at tip is computing by Eq. (A.13).

$$w_{1t} = [c_{m1}^2 + (u_{1t} - c_{\theta 1})^2]^{1/2} \quad (\text{A.13})$$

The flow angle of the relative velocity with respect to axial direction is calculated as follow [60] :

$$\beta_1 = \arctan \left[(u_{1t} - c_{\theta 1}) / c_{m1} \right] \quad (\text{A.14})$$

The process for having the minimum relative Mach number is based on changing c_{m1} until finding the minimum relative velocity at tip to determine the inducer inlet section [60]. Further iterations are completed in order to investigate the effect of different hub radius on the design variables.

The input and output parameters of the iterative calculation are represented in Table A.1

Table A.1 Input and output data of the inducer design

Inducer (input data)		Inducer (output data)	
p_{01}	98758 [Pa]	$c_{\theta 1}$	0 [m/s]
T_{01}	299.6 [K]	c_1	140 [m/s]
\dot{m}	1 [kg/s]	T_1	289.84 [K]
α_1	0 [°]	M_1	0.41 [-]
r_{1h}	0.022 [m]	p_1	87953 [Pa]
B_1	0.057 [-]	ρ_l	1.06 [kg/m ³]
c_{m1}	140 [m/s]	A_f	0.0073 [m ²]
N	43000 [rev/min]	r_{1t}	0.052 [m]
		u_{1t}	236.8 [m/s]
		w_{1t}	275 [m/s]
		β_1	59.4 [°]

Impeller design is the next step of the centrifugal compressor design process by means of calculating the impeller diameter and depth, flow state and velocity triangle at impeller tip [60]. The calculation process applies parameters provided by the inducer design also: the absolute inlet velocity and its flow angle comes from the inducer design. The predefined data of the design is the inlet total pressure and total temperature, mass flow rate and total pressure ratio of the compressor stage, meanwhile the rotor efficiency, pressure recovery coefficient and slip factor are given as empirical data. The axial component and the flow angle of the absolute velocity at the inlet section, the RPM, the number of vanes, the swirl factor at the mean section of the impeller exit and the relative flow angle measured from radial direction at the outlet section of the impeller are given by the designer's choice.

The slip factor is introduced in the present paragraph before discussing the used equations and iteration process in detail. The tangential component of the absolute velocity at the impeller discharge depends on the outlet angle of the blade [31]. Ideally, one can assume that the flow direction is tangential to the blade surface at the exit of the impeller. However, in reality, due to the Coriolis force in the rotating frame of reference, the flow direction changes, so there is a certain difference between ideal and real flow directions. Hence, slip factor σ is introduced, which is the ratio of tangential component of the absolute velocity under real and ideal conditions at the exit of the impeller [81]. Therefore, tangential component of the real outlet absolute velocity is obtained by multiplying the slip factor with the tangential component of the absolute velocity, which is purely based on the blade geometry. There are several ways to define the slip factor based on countless researches, which have come up with various formulas, utilizing different input parameters. In this case the slip factor is determined by Stanitz formula as follow [80]:

$$\sigma = 1 - \frac{2}{z} \quad (\text{A.15})$$

where z is the number of vanes.

The iteration process for the impeller design starts with selecting an isentropic efficiency for the compressor stage ($\eta_{s,stage}$) and recalculating that till the resulted total pressure ratio of the compressor unit is equal with the already specified input data (2.5 in the present case) meanwhile the outlet diameter and the width of the impeller-exit are the resulted geometrical parameters. The next step is the determination of the specific total enthalpy change by Eq. (A.16) based on the available data [60].

$$\Delta h_{0s} = \frac{\gamma R T_{01}}{\gamma - 1} \left(pr_{stage}^{(\gamma-1/\gamma)} - 1 \right) \quad (\text{A.16})$$

As the value of the stage efficiency is assumed, total specific shaft work is determined [60]:

$$W_X = \Delta h_0 = \frac{\Delta h_{0s}}{\eta_{s,stage}} \quad (\text{A.17})$$

The total outlet temperature at meridional blade section is given by Eq. (A.18) [60].

$$T_{02m} = T_{01} + \Delta h_0 \frac{\gamma - 1}{\gamma R} \quad (\text{A.18})$$

Although impeller configurations with backward turning blade-end has the highest total pressure ratio, the highest efficiency and wider operational range at the given conditions [82], radial blade-end configuration is selected due to the moderate total pressure ratio, structural robustness and favourable cost [82]. Hence, the

tangential velocity component of the absolute velocity equals to the peripheral speed in ideal case. Therefore, the peripheral speed is calculated by using slip factor and the Euler's turbine equation as follow [60]:

$$u_2 = \left[(u_1 c_{\theta 1} + W_x) / \sigma \right]^{1/2}, \quad (\text{A.19})$$

where $c_{\theta 1} = c_{m1} \tan \alpha_1$ is the tangential component of the absolute velocity.

As the value of the rotational speed is given like input data, the outlet diameter of the impeller is given by Eq. (A.20).

$$D_2 = u_2 / \pi N \quad (\text{A.20})$$

So, the tangential and axial (meridional) component of the absolute velocity at the mean section of the blade exit is determined by the following equations [60]:

$$c_{\theta 2m} = \sigma u_2 \quad (\text{A.21})$$

$$c_{m2m} = c_{\theta 2m} / \lambda_{2m} \quad (\text{A.22})$$

The tangent of the absolute flow angle (angle between the meridional and peripheral components of the absolute velocity) at the vane exit is equal with the swirl factor (λ_{2m}) [83].

The static temperature at the vane exit is calculated by Eq. (A.23) [60].

$$T_{2m} = T_{02m} - \frac{\gamma - 1}{2\gamma R} (c_{\theta 2m}^2 + c_{m2m}^2) \quad (\text{A.23})$$

The rotor (isentropic) efficiency is given by an empirical parameter, so the total pressure ratio of the impeller is the following [60]:

$$\frac{p_{02m}}{p_{01}} = \left[\left(\frac{\gamma - 1}{\gamma R T_{01}} W_x \eta_{s, rotor} \right) + 1 \right]^{\gamma / \gamma - 1} \quad (\text{A.24})$$

The static pressure is determined by using the next equation to calculate the density at the meridian section of the impeller exit [60]:

$$p_{2m} = p_{02m} / \left(\frac{T_{02m}}{T_{2m}} \right)^{\gamma / \gamma - 1} \quad (\text{A.25})$$

$$\rho_{2m} = \frac{p_{2m}}{RT_{2m}} \quad (\text{A.26})$$

The required cross-sectional area for the flow is computed by Eq. (A.27).

$$A_{2m} = \dot{m} / (\rho_{2m} c_{m2m}) \quad (\text{A.27})$$

Hence, the depth of impeller at its exit is the following:

$$b_2 = A_{2m}/(\pi D_2) \quad (\text{A.28})$$

The static pressure at the exit of the diffuser is determined by considering the pressure recovery coefficient that is shown in the Eq. (A.29) [60].

$$p_4 = p_{2m} + C_{pD}(p_{02m} - p_{2m}) \quad (\text{A.29})$$

The stage efficiency is computed by Eq. (A.30) [60].

$$\eta_{s,stage} = \frac{\left(\frac{p_4}{p_{01}}\right)^{(\gamma-1)/\gamma} - 1}{\left(T_{02m}/T_{01}\right) - 1} \quad (\text{A.30})$$

The iteration continues by updating the $\eta_{s,stage}$ input data till the resulted total pressure ration is equal with the expected one.

The impeller design provides total stage pressure ratio of 2.5 at mass flow rate 1 kg/s when it is coupled with diffuser. The total isentropic efficiency for the stage is 0.65 %. The impeller consists of 20 blades. The all input and resulted data of the mean line design are listed in Table A.2.

Table A.2 Input and output parameters of the mean line design of the impeller

Input		Output	
p_0	98758[Pa]	Δh_{0s}	90063 [J/kg]
T_0	299.6 [K]	W_x	137713 [J/kg]
\dot{m}	1 [kg/s]	T_{02m}	436.7 [K]
pr_{stage}	2.5 [-]	u_2	391.2 [m/s]
N	43000 [rev/min]	D_2	0.174 [m]
β_{2b}	90 [deg]	$c_{\theta 2m}$	352 [m/s]
$\eta_{s,rotor}$	0.8 [-]	c_{m2m}	132.85 [m/s]
z	20 [-]	T_{2m}	366.2 [K]
C_{pD}	0.65 [-]	p_{02m}	294262.7 [Pa]
σ	0.9 [-]	p_{2m}	158926.4 [Pa]
λ_{2m}	2.65 [-]	ρ_{2m}	1.512 [kg/m ³]
c_{m1}	140 [m/s]	A_{2m}	0.005 [m ²]
α_1	0 [°]	b_2	0.01 [m]
		$\eta_{s,stage}$	0.65
		α_2	70 [°] (measured from radius)
		β_2	16.41 [°] (measured from radius)

The impeller connects to the diffuser. The last step of the compressor unit design is to determine the flow characteristics and the geometry of the diffuser. The section 2-3 corresponds to the vaneless meanwhile the section 3-4 represents the vanned diffuser. The input for the calculation is the outlet thermodynamic state of the impeller together with the loss coefficient (K_{2m-3}) of the vaneless diffuser, the pressure recovery coefficient (C_{p3-4}) of the vanned diffuser and the Mach number (M_3).

As the total temperature at the impeller exit is equal with total temperature in the diffuser:

$$T_{03} = T_{02m} \quad (\text{A.31})$$

the static temperature is determined with gas dynamic equations as follow [60]:

$$T_3 = \frac{T_{03}}{1 + \frac{\gamma - 1}{2} M_3^2} \quad (\text{A.32})$$

Taking into consideration the pressure loss between the impeller exit and vaneless diffuser outlet, the total pressure can be determined at section 3 [60]:

$$p_{03} = p_{02m} - K_{2m-3}(p_{02m} - p_{2m}) \quad (\text{A.33})$$

Static pressure, density and velocity at the exit of the vaneless diffuser are calculated by the Eqs. (A.34)-(A.36) [60].

$$p_3 = p_{03} \left(\frac{T_3}{T_{03}} \right)^{\gamma/(\gamma-1)} \quad (\text{A.34})$$

$$\rho_3 = p_3 / RT_3 \quad (\text{A.35})$$

$$c_3 = M_3 \sqrt{\gamma RT_3} \quad (\text{A.36})$$

The cross-sectional area of the vaneless diffuser is computed by the following equation:

$$A_3 = \frac{\dot{m}}{\rho_3 (c_3 \cos(\text{atan}(c_{\theta 2m}/c_{m2m})))} \quad (\text{A.37})$$

It is supposed in Eq. (A.37) that the angular momentum is not changed significantly with respect to the section 2 and normal velocity to the area is considered. The total pressure at the exit of the vanned diffuser is computed by Eq. (A.38).

$$p_{04} = r_{03-04} p_{03} \quad (\text{A.38})$$

r_{03-04} total pressure recovery rate is considered for pressure loss in the vanned diffuser due to the strong adverse pressure gradient.

The combustion chamber is the next unit of the engine after the compressor. Hence, the flow should be guided to turn from rather radial to axial direction in the vaneless diffuser. This requires a curved axisymmetric flow channel here, ended by increased hub and shroud radiuses (see Fig. A.8). The thickness of the flow channel after the curved section is set 10 mm, which results higher cross-sectional area than it is at the exit of the impeller at about 23 %. However, there are vanes in section 3-4, which reduce the trough-flow area.

The all input and output data of the diffuser design is shown in Table A.3.

Table A.3 Input and output parameters of the diffuser-design

Input		Output	
T_{03}	436.7 [K]	T_3	403.3 [K]
K_{2m-3}	0.166	p_{03}	271797 [pa]
M_3	0.643	p_3	205817 [pa]
r_{03-04}	0.91	ρ_3	1.78 [kg/m ³]
		c_3	258.85 [m/s]
		A_3	0.006154 [m ²]
		p_{04}	246927 [Pa]

The meridional view with the sections of the compressor flow domain, main dimensions and the proportionally scaled velocity triangles at the inlet and outlet of the impeller are shown in the Fig. A.8 and A.9 respectively.

All thermodynamic parameters and geometrical sizes are available after the mean line design of the compressor at the design condition. The next step of the development is to create the 3D model of the assembly for the analysis and continue the design – after the inlet nozzle – with the next part of the engine, which is the combustion chamber.

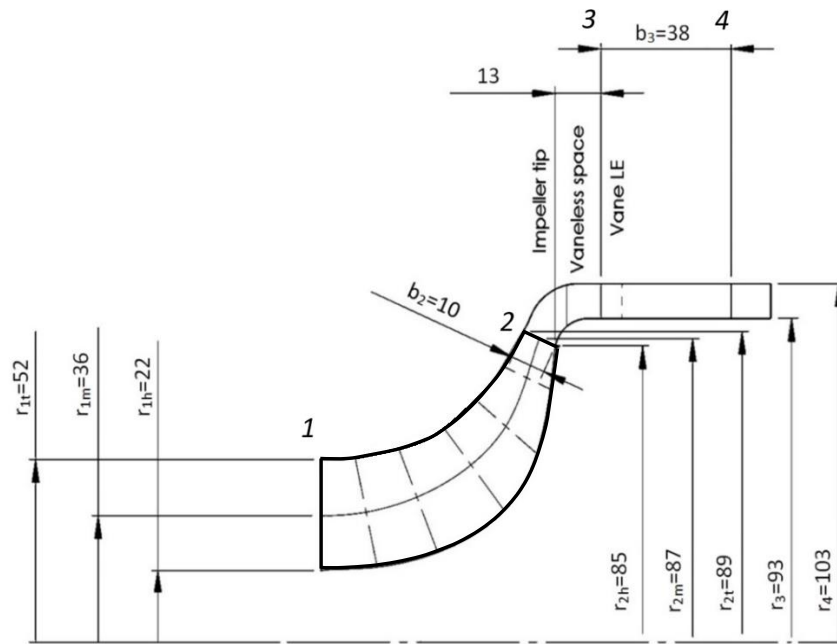


Figure A.8 Meridional view of the centrifugal compressor flow domain with the sections (1-4) and main dimensions (the dimensions are in [mm])

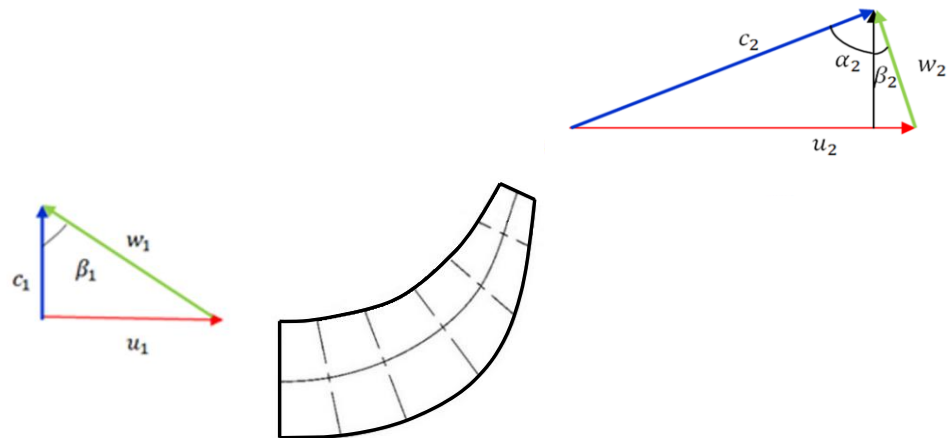


Figure A.9 Meridional view of the impeller channel with the scaled velocity vectors at the inlet tip and at the outlet meridional sections

A.2 Inlet Channel

As the dimensions of the compressor unit are available, the next step is the determination of the geometrical sizes and creating the 3D CAD model of the inlet channel. The structure of the intake manifold is designed to be as simple as possible meanwhile the flow transfer from the ambient into the compressor should have minimal entering and outgoing loss and minimal pressure recovery factor. The geometry of the diffuser is a tube with annular cross section, which is fit to the intake of the compressor. The geometry of the intake channel is shown in Fig. 4.1 in the wire frame model of the complete academic jet engine.

A.3 Design Aspects of the Combustion Chamber

The combustion chamber has the challenging task of burning certain amount of fuel that is supplied through the fuel burners with wide range of volume of air. The air leaving the compressor goes through the combustors, expanding and accelerating to give a smooth stream of uniformly heated gas at all conditions required by the turbine. The fuel is burned almost stoichiometrically with only 25 to 35 percent of total air entering [84] in general and it is 28 % in the present case ($\dot{m}_{fcc} = 0.019 \frac{kg}{s}, L_0 = 14.72 \frac{kg}{kg} \Rightarrow \dot{m}_{air,st,cc} = \dot{m}_{fcc} L_0 = 0.2797 \frac{kg}{s}$) in order to keep the turbine inlet temperature down to permissible limits. As a result, combustion must be completed without causing high pressure loss and taking into consideration the huge heat release for the limited space existing. In providing adequate turbulence and mixing, a total pressure loss changing from about 2 to 9 percent of the air pressure at which it goes through the chamber [84]. It is 6 % based on the inlet total pressure at the combustion chamber in this case by the thermo-dynamical analysis.

For many years the combustion has had less capability to theoretical treatment in comparison with other parts of the gas turbine and any development software involved some trial and error. With high cycle temperature of modern gas turbine, mechanical design stays complex task and need for improvement of technical development is obvious. Concerning the industrial gas turbines they have a certain range of usable types of fuel amongst them natural gas is included frequently beside the liquid based hydrocarbons [84].

Combustion chambers can be distinguished based on their structure. Regarding flow direction, reverse-flow and one-directional flow combustion chambers exist.

The reverse-flow combustion chambers have the advantage of obtaining shorter gas turbine design, because the flow path is shortened by half in one direction as the combustor is located to sit on perimeter of the compressor and turbine. Thus, this design does not require so improved shaft materials and bearing design compared to the one-directional flow combustion chambers. Due to this, the reverse-flow combustion chambers are basically applied on older gas turbines, however, where a short and compact design is required, this combustion chamber is still applied nowadays. As a disadvantage, reverse-flow combustion chambers have high pressure losses compared to one-directional chambers. Furthermore, due to the noticeable cross section, reverse-flow combustion chamber produces high aerodynamic drag, thus they are very rarely used in aircraft propulsion systems.

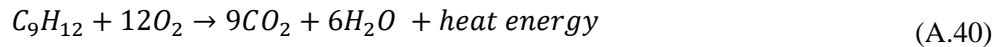
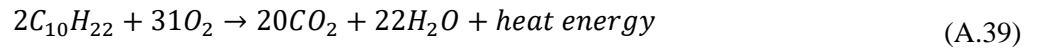
Although gas turbines, which are applied with one-directional flow combustion chambers are longer, hence better shaft materials and improved bearing designs are required, due to the lower cross section and better total pressure recovery factor and burning efficiency; they are more widespread in aviation industry.

Regarding the one-directional flow combustion chambers, there are three main types of the structure can be distinguished. They are the multiple can, can-annular and the annular type combustion chambers. All the three kinds of combustors have the recirculation, burning and dilution zone. First, fuel is partially burned in the recirculation zone. But there is some fuel, which is not completely burned, so the remainder of fuel is completely burned in the burning zone. The hot gas is then mixed in the dilution zone with the cooling air and provides a suitable inlet temperature for the turbine section. One part of the cooling air works on the principle of film cooling, it separates hot working fluid from the walls of the combustor; hence higher operating temperatures can be allowed. Furthermore, appropriate application of cooling air contributes to flame stabilization and more even mixture distribution while proceeding to the turbine inlet cross section [84].

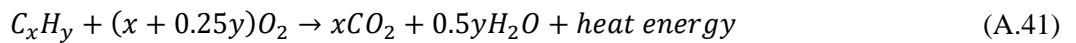
The combustion chamber design is a complex and challenging task in small gas-turbine engines due to the size limitation by means of couplings the compressor and turbine, typically constructive limitations on shaft length and diameter. These requirements have focused also in the present case to highlight the annular combustion chamber, as it is used today mostly. This kind of chamber is ideal because of “clean” aero-dynamic layout results in a compact unit and better characteristics than other combustor types. The annular combustor has the benefit of being able to use smaller cross section, achieves smaller pressure loss if compared with can-type one [84]. The other advantages of this kind combustor that the limited space available is used more effectively,

allowing better mixing of the fuel and air within a simple structure. Also more uniform combustion than in can type combustion chamber, better flame propagation and for the same output, it is 75 % shorter in general than the can-annular type chambers of the same diameter, hence less weight, less production and maintenance cost may be achieved [84]. In addition, there is less wall area needed in comparison with other types, consequently less cooling air, better combustion efficiency and less pollution are resulted. In development of turbojet engines, the use of annular combustion chamber is confined to relatively high pressure recovery factor, so for small gas turbines would seem to be more appropriate to apply an annular combustion chamber [84]. This kind of combustors includes a single flame tube, completely annular form, which is consisted in an inner and outer casing. The fuel enters through sequences of nozzle at the upstream end of the flame tube. At the front of compressor and the back of the turbine nozzle the chamber is open. The holes, which are placed in the shroud section of casing, allow the secondary air to enter the combustion chamber and guide the flame away from the shrouds to preserve the wall of the combustion chamber at a permissible relatively low temperature.

Combustion is a chemical reaction between fuel and air (oxygen) in the present case and this is usually approached by reaction kinetic equations. Heat is released during this reaction thus an exothermal process occurs during burning in the combustion chamber. Jet-A (kerosene) fuel has been considered with two-component surrogate fuel as mass fraction 60 % of n-C₁₀H₂₂ and mass fraction of 40 % TMB-C₉H₁₂ [85]. The combustion reaction process of hydrocarbon fuel and oxidant usually consists massive intermediate species/states and radical reactions, of which the full computation could almost be inaccessible. The one of the most simple approach for describing the actual combustion in ideal conditions (complete combustion and oxidation at stoichiometric condition) are summarized in Eq. (A.39) and Eq. (A.40) [86], [87].



or in general [88]:



Based on the all characteristics and consideration described above, for a small-scale academic gas turbine, due to its advantageous properties, an annular-type combustion chamber is selected. The combustor is created in a CAD software. The geometry with the main dimensions is shown in Fig. A.10. The primary inlet air is guided by longer slots in axial direction on the four injection domes. The injection bores of the fuel are found in the centre of each injection dome. Their diameter is 0.8 mm. The secondary air is injected in the combustion chamber across 6 mm bores. The dilution bore diameters are 12 mm. The CAD model of the combustion chamber is shown in Fig. 4.6.

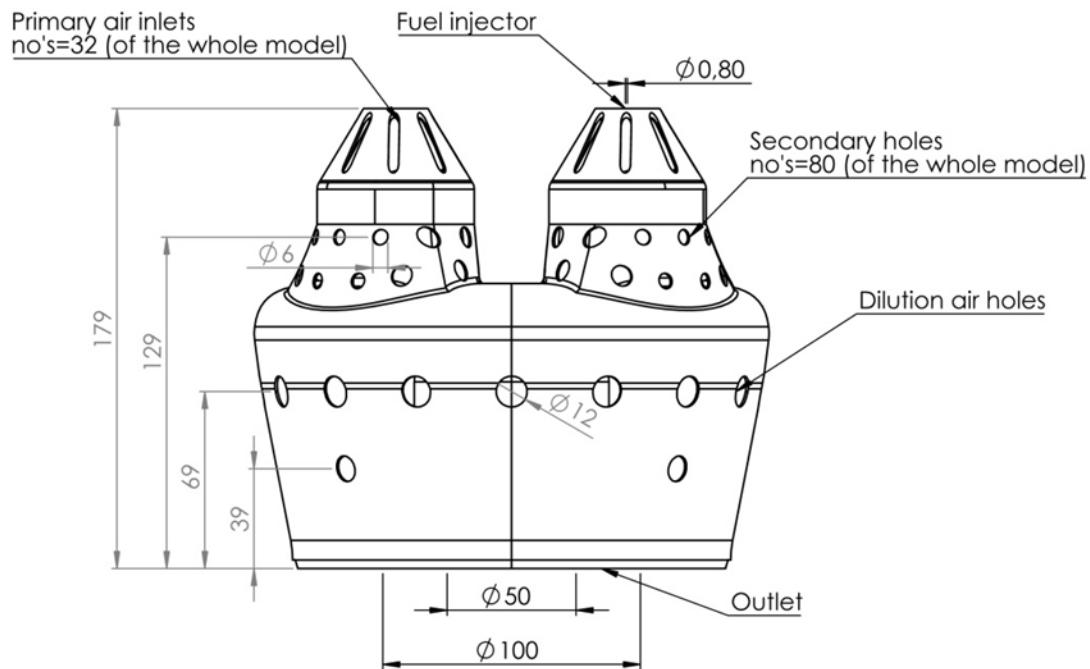


Figure A.10 Geometry of the annular type combustion chamber with the main sizes (the dimensions are in [mm])

A.4 Turbine Design

Introduction:

Turbines are essential part of turbo-machinery devices, which are used to convert the potential and kinetic energy of the working fluid into mechanical energy. There is a wide range of use of turbines in the different segments of industry, providing a reliable, efficient energy conversion method for rotating machines. The first application of the modern turbine technology can be deduced to the late 18th century where steam was used as the working fluid to drive turbine blades. Remarkable contributors to steam turbine development were Carl Gustav De Laval and Sir Charles Parsons. Despite De Laval was involved in developing the convergent-divergent nozzle - nowadays the so-called Laval nozzle - he also designed a steam turbine in 1870, which had an impeller speed of 30 000 rpm and a performance of 150 kW. The appearance of turbines was very different from nowadays steam turbines; however, the concept of blade design is almost identical what we call today as an impulse turbine blade design. As developments proceeded, Sir Charles Parsons came up with at that time, revolutionary multiple stage steam turbines. The blades were designed to form a so-called reaction turbine. As Sir Parsons continued his developments, by 1893, his multiple stage designs were producing first 25 000 kW, then 50 000 kW. As technology improvement and turbine developments continued, steam turbines were used in more and more fields of industry. First, accompanied with the appropriate reduction gears, steam turbines were driving pumps, then became a standard device to create electricity, and essential in maritime application. A good evidence of naval application is the propulsion system of the 70 000 horsepower Mauretania and Lusitania [89].

Although the first patent for gas turbines was released in 1791 by John Barber, due to insufficient efficiency levels which originated from manufacturing reasons, researchers had to wait until the early 20th century to create the first working gas turbine. From the aspect of the turbine, at the time, metallurgical development

made it only possible to achieve turbine inlet temperatures of only 400 °C. The very first gas turbines were developed for industrial application. As it is briefly mentioned above, the turbine uses the energy of the working fluid to rotate the shaft which it is mounted on, thus the higher the turbine inlet temperature, the more work the turbine can produce. The manufacturing and metallurgical developments between the world wars made it possible to achieve turbine inlet temperatures of 775°C [89]. In this aspect, one of the pioneers in turbine development was the Junkers Jumo 004 engine in 1937. The turbine blades of Jumo variant 004A were solid, while variant 004B were made of hollow Cromandur alloy. Approximately thirty years later, in the late 1960s aviation industry achieved a turbine inlet temperature of 1010°C in the JT9D-7 gas turbine, which powered the Boeing 747-100. The almost 300°C increment of turbine inlet temperature was made possible by the new turbine blade materials, the introduction of superalloys, and by the turbine blade cooling system also. Since the Jumo 004 gas turbine, roughly 100°C increment of turbine inlet temperatures was achieved in each decade until early 2010. Thus, the latest gas turbines in the aviation industry, such as the Rolls Royce Trent 1000 (powering the Airbus A380), the GE NX (powering the Boeing 787) can operate with turbine inlet temperatures around 1500 °C. Most recent developments, such as the Mitsubishi M501J industrial gas turbine with an advanced turbine blade barrier coating and cooling system, achieves a turbine inlet temperature of 1600 °C [90].

In the aviation industry, besides blade cooling, metallurgical developments and material sciences made it possible to attain such high turbine inlet temperature as previously mentioned. In turbine blade construction, wide range of materials are used, one of them are superalloys. Superalloys are high performance alloys, which are capable of withstanding high temperatures, high stresses and often highly oxidizing atmospheres. First in the material development of turbine blades, the emphasis was based on to apply materials that have high temperature tensile strength. As operating temperatures increased, the priority became to find superalloys, that are characterized by favourable creeping properties and favourable low and high cycle fatigue. Consequently, the superalloys used in turbine blade construction are mainly cast Nickel based alloys, where also noticeable amount of Chromium is added to resist corrosion. Another achievement in turbine material research was the introduction of directionally solidified (DS) castings. Blades created with DS technology, can bear higher temperatures as without this technology, the grain boundaries in the alloy had better quality, than conventionally casted alloys. Turbine blades are also produced from single crystals, which have better temperature and stress withstanding capabilities than directionally solidified castings, as the crystal structure is uniform, because grain boundaries are eliminated. Turbine blade coating is also an efficient method of allowing higher turbine inlet temperatures. The advantage of applying blade coating is to reduce blade oxidation and keep the blade as heat resistant as possible, while the original favourable mechanical properties of the blade is still present. Thermal barrier coatings (TBC) are one of the most efficient coating methods. The operating temperatures of TBC coated blades may be about 150 °C above the original operating temperature of the superalloy [91]. TBC is usually multi-layer coatings, as a corrosion protective layer is also sublimated under the TBC upper layer. Besides thermal barrier coating, diffusion and overlay coatings are applied in turbine blade development [91].

Parallel with the improvements on material and production process including heat- and surface treatment, turbine blade cooling also increases the maximum achievable turbine inlet temperature. Blade cooling started to develop in the 1950s where besides air; water was also used for turbine cooling. However due to its weight and complicated application, only air, which is withdrawn from the compressor stages is used for turbine blade cooling. As turbine temperatures increased and technology developed hollow turbine blades were introduced, into which cooling air was supplied from the compressor stages. The cooling air flowing out from the blade also creates an insulation film between the turbine blade and the hot working fluid.

As previously indicated, turbines use the kinetic energy of the usually high temperature working medium to produce shaft power, which drives a compressor in aviation gas turbine applications. There are two main types of turbines in the aspect of flow direction: axial (see Fig. 3.16) and radial turbines. In the axial turbine, the working fluid flows through the turbine parallel to the shaft, while entering one or more stages. Axial turbines are more suitable for higher mass flow rates (approximately at and above 1 kg/s), usually applied in machines that have approximately 15-20 cm nominal diameter or more. Compared to radial turbines, the blade cooling can be realized easier and more efficiently, hence higher turbine inlet temperatures are achievable. A typical single stage axial flow turbine is shown in Fig. A.11. Radial turbines are rotary machines, where the hot working fluid enters the impeller in a perpendicular direction to the shaft and exits in axial direction. Radial turbines are more compact devices than axial turbines, and at same working medium conditions are capable to produce more shaft power than an axial turbine, as expansion ratio is higher. Choosing between the two types of turbines indicated previously are highly dependent on the type application; however, it can be said that radial turbines can attain better efficiencies at small mass flow rates than axial turbines. Consequently, radial turbines are applied in small gas turbines, or as a part of a turbocharger in vehicles where approximately 700 °C exhaust gas drives the device, thus no cooling is required. Due to small sizes, in some cases, contrary to axial turbines, radial turbines are designed without nozzle vanes, to keep friction losses as low as possible. Comparing radial and axial turbines, multiplying stages is more demanding in case of radial ones than axial ones. Furthermore, due to the lower appropriate mass flow rates for radial turbines, the impeller size rarely exceeds a diameter of 20 cm, while axial turbines in industrial applications can be designed with diameters greater than 2 m.

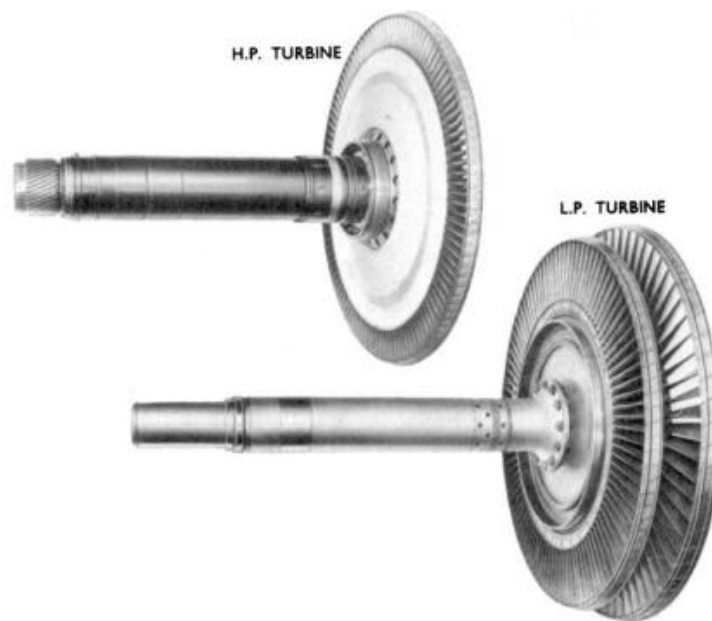


Figure A.11 Axial flow turbine rotors (Courtesy Rolls-Royce) [92]

The conversion of kinetic energy to mechanical energy in turbines can be divided into two types, impulse and reaction turbines. In the impulse turbines the working fluid accelerates only between the stator vanes while decreasing the pressure and the direction of flow changes from axial to nearly radial. Then the fluid changes direction on the rotor blades, creating a torque on the shaft and gets rather axial direction at the end of the blades. In case of an impulse turbine stage, apart from losses, the pressure does not change on the rotor blades, while the absolute speed of the flow decreases compared to the stator outlet cross section meanwhile the relative velocity remains constant as the cross section between two blades is not changed. In the turbine blade

design, due to the frictional losses, clearly impulse blades with zero degree of reaction are not built, however usual degree of reaction for impulse turbine is approximately between 0.05-0.1 [8]. In reaction turbines expansion of the working fluid takes place on both the stator and rotor blades. The absolute velocity increases in the stator blade accompanied by a pressure drop, while in the rotor blade the absolute velocity of the gas decreases, with increasing in relative velocity and decrease in pressure due to the decreasing flow cross section. The degree of reaction of a reaction turbine stage is 0.5 in general. In comparison of impulse and reaction turbines, it can be said that at the same size and conditions, higher performance is produced by an impulse turbine, furthermore, due to no pressure change on the rotor blades, no axial force is present on the blades, while axial forces are present on the reaction turbine, thus design is more complicated for the reaction turbine [8], [93] and [94].

To understand more the main analysis of turbine stage, the essential of work extraction via expansion of working fluid in the turbine part will be discussed. Generally, moving fluid through a turbine blade row consists of velocity components in radial, axial and tangential directions, which are represented in Fig. A.12.

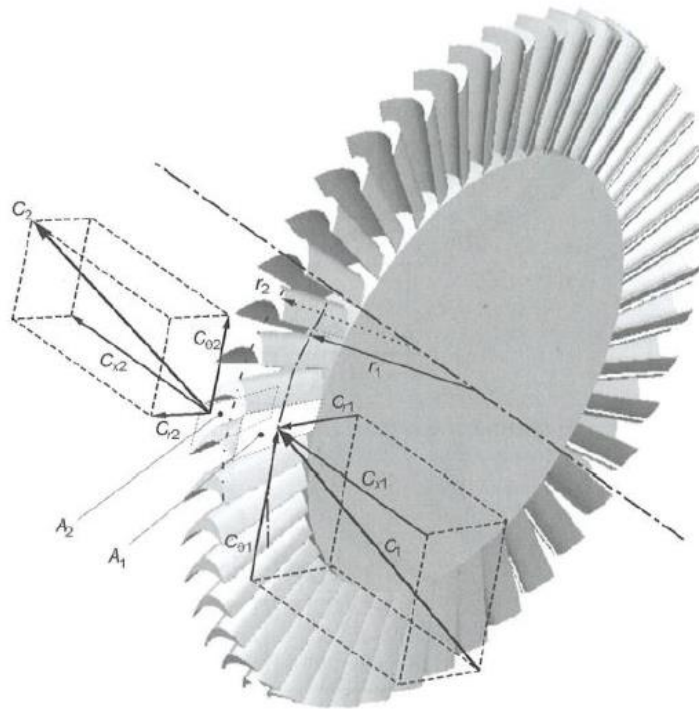


Figure A.12 Flow through the blade row of a turbo machine turbine disc [95]

Considering the axial turbine, the flow enters in state 0 and expands into state 1 by stator and goes through the rotor to reach state 2 (see Fig. A.13) and the total enthalpy of the hot gas decreases as power is added to the turbine.

The direction of the flow how it develops through turbine stage in the aspect of relative and absolute velocities is shown in the velocity triangle in Fig. A.14. These parameters are at the same radius, so the tangential velocity (u) is equal at sections 1 and 2. The flow reaches the stage with certain velocity c_0 with angle α_0 at nearly axial direction. Then the flow accelerates and turns in the stator, which results rather tangential flow direction than axial one at the outlet of the stator as absolute velocity c_1 at angle α_1 (measured from peripheral direction). The relative velocity is found by subtracting the blade speed vector u from the absolute velocity vectorially.

The relative angle of the gas at section 1 (β_1) is found between the relative velocity w_1 and tangential direction at the inlet of the rotor blade. The relative velocity at section 2 (w_2) is in line with rotor exit blade direction and the relative flow angle (β_2) is between the relative velocity and peripheral direction also. The absolute velocity at that stage can be determined by adding the relative velocity to the tangential speed (u) vectorially. The absolute flow angle (α_2) is found between the absolute velocity (c_2) and tangential direction.

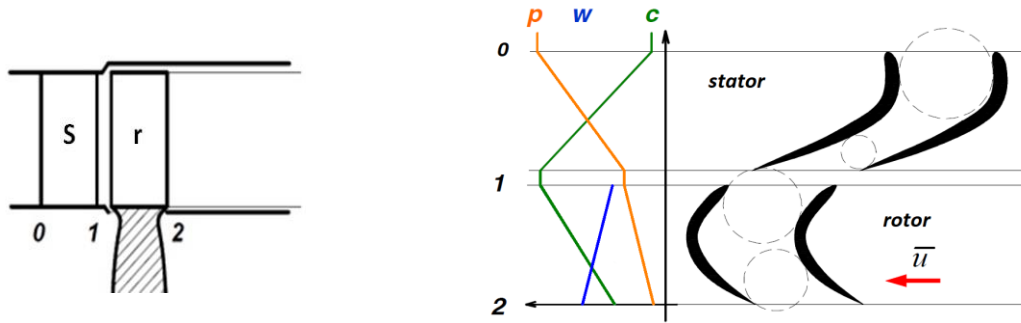


Figure A.13 Typical axial flow turbine stage (s: stator, r: rotor) [8]

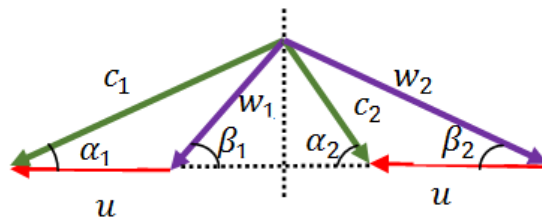


Figure A.14 Typical velocity triangles of an axial turbine [8]

A decision has been made to consider axial turbine in the present case due to the reasons are found in the introduction part of the present subchapter.

Mean line and 3D design of the axial turbine:

The used process for the turbine design is based on the procedure found in [1] and [96]. The numbering of the used parameters for representing the different engine sections are shown in Fig. 3.5.

Prior the mean line design, it is indispensable to determine the number of turbine stages are applied. The number of stages depends on the overall enthalpy drop of the turbine corrected for efficiencies and losses with the constraint to produce enough shaft power to drive the compressor in the present case. Single stage turbine is selected based on the Parson's number approach, which is described in [1] and [96]. It is also cross checked that single stage turbine assembly is found in the already existing gas turbines are similar to this work and the recommended margin of turbine stage pressure ratio varies between $1.7 \div 2.2$ [1], [96].

First, based on the available data by the thermodynamic calculation, the main geometrical sizes of the turbine are determined. The input data for this calculation are 1. the mean diameter of the compressor unit at its outlet section, 2. the mass flow rate, 3. the expected turbine inlet absolute velocity, 4. the given turbine inlet total temperature, 5. the inlet total pressure determined by the compressor exit total pressure and the pressure recovery factor of the combustion chamber, 6. material properties of the gas, 7. the expected dimensionless

speed at the exit of the turbine, 8 total specific enthalpy drop, 9. isentropic turbine efficiency and 10. the exit total temperature and pressure. The material properties of the gas (specific heat at constant pressure and the ratio of specific heats) are constants, they are not a function of the temperature and the mass fraction of the material components because it has negligible effect for the final outcomes as it was shown in subchapter 2.4.2. The main outputs of the calculation are the static pressure, temperature, density, velocity, cross section, diameter (inner and outer) and the blade height at the inlet and outlet section of the turbine. The calculation in detail is the following. First, the static temperature, static pressure, density and the cross section of the inlet section are determined by Eq. (A.42)-Eq. (A.45) [1].

$$T_4 = T_{04} - \frac{c_4^2}{2c_{p,gas}} \quad (\text{A.42})$$

$$p_4 = p_{04} \left(\frac{T_4}{T_{04}} \right)^{\gamma_{gas}/(\gamma_{gas}-1)} \quad (\text{A.43})$$

$$\rho_4 = \frac{p_4}{R_{gas}T_4} \quad (\text{A.44})$$

$$A_4 = \frac{\dot{m}_4}{c_4\rho_4} \quad (\text{A.45})$$

The direction of the velocity c_4 is supposed to be axial, it has no tangential component. The next step is the determination of the mean diameter with especial care for the low centrifugal force, the blade height and the hub and tip diameters at constant mean diameter design choice for the turbine unit due to the streamline flow path and low production cost. The calculation is shown in the following equations [1]:

$$D_{4m} = 0.68 D_{3m} \quad (\text{A.46})$$

$$l_4 = \frac{A_4}{\pi D_{4m}} \quad (\text{A.47})$$

$$D_{4h} = D_{4m} - l_4 \quad (\text{A.48})$$

$$D_{4t} = D_{4m} + l_4 \quad (\text{A.49})$$

Determination of the static thermodynamic parameters and the main geometrical sizes of the turbine exit is show in Eq. (A.50)-Eq. (A.59) [1].

$$c_{5crit} = \sqrt{\frac{2\gamma_{gas}}{\gamma_{gas} + 1} R_{gas}T_{05}} \quad (\text{A.50})$$

$$c_5 = \lambda_5 c_{5crit} = c_{5a} \quad (\text{A.51})$$

$$T_5 = T_{05} - \frac{c_5^2}{2c_{p,gas}} \quad (\text{A.52})$$

$$p_5 = p_{05} \left(\frac{T_5}{T_{05}} \right)^{\gamma_{gas}/(\gamma_{gas}-1)} \quad (\text{A.53})$$

$$\rho_5 = \frac{p_5}{R_{gas}T_5} \quad (\text{A.54})$$

$$A_5 = \frac{\dot{m}_5}{c_5\rho_5} \quad (\text{A.55})$$

$$D_{5m} = D_{4m} \quad (\text{A.56})$$

$$l_5 = \frac{A_5}{\pi D_{5m}} \quad (\text{A.57})$$

$$D_{5h} = D_{5m} - l_5 \quad (\text{A.58})$$

$$D_{5t} = D_{5m} + l_5 \quad (\text{A.59})$$

The total temperature and pressure at the exit of the turbine are pre-calculated from the total specific enthalpy drop and the isentropic efficiency of the turbine. $\dot{m}_4 = \dot{m}_5$ as there is no blade cooling considered. The summary of the all input data and the resulted parameters are shown in Table A.4.

The second main part of the turbine design is the determination of the unknown thermodynamic, aerodynamic and flow parameters together with the velocity triangles at the mean line of each section (0, 1 and 2) of the turbine stage. The input and the output data for this calculation are shown in the Table A.5.

The computation starts with quantifying the exit pressure of turbine by the inlet total temperature and pressure and the adiabatic enthalpy drop of the stage with supposing an ideal adiabatic expansion till the same pressure as it is in the real turbine process. Hence, first the critical isentropic velocity at the inlet of the turbine stage is determined [1], [96]:

$$c_{s,crit} = \sqrt{\frac{2\gamma_{gas}}{\gamma_{gas} + 1} R_{gas}T_{00}} \quad (\text{A.60})$$

The available velocity by the isentropic energy change is calculated by Eq. (A.61) [1], [96].

$$c_s = \sqrt{2\Delta h_{0s}}, \text{ where } \Delta h_{0s} = c_{pgas}T_{00} \left(1 - \frac{1}{\left(\frac{p_{00}}{p_2}\right)^{\frac{\gamma_{gas}-1}{\gamma_{gas}}}} \right) \quad (\text{A.61})$$

Table A.4 Input and output parameters of the mean line design of the turbine for determining its main inlet and exit geometrical sizes

Input		Output	
D_{3m}	0.2 [m]	c_{4crit}	568.26 [m/s]
\dot{m}_4	1 [kg/s]	T_4	994.69 [K]
c_4	110 [m/s]	p_4	227187 [Pa]
T_{04}	1000 [K]	ρ_4	0.81 [kg/m ³]
p_{04}	232111.85 [Pa]	A_4	0.01 [m ²]
γ_{gas}	1.33 [-]	D_{4m}	0.13 [m]
R_{gas}	282.86 [J/kg/K]	l_4	0.027 [m]
λ_4	0.36 [-]	D_{4h}	0.103 [m]
Δh_{T0}	137713 [J/kg]	D_{4t}	0.157 [m]
η_{sT}	0.87	c_{5crit}	532.83 [m/s]
T_{05}	879.2 [K]	c_5	191.82 [m/s]
p_{05}	127070.3 [Pa]	T_5	863.06 [K]
		p_5	117928.14 [Pa]
		ρ_5	0.48 [kg/m ³]
		A_5	0.01 [m ²]
		l_5	0.027 [m]
		D_{5m}	0.13 [m]
		D_{5h}	0.103 [m]
		D_{5t}	0.157 [m]

The dimensionless speed at the turbine outlet cross section is expressed as follow [1]:

$$\lambda_s = \frac{c_s}{c_{s,crit}} \quad (\text{A.62})$$

The static pressure at the outlet of the stage can then be computed with the help of dimensionless gas dynamic equation [1]:

$$\frac{T_2}{T_{00}} = \left(\frac{p_2}{p_{00}} \right)^{\frac{\gamma_{gas}-1}{\gamma_{gas}}} \quad (\text{A.63})$$

$$1 - \frac{\gamma_{gas}-1}{\gamma_{gas}+1} \lambda_s^2 = \left(\frac{p_2}{p_{00}} \right)^{\frac{\gamma_{gas}-1}{\gamma_{gas}}} \quad (\text{A.64})$$

$$p_2 = \left(1 - \frac{\gamma_{gas}-1}{\gamma_{gas}+1} \lambda_s^2 \right)^{\frac{\gamma_{gas}}{\gamma_{gas}-1}} p_{00} \quad (\text{A.65})$$

The degree of reaction is determined to be 0.2 to be closer to the impulse-type turbine in order to utilize its advantages discussed in the introduction part of subchapter of Appendix A.4. Then the enthalpy drop of the stator and rotor can be determined by the following ways (the s and r in the subscripts indicate the stator and rotor respectively) [1]:

$$\Delta h_{s,s} = (1 - r^o)\Delta h_{os} \quad (\text{A.66})$$

$$\Delta h_{s,r} = r^o\Delta h_{os} \quad (\text{A.67})$$

The total enthalpy drop across the stator turns to increase the velocity. So, the theoretical absolute velocity at the exit of the stator is given by Eq. (A.68) [1].

$$c_{1,th} = \sqrt{2\Delta h_{s,s}} \quad (\text{A.68})$$

However, due to the fluid dynamic losses, this velocity is less in the reality. The speed coefficient is used to determine the real velocity at the exit of the stator [1]:

$$c_1 = \varphi_s c_{1,th} \quad (\text{A.69})$$

Then, the static temperature at this section can be calculated by the Eq. (A.70) [1].

$$T_1 = T_{00} - \frac{c_1^2}{2c_{p,gas}} \quad (\text{A.70})$$

The critical speed and the theoretical dimensionless speed at the stator exit are computed by Eq. (A.71) and Eq. (A.72) respectively [1].

$$c_{1,crit} = \sqrt{\frac{2\gamma_{gas}}{\gamma_{gas} + 1} R_{gas} T_{00}} \quad (\text{A.71})$$

$$\lambda_{1,th} = \frac{c_{1,th}}{c_{1,crit}} \quad (\text{A.72})$$

The static pressure at the outlet of the stator can be determined in the function of the inlet total pressure, theoretical dimensionless speed and ratio of specific heats [1]:

$$p_1 = \left(1 - \frac{\gamma_{gas} - 1}{\gamma_{gas} + 1} \lambda_{1,th}^2\right)^{\frac{\gamma_{gas}}{\gamma_{gas} - 1}} p_{00} \quad (\text{A.73})$$

The flow angle of the absolute velocity (measured from tangential direction) at the stator outlet section is given by Eq. (A.74) [1], [96].

$$\alpha_1 = \arcsin \frac{\dot{m} \sqrt{T_{00}}}{\beta p_{00} A_1 \varphi_s q(\lambda_{1,th}) \varepsilon_1} \quad (\text{A.74})$$

Typically, the gas dynamic constant is $\beta = 0.0396$ and ε_1 is a factor considers the flow cross section, which is affected (reduced) by the blades. It needs to be taken into account when the blades are shorter than 12 mm [1]. The $q(\lambda_{1,th})$ is the dimensionless mass flow rate [1]:

$$q(\lambda_{1,th}) = \left(\frac{\gamma_{gas} + 1}{2}\right)^{\frac{1}{\gamma_{gas}-1}} \lambda_{1,th} \left(1 - \frac{\gamma_{gas} - 1}{\gamma_{gas} + 1} \lambda_{1,th}^2\right)^{\frac{1}{\gamma_{gas}-1}} \quad (A.75)$$

The relative velocity at the rotor inlet section is computed from the known components of the velocity triangle as [1], [96]:

$$w_1 = \sqrt{c_1^2 + u_1^2 - 2c_1u_1\cos\alpha_1} \quad (A.76)$$

The tangential velocity (u_1) is determined by the diameter (radius) at the mean line and RPM (angular speed). The incoming flow angle of the relative velocity measured from tangential direction is given by Eq. (A.77) [1], [96].

$$\beta_1 = \arcsin \frac{c_1 \sin \alpha_1}{w_1} \quad (A.77)$$

In the relative frame of reference, the relative total temperature at the rotor inlet is calculated as follow [1], [96]:

$$T_{0w1} = T_1 + \frac{w_1^2}{2c_{p,gas}} \quad (A.78)$$

and it is constant in the rotor segment. So one can write [1], [96]:

$$T_{0w1} = T_{0w2} \Rightarrow C_{p,gas}T_1 + \frac{w_1^2}{2} = C_{p,gas}T_2 + \frac{w_2^2}{2} \quad (A.79)$$

The relative velocity at the outlet section of the rotor is determined by Eq. (A.80) [1], [96].

$$w_2 = \varphi_r \sqrt{w_1^2 + 2\Delta h_{s,r}} \quad (A.80)$$

where φ_r is the speed coefficient of the rotor for considering the losses. The relative critical speed and the dimensionless speed at the rotor exit are computed as follow [1], [96]:

$$w_{2,crit} = \sqrt{\frac{2\gamma_{gas}}{\gamma_{gas} + 1} R_{gas} T_{0w2}} \quad (A.81)$$

$$\lambda_{w2} = \frac{w_2}{w_{2,crit}} \quad (A.82)$$

The total pressure in the relative frame of reference can be calculated as the p_2 static pressure is known [1], [96]:

$$p_{0w2} = \left(1 - \frac{\gamma_{gas} - 1}{\gamma_{gas} + 1} \lambda_{w2}^2\right)^{\frac{\gamma_{gas}}{\gamma_{gas}-1}} p_2 \quad (\text{A.83})$$

The outlet static temperature is determined by the temperature ratio in terms of gas dynamic function (see Eq. (A.84) [1], [96]).

$$T_2 = \left(1 - \frac{\gamma_{gas} - 1}{\gamma_{gas} + 1} \lambda_{w2}^2\right) T_{0w2} \quad (\text{A.84})$$

The flow angle of the relative velocity measured from tangential direction is given by Eq. (A.85) [1], [96].

$$\beta_2 = \arcsin \frac{\dot{m} \sqrt{T_{0w1}}}{\beta p_{0w2} A_2 \varphi_{r,q}(\lambda_{w2}) \varepsilon_2}, \quad (\text{A.85})$$

where the $q(\lambda_{w2})$ is the dimensionless mass flow rate [1]:

$$q(\lambda_{w2}) = \left(\frac{\gamma_{gas} + 1}{2}\right)^{\frac{1}{\gamma_{gas}-1}} \lambda_{w2} \left(1 - \frac{\gamma_{gas} - 1}{\gamma_{gas} + 1} \lambda_{w2}^2\right)^{\frac{1}{\gamma_{gas}-1}} \quad (\text{A.86})$$

The outlet absolute velocity is calculated by the cosine theorem [1], [96]:

$$c_2 = \sqrt{w_2^2 + u_2^2 - 2w_2u_2 \cos \beta_2} \quad (\text{A.87})$$

as the tangential velocity is computed similarly to the same speed but at the inlet section of the rotor. The flow angle of the absolute velocity measured from the tangential direction is shown by Eq. (A.88) [1], [96].

$$\alpha_2 = \arcsin \frac{w_2 \sin \beta_2}{c_2} \quad (\text{A.88})$$

Concerning the total temperature, the critical velocity, the dimensionless speed and the total pressure at the exit of the rotor, they are determined by Eq. (A.89)-Eq. (A.92) [1], [96].

$$T_{02} = T_2 + \frac{c_2^2}{2c_{p,gas}} \quad (\text{A.89})$$

$$c_{2,crit} = \sqrt{\frac{2\gamma_{gas}}{\gamma_{gas} + 1} R_{gas} T_{02}} \quad (\text{A.90})$$

$$\lambda_2 = \frac{c_2}{c_{2,crit}} \quad (\text{A.91})$$

$$p_{02} = \left(1 - \frac{\gamma_{gas} - 1}{\gamma_{gas} + 1} \lambda_2^2\right)^{\frac{\gamma_{gas}}{\gamma_{gas}-1}} p_2 \quad (\text{A.92})$$

The input and the output parameters of the mean line design of the turbine are shown in Table A.5.

Table A.5 Input and output data of the mean line design of the turbine

Input		Output	
N	43000 [rev/min]	z	1 [pc]
α	0 [-]	c_s	593.82 [m/s]
γ	0.5 [-]	$c_{s,crit}$	568.262 [m/s]
Δh_{os}	176311 [J/kg]	λ_s	1.04 [-]
u_1	292.7 [m/s]	$\pi(\lambda_s)$	0.508 [-]
u_2	292.7 [m/s]	p_2	117928 [Pa]
u_m	292.7 [m/s]	$\Delta h_{s,s}$	141049 [J/kg]
\dot{m}	1 [kg/s]	$\Delta h_{s,r}$	35262.2 [J/kg]
γ_{gas}	1.33 [-]	$c_{1,th}$	531.13 [m/s]
R_{gas}	282.86 [J/kg/K]	c_1	520.5 [m/s]
β	0.0396 [-]	T_1	881.17 [K]
T_{00}	1000 [K]	$c_{1,crit}$	568.26 [m/s]
p_{00}	232111.85 [Pa]	$\lambda_{1,th}$	0.9347 [-]
r^o	0.2 [-]	$\pi(\lambda_{1,th})$	0.587 [-]
φ_r	0.96 [-]	$q(\lambda_{1,th})$	0.995 [-]
φ_s	0.98 [-]	p_1	136307 [Pa]
ε_1	0.97 [-]	α_1	19.26 [°]
ε_2	0.971 [-]	u_1	292.7 [m/s]
D_{1h}	0.103 [m]	w_1	262.59 [m/s]
D_{1t}	0.157 [m]	β_1	40.83 [°]
D_{1m}	0.13 [m]	T_{0w1}	911.4 [K]
l_1	0.027 [m]	T_{0w2}	911.4 [K]
A_1	0.01 [m ²]	T_{0wm}	911.4 [K]
D_{2h}	0.103 [m]	w_2	358.53 [m/s]
D_{2t}	0.157 [m]	$w_{2,crit}$	542.5 [m/s]
D_{2m}	0.13 [m]	λ_{w2}	0.661 [-]
l_2	0.027 [m]	$\pi(\lambda_{w2})$	0.7731 [-]
A_2	0.01 [m ²]	p_{02w}	152540 [Pa]
		$\tau(\lambda_{w2})$	0.938 [-]
		$q(\lambda_{w2})$	0.865 [-]
		T_2	855.04 [K]
		β_2	32.65 [°]
		u_2	292.7 [m/s]
		c_2	193.66 [m/s]
		α_2	87.3 [°]
		T_{02}	871.49 [K]
		$c_{2,crit}$	530.49 [m/s]
		λ_2	0.365 [-]
		$\pi(\lambda_2)$	0.926 [-]
		p_{02}	127342 [Pa]
		p_2	117928 [Pa]

The 3D extension of the blade design by means of blade twisting is the next step in the aerodynamic design of the turbine stage. So, the velocity vectors at the hub and tip sections are determined in the present paragraph. The ISRE (Isentropic Radial Equilibrium Equation) is used as governing equation for that purpose [70]:

$$\frac{dh_0}{dr} = c_a \frac{dc_a}{dr} + c_w \frac{dc_w}{dr} + \frac{c_w^2}{r} \quad (\text{A.93})$$

Eq. (A.93) includes that the effect of the inertial (centrifugal) force due to the high-speed rotation is balanced by the pressure force for the flow in radial direction. Furthermore, the entropy-variation in the radial direction is supposed to be zero. Constant blade loading provides uniform energy decrease in the spanwise direction of the turbine blades, so the enthalpy change of the flow in the function of radius is zero also. This is considered in Eq. (A.94).

$$0 = c_a \frac{dc_a}{dr} + c_w \frac{dc_w}{dr} + \frac{c_w^2}{r} \quad (\text{A.94})$$

Constant nozzle outlet angle ($\alpha_1 = \text{const.}$) blade twisting method is used in the present case due to the favourable production cost. The axial and tangential velocity components of the absolute velocity along the radius is determined from Eq. (A.94). The detailed derivations of the final expressions are presented hereafter.

Using trigonometric relation, the tangent of the absolute flow angle at the inlet section of the rotor is given by Eq. (A.95) [70].

$$\text{tg}\alpha_1 = \frac{c_{1a}}{c_{1w}} \quad (\text{A.95})$$

The α_1 is measured from tangential direction. Furthermore, the partial derivatives can be constituted in radial direction [70]:

$$\frac{dc_{1a}}{dr} = \frac{dc_{1w}}{dr} \text{tg}\alpha_1 \quad (\text{A.96})$$

Thus, using Eq. (A.95) and Eq. (A.96), Eq. (A.94) can be rewritten as follow:

$$0 = c_{1w} \text{tg}^2\alpha_1 \frac{dc_{1w}}{dr} + c_{1w} \frac{dc_{1w}}{dr} + \frac{c_{1w}^2}{r} \quad (\text{A.97})$$

or after rearrangements:

$$0 = (1 + \text{tg}^2\alpha_1) \frac{dc_{1w}}{dr} + \frac{c_{1w}}{r} \quad (\text{A.98})$$

The final form of the differential equation before its analytical solution is given Eq. (A.99) [70].

$$\frac{1}{\cos^2\alpha_1} \frac{dc_{1w}}{dr} = -\frac{c_{1w}}{r} \quad (\text{A.99})$$

The solution of Eq. (A.99) is the following [70]:

$$c_{1w} r^{\cos^2 \alpha_1} = \text{const.} \quad (\text{A.100})$$

and because $\frac{c_{1a}}{c_{1w}} = \text{tg} \alpha_1$ and it is constant:

$$c_{1a} r^{\cos^2 \alpha_1} = \text{const.} \quad (\text{A.101})$$

Based on the fact that the total enthalpy reduction along the radius is constant and the inlet and outlet section is on the same radius, the Euler's turbine equation gives [70]:

$$u(c_{1w} - c_{2w}) = u_m(c_{1wm} - c_{2wm}), \quad r(c_{1w} - c_{2w}) = r_m(c_{1wm} - c_{2wm}) \quad (\text{A.102})$$

The tangential velocity component of the absolute velocity at the outlet of the rotor and at given r radius can be expressed from Eq. (A.102) and it is shown in Eq. (A.103) [70], [97].

$$c_{2w} = \frac{c_{1wm}}{R \cos^2 \alpha_1} - \frac{(c_{1wm} - c_{2wm})}{R} \quad (\text{A.103})$$

Here, the equalities $c_{1w} = \frac{c_{1wm}}{R \cos^2 \alpha_1}$ and $R = r/r_m$ are considered. As c_{2w} is known, c_{2a} can be calculated by integrating Eq. (A.94) for the outlet cross section (cross section 2) between l and R and using Eq. (A.103) [97]:

$$c_{2a} = \sqrt{c_{2am}^2 + 4c_{1wm}^2 \left(\frac{1}{R \cos^2 \alpha_1} - 1 \right) \sin^2 \alpha_1 \cos^2 \alpha_1 - 2c_{1wm}^2} \quad (\text{A.104})$$

$$\sqrt{\left(1 - \frac{c_{2wm}}{c_{1wm}}\right) (1 + \cos^2 \alpha_1) \left(\frac{1}{R(1 + \cos^2 \alpha_1)} - 1\right) \sin^2 \alpha_1}$$

As the absolute velocity components at the rotor outlet are determined, the flow angles, the absolute and relative velocities are calculated as follows:

$$\alpha_2 = \arctan \left(\frac{c_{2a}}{c_{2w}} \right) \quad (\text{A.105})$$

$$c_2 = \sqrt{c_{2a}^2 + c_{2w}^2} \quad (\text{A.106})$$

$$w_2 = \sqrt{c_2^2 + u_2^2 - 2c_2 u_2 \cos \alpha_2} \quad (\text{A.107})$$

$$\beta_2 = \arcsin \left(\frac{c_{2a}}{w_2} \right) \quad (\text{A.108})$$

The final outcomes for the velocity triangles at hub, mean and tip section are shown in Table A.6.

Table A.6 Components and angles (measured from the tangential direction) of the velocity triangles in the turbine at hub, mean and tip sections

Data	Hub section	Mean section	Tip section
r [m]	0.0515	0.065	0.0785
R [m]	0.7923	1	1.2077
u_1 [m/s]	231.9	292.7	353.48
u_2 [m/s]	231.9	292.7	353.48
c_1 [m/s]	640.52	520.5	439.93
c_{1a} [m/s]	211.2821	171.7	145.12
c_{1u} [m/s]	604.667	491.37	415.3
c_2 [m/s]	72.08	193.66	229.021
c_{2a} [m/s]	71.22	193.445	228.46
c_{2u} [m/s]	-11.04	9.162	16.027
w_1 [m/s]	376.787	269.59	189.985
w_2 [m/s]	290.516	343.235	358.8
α_1 [°]	19.26	19.26	19.26
α_2 [°]	-81.188	87.288	85.987
β_1 [°]	34.1	40.8	49.8
β_2 [°]	14.19	34.3	39.55

The absolute Mach number at the exit and at the hub section of the turbine stator is higher than 1, so the flow is deviated due to the expansion in the obliquely cut blade nozzle section. Hence, the new absolute flow angle is computed (see Eq. (A.109) [1], [96]) and considered hereafter.

$$\alpha_{1,new} = \arcsin\left(\frac{\sin(\alpha_{1,original})}{q(\lambda_1)}\right) = 23.9^\circ \text{ where } \lambda_1 = \frac{c_1}{c_{1,crit}} \quad (\text{A.109})$$

Following the 3D extension of the mean line design by means of blade twisting, the next step of the turbine, particularly the turbine blade design is the determination of the blade chord, pitch and the number of blades.

The chord is computed by the length of the blade and the blade aspect ratio (l/c) as it is shown in Eq. (A.110) [1].

$$c = \frac{l}{\left(\frac{l}{c}\right)} \quad (\text{A.110})$$

The $\frac{l}{c} = 0.73$ and 1.17 has been defined in the present case for the stator and rotor blade respectively and l is 0.027 m for both. The optimum ratios of the blade spacing to chord length in the function of the flow angles are shown in Fig. A.15. As these flow angles are known, the value of t/c can be determined. It results 0.7 for

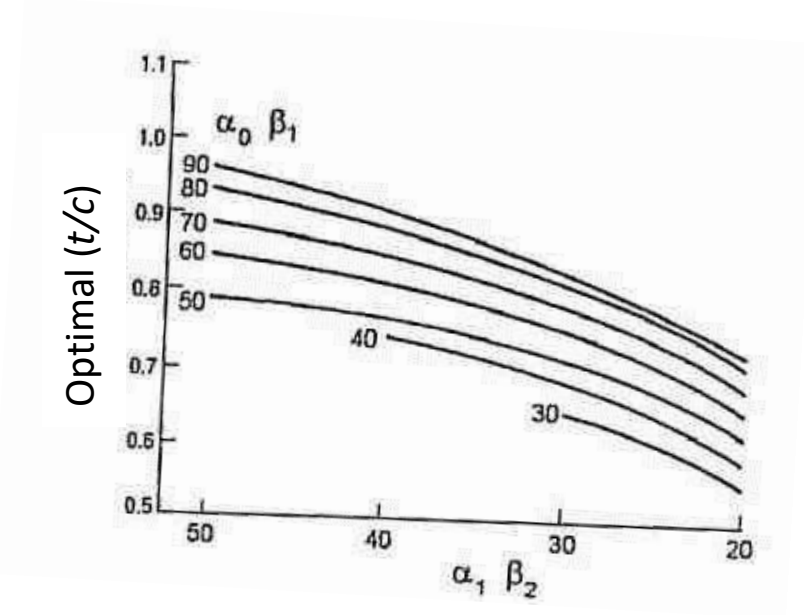


Figure A.15 The relationship between the optimal t/c ratio vs. absolute and relative flow angles [1]

the stator and 0.72 for the rotor. Hence, the spacing at the mean section of the turbine is calculated by Eq. (A.111) [1].

$$t = c \left(\frac{t}{c} \right)_{opt} \quad (\text{A.111})$$

The blade numbers are determined by Eq. (A.112).

$$z = \frac{\pi D_{1m}}{t} \quad (\text{A.112})$$

The results of the chord, blade spacing and the number of blades at the mean section of the turbine are shown in Table A.7.

Table A.7 Chord (c), blade pitch (t) and the number of the blades (z) at the mean section of the turbine stator and rotor

Data	Stator	Rotor
c [m]	0.037	0.023
t [m]	0.025	0.016
z [piece]	17	27

The flow angles in the turbine segments at the hub, mean and tip sections are calculated already and they are shown in Table A.6. The next step before creating the 3D models of the blades is to determine the corresponding blade angles and profiles, which, beside the flow deviation over Mach number 1 at the exit of the blade, considers the slip below $M=1$ and the contraction too [1]. The design of the blade geometry is completed by the method of using profile catalogue described in detail in [1] in chapter 7: Blade Profile Construction.

A.5 Aspects and Design of Exhaust Nozzle

A simple convergent-shaped exhaust nozzle is designed with 75 cm² effective exit area, which makes the nozzle unchoked at the design point with low pressure recovery factor. The inlet size of the nozzle is fit to the dimensions of the turbine exit annular section. The nozzle is shown in Fig. 4.1 as a part of the complete jet engine.

The last step of the mean line design is the determination of the exhaust velocity and the thrust. The velocity of the exhaust gas at the exit of the nozzle is calculated by Eq. (A.113):

$$u_9 = \sqrt{2C_{p,gas}T_{05} \left(1 - \frac{1}{\left(\frac{p_{05}}{p_9}\right)^{\frac{\gamma_{gas}-1}{\gamma_{gas}}}} \right) \eta_n} \quad (\text{A.113})$$

The exhaust gas velocity is 333.1 m/s at the exit of the nozzle. The thrust is 333.1 N as the mass flow rate is 1 kg/s. The flow is fully expanded (unchoked) and start condition is considered. The subscripts are based on the numberings, which are shown in Fig. 3.6.

APPENDIX B - Introduction of the Used CFD Methodology by Means of ANSYS CFX

B.1 Governing Equation

The basics of the used commercial CFD technology for computing the flow characteristics of the redesigned academic jet engine are the continuity, momentum and energy conservation laws. These equations are the most suitable mathematical expressions in flow complexity point of view, and they form the system of the nonlinear partial differential equations.

The mass conservation law is the following [48]:

$$\frac{\partial \rho}{\partial t} + \nabla \cdot (\rho \mathbf{U}) = 0 \quad (\text{B.1})$$

The moment equation is expressed [48]:

$$\frac{\partial(\rho \mathbf{U})}{\partial t} + \nabla \cdot (\rho \mathbf{U} \otimes \mathbf{U}) = -\nabla p + \nabla \cdot \boldsymbol{\tau} + \mathbf{S}_M \quad (\text{B.2})$$

where the stress tensor, $\boldsymbol{\tau}$, is related to strain rate [48]:

$$\boldsymbol{\tau} = \mu(\nabla \mathbf{U} + (\nabla \mathbf{U})^T - \frac{2}{3} \delta \nabla \mathbf{U}) \quad (\text{B.3})$$

The conservation of the specific total enthalpy is next [48]:

$$\frac{\partial(\rho h_{tot})}{\partial t} - \frac{\partial p}{\partial t} + \nabla \cdot (\rho \mathbf{U} h_{tot}) = \nabla \cdot (\lambda \nabla T) + \nabla \cdot (\mathbf{U} \cdot \boldsymbol{\tau}) + \mathbf{U} \cdot \mathbf{S}_M + \mathbf{S}_E \quad (\text{B.4})$$

where h_{tot} is related to the static $h(T, p)$ enthalpy by [48]:

$$h_{tot} = h + \frac{1}{2} \mathbf{U}^2 \quad (\text{B.5})$$

The term $\nabla \cdot (\mathbf{U} \cdot \boldsymbol{\tau})$ represents the work due to viscous stresses and is called the viscous work term. This models the internal heating by viscosity in the fluid and is considered in the present case. The term $\mathbf{U} \cdot \mathbf{S}_M$ is the work due to external momentum sources and is currently neglected [48].

These equations above are used in Reynolds averaged manner and turbulence modelling (see the next subchapter) is considered to closure the system of the nonlinear partial differential equations following the Boussinesq approximation. The reason why this methodology is used, that this approach is the most suitable from the accuracy and computational effort point of view in general and in rather complex engineering problems (compressible flow with high turbulence intensity at strong adverse pressure gradient conditions) and at complex geometry.

B.2 Turbulence Modelling [48]

Turbulence occurs when the inertia forces in the fluid become significant compared to viscous forces and is characterized by high Reynolds number. It consists of fluctuations in the flow field in time and space. The turbulence is a complex process, mainly because it is three dimensional, non-isotropic, unsteady and consists of many scales. It can have a significant effect on the characteristics of the flow.

In principle, the considered governing equations (including conservation of momentum, which are also called Navier-Stokes¹ equations) describe both laminar and turbulent flows without the need for additional information. However, turbulent flows at high Reynolds numbers span a large length and time scales and would generally involve length scales much smaller than the smallest finite volume mesh, which can be practically used in a numerical analysis. The Direct Numerical Simulation (DNS) of these flows around the complex geometry would require computing power, which are many orders of magnitude higher than the available in the foreseeable future.

Turbulence models expect to modify the original unsteady Navier-Stokes equations by the introduction of the averaged and fluctuating quantities to produce the Reynolds Averaged Navier-Stokes (RANS) equations. These equations are going to be solved for the mean flow quantities, while the turbulence effects are modelled without a need for resolving the turbulent fluctuations. All scales of the turbulence field are being modelled. Turbulence models based on the RANS equations are known as statistical turbulence models due to the statistical averaging procedure employed to obtain the equations.

The $k-\omega$ based SST turbulence model accounts for the transport of the turbulent shear stress and gives highly accurate predictions of the onset and the amount of flow separation under adverse pressure gradients [98]. The SST model uses a $k-\omega$ formulation in the inner parts of the boundary layer that makes the model directly usable all the way down to the wall through the viscous sub-layer, hence the SST model can be used as a Low-Re turbulence model without any extra damping functions. The SST formulation also switches to $k-\epsilon$ behaviour in the free-stream and thereby avoids the common $k-\omega$ problem, that the model is too sensitive to the inlet free-stream turbulence properties [99]. The SST model takes the transport of the shear stress into account; it modifies the turbulence eddy-viscosity function. The model is based on Bradshaw's assumption that the principal shear stress is proportional to the turbulent kinetic energy. The model improves the accuracy of prediction of flows with strong adverse pressure gradients and pressure-induced boundary layer separation. Thus, the SST model is used in this work. More detailed information about turbulence model is found in [98], [99] and [100].

B.3 Spray Breakup Models for Combustion

The combustion chamber is the mechanical component of the gas turbine where the heat is added to the system. The combustion develops in the combustion chamber. The fuel enters the combustion chamber in continuous liquid phase and then becomes dispersed one. Following the disintegration of the liquid continuous phase into the dispersed phase, the resulting droplet system is called spray. So, the spray breakup models for combustion are introduced in the present subchapter.

The breakup of liquid stream happens in the atomizer. Various atomizer types, based on their energy that is converted into the fluid to achieve atomization, can be realized, such as pressure atomizer - where the energy of the liquid is utilized -, rotational atomizer - where the mechanical energy utilized - and further types such as pneumatic based, electrical and acoustic can be distinguished for example.

As gas turbine engines are considered, the most used atomizer is the pressure type one. In the pressure atomizer, pressurized liquid passes through a narrow channel before injected into the gas stream or passed onto swirlers. Although the pressure type atomizer is the most widespread in the industry, it has some

¹ Claude-Louis Navier and George Gabriel Stokes described the motion of the fluid flow in 1822 and in 1845 respectively.

disadvantages, as it is suitable only for low mass flow rates, relatively coarse droplet sizes can be achieved and of course there is a need to pressurize the liquid [51].

The one of the most challenging parts of flow modelling is the breakup treatment of the liquid fuel in the combustion chamber. During the atomization process, the liquefied continuous phase fuel is dispersed to droplets to mix with air as much as possible. The purpose of atomization is to increase the area of the liquid; thus, the molecules are surrounded by more oxygen, which contributes to a more efficient combustion. On the other hand, better heat and momentum transfer is realized. Atomization process happens due to different types of forces within the liquid and gas, such as cavitation forces, forces due to turbulence and external aerodynamic forces resulting from the interaction of the two phases [51].

Multiphase flow

The examined process of fluid disintegration as two different state mediums are present needs to be considered as a multiphase flow phenomenon occurs. Multiphase flow can be modelled by two different ways: the Eulerian or the Lagrangian model. The Eulerian two-fluid model treats the dispersed phase as a continuous phase and different formulations are applied based on the mixed phases, such as gas-fluid or gas-solid mixture. In this model particle-particle forces are modelled, and also coupling of the two phases are represented by a pressure force, gravity force, interaction force and viscous force, which act on the two phases in the two-fluid model for a laminar case. The Lagrangian model is based on solving the equations of motion - second law of Newton - to determine the position and velocity of each particle. Solving and storing the state of each particle requires high computational capacity. Thus, the Lagrangian model is rather suitable for applications where relatively small numbers of particles are present and/or the collisions of particles are rare. There are three level of coupling between the fluid phase and dispersed phase based on assumptions made to reduce complexity of the problem and they include different levels of physical detail. If it is considered that just the fluid phase affects the dispersed phase and dispersed phase does not affect the fluid phase, there is one-way coupling between phases. When it is assumed that both phases affect each other, there is two-way coupling between phases. The most realistic model is four-way coupling, where besides the two phases affecting each other the particles also interact and affect each other as well [51]. Regarding the spray-type breakup model, which is implemented in CFX and can be applied for fuel injection systems, particle transport modelling is used. It is a type of multiphase model, where particulates are tracked through the flow in a Lagrangian way, rather than being modelled as an extra Eulerian phase. The full particulate phase is modelled by just a sample of individual particles. The tracking is carried out by forming a set of ordinary differential equations in time for each particle, consisting of equations for position, velocity, temperature, and masses of species. These equations are then integrated using a simple integration method to calculate the behaviour of the particles as they traverse the flow domain [48].

The atomization process can be divided into more steps till the combustion. First the injected liquid starts to breakup into larger structures, then, after the first interactions between liquid and gas, both large and small structures evolve. This stage of atomization is called primary breakup (see Fig. B.1) [101]. After this, during the secondary breakup, droplets disintegrate into finer drops [102], and finally evaporate. Including these steps, the spray combustion process can be divided into six parts: primary breakup, secondary breakup, droplet motion, droplet evaporation, mixing and combustion. Fuel droplets travel through the combustor with an initial velocity that they have after injector and they live until they evaporate totally. The evaporated fuel mixes with air and this mixture starts to burn when its temperature reaches the ignition temperature and fuel/air mixture ratio is within the flammability.

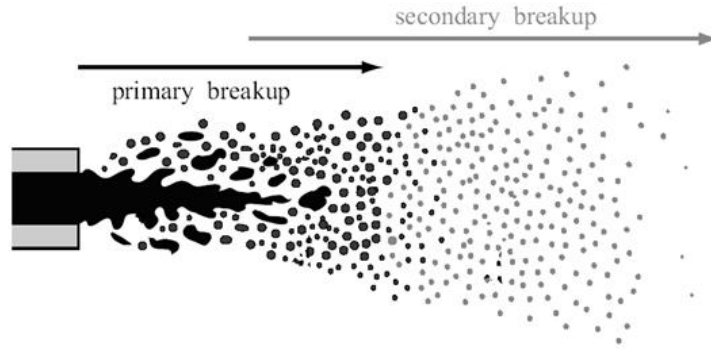


Figure B.1 Breakup of a liquid jet [102]

The primary breakup happens at the stage when the liquid state fuel first leaves the injector and enters the combustion chamber. In the combustion chamber, the continuous liquid breaks up into smaller particles, but still rather coarse droplets are present. The process of the primary breakup is highly dependent on the initial particle size, initial particle velocity, speed of liquid jet and initial spray angle at the outlet of the fuel nozzle. Based on the nozzle geometry, primary breakup model can be categorized into three types in ANSYS CFX. The simplest method is achieved by the Blob model. This method assumes that in the moment when particles exit the nozzle, the diameter of particles equal the diameter of the nozzle bore, from which the liquid jet comes (see Fig. B.2). The velocity of the particles is then retrieved according to the conservation of mass (see Eq. (B.6)). A_{nozzle} is the cross section of the nozzle and \dot{m}_{nozzle} is the mass flow through injector in Eq. (B.6)

$$U_{P,initial}(t) = \frac{\dot{m}_{nozzle}}{A_{nozzle}\rho_P} \quad (B.6)$$

[48]. The Blob method is the default injection approach in ANSYS CFX, does not require additional settings, however it has constraints such as possible turbulence, cavitation in the nozzle are not considered. In this approach all particles leaving injector are of spherical shape and with uniform size of the injector nozzle's diameter (B.7) [48], [101]. The injector must have a sharp corner at the end where the liquid enters the chamber. This sharp corner plays an important role since it helps the liquid to turn into smaller parts.

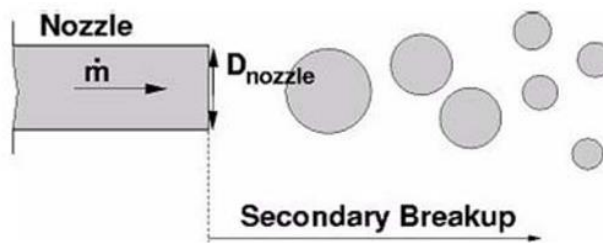


Figure B.2 Blob method [48]

$$D_p = D_{Nozzle} \quad (B.7)$$

Enhanced Blob method is based on the previous method; thus, it also assumes that atomization process need not be resolved in detail. However, in opposition to the Blob method, it takes into consideration the possible cavitation in the nozzle. This model is capable to determine whether there is a possibility for cavitation by comparing the static pressure at the “vena contracta” to the vapor pressure [48]. The ANSYS CFX also utilizes a liquid contraction coefficient in the nozzle to determine the jet velocity in the nozzle. Once “vena contracta” pressure is higher than vapor pressure, no cavitation occurs, and the model is simplified into the Blob model. If cavitation occur the Enhanced Blob method determines the effective injection velocity and particle diameter. Besides Blob and Enhanced Blob methods also Linearized Instability Sheet Atomization model and Turbulence Induced Atomization is available in ANSYS CFX to model the primary breakup [48]. The characteristics of the previously mentioned primary breakup models are that they present average information (liquid velocity, turbulence, location and distribution of gas zones, etc.) about the disintegration, thus quasi one-dimensional data is shown instead of a spectrum of data. Primary breakup injection is only available for cone type injection and only if the nozzle cross section data is greater than 0 [48].

After primary breakup process, coarse liquid particles disintegrate into finer droplets before they evaporate. This stage is called the secondary breakup of the liquid. Different mechanisms, such as turbulence, implosion of cavitation and external aerodynamic forces act on the liquid jet in this stage [48]. Based on the ratio of these parameters, the secondary breakup characteristics vary. For the description of the vast variety of secondary breakups, dimensionless numbers, such as the Ohnesorge and Weber numbers are used. Ohnesorge number indicates the ratio of viscous and surface tension in the liquid by involving only drop properties. On the other hand, Weber number indicates the ratio between the inertia forces and the surface tension forces in the liquid. Surface tension coefficient of fuel droplets are considered with value of 0.027 N/m [103]. Dependent on the size of Weber number, in increasing order, the following breakup regimes occur: vibrational breakup, bag breakup, bag-and-stamen breakup, sheet stripping and catastrophic breakup [48]. Vibrational breakup occurs when particles can oscillate around their natural frequencies and disintegrate due to the forces present. This type of breakup is relatively long. Bag-and-stamen break up occurs via a formation of a rim and a bag in the liquid before disintegrating into fine droplets and evaporating. During sheet stripping, a sheet of liquid is formed, and the fine droplets detach from the edges of the sheet.

ANSYS CFX uses a statistical modelling for secondary breakup, where droplets breakup into child droplets, and during this their quantity increases while their size decreases [48]. During this process the total particle mass remains constant. The statistical models available in ANSYS CFX for breakup are mentioned briefly in the followings. Reitz and Diwakar Breakup model distinguishes between bag breakup and stripping breakup and applies them accordingly when the related Weber number is achieved. Schmehl breakup model besides monitoring the Weber number uses experimental results in determining the breakup time and droplet deformation. In this model, depending on the Weber number, three droplet breakup scenarios are possible. The Taylor Analogy Breakup (TAB) model assumes that the droplet distortion is a one-dimensional forced, damped harmonic oscillation system, like a spring-damper system. The droplet deformation is expressed in a dimensionless quantity. When the forces exerted on the droplet exceed unity, the particle disintegrates. In other words, the disintegration in this model occurs, when the distorted particle radius becomes smaller than half of the equilibrium particle radius. The Enhanced Taylor Analogy Breakup (ETAB) model works on the same principle as TAB model, however it also takes into consideration that the rate of child droplet generation is proportional to the child droplets [48]. The ETAB model estimates more accurately the penetration depth, cross-sectional droplet size distribution than the TAB model, where it is usually underestimated. Finally, the Cascade Atomization Breakup (CAB) model is a further development of the ETAB model as it uses additional equations to determine the child droplet sizes more accurately, furthermore it can consider catastrophic breakup as well [48].

Considering propagation of liquid particles after being injected into the gas stream, drag plays an essential role. Many particles drag models assume a spherical shape during breakup process, however in reality, shape of particles can vary in a vast range. Thus, ANSYS CFX provides dynamic modelling of particle drag by changing drag coefficient, based on the distortion of the shape. As distortion of the particles are involved, dynamic drag model can only be applied for TAB, ETAB and CAB break up models. Two dynamic drag modelling methods are available in ANSYS CFX, Liu - where drag coefficient varies linearly between sphere and disk shape - and Schmehl - which operates similarly for Liu's, however it can be only applied in Schmehl breakup model [48].

As liquid-liquid, liquid-gas particles interact with each other during breakup heat transfer and mass transfer must also be mentioned. Droplet heat transfer can occur by convective, latent or radiative heat transfer [48].

B.4 Combustion

Combustion process consists of reactions between multiple components, specifically between fuel - which can be anything that conserves its energy until released by chemical reaction - and oxidizer. JET-A (kerosene) as fuel and oxygen content of the air as oxidizer have been applied in the present analyses of the redesigned academic jet engine. Following the breaking up process of the liquid fuel, multi component flow should be considered with Eulerian approach for cost effective numerical treatment of the combustion. The formulation used for multicomponent flows in ANSYS CFX is used here with considering source/sink term due to chemical reactions [48]. Dealing with multi component flow in the applied software assumes that components are mixed in a molecular level that they share the same mean velocity, pressure and temperature field. In multi component flow terminology, pure substance is used for materials that comprise from only one kind of molecule and have specified properties. When a pure substance is used as a part of a multi component fluid, it is called a component of that fluid. Furthermore, ideal mixture is used for mixtures where properties of the mixture can be calculated directly from the properties of the component and their proportion in the mixture. In studying combustion, flame characteristics, such as propagation, flame front and occurrence of component mixing are considered. Flame is the part of combustion, where the released chemical energy from the hot gases emit energy in a visible spectrum. The flame front or reaction zone is a small region where chemical reactions take place. Flames can also be categorized regarding where the oxidizer meets the fuel. Based on this, premixed, partially premixed and non-premixed flames can be distinguished. In many industrial combustion devices, pure non-premixed combustion is less present than premixed or partly premixed combustion [48].

As the combustion process are briefly initiated above, the characteristics of the most dominant models available in ANSYS CFX are described: i. Eddy Dissipation Model (EDM), ii. Finite Rate Chemistry (FRC) Model iii. EDM/FRC Model iv. Flamelet Model, v. Burning Velocity Model (BVM), and vi. Extended Coherent Flame Model (ECFM) [48].

The EDM is based on that the chemical reaction of the combustion is relatively fast compared to the transport processes in the flow. In practice, it means that once the fuel and the oxidizer become mixed at molecular level, the combustion process instantaneously occurs. The time of mixing highly depends on the eddies of the flow, thus on the turbulent kinetic energy and its dissipation. This concept of reaction control is applicable in many industrial combustion problems where reaction rates are fast compared to reactant mixing rates [48]. The EDM model is best applied in turbulent conditions, has a robust performance, suitable for premixed, partially premixed and non-premixed combustions [104]. As a downside, EDM can produce unrealistic results as there is no kinetic control of the reaction process; however, it is handled by product limiters [51]. FRC model enables the computation of reaction rates described by the molecular interactions between the components in the fluid [48]. This model is suitable for situations where the chemical time scale of the process

has a great influence on combustion, furthermore it is applicable for both laminar and turbulent flow conditions. EDM and FRC model can be combined, where both the mixing times and reaction rates are computed, and the minimum is utilized out of them [51]. This model is usually advisable for combustion processes where one part of the flow is limited by kinetics and the other part is limited by turbulent mixing. Flamelet model assumes that the combustion occurs in thin sheets with stoichiometric inner structures, which are called flamelets. The turbulent flame itself is built up by the flamelets, which are embedded in the flow field. The flamelet concept can be used for non-premixed combustion describes the interaction of chemistry with turbulence in the limit of fast reaction [48]. The advantage of the flamelet model is that detailed information is retrieved about the molecular transport processes and about the elementary kinetic reactions by solving only two scalar equations in case of turbulent flow. However, as it is already mentioned, the model is performed by assuming fast reactions, and is applicable in only two-feed systems such as fuel and oxidizer and requires chemistry library as input. Flamelet libraries provide information about mean species of mass fractions as a function of mean mixture fraction, variance of mixture fraction and scalar dissipation rates. Fluid properties, such as density and temperatures are computed from the mean composition of the fluid as in the EDM model. Concerning combustion of the analysed academic jet engine, as a non-premixed, turbulent and fast combustion is realized, Probability Density Function (PDF)-mixture fraction based flamelet model is used in the present thesis. The next model is the BVM, which is suitable for premixed or partially premixed combustion and it can be split into two independent parts [48]:

- Model for the progress of the global reaction: Burning Velocity Model (BVM), also called Turbulent Flame Closure (TFC) [48].
- Model for the composition of the reacted and non-reacted fractions of the fluid: Laminar Flamelet with PDF [48].

The mass fractions in the non-reacted fraction of the fluid are obtained by linear blending of fuel and oxidizer compositions. The species mass fractions in the burned fraction of the fluid are computed by applying the flamelet model [48]. ECFM shares the framework for premixed or partially premixed combustion with the BVM. The transport equations are solved for mean mixture fraction, variance of mixture fraction and for either reaction progress or weighted reaction progress [48].

B.5 Numerical Method

The considered governing equations has no general closed form solution in the most complex form over arbitrary kind and size of flow domains. However, in the consideration of increasing expectations arisen from the industry and the high-level evolution of the computer technology, the different numerical methods have been developed and implemented in the complex framework of CFD programs as it is the case also at ANSYS CFX.

ANSYS CFX uses an element-based finite volume method, which involves discretizing the spatial domain using a mesh. The mesh is used to construct finite volumes, which are used to conserve relevant quantities such as mass, momentum, energy and other relevant transport properties [48].

Many discrete approximations developed for CFD are based on series expansion approximations of continuous functions (such as the Taylor series). The order accuracy of the approximation is determined by the exponent on the mesh spacing or time step factor of the largest term in the truncated part of the series expansion, which is the first term excluded from the approximation. Increasing the order-accuracy of an approximation generally implies that errors are reduced more quickly with mesh or time step size refinement. Unfortunately, in addition to increasing the computational load, high-order approximations are also generally less robust (that is, less

numerically stable) than their low-order counterparts. ANSYS CFX uses second order accurate approximations as much as possible [48]. Detailed information about discretization in CFX are found in [48].

The used commercial code applies a co-located (non-staggered) grid layout such that the control volumes are identical for all transport equations. However, according to Pantankar, naïve co-located methods lead to a decoupled (checkerboard) pressure field. Rhie and Chow proposed an alternative discretization for the mass flows to avoid the decoupling, and this discretization was modified by Majumdar to remove the dependence of the steady-state solution on the time step. A similar strategy is adopted in ANSYS CFX [48].

ANSYS CFX uses a coupled solver, which solves the hydrodynamic equations (for u , v , w , p) as a single system. This solution approach uses a fully implicit discretization of the equations at any given time step. For steady state problems, the time-step behaves like an ‘acceleration parameter’, to guide the approximate solutions in a physically based manner to a steady-state solution. This reduces the number of iterations required for convergence to a steady state, or to calculate the solution for each time step in a time-dependent analysis [48].

ANSYS CFX applies an algebraic multigrid accelerated Incomplete Lower Upper (ILU) factorization technique for solving the discrete system of the linearized equations. It is an iterative solver whereby the exact solution of the equations is approached during several iterations. It applies a series of coarse meshes in order that the longer wavelength errors disappear from the computational domain as close short as the shorter wavelength errors do [48]. ANSYS CFX uses an implementation of the above-mentioned Algebraic Multigrid called Additive Correction method. This approach is ideally suited to the CFX-Solver implementation because, it takes advantage of the fact that the discrete equations are representative of the balance of conserved quantities over a control volume. The coarse mesh equations can be created by merging the original control volumes to create larger [48].

More detailed information and the theoretical background about the used CFD program can be found in [48].

APPENDIX C - Numerical Algorithm of 2D Inhouse Inviscid Flow Solver [54]

C.1 Governing Equations

Due to the aeronautical application with the assumption of non-viscous flow, the conservative form of the unsteady 2D Euler equations has been used as governing equations for compressible and rotational flow modelling, which are given in Cartesian coordinate system by Eq. (C.1) [105] in $\Lambda(x,y)$ [54],

$$\frac{\partial \mathbf{U}}{\partial t} + \frac{\partial \mathbf{F}(\mathbf{U})}{\partial x} + \frac{\partial \mathbf{G}(\mathbf{U})}{\partial y} = 0 \quad (\text{C.1})$$

where $x, y \in \mathbf{R}$ and $t \in \mathbf{R}^+$. The conservative variables and convective fluxes are given by Eq. (C.2),

$$\mathbf{U} = \begin{pmatrix} \rho \\ \rho u \\ \rho v \\ \rho E \end{pmatrix}, \mathbf{F}(\mathbf{U}) = \begin{pmatrix} \rho u \\ \rho u^2 + p \\ \rho uv \\ \rho u h_0 \end{pmatrix}, \mathbf{G}(\mathbf{U}) = \begin{pmatrix} \rho v \\ \rho v u \\ \rho v^2 + p \\ \rho v h_0 \end{pmatrix} \quad (\text{C.2})$$

Here, ρ is the density, u and v are the Cartesian components of velocity and p is the static pressure. The specific total energy and specific total enthalpy are the following [54]:

$$E = \frac{1}{\gamma-1} \frac{p}{\rho} + \frac{u^2+v^2}{2}, h_0 = \frac{\gamma}{\gamma-1} \frac{p}{\rho} + \frac{u^2+v^2}{2} \quad (\text{C.3})$$

The γ is the ratio of specific heats.

C.2 Finite Volume Discretization Method

Integrating system of Eqs. (C.1) over a control surface Ω , which is bounded by interface Γ , and applying the Gauss divergence theorem gives [105]:

$$\frac{\partial}{\partial t} \iint_{\Omega} U d\Omega + \int_{\Gamma} \vec{H} \vec{n} d\Gamma = 0, \quad (\text{C.4})$$

where $\vec{n} = (n_x, n_y)$ is the local outward pointing unit normal vector of the cell boundary, $\vec{H} = F\vec{e}_x + G\vec{e}_y$ and $\vec{H}\vec{n}$ is given by

$$H_n = \vec{H}\vec{n} = \begin{pmatrix} \rho V_n \\ \rho u V_n + p n_x \\ \rho v V_n + p n_y \\ \rho V_n h_0 \end{pmatrix}, \quad (\text{C.5})$$

where

$$V_n = \vec{V}\vec{n} = (u\vec{e}_x + v\vec{e}_y)(n_x\vec{e}_x + n_y\vec{e}_y) \quad (\text{C.6})$$

Finite volume method has been applied for the discretization. The second integral in Eq. (C.4) is replaced by summation over the all boundaries N_b of the control surface Ω_j . Eq. (C.4) can be written in the following semi-discrete form for the point, j :

$$\frac{d}{dt}U_j = -\frac{1}{\Omega_j} \sum_{k=1}^{N_b} [H_n]_{j,k} \Gamma_{j,k} = \mathfrak{R}_j \quad (\text{C.7})$$

where $[H_n]_{j,k}$ is the total inviscid flux normal to the cell boundary at cell face boundary k and U_j is the vector of conservative variables in Eqs. (C.2). In present case, in 2D, Ω_j is the area of the finite surface and $\Gamma_{j,k}$ is the length of a cell boundary number k of Ω_j [54]. In case of upstream differencing (or upwind) schemes, the quantity $[H_n]_{j,k}$ are characterized by a flux function \hat{H}_n , which takes into account the sign of the Jacobian matrices, or in other words the relevant propagation directions between the left (L) and right (R) states (sides) of the cell boundary [105]:

$$\hat{H}_n(U^L, U^R) \quad (\text{C.8})$$

The $\hat{H}_n(U^L, U^R)$ can be evaluated by linear wave decomposition where an unique average state (which is denoted by a hat) of the left and right states exist [106]:

$$\hat{H}_n(U^L, U^R) = \frac{1}{2} \{H_n(U^L) + H_n(U^R) - |\hat{D}_n(U^L, U^R)|(U^R - U^L)\} \quad (\text{C.9})$$

For ideal gas, Roe has shown that the matrix \hat{D}_n is equal to the Jacobian D_n [106] when expressed as a function of the variables of $\hat{\rho}$, \hat{u} , \hat{v} , and \hat{h}_0 , which are weighted variables of the square root of density [54]. Detailed information about the Roe's method of the approximate Riemann solver is found in [106]. The method of Roe is highly non-dissipative and closely linked to the concept of characteristic transport. It is one of the most powerful linear Riemann solvers due to the excellent discontinuity-capturing property including shear waves [54]. However, it is well-known that flux function mentioned above can produce non-physical expansion shocks that violate the entropy condition [54]. This can be avoided, by modifying the modulus of the eigenvalues for the non-linear fields and method of Yee [107] is used at the present case [54].

Monotone Upstream Schemes for Conservation Laws (MUSCL) approach is implemented for higher order spatial extension by which, the piece-wise constant distribution of the initial variables over the cell can be replaced by a piecewise linear or quadratic one. The mathematical deduction starts with the introduction of Taylor series expansion around point i [54]:

$$U(x) = U_i + \frac{\partial U}{\partial x} \Big|_{x_i} (x - x_i) + \frac{1}{2} \frac{\partial^2 U}{\partial x^2} \Big|_{x_i} (x - x_i)^2 + O(\Delta x^3) \quad (\text{C.10})$$

The x spatial direction corresponds to local curvilinear coordinate in each direction. After discretization and integration of Eq. (C.10) yields:

$$\begin{aligned} (U^R =) \bar{U}_{i+\frac{1}{2}}^R &= U_{i+1} - \frac{1}{4} \left[(1 - \kappa) \Delta_{i+\frac{3}{2}} + (1 + \kappa) \Delta_{i+\frac{1}{2}} \right] \text{ and} \\ (U^L =) \bar{U}_{i+\frac{1}{2}}^L &= U_i + \frac{1}{4} \left[(1 - \kappa) \Delta_{i-\frac{1}{2}} + (1 + \kappa) \Delta_{i+\frac{1}{2}} \right] \end{aligned} \quad (\text{C.11})$$

where $\Delta_{i-\frac{1}{2}} = U_i - U_{i-1}$, $\Delta_{i+\frac{1}{2}} = U_{i+1} - U_i$, $\Delta_{i+\frac{3}{2}} = U_{i+2} - U_{i+1}$ and the new left and right states next to the cell boundary $i + \frac{1}{2}$ (between points i and $i+1$) are denoted by U^L and U^R . The $\kappa = 1/3$ in Eq. (C.11) corresponds to the third order accurate space discretization in one dimensional problem [105]. The spurious oscillations (wiggles) can occur with high order spatial discretization schemes due to shocks, discontinuities or sharp changes in the solution domain. Hence, in this case, Mulder limiter is implemented in the high resolution schemes for monotonicity preserving [105]:

$$(U^R =) \bar{U}_{i+\frac{1}{2}}^R = U_{i+1} - \frac{1}{4}\psi^R \left[(1 - \kappa\psi^R)\Delta_{i+\frac{3}{2}} + (1 + \kappa\psi^R)\Delta_{i+\frac{1}{2}} \right] \text{ and} \quad (\text{C.12})$$

$$(U^L =) \bar{U}_{i+\frac{1}{2}}^L = U_i + \frac{1}{4}\psi^L \left[(1 - \kappa\psi^L)\Delta_{i-\frac{1}{2}} + (1 + \kappa\psi^L)\Delta_{i+\frac{1}{2}} \right] \quad (\text{C.13})$$

where

$$\psi^R = \frac{2\Delta_{i+\frac{1}{2}}\Delta_{i+\frac{3}{2}+\varepsilon}}{\Delta_{i+\frac{1}{2}}^2 + \Delta_{i+\frac{3}{2}+\varepsilon}^2}, \quad \psi^L = \frac{2\Delta_{i-\frac{1}{2}}\Delta_{i+\frac{1}{2}+\varepsilon}}{\Delta_{i-\frac{1}{2}}^2 + \Delta_{i+\frac{1}{2}+\varepsilon}^2} \text{ and } 10^{-7} \leq \varepsilon \leq 10^{-5} \quad (\text{C.14})$$

A widely used class of non-linear multi-stage time integration techniques is given by the Runge-Kutta (RK) schemes. They are usually designed to obtain higher order temporal accuracy with minimum computational storage and the large stability range with the specific coefficients, even though it has been often used for steady state calculations as herein. The 4 stages RK method (RK4) is used to solve the time derivatives of the conservative variables in Eq. (C.7) [105]:

$$\begin{aligned} U^0 &= U^n \\ U^k &= U^0 + \alpha_k \Delta t \mathcal{R}(U^{k-1}), \quad k = 1, \dots, 4 \\ U^{n+1} &= U^m \end{aligned} \quad (\text{C.15})$$

where $\alpha_1 = \frac{1}{8}$, $\alpha_2 = 0.306$, $\alpha_3 = 0.587$, $\alpha_4 = 1$ [108], n is the previous time step and $n+1$ is the next time step. The RK4 index is denoted by k and it runs from 1 to m with its maximum value of 4. Due to the steady state assumption, the time accuracy is not required; hence the RK4 coefficients are applied to have high stability and smoothing properties of the upwind scheme with MUSCL reconstruction. In order to optimize the time step behind the stability criterion, the local time stepping has been used for every cells j as follows [109]:

$$\Delta t_j = \frac{\Omega_j \nu}{\sum_{k=1}^{N_b} (|V_n| + a)_{j,k} \Gamma_{j,k}} \quad (\text{C.16})$$

where Ω_j is the area of the finite surface j , ν is the Courant number, $\Gamma_{j,k}$ is the length of the cell boundary k of Ω_j , V_n is the cell face normal velocity and a is the sound speed. Detailed description of the finite volume discretization and the analysis of numerical methods are found in [110] and [111].

C.3 Boundary Conditions

The numerical treatment of the boundary conditions strongly influences not only the convergence properties but the accuracy of the results in solving partial differential equations. The hyperbolic system that consists of N_e partial differential equations, $N_p \leq N_e$ physical boundary conditions (PBC) and $N_n = N_e - N_p$ numerical boundary conditions (NBC) are necessary to be prescribed [112]. The former must secure the existence and

uniqueness of the exact solution, while the latter are supposed to ensure that various perturbations generated in the interior of the computational domain leave it without being reflected at the boundaries [108]. Hence, a proper combination of PBC and NBC must be imposed by means of some extra calculations.

The characteristic form of the governing equations in outward cell face normal direction yields a sequence of decoupled convection equations as follows [110]:

$$\begin{aligned}
\frac{\partial W_n^{(1)}}{\partial t} + V_n \frac{\partial W_n^{(1)}}{\partial n} &= 0 \\
\frac{\partial W_n^{(2)}}{\partial t} + V_n \frac{\partial W_n^{(2)}}{\partial n} &= 0 \\
\frac{\partial W_n^{(3)}}{\partial t} + (V_n + a) \frac{\partial W_n^{(3)}}{\partial n} &= 0 \\
\frac{\partial W_n^{(4)}}{\partial t} + (V_n - a) \frac{\partial W_n^{(4)}}{\partial n} &= 0
\end{aligned} \tag{C.17}$$

Where n is the unit normal direction to the cell face, V_n is the scalar product of vector \vec{V} and \vec{n} , a is the sound speed and W_n is the characteristic variables or Riemann invariants. These invariants are transported along the characteristic curves at the respective speeds. The direction of wave propagation (V_n , V_n , V_n+a , V_n-a) depends not only on the sign of the velocity V_n but also on the local speed of sound a . At the boundary, the number of PBC to be imposed equals the number of negative eigenvalues, which correspond to the incoming characteristics from the outside (boundary) to the computational domain. The need for NBCs comes from the fact that the actual problem to be solved is formulated in terms of the conservative variables rather than Riemann invariants. Therefore, it is impossible to impose the Dirichlet boundary conditions in the usual way. It is common practice to recover the boundary values by changing to the characteristic variables, evaluating the incoming Riemann invariants from the PBCs and extrapolating the outgoing ones from the interior of the computational domain [112].

Regarding the specific and detailed description of the inlet, outlet, solid wall, opening and translational periodic boundary conditions, in theoretical manner, they are found in [54].

C.4 Wall Modification Algorithm

While the incoming and out coming velocity distribution is given at the solid wall, based on the inverse mode of the analysis by using so called opening boundary condition, the last step of the iterative design cycle is the modification of the geometry. The new position of the solid boundary coordinates is calculated by setting the wall parallel to the local velocity vector:

$$\Delta y_i(x_i) = \sum_{k=Le}^i \left(\frac{v_k}{u_k} \Delta x_k \right) \tag{C.18}$$

where u and v are the Cartesian component of the velocity vector. The wall modification starts from the leading edge or inlet stagnation point till the trailing edge or the outlet stagnation point and completed in vertical directions (see Fig. C.1).

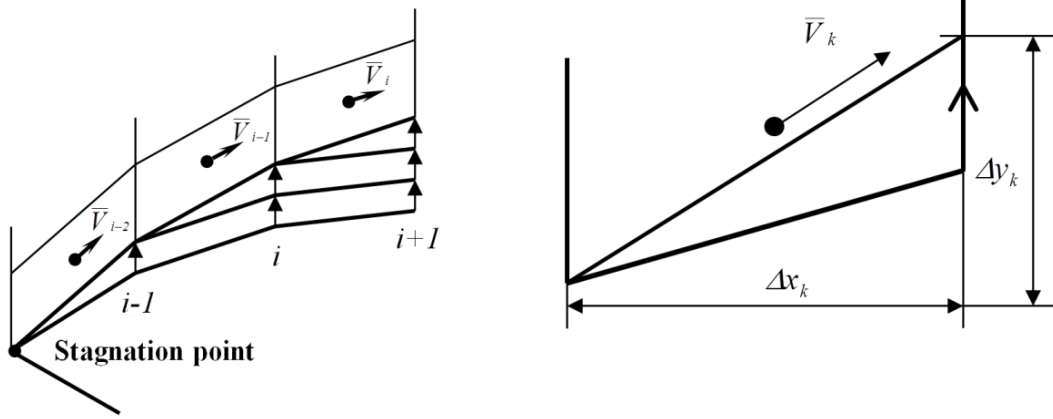


Figure C.1 Schematic view of the wall modification process based on the local velocity vector [54]

APPENDIX D - Constrained Optimization

[54]

D.1 Introduction

The inverse design methods require optimal pressure or velocity distributions to determine the adherent geometry. Hence, the main goal of the present chapter is to introduce the complete procedure how the pressure distribution is optimized. The method is based on Stratford's experimental investigation on separation prediction and SQP (Sequential Quadratic Programming) nonlinear constraint optimization algorithm.

D.2 Stratford's Separation Prediction Method

In order to maximize the blade loading or the lift force of the suction side of a profile at given and constant operational (boundary) conditions, the pressure distribution should be as low as possible over the solid surface. However, the adverse pressure gradient must be present after the location of the maximum velocity (and minimum pressure) in order to recover downstream conditions. The adverse pressure gradient till the trailing edge should be limited in each discretized point to be just below the condition of causing separation. The maximum closed area bounded by the suction and the pressure side distributions in conjunction with the mentioned limited values of pressure gradients will provide the optimum solution as a target distribution to be specified for the inverse design method.

There are several existing methods for predicting separation as Goldschmied, Stratford, Head, and Cebeci-Smith for example. The accuracy these methods were examined several times. One of the outputs of these investigation shows that the operation of Goldschmied's method is unreliable. The other three are in reasonable agreement and Stratford's method tended to predict separation slightly early. The Cebeci-Smith method is appeared to be the best and the Head method is a strong second one [113]. Due to the good accuracy, simple expressions and conservative characteristics for predicting separation, Stratford's method has been used in the present case.

Stratford has derived an empirical formula for predicting the point of separation in an arbitrary decelerating flow at the order of $Re=10E+6$ [114],

$$\frac{\bar{C}_p [x(d\bar{C}_p/dx)]^{1/2}}{(10^{-6}Re)^{1/10}} = S \quad (D.1)$$

where the canonical pressure distribution is

$$\bar{C}_p = \frac{p - p_0}{\frac{1}{2}\rho_0 u_0^2} \quad (D.2)$$

and if $d^2p/dx^2 \geq 0$ then $S = 0.39$ or if $d^2p/dx^2 < 0$ then $S = 0.35$. Additionally, $\bar{C}_p \leq 4/7$. The flow under investigation is flat-plate flow. Hence, x is distance measured from the leading edge of the plate, and, $Re = u_0 x / \nu$. If in a flow pressure begins to rise at a point x_0 (it is the position of minimum pressure and maximum velocity and its parameters belong to subscript of 0), left-hand side of Eq. (D.1) starts from zero value. The left-hand side then grows. When it reaches the limiting value of S , separation is said to occur. If S is held at its limiting value of 0.39 for $d^2p/dx^2 > 0$, Eq. (D.1) amounts to an ordinary differential equation for $\bar{C}_p(x)$. It is evident from Eq. (D.1) that the equation describes a flow that is ready everywhere to separate. Stratford presents the following solutions [114]:

$$\bar{C}_p = 0.645 \left\{ 0.435 Re_0^{1/5} [(x/x_0)^{1/5} - 1] \right\}^{2/n} \quad \text{for } \bar{C}_p \leq (n-2)/(n+1) \quad \text{and} \quad (D.3)$$

$$\bar{C}_p = 1 - \frac{a}{[(x/x_0) + b]^{1/2}} \quad \text{for } \bar{C}_p \geq (n-2)/(n+1) \quad (D.4)$$

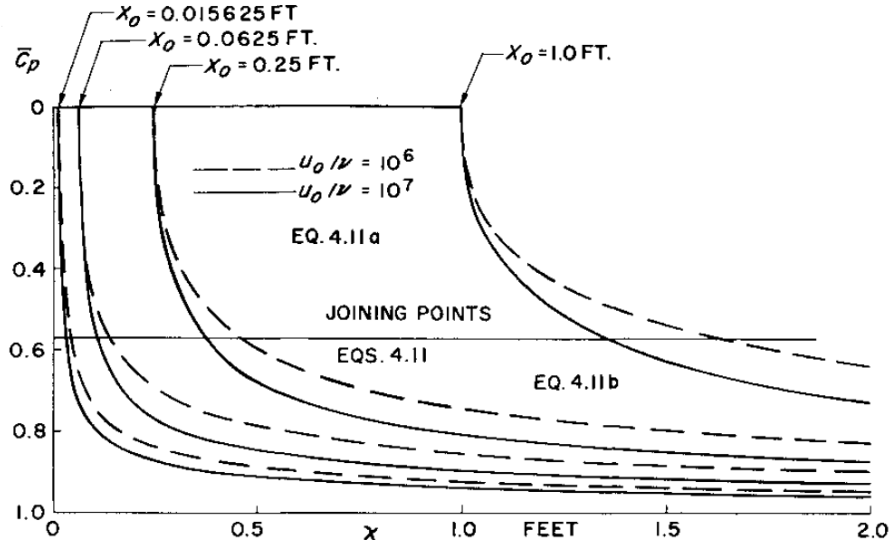


Figure D.1 Stratford limiting flows at two values of unit Reynolds number [113]

In that two-part solution (see Fig. D.1), x_0 is the start of pressure rise, $Re_0 = u_0 x_0 / \nu$, x is the distance measured from the very start of the flow, which begins as flat-plate, turbulent flow. The number n is a constant that Stratford finds to be about 6. The quantities a and b are arbitrary constants used in matching values and slopes in the two equations at the joining point, $\bar{C}_p \geq (n-2)/(n+1)$. Eq. (D.3) describes the beginning of the flow and Eq. (D.4) the final part. The flow is an equilibrium flow that always has the same margin, if any, against separation. More information about Stratford's separation prediction method is found in [113], [114] and [115].

D.3 Constrained Optimization of Stratford's Limiting Pressure Distribution

The method presented above is used for determining the pressure distribution at maximum blade loading and at the limit of separation on the suction side for given boundary conditions:

$$\aleph(\bar{C}_p(x)) = \Im(C_p(x)) = \oint C_p(x) dx = \oint \frac{p - p_\infty}{\frac{1}{2} \rho_\infty u_\infty^2} dx = \oint \frac{p - p_\infty}{0.5 \gamma p_\infty M_\infty^2} dx \quad (D.5)$$

where p is the static pressure at the given location and the other primitive variables correspond to inlet condition denoted by ∞ . The connection between $\bar{C}_p(x)$ and $C_p(x)$ is given by:

$$\bar{c}_p = \frac{p - p_0}{\frac{1}{2}\rho_0 u_0^2} = \frac{C_p - C_{p,0}}{1 - C_{p,0}} = \frac{\frac{p - p_\infty}{\frac{1}{2}\rho_\infty u_\infty^2} - \frac{p_0 - p_\infty}{\frac{1}{2}\rho_\infty u_\infty^2}}{1 - \frac{p_0 - p_\infty}{\frac{1}{2}\rho_\infty u_\infty^2}} = \frac{p - p_0}{p^{total} - p_0} = \frac{p - p_0}{\frac{1}{2}\rho_0 u_0^2} \quad (D.6)$$

The objective function is to

$$\text{minimize } \frac{1}{\kappa(\bar{c}_p(x))} \quad (D.7)$$

$$\text{subject to } p_{opt}^{TE} - p_{outlet} = 0 \quad (D.8)$$

The reason of the constraint to be specified at the presented way is to fix trailing edge condition of Stratford's method expecting that the pressure at the cascade outlet is close to the outlet static pressure.

The optimization procedure is divided by two sub steps. In the first sub step the physical connections between different parameters are described by Stratford's criteria to evaluate limiting pressure distribution. The pressure coefficient at the minimum pressure (p_0) is given by:

$$C_{p,0} = \frac{p_0 - p_\infty}{\frac{1}{2}\rho_\infty u_\infty^2} = \frac{p_0 - p_\infty}{0.5\gamma p_\infty M_\infty^2} = \frac{p_0 - p_\infty}{0.7p_\infty M_\infty^2} \quad (D.9)$$

where p_0 and maximum velocity u_0 is supposed to be constant starting from the leading edge of the suction side till the starting of the increasing pressure gradient (x_0). The Mach numbers M_0 at these points are calculated by:

$$C_{p,0} = \frac{p_0 - p_\infty}{0.7p_\infty M_\infty^2} = \frac{1}{0.7M_\infty^2} \left[\left(\frac{1 + 0.2M_\infty^2}{1 + 0.2M_0^2} \right)^{\frac{\gamma}{\gamma-1}} - 1 \right] \quad (D.10)$$

The T_0 , u_0 and ρ_0 are given by the energy equation of the isentropic flow and ideal gas law:

$$T_0 = T^{total} \left(1 + \frac{\gamma-1}{2} M_0^2 \right)^{-1} \quad (D.11)$$

$$u_0 = \sqrt{\frac{\gamma}{\gamma-1} R(T^{total} - T_0)} \quad (D.12)$$

$$\rho_0 = \frac{p_0}{RT_0} \quad (D.13)$$

The total quantities are equal to the given inlet boundary conditions.

A general way of determining pressure distribution starts with specifying a possible p_0 . All parameter belongs to p_0 can be calculated by Eqs. (D.9)-(D.13). The next step is to find location x_0 , which gives back the required trailing edge static pressure by using Stratford Eqs. (D.3) and (D.4) over x . Hence, the location of starting flow deceleration (x_0) and the Stratford's limiting pressure distribution till the required trailing edge pressure is the output of the first sub step of the optimization procedure. There are infinite possible pressure distributions

exist by the presented method and some of them are shown in Fig. D.2 at given total quantities for a wing profile NACA 65-410 for example.

The second sub step of the optimization procedure is the constraint optimization in order to determine the corresponding flow parameters and location belongs to the minimum pressure and maximum velocity point on the suction surface, which provide the maximum closed surface area bounded by the pressure distribution of the suction side of the profile. p_0 , T_0 , u_0 , ρ_0 , x_0 and $p(x)$ (by Stratford's criteria) parameters will change in the second sub step to satisfy Eq. (D.7) with considering the constraint in Eq. (D.8).

The pressure side distribution is also modified together with the pressure distribution close to the leading-edge stagnation point in order to keep the trailing edge closed (see Fig. 6.5). Linear distribution has been used on the pressure side with keeping open the possibilities for further investigations in the direction of less choking and drag reduction.

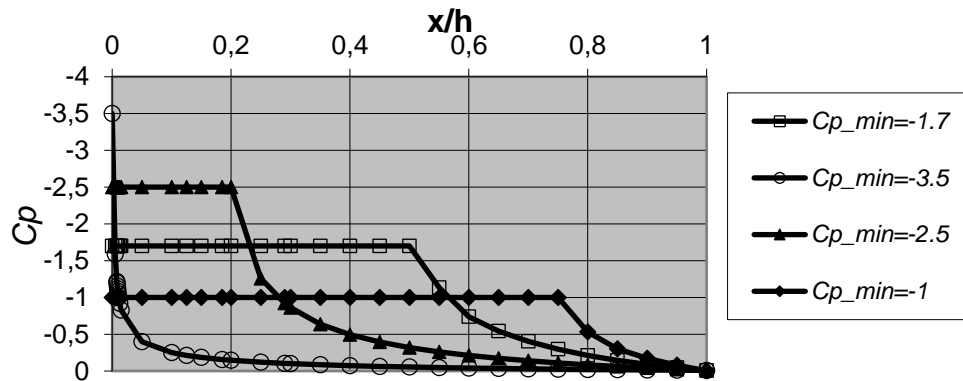


Figure D.2 Suction side pressure coefficient distribution using Stratford pressure distribution close to the separation ($C_p \approx 0$ at trailing edge) for wing profile NACA 65-410 [54]